MICROSTRUCTURAL EVOLUTION AND MECHANICAL PROPERTIES OF HETEROGENEOUS NANOSTRUCTURED HIGH-ENTROPY ALLOYS GENERATED BY SURFACE PROCESSING

YANG WENQING

PhD

The Hong Kong Polytechnic University

2025

The Hong Kong Polytechnic University

Department of Industrial and Systems Engineering

Microstructural Evolution and Mechanical Properties of Heterogeneous Nanostructured High-entropy Alloys Generated by Surface Processing

Yang Wenqing

A thesis submitted in partial fulfilment of the
requirements for the degree of Doctor of Philosophy

April 2025

CERTIFICATE OF ORIGINALITY

I hereby declare that this thesis is my own work and that, to the best of my knowledge and belief, it reproduces no material previously published or written, nor material that has been accepted for the award of any other degree or diploma, except where due acknowledgement has been made in the text.

_______________ (Signed)

___________YANG Wenqing________ (Name of student)

Abstract

Nanostructured materials have garnered significant attention due to their superior properties to coarse-grained materials, such as ultrahigh strength. According to the Hall-Petch relationship, the abundant grain boundaries in nanostructured materials contribute effectively to grain boundary strengthening. However, reducing grain size limits dislocation mobility, leading to poor ductility. To address this strength-ductility trade-off, heterogeneous nanostructured materials have been developed, as their microstructural heterogeneities—such as variations in grain size and phase composition—can facilitate strain redistribution under applied forces, evading strain localization and enhancing overall mechanical performance.

Medium and high entropy alloys (M/HEAs), characterized by their multi-component systems, emerge as promising candidates for structural applications due to their exceptional properties like high strength, superior wear resistance, high corrosion resistance and so on. However, a key challenge lies in overcoming the traditional trade-off between strength and ductility, limiting their broader application in engineering. This challenge is further compounded by the complex interplay between microstructural evolution and deformation mechanisms in heterogeneous systems. While existing studies highlight the potential of microstructural heterogeneities—such as grain size and phase composition variations, improving mechanical properties, the optimal combination of fabrication methods, microstructural characteristics, and deformation behaviors remains insufficiently understood. In particular, some metastable M/HEAs with low stacking fault energy exhibit unique phase transition behaviors, including transformation-induced plasticity, which could play a significant role in enhancing plasticity and work-hardening capabilities. A systematic investigation of the interaction between microstructural features and phase transitions is therefore crucial for advancing the design of M/HEAs with tailored properties. To address these gaps, this thesis employs surface processing techniques—including plastic deformation and thermal treatments—to generate heterogeneous nanostructures in both bcc-based and fcc-based metastable M/HEAs. The heterogeneous structure is generated through different formation mechanisms: gradient plastic strain and accumulated total plastic strain from the surface to the matrix of severe plastic deformation on the surface; and the unique thermal conditions and rapid solidification dynamics with high cooling rate and suppressed grain growth of laser treatment. The effects of these processes on microstructural evolution, phase transition behaviors and its corresponding mechanical properties and deformation mechanism are comprehensively explored to develop effective strategies for overcoming the strength-ductility trade-off. According to the main work done during the research study, the thesis will be divided into the following three parts:

In the first part, a repeated sliding wear process on the surface is adopted to generate a gradient nanostructure (GNS) on a bcc-based dual-phase $TiZrHfTa_{0.5}$ RHEAs with a high content of hcp phase up to 66% acquired from pre-plastic deformation and thermal treatment, which accommodates sliding-caused gradient plasticity and contributes to the enhanced wear resistance. The average grain size decreases significantly when decreasing distance to the worn surface, e.g. from ~100 nm at the depth of ~ 3 μm to ~30 nm in the topmost worn surface region. Also, more hcp phase is formed due to the deformation-induced bcc → hcp phase transition activated within the self-organized gradient worn subsurface, facilitated by atom shuffling and partial dislocation dipole gliding. This heterogeneous structure, characterized by gradients in grain size and hcp phase content, redistributes strain and suppresses localization, significantly improving wear resistance. Consequently, this heterogeneous structure of grain size and hcp phase content formed on this dual-phase $TiZrHfTa_{0.5}$ RHEA exhibits an exceptionally low coefficient of friction at 0.12-0.15 and wear rate at $4.08\text{-}9.68\times10^{-5}$ $mm^3/N\cdot m$, demonstrating the potential of wear-induced surface treatments to enhance tribological properties.

In the second part, a high-strain rate ultra-precision machining technology named single point cubic boron nitride turning (SPCBNT) is employed to fabricate a 60 μm-depth GNS surface layer on a fcc-based dual-phase $Fe_{45}Mn_{35}Cr_{10}Co_{10}$ HEAs with significant phase transition, significantly enhance the strength. The cost-effective SPCBNT can impart a high strain rate (10^4 s^{-1}) in the topmost surface of the specimen and achieve a high-quality surface with nanometer-level surface roughness. This method reduces the average grain size from ~ 30 μm in the matrix core to ~ 13 nm at the surface. Notably, during the machining process, the deformation-induced fcc → hcp phase transitions are activated in this GNS, but a further step of fcc → hcp → bcc only be introduced in the topmost surface as the gradient distribution of plastic strain and strain rate along the depth direction. The nanohardness of the topmost surface of this GNS attains ~6.7 GPa, which is much higher than it at the matrix (~4.3GPs). Analysis based on high-resolution transmission electron microscope unveils the fcc → hcp is facilitated by the movement of Shockley partial dislocations on every second (111)fcc plane, and the subsequent transition hcp → bcc is accomplished by the interaction of two sets of Shockley partial dislocation dipoles on either side of the (0001)hcp planes. This phase transition mechanism of coordinated dislocation dipole interaction and atomic shuffling relieves and accommodates the significant stress and strain fields produced by the plastic deformation on the surface, which significantly influences mechanical properties.

In the third part, different from the above two plastic deformation methods, a thermal-typed laser surface treatment produces a nanostructured layer with crystalline-amorphous microstructure on a fcc-based dual-phase $Fe_{45}Mn_{35}Cr_{10}Co_{10}$ HEAs. The remelting and solidification of the gradient heating and cooling induced by high-power laser beams, with a rapidly high cooling rate of 10^4–10^6 °C/s contributes to the formation of heterogeneous nanostructure. The rapid cooling rate (~10^5 K/s) calculated by simulation during laser remelting produces refined grains (~8 nm) interspersed with amorphous regions along grain boundaries. Based on this formation mechanism, the mechanical properties of this unique crystalline-amorphous microstructure are analyzed to investigate its deformation mechanism and the deformation-induced crystallization mechanism. This unique structure achieves exceptional strength (~3.8 GPa) and compressive strain (~28%) during micro-pillar compression tests. During plastic deformation, dislocations are confined within nanograins and impeded by amorphous boundaries, promoting deformation-induced crystallization and grain coalescence. This process balances strength and ductility by leveraging the interaction between nanocrystals and amorphous grain boundaries, highlighting the effectiveness of laser-based surface treatments for enhancing mechanical properties.

In summary, this thesis systematically investigates microstructural evolution, mechanical properties and corresponding deformation mechanisms of heterogeneous nanostructured M/HEAs generated through surface processing techniques, including sliding wear, high-strain-rate machining, and laser treatment. By elucidating the interplay between microstructural heterogeneities, phase transitions mechanism, and deformation mechanisms, the findings provide essential guidelines for designing advanced HEAs with tailored properties, advancing their potential for technological applications.

Publications Arising from the Thesis

1. **Yang, W.,** Luo, J., Fu, H., Cheung, C. F., Ruan, H., & Yang, X. S. (2022). bcc→hcp phase transition significantly enhancing the wear resistance of metastable refractory high-entropy alloy. *Scripta Materialia*, 221, 114966.

2. **Yang, W.,** Qian, L., Luo, J., & Yang, X. S. (2024). A novel atomic mechanism of fcc → hcp → bcc phase transition in a gradient nanostructured compositionally complex alloy. *Materials Research Letters*, 12(12), 929–938.

3. **Yang, W.,** Lu W., Qian, L., & Yang, X. S. (2025). Achieving enhanced strength-ductility synergy in an additive manufactured eutectic compositionally complex alloy via optimizing alloy composition. *Materials Science and Engineering A*, 941, 148644.

4. **Yang, W.,** Qian, L., Luo, J., Lu W. Gao, Z., Cheung, C., Ruan, H., Wang, Y. & Yang, X. S. (2025). Amorphous boundary crystallization-involved cooperative deformation mechanism in a nanostructured crystalline-amorphous compositionally complex alloy. *Acta Materialia*, under review.

5. Lu, W., **Yang, W.,** Hu, R., Yang, X. S. (2025). Coherent intergranular precipitates overcome intermediate-temperature embrittlement of a L12-strengthened medium-entropy alloy. *Scripta Materialia*, 268, 116876.

6. Gao, Z., Hou, X., **Yang, W.,** Chan, K. C., Fu, H., Wang, D., & Yang, X. S. (2025). Achieving the strength-ductility balance in heterogeneous (FeCrCoNi) 95B5 high-entropy alloy by laser surface remelting. *Materials Science and Engineering: A*, 148644.

7. Zhang, J., Qian, L., **Yang, W.,** Wang, J., & Yang, X. S. (2025). Dislocation nucleation and shear sliding at dual-phase high-entropy alloy semi-coherent interface with atomic complexity. *Acta Materialia*, 121118.

8. Qian, L., **Yang, W.,** Luo, J., Wang, Y., Chan, K. C., & Yang, X. S. (2023). Amorphous Thickness-Dependent Strengthening–Softening Transition in Crystalline–Amorphous Nanocomposites. *Nano Letters*, 23(23), 11288-11296.

Acknowledgements

First and foremost, I would like to express my deepest gratitude to my supervisor, Dr. YANG Xusheng, for his invaluable guidance, support, and constant encouragement throughout my Ph.D. journey. I am deeply grateful for the opportunity to learn and grow under his mentorship. His expertise and constructive advice have been a cornerstone of my academic research and personal development.

I would also like to extend my heartfelt appreciation to my research group members for their thoughtful guidance and inspiring advice. I am grateful to Dr. FU Hui, Dr. WU Bo, Dr. YUAN Shuqing, Dr. LUO Jiasi, Dr. QIAN Lei, Dr. LU Wenjie, Dr. WANG Yilin, Mr. GAO Zhenguang, and Mr. QIN Bailiang for their generous advice on my research and kind encouragement in my daily life. A special thanks to my dear friend, Ms. YANG Lei, for her understanding and support, and to my best Brazilian jiu-jitsu partner, Ms. Ocean Annika, for her companionship at my whole training time. Oss!

I owe my deepest gratitude to my parents, Mr. YANG and Ms. LI, for their endless love, encouragement, steadfast belief and unwavering support, which have been my anchor during the hard period. Finally, I would like to express my deepest gratitude to my husband, Mr. WEI Ziyao, for his unwavering support, patience, and encouragement throughout this challenging journey. Thank him for being my remote pillar of strength, for the great sacrifices he made, and for always reminding me of my capabilities.

Contents

List of Figures

Chapter 1 Introduction

Throughout history, the exploration for developing new materials has been a key pursuit of human civilization [1]. This endeavor has led to the discovery of new metals and the invention of various alloys, which have played a crucial role in shaping our world for thousands of years. Traditionally, alloys have been developed based on a 'major element' paradigm, where one or occasionally two principal elements, such as iron in steel, copper in bronze, or nickel in superalloys, form the foundation. Minor alloying elements are then added to enhance the properties of the alloys.

However, a novel concept for alloy design emerged approximately a decade ago [2]. This approach involves mixing multiple elements in an equimolar or near-equimolar composition, deviating from the traditional 'major element' concept. These specially designed alloys, called 'high-entropy alloys' (HEAs), were coined by Yeh et al.[3]. The term 'high entropy' signifies the high configurational entropy resulting from the random mixing of elements in these alloys. Over time, there has been a growing interest in the study of HEAs [4, 5]. Nevertheless, despite the increasing research focus on HEAs, the study of HEAs still needs to be improved, and there is much more to explore and understand to grasp their potential and applications fully. Continued investigation and exploration of HEAs hold great promise for advancing the field of materials science and engineering.

1.1 High-entropy Alloys (HEAs)

1.1.1 Definition

Unlike conventional alloys, HEAs contain multiple elements in equiatomic or near-equiatomic fractions and the concentration of each element is between 5% and 15% [6]. Instead of complicated phases, HEAs tend to have solid solution structures, which are stabilized by their high configurational entropy of mixing. The following equation expresses how the configurational entropy of mixing increases as the number of composing elements and their concentrations rise [7]:

$$\Delta S_{\mathrm{conf}} = -\mathrm{R}\sum \mathrm{n_i} \ln(\mathrm{n_i}) \qquad (1.1\text{-}1)$$

where $\mathrm{n_i}$ is the atomic fraction of the ith element and R is the gas constant. Based on that, these alloys are divided into the following four categories: (i) HEAs with $\Delta S_{\mathrm{conf}} \geqq 1.61\mathrm{R}$, (ii) medium-entropy alloys (MEAs) with $1.61\mathrm{R} \geqq \Delta S_{\mathrm{conf}} \geqq 0.69\mathrm{R}$, and (iii) low-entropy alloys (LEAs) with $\Delta S_{\mathrm{conf}} \leqq 0.69\mathrm{R}$ [8].

Moreover, two parameters were proposed to design HEAs, namely, the atomic size difference d and the mixing enthalpy ΔH_{mix} [9]:

$$\delta\% = 100\% \sqrt{\sum_{i=1}^{n} c_i \left(1 - \frac{r_i}{\sum_{j=1}^{n} c_j r_j}\right)^2} \qquad (1.1\text{-}2)$$

where c_{i} and r_{i} denote the atomic fraction and atomic radius of the ith element, respectively.

$$\triangle H_{mix} = \sum_{i=1,i\neq j}^{n} \Omega_{ij} c_i c_j = \sum_{i=1,i\neq j}^{n} 4 \triangle H_{ij}^{mix} c_i c_j \qquad (1.1\text{-}3)$$

where $\triangle H_{ij}^{mix}$ is the enthalpy of mixing of the binary liquid between the ith and jth elements at an equiatomic composition. In general, the formation of a single-phase solid solution corresponds to the region -15 kJ/mol < $\triangle H_{mix}$ < 5 kJ/ml and 0 < δ < 5. Different phases then appear with the variation in $\triangle H_{mix}$ and δ. With the further increase in δ (>8) and decrease in the negative $\triangle H_{mix}$ value (< -15 kJ) [9].

The high-entropy phases like solid-solution phases are normally stabilized by high-entropy effect, which also form intermetallic compound phases for equi- or near-equi-atomic alloy compositions. The Gibbs free energy of mixing is listed [8]:

$$\triangle G_{mix} = \triangle H_{mix} - T \triangle S_{mix} \qquad (1.1\text{-}4)$$

where $\triangle H_{mix}$ and $\triangle S_{mix}$ are the enthalpy of mixing and entropy of mixing, respectively. Although increasing the number of constituent elements in an alloy enhances configurational entropy, which can promote the formation of solid solutions. However, the $\triangle H_{mix}$ depends on atomic size mismatch, chemical affinities, and electronic interactions among components. This entropic effect competes with enthalpic contributions, and does not guarantee solid solution stability in all cases. A highly positive $\triangle H_{mix}$ can outweigh the entropic contribution, leading to phase separation or the formation of intermetallic compounds, even in systems containing multiple principal elements.

According to the Gibbs phase rule, the number of phases (P) in a given alloy at constant pressure in equilibrium condition is [10]:

$$P=C+1-F \qquad (1.1\text{-}5)$$

The number of components (C) and the maximum number of thermodynamic degrees of freedom (F) in a system are linked by certain constraints. However, it is noteworthy that not all multi-component alloys in an equal molar ratio will form solid solution phases at the center of the phase diagram. The formation of solid solutions, rather than intermetallic compounds, is limited to carefully selected compositions that meet specific criteria for HEA formation.

Given the equimolar nature of HEAs, differentiating the solvent from the solute based on Gibbs phase rules can be challenging. Consequently, many multi-principal-element alloys tend to form simple phases, such as bcc or fcc solid solutions, leading to a considerably reduced number of phases compared to the maximum possible. This phenomenon suggests that the high entropy characteristic of HEAs widens the solution limits between the constituent elements, favoring the formation of high-entropy phases, i.e., solid-solution phases, over intermetallic phases. Intermetallic phases, in contrast, typically exhibit organized structures with low configurational entropy.

The periodic table comprises a total of 118 elements that have been verified, of which 72 elements are classified as neither noble gases, halogens, nor radioactive [1]. Consequently, these 72 elements offer potential for utilization in the alloying of HEAs [1]. The versatility of HEAs is reflected in the extensive range of elements employed, with over 37 elements being utilized in the creation of numerous HEA compositions. Notable among these elements are Fe, Ni, Cr, Co, Al, Cu, Ti, Mn, V, Zr, Mo, Nb, Si, Ta, and Sn, which have demonstrated significant contributions to HEA development [7]. In the early stages of HEA composite formulation, particular emphasis was placed on the utilization of Fe, Ni, Cr, Co, Cu, and Mn as primary constituent elements. Notably, approximately 85% of 3d transition metal-based HEAs incorporate a minimum of four elements in Figure 1.1, selected from Al, Co, Cr, Cu, Fe, Mn, Ni, Ti, and V [11]. On the other hand, refractory elements characterized by relatively large atomic sizes, such as V, Zr, Mo, Nb, and Ta, are frequently employed in the fabrication of bcc-structured refractory HEAs (RHEAs) [12].

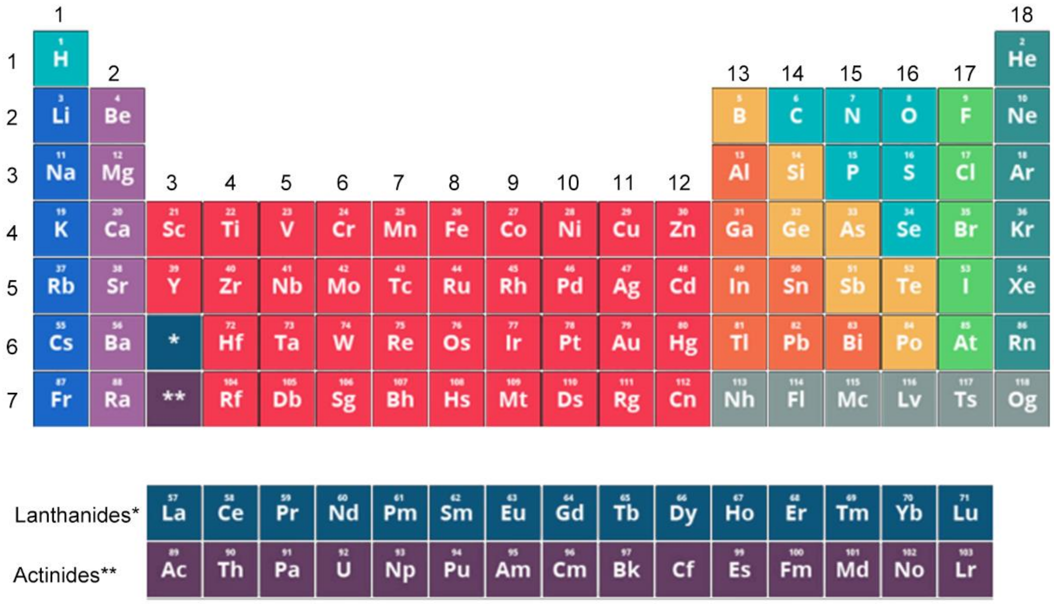

Figure 1.1 Periodic table of elements used in HEAs [7].

1.1.2 Notable HEAs

Single-phase, solid-solution HEAs with fcc, bcc, hcp and orthorhombic crystal structures have been identified [2].

1.1.2.1 fcc-based HEAs

The equiatomic fcc-based CoCrFeMnNi HEA, known as the Canter alloys, was proposed as single-phase fcc solid solution, which is one of the most widely studied HEAs [13, 14]. The Cantor alloys exhibit excellent properties at room temperature, high temperature and cryogenic temperature. As shown in Figure 1.2(a), with enhanced work-hardening rate, the strength and ductility increased with the decrease of temperature, with ultimate strength and elongation at cryogenic temperature in excess of 1 GPa and 60%, respectively [15, 16].

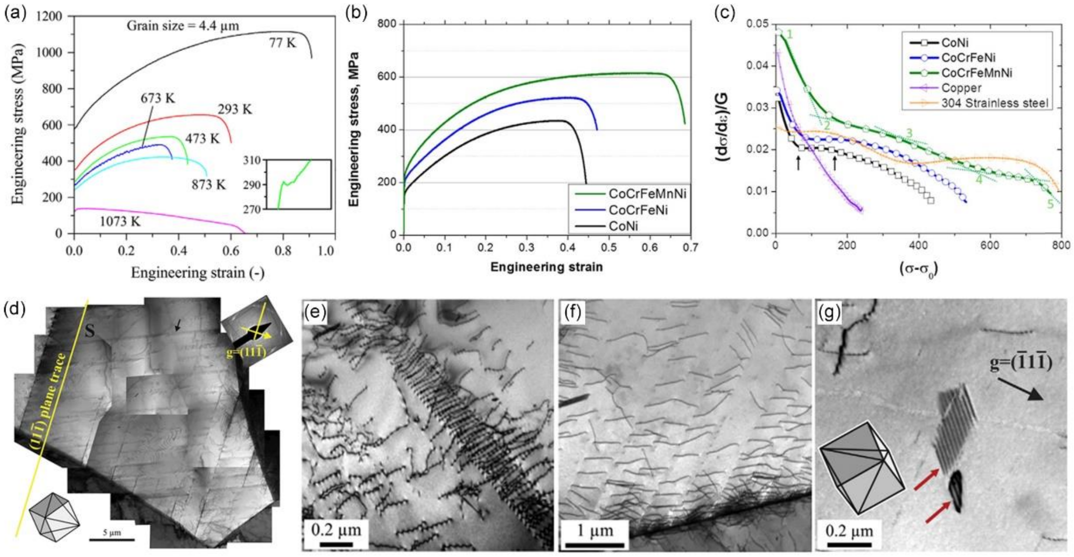

Figure 1.2 (a) Representative engineering stress–strain curves of the CoCrFeMnNi alloy at the six testing temperatures [16]. (b) Stress-strain curves and (c) normalized strain hardening curves of different equiatomic HEAs [17]. (d-g) Representative TEM BF images of tensile test specimens of the CoCrFeMnNi HEAs with planar slip of 1/2<110>-type dislocations on the {111} planes [16].

Based on the empirical verification of the HEAs, it is proposed that the microstructure has a significant effect on critical property, including the dislocation mobility and stacking-fault energy (SFE), processing method and so on. Currently, it is well-established that three primary deformation mechanisms (dislocation slip, deformation-induced twinning, and deformation-induced martensitic transformations) play crucial roles in materials. These mechanisms are significantly influenced by the SFE and the conditions of deformation temperature and pressure. For metals with low SFE values, the difficulty of cross-slip facilitates the occurrence of deformation-induced twinning and martensitic phase transformations as ways to accommodate the applied strain during deformation [18]. Basically, the deformation mechanism of Cantor alloys is mainly accomplished by dislocation slip as the high activity of slip systems. For example, the plastic deformation occurred exclusively through the planar gliding of dislocation 1/2<110> on the {111} planes denoted in Figure 1.2(d-g), the slip became more homogeneous as the strain increased, leading to the development of cell structures [16].

Consequently, several variants derived from the equimolar Cantor alloy, either with fewer alloying elements or non-equimolar compositions, have been developed [13, 19]. One of the underlying motivations for these variants was to minimize the SFE, thereby facilitating the occurrence of phase transformation and/or deformation twining [20]. This deliberate approach aimed to create materials that possess enhanced potential for strain-hardening, as exemplified by the equiatomic CrCoNi medium-entropy alloy [21]. Through subjecting the single-phase CrCoNi alloy to cold work followed by partial recrystallization, a notable enhancement in yield strength beyond 1 GPa has been achieved; however, this improvement came at the expense of reduced tensile ductility, which decreased to approximately 20-30%. In comparison to the Cantor alloy, the CrCoNi alloy displayed a lower SFE and higher yield strength, rendering it more susceptible to reaching the twinning stress and exhibiting abundant nano-twinning. Another example is the non-equiatomic Fe-Mn-Co-Cr-Ni HEA in Figure 1.2(b-c), that primarily underwent planar dislocation slip during the initial stages of deformation and subsequently experienced deformation twinning at high strains (>10%) at room temperature [18, 22]. Conversely, within the equiatomic Cantor alloy, such twinning behavior is typically observed only under cryogenic conditions or applying exceedingly high strains. The non-equiatomic multi-component Cr-Mn-Fe-Co-Ni HEAs have been developed with the addition of interstitial elements like C, N and O [15, 23], which displayed distinct deformation mechanisms include forming planar slip substructures at low strain levels and intricate cell structures characterized by high dislocation-density walls at higher strains.

Kim et al. [24] investigated the transformation of deformation mechanisms at room temperature and 223 K. The results revealed that at room temperature, the alloy primarily exhibits deformation twinning, whereas at the lower temperature of 223 K, strain-induced hcp phase transformation occurs. Despite the different deformation mechanisms, the alloy showed relatively large elongation at both temperatures (48% and 55%), with a higher strain hardening rate at the lower temperature, as illustrated in Figure 1.3. The formation of the hcp phase at lower temperatures enhanced the ability of interface to impede dislocation motion, thereby increasing the strain hardening rate. This temperature-dependent shift in deformation mechanisms is linked to a decrease in SFE. Additionally, the alloy displayed a complex dislocation structure at varying temperatures, including extended dislocations, dislocation loops, high-density dislocation walls, and subgrain structures, all of which significantly influence the mechanical properties of the alloy.

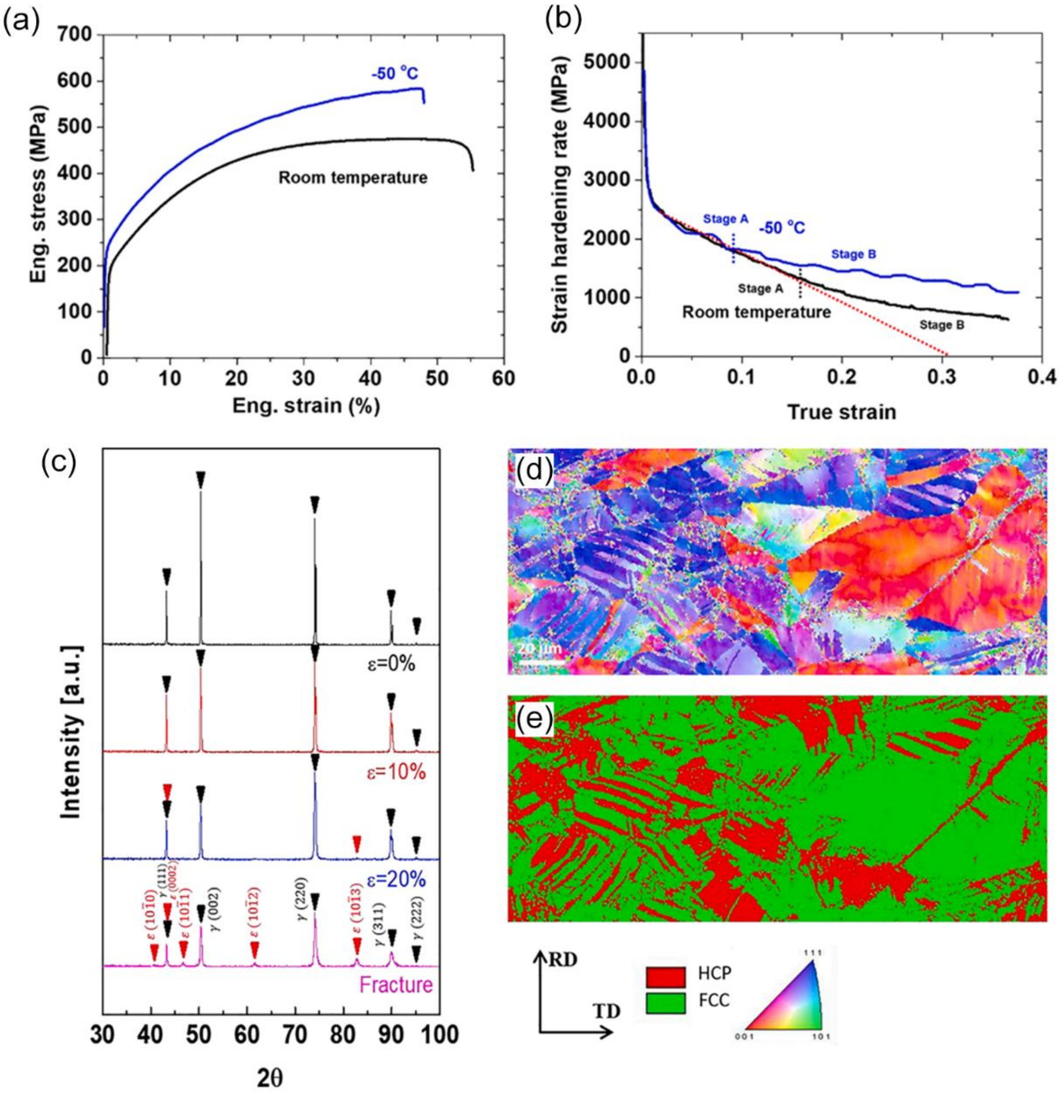

Figure 1.3 Mechanical properties of Fe40Mn40Co10Cr10. (a) Engineering stress-strain curves at 273 K and 223 K and (b) strain hardening rate curves. (c) XRD patterns and (d-e) EBSD micrographs of the material deformed at 223 K [24].

1.1.2.2 bcc-based HEAs

Compared with fcc-based Cantor-based HEAs, the RHEAs composed of refractory elements with high melting pointed were developed with the increased requirements of applications. The RHEA compositions that are most frequently used are HfNbTaTiZr, MoNbTaW, MoNbTaVW, NbTiVZr, AlMoNbTaTiZr [11]. For example, the most well-known HfNbTaTiZr RHEA with single bcc phase showed high compressive yield strength ($\sigma_{0.2}$ = 929 MPa) and ductility ($\varepsilon > 50\%$) with considerable strain hardening and homogeneous deformation [25]. Notably, the HfNbTaTiZr RHEA exhibits asymmetrical strain-hardening behavior under compression and tension, primarily due to distinct deformation mechanisms and internal microstructure evolution under different loading conditions. Typically, the compressive stress-strain curve exhibits a higher strain hardening rate compared to tension. Under compression, the samples can sustain continuous plastic deformation until fracture occurs due to accumulated plastic strain and structural instability [26]. The compressive stress state suppresses crack propagation and enhance plastic stability. In contrast, under tensile loading, necking occurs in the fracture region, leading to localized deformtation and early crack initiation, which limits the strain hardening [27]. Moreover, tension tends to favor dislocation slip-dominated deformation, while compression promotes shear-dominated mechanisms that can accommodate larger plastic strains.

Then Senkov et al. [28] continued investigating the microstructure and mechanical properties of Nb25Mo25Ta25W25 and V20Nb20Mo20Ta20W20 RHEAs, which maintained single bcc structure after annealing at 1400 °C for 19 h. Based on the mechanical properties of coarse grains, plastic deformation like cold rolling was used to control grain size, thereby enhancing the mechanical properties with yield stress at 1145 MPa and ultimate tensile strength at 1262 MPa, as shown in Figure 1.4 [29].

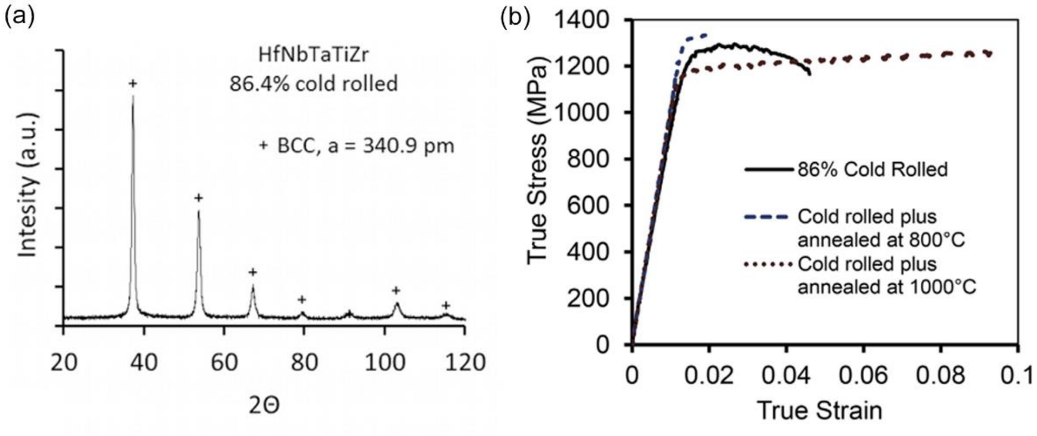

Figure 1.4 (a) X-ray diffraction patterns for HfNbTaTiZr (b)True stress-strain curves of as-cold-rolled and rolled-and-annealed sheet of HfNbTaTiZr [29].

The CrMoNbV RHEA was designed with excellent high-temperature strength which exceeds 1000MPa at1273K [30]. This outstanding high-temperature strength originates from the large atomic size and elastic modulus mismatch, temperature-insensitive elastic constants, and the predominance of non-screw dislocations pinned by vital solute atoms. The addition of Cr elements (smaller atomic radius, larger shear modulus) and Mo elements (smaller shear modulus) is the main reason for the large mismatch in atomic size and elastic modulus. The use of tempering elements Nb and V with temperature-insensitive elastic constants also helps the alloy maintain excellent mechanical performance at high temperatures. Moreover, the dislocation slip is one of the essential deformation mechanisms. The bcc structure of these alloys provides multiple slip systems, allowing for plastic deformation, with dislocations typically moving on {110} planes in Figure 1.5 [30].

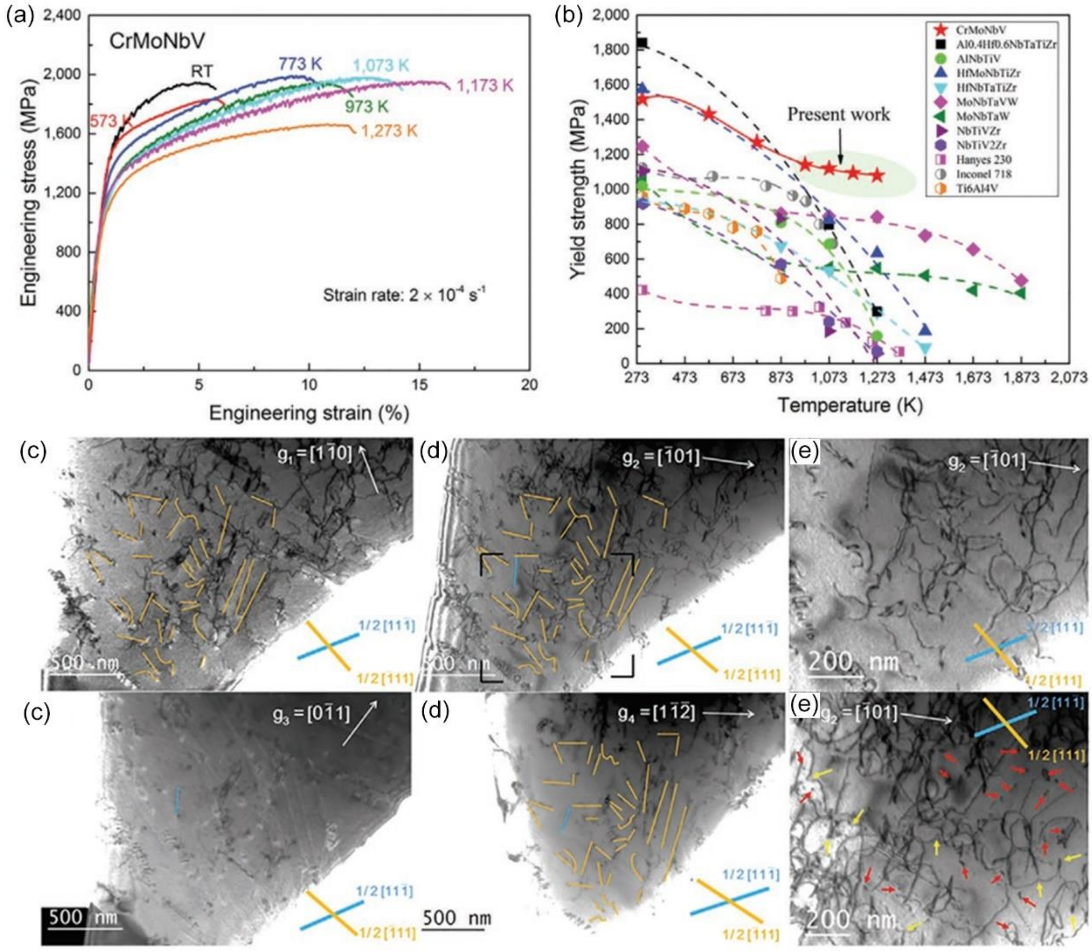

Figure 1.5 Mechanical properties of the CrMoNbV alloy as (a) room temperature and (b) elevated temperature (573 K- 1273 K). (c-e) TEM images of dislocations with different g vectors along the zone axes of [111] or [110] [30].

Therefore, based on the abovementioned representative HEAs, it is evident that phase composition plays a pivotal role in governing the mechanical response of these alloys. One effective empirical approach to estimate phase stability is through the valence electron concentration (VEC), which is calculated as follows [31]:

$$VEC = \sum_{i=1}^{n} c_i VEC_i \qquad (1.1\text{-}6)$$

The crystal structure of HEAs correlates strongly with VEC. Alloys with VEC ≤ 6.87 generally favor the formation of bcc structures, whereas fcc phases are typically stabilized when VEC ≥ 8.0. In the intermediate range (VEC ≈ 4.09–4.18), a combination of bcc and hcp phases can be observed. These phase types directly influence mechanical behavior. Fcc-structured HEAs usually exhibit higher ductility and lower strength due to the abundance of slip systems facilitating dislocation motion. In contrast, bcc-structured HEAs possess fewer slip systems and are subject to higher Peierls stress [32], which is the lattice resistance to dislocation motion, leading to reduced dislocation mobility. Consequently, bcc-phase HEAs tend to exhibit greater strength and hardness but limited ductility [33]. For example, the AlCoCrFeNi alloy modified with 5 wt% NiTi forms a dual-phase (fcc + bcc) lamellar eutectic structure [34]. The increased bcc phase fraction, combined with the strengthening effect of NiTi particles, results in a low wear rate of 0.71 ± 0.01 $mm^3/N \cdot m$, demonstrating the performance advantages conferred by tailored phase composition. Furthermore, mechanical properties can be further tuned by adjusting the alloying elements to manipulate the VEC. Specifically, incorporating elements with lower valence electron counts, such as Mo and Nb, into bcc-based HEAs decreases the ideal shear strength, thus promoting dislocation activity and improving ductility [35].

1.1.3 Properties and Applications of HEAs

1.1.3.1 Mechanical Properties of HEAs

The HEAs offer numerous remarkable features, including high strength [22, 36, 37], high fracture toughness at different temperatures [38, 39], enhanced thermal stability [40] and strong corrosion resistance [41]. Their unique structure and balanced elemental composition endow

HEAs with exceptional mechanical and physical properties.

(1) Mechanical behavior at room temperature: In engineering area, ideal HEAs could typically satisfy the requirements of low density and high strength/hardness, particularly for structural applications in civil transportation and aerospace engineering, where reducing the weight of components is crucial for energy efficiency [9]. Figure 1.6(a) shows maps of yield strength versus Vickers hardness, placing HEAs in the top-right region, indicating their superior yield strength and hardness compared to traditional materials like stainless steel, magnesium, nickel alloys, and glasses [8]. Moreover, the mechanical properties of HEAs vary significantly depending on their phase composition, as shown in Figure 1.6(b-c) [35]. Different content of Mo was added in CrMnFeCoNi to form sigma phase, which increased yield strength from 216MPa to 765MPa [42]. Similarly, the fine orthorhombic needle-like plates within bcc Al10Hf25Nb5Sc10Ti25Zr25 HEAs exhibited ultimate strength at 1240MPa, which revealed that twins and hcp plates play a crucial role in plastic deformation and strengthening of the materials [43].

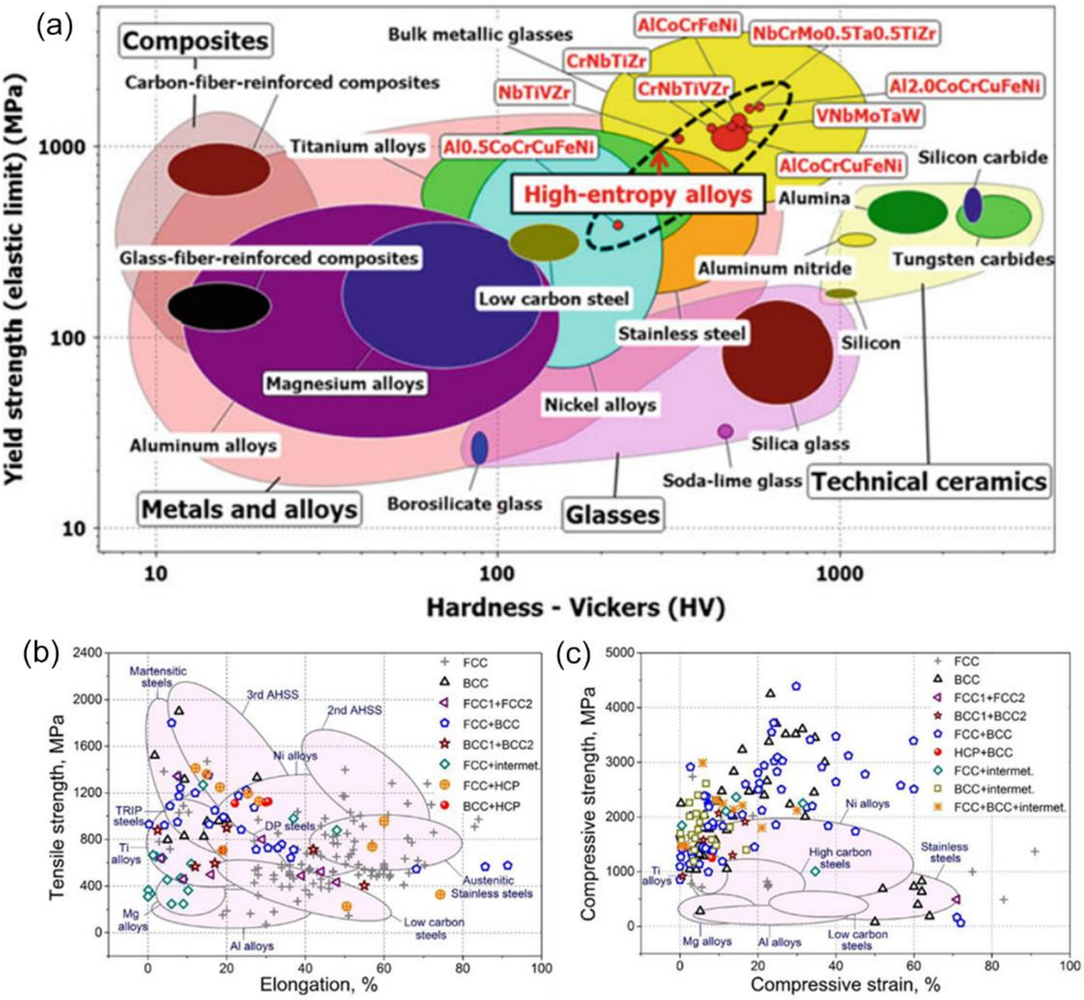

Figure 1.6 (a) Maps showing the range of yield strength versus HV for structural materials [8]. (b) tensile strength vs elongation and (c) compressive strength vs compressive strain of HEAs composed with different phase [35].

(2) Mechanical behavior at wide temperature range: As discussed earlier, the fcc-based CrMnFeCoNi alloy is one of the most HEA in terms of mechanical properties at room temperature and below. These HEAs exhibit a strong temperature dependence, with yield strength increasing as temperature decreases [44]. This is due to a shift in the deformation mechanism from single dislocation movement to a combination of deformation-induced twinning and dislocation gliding. Conversely, TaNbHfZrTi RHEAs demonstrate continuous

strain hardening and good ductility at high temperatures [45]. The yield strength of this alloy ranged from 929 MPa at 296 K to 92 MPa at 1473 K. The mechanical behavior of HEAs at elevated temperatures is illustrated in Figure 1.7 (a) [35]. Compared to traditional metals, the HEAs maintain good mechanical properties at temperatures exceeding 600°C. Currently, the AlCoCrFeNi HEAs were introduced as hypoeutectic, eutectic and hypereutectic states by Guo. et al [46], which showed good mechanical properties with stable phase boundaries achieved in a wide compositional range, and at both room and cryogenic temperatures, as shown in Figure 1.7 (b).

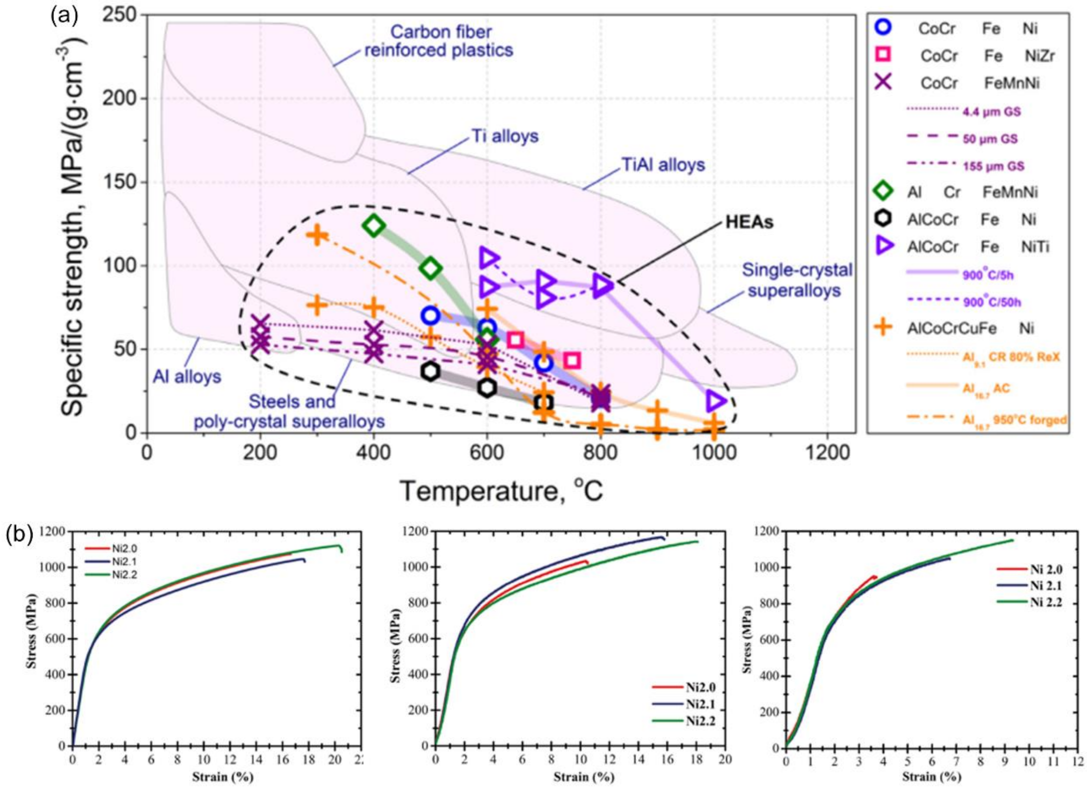

Figure 1.7 (a) Specific strength vs. temperature of HEA with respect to conventional high temperature materials [35]. (b) Engineering tensile stress-strain curves of AlCoCrFeNix(x = 2.0, 2.1 and 2.2) alloys at RT, at -70 ºC, and at -196 ºC [46].

(3) Creep behavior: The creep behavior of a number of HEAs has been studies in a range of temperature, for example, dislocation creep behaviors of CoCrFeMnNi at room temperature [47], time-dependence plastic deformation behavior of nanocrystalline and coarse-grained CoCrFeMnNi [48], creep behavior of the AlTiVNbZr0.25 HEAs by employing the uniaxial stress-relaxation tests at 1073K [49]. The creep characteristics are typical for class A behavior with viscous glide by interaction of dislocations and specific atoms [49]. The quasi-stationary creep rate obeys a three-power law and the transients after stress changes are inverted.

(4) Fatigue behavior: Given that many potential applications for HEAs, such as aircraft engine components, frequently encounter cyclic loading, the fatigue properties of HEAs are critically important. Generally, fatigue failures occur through the fundamental stages of crack initiation and propagation, and the fatigue mechanism of different crystal structure in HEAs are compared in Figure 1.8 [50]. For example, the fatigue behavior of wrought Al0.5CoCrCuFeNi HEAs with dual fcc phases has been investigated in terms of high-cycle stress-lifetime (S-N) relations and fatigue strength. This assessment involved conducting four-point bending fatigue tests at room temperature with a stress ratio (R) of 0.1, where R is defined as the ratio of applied minimum stress (σ_{min}) to maximum stress (σ_{max}). The fatigue-endurance limit and the ratio of fatigue-endurance limit to ultimate tensile strength were determined to be within the ranges of 540-945 and 0.402-0.703, respectively [51]. Additionally, the impact of temperature on fatigue-crack growth was examined for the CrMnFeCoNi HEAs, utilizing disc-shaped compact-tension specimens subjected to a load ratio of R=0.1 [52]. The lower fatigue ratios of HEAs

are notably superior to those of steels, titanium, and nickel alloys, and they also outperform zirconium alloys and certain Zr-based bulk metallic glasses.

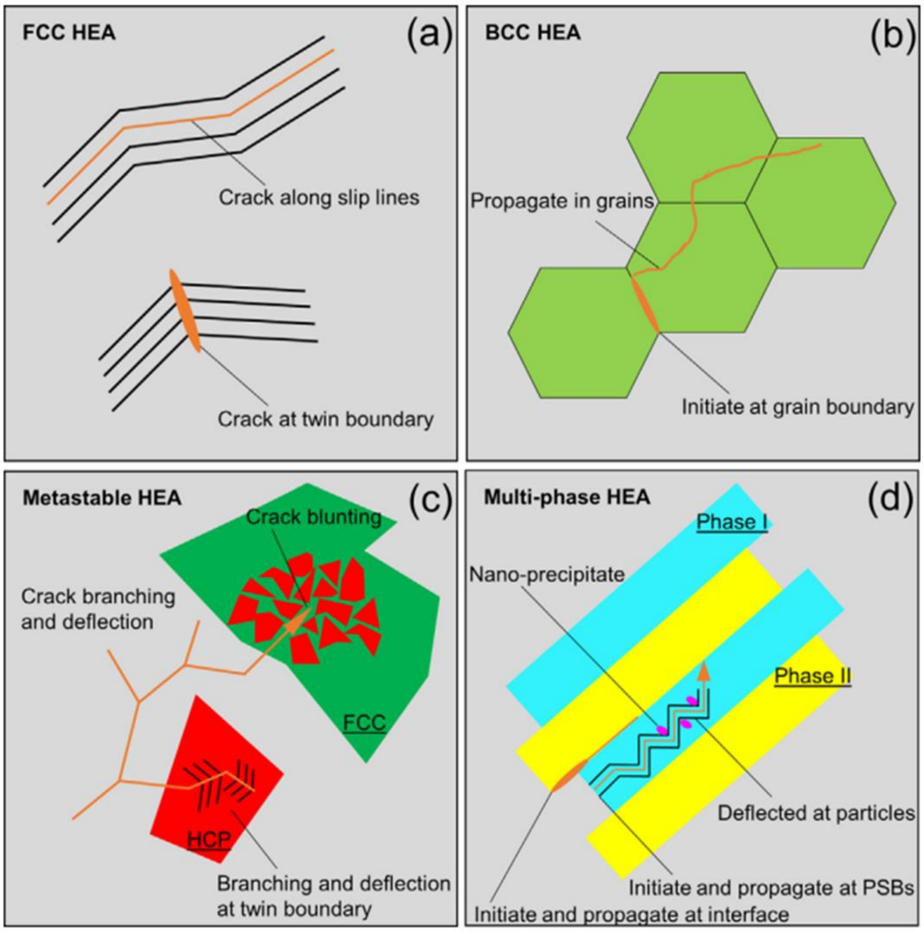

Figure 1.8 Schematic illustration of the fatigue mechanism in the (a) fcc-based, (b) bcc-based, (c) metastable with phase transformation from fcc to hcp and (d)multi-phase HEAs [50].

(5) Wear behavior: Wear is a significant problem limiting the lifetime of metallic components in a variety of functional and structural applications. As a result, the development of novel metallic alloys with excellent wear resistance is in high demand to ensure the reliability, longevity, and efficiency of metallic contacts in severe situations. This enhancement is

attributed to its high hardness, which not only prevents plastic deformation and delamination but also contributes to oxidative wear resistance, facilitated by the formation of an oxide film. For example, the wear performance AlCoCrFeNi HEAs was enhanced with the increase of temperature as the formation of a compact oxides in the contact region and a precipitation strengthening in the subsurface [53]. The TiZrNbTaMo HEAs exhibited superior dry- and wet-wear resistance with low wear rates at 3×10^{-7} $mm^3\cdot N^{-1}\cdot mm^{-1}$ and 2.6×10^{-7} $mm^3\cdot N^{-1}\cdot mm^{-1}$, respectively [54].

1.1.3.2 Applications for HEAs

HEAs have the potential to be employed in a wide range of applications, including structural and functional materials. Additionally, HEAs can be used with liquids, polymers, and even ceramics [10]. With excellent wear and corrosion resistance, HEAs can be used as coasting to resist the high-temperature friction and corrosion. Besides, the introduction of Al and Cr elements into HEAs, for example, AlCoCrFeNi2.1 HEAs, enhanced the oxidation resistance and corrosion resistance of HEAs [55], which exhibited potential power to be ice-breakers, pipelines in ships, motor housing, valves, offshore oil platform, acid pump components, instead of copper alloys and stainless steels, and be complex structural castings requiring both excellent mechanical properties and corrosion resistance. Moreover, the fcc-based HEAs can keep superior mechanical properties in a wide range of temperatures from 77K to as high as 1000K. In addition, the RHEAs and some eutectic HEAs could be helpful to for thermal barrier coatings and heat-resistant/ wear-resistant coatings as they have excellent high-temperature mechanical performance [56]. As a new class of metal materials containing multi-principal elements, HEAs demonstrate unique and attractive engineering properties.

Another promising application for HEAs is functional materials. For instance, adding lightweight elements can reduce the density of HEAs, making them suitable for mobile devices, battery anodes, and the transportation industry. Additionally, the excellent damping properties of certain HEAs make them ideal for manufacturing shock absorbers [31]. Furthermore, HEAs with lamellar structures can exhibit magnetoresistance between hard and soft magnetic phases. In summary, HEAs, with their tailored structures and properties, can potentially revolutionize metallic materials.

1.2 Strategies to Improve Mechanical Properties

Like traditional polycrystalline metals and alloys, HEAs derive their primary strength from inherent lattice friction, which impedes dislocation motion. Additionally, they benefit from multiple strengthening mechanisms such as solution strengthening, precipitation strengthening, grain refinement, phase transformation-induced strengthening, and deformation twin strengthening, further enhancing their mechanical properties.

1.2.1 Grain-boundary strengthening

Grain boundary (GB) plays a crucial role in impeding dislocation movement during the plastic deformation process. This strengthening effect is due to two microstructural factors: the requirement for dislocations to change direction at GBs because of varying grain orientations and the discontinuity of slip planes between adjacent grains [12]. Based on the classical Hall-Petch relationship, it is known that reducing grain size can increase pinning points impeding the propagation of dislocations. The Hall-Petch equation between yield stress (σ) and grain size (d) is listed below:

$$\sigma = \sigma_0 + k_\sigma d^{-1/2} \qquad (1.2\text{-}1)$$

where σ_0 is the intrinsic stress, d is the grain size and k_σ is the Hall-Petch coefficient. Numerous disordered GBs necessitate more energy for dislocation to traverse into adjacent grains. This impediment restricts dislocation movement within slip planes, reducing plasticity and increasing strength. Additionally, grain morphology significantly affects the GB strengthening mechanism. Coarse grains weaken GBs and inter-grain bonding, leading to rapid deterioration of thermo-plasticity in the solidified microstructure. Therefore, refining grains hinders dislocation motion by providing more obstacles and increasing the GB fraction relative to grain volume, effectively restricting interaction between GB and dislocations, as shown in Figure 1.9(a) [57]. The comparison of synergistic strength and ductility for various HEAs, MEAs, and traditional nanocrystalline alloys with different compositions is shown in Figure 1.9(b) [58]. While increased strength typically results in decreased ductility, like traditional nanocrystalline alloys, grain refinement notably enhances the strength of HEAs.

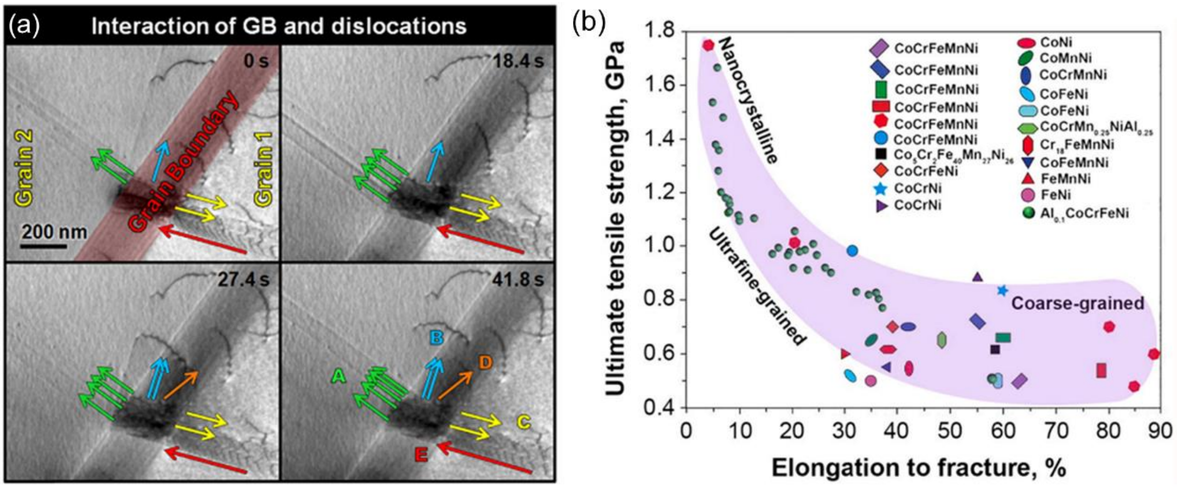

Figure 1.9 (a) Interactions between GBs and dislocations in the CrFeCoNiPd HEAs [57] (b) Strength-ductility synergy in single phase HEAs, MEAs and traditional nanocrystalline alloys with compositional variations [58].

For instance, the research results of fully recrystallized CrCrFeMnNi HEAs with different grain size ranging from 503 nm to 88.9 nm showed that yield strength significantly increased from 236 MPa to 888 MPa, and the strain-hardening curves changed as well, as shown in Figure 1.10 [59]. For materials with low SFE, strain-hardening is sensitive to grain size as the dislocation and deformation twin could be activated at different strains. Similarly, the grain size of HfNbTaTiZr RHEAs was controlled by heat treatment [60], which increased both strength and ductility as the grain growth rate was controlled by the slowest element, i.e., Nb and Ta, of these materials.

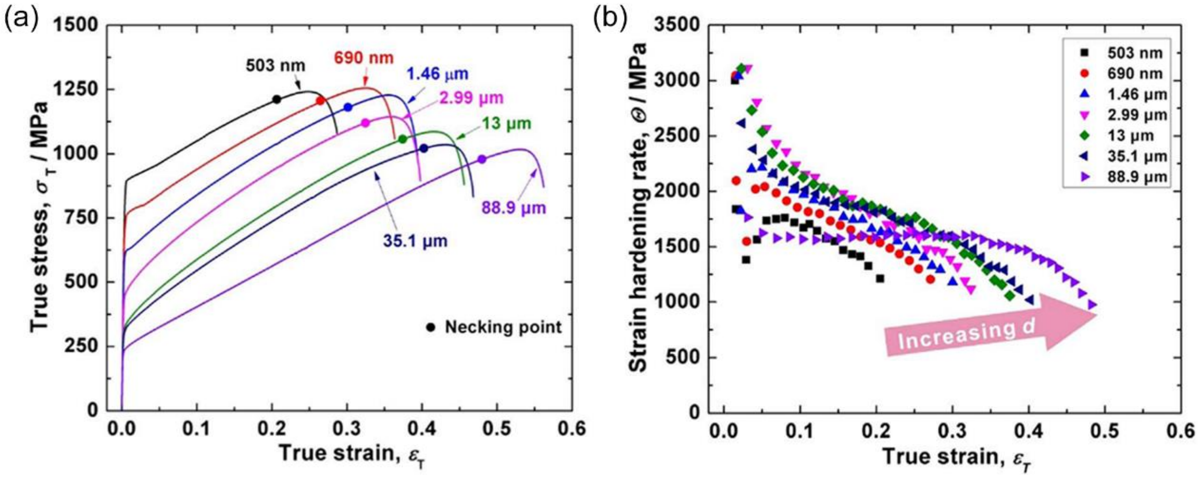

Figure 1.10 (a) Tensile true stress-strain curves and (b) strain-hardening rate curves of CoCrFeMnNi HEAs with different grain sizes [59].

Moreover, grain refinement can be applied to reinforce the effect of twinning and phase transformation during deformation process. The TWIP effect was activated in Cr20Mn15Fe34CoNi11 HEAs after grain refinement, which simultaneously increased strength and maintained ductility [61]. When the grain size is reduced to ~1.5 μm, the deformation twinning ensures a high strain hardening rate at high strain levels to keep a high uniform elongation. Furthermore, apart from plastic deformation, reducing grain size can also be accomplished through introducing new elements, i.e. carbon in HEAs. A series of (AlCoCrFeNi)100–xCx (x = 0–8, atomic ratio) HEAs were prepared to reduce grain size from ~250μm to 50μm with the alloying effects of C, which increased yield strength from 1120MPa to 1426MPa [62]. Yang et al. introduced a unique disordered interfacial nanolayer at GBs between adjacent micrometer-scale superlattice grains in Ni43.9Co22.4Fe8.8Al10.7Ti11.7B2.5 alloys, as shown in Figure 1.11 [63]. This nanolayer is a persistent source of toughness by facilitating dislocation migration, effectively preventing brittle fractures at GBs. As a result, the alloy demonstrates remarkable mechanical properties, including ultra-high strength (1.6 GPa) and 25% tensile elongation at room temperature, along with excellent thermal stability and resistance to softening.

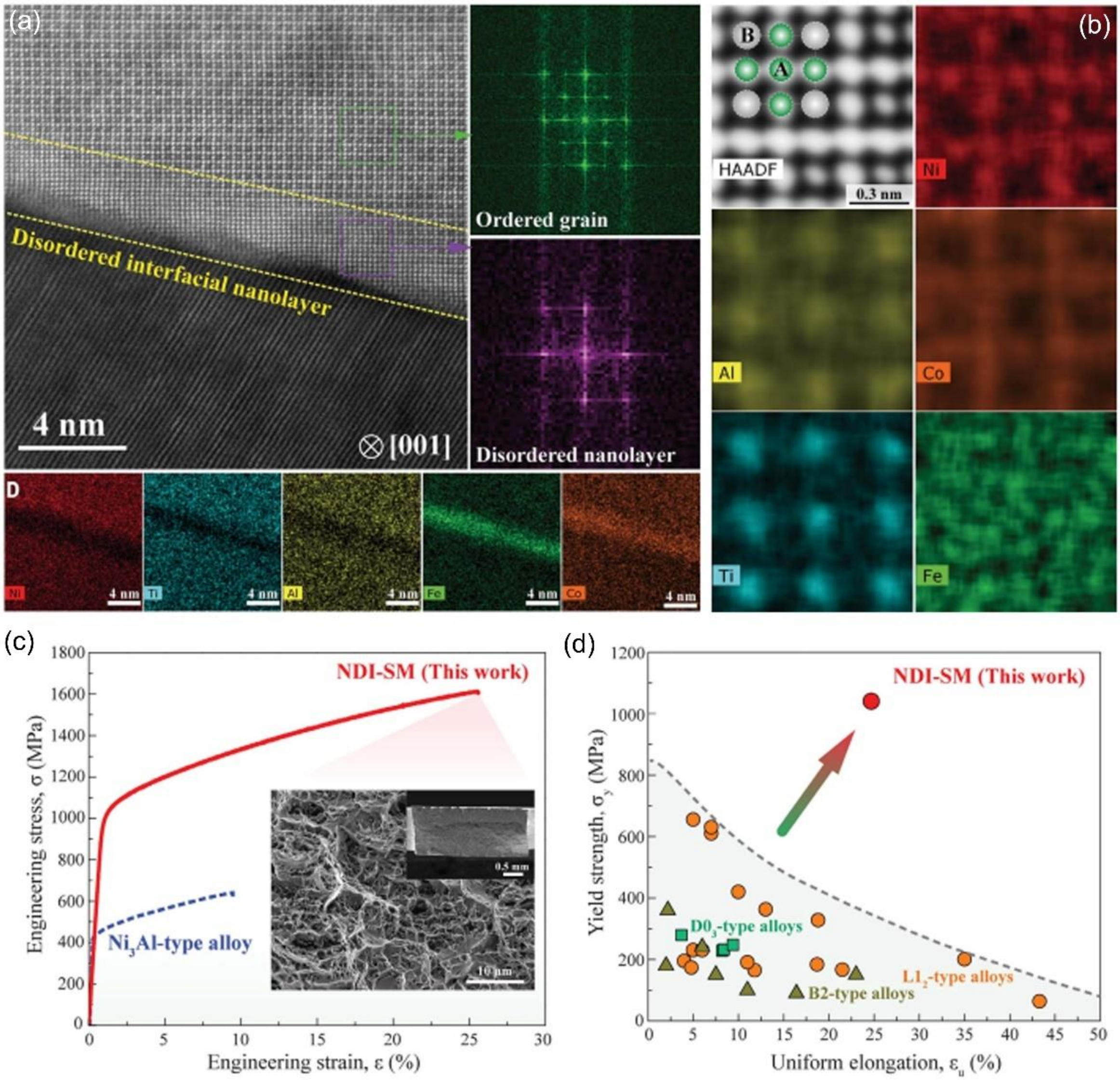

Figure 1. 11 (a) High-resolution HAADF-STEM image revealing the ultrathin disordered layer at the GBs with a nanoscale thickness. (b) Atomic-resolution HAADFSTEM image and corresponding EDX maps taken from the inner L12-type OSG, revealing the sublattice

occupations. (c-d) stress-strain curves and the yield strength versus uniform elongation compared with other bulk ordered alloys [63].

1.2.2 Deformation-induced Phase transformation and Twinning Strengthening

The transformation-induced plasticity(TRIP) and twinning-induced plasticity (TWIP) observed in some steels have been employed in HEAs to improve strength and ductility as the metastability of the parent phase. Because the parent phase is metastable, it can partially change into a new phase when subjected to thermal processing or, more typically, plastic deformation. Currently, metallic alloys can be metastable by tuning their SFE, practically through adjusting the chemical composition or changing the deformation temperature. More interfaces and boundaries could be introduced, which offers fewer accessible paths for dislocation movement, thus contributing to strengthening.

An example of metastability-engineering was found in fcc-based non-equiatomic Fe80-xMnxCo10Cr10 (x= 45 at%, 40 at%, 35 at% and 30 at%) HEAs [22]. The parent fcc phase in this system is metastable by reducing the content of Mn with the phase transformation from fcc to hcp. The twins and dual phase can be achieved when the content of Mn is decreased to 40 at% and 30 at%, respectively, which is in line with the rule of decreasing SFE. In Figure 1.12, deformation-induced martensitic transformation (fcc → hcp) is the primary deformation mechanism in Fe50Mn30Co10Cr10 HEAs at the early stage of deformation, which increases additional obstacle of phase boundary to prohibit dislocation movement, thus causing strain hardening. When the content of fcc decreases significantly at high strain, the hcp phase plays an essential role in the plastic deformation and strain hardening by contributing to dislocation slip, twinning, and stacking faults. Therefore, this enabled TRIP HEAs to display excellent strength-ductility tradeoff.

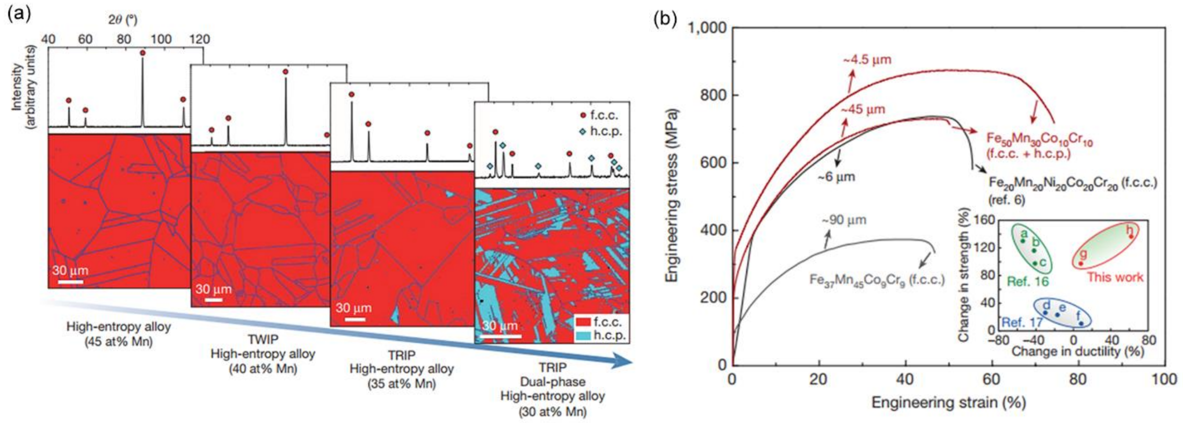

Figure 1.12 The evolution of deformation mechanism of TWIP- TRIP HEAs: (a) XRD patterns and EBSD phase maps and (b) Mechanical properties of Fe80 − xMnxCo10Cr10 (x=45 at%, 40 at%, 35 at% and 30 at%) HEAs [22].

Similarly, the phase transformation fcc → hcp also can be found in Fe40Mn10Co20Cr20Ni10 HEAs [64], 49.5Fe30Mn10Co10Cr0.5C HEAs [65] and Fe42Mn28Co10Cr15Si5 HEAs [66]. Another important phase transformation case is fcc → bcc transformation, as that activated in the Fe60Co15Ni15Cr10 HEAs [67] at cryogenic temperatures. The bcc nucleated at the intersections of shear bands in grain with the fcc phase and gradually grow up to offer abundant barriers for dislocation movement (Figure 1.13). The initial phase constitution of a metastable HEA can be either a single parent phase or a dual phase.

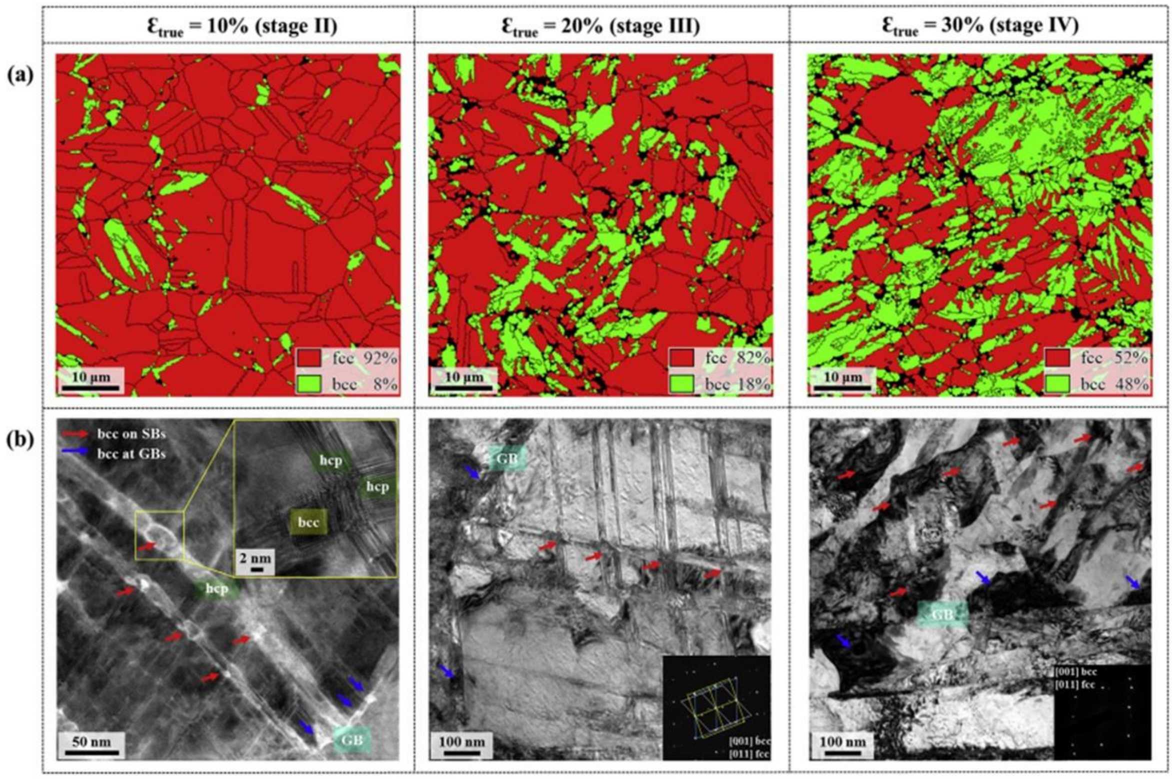

Figure 1.13 Microstructure evolution during 77K-deformation of the alloy Fe60Co15Ni15Cr10 with respect to an increase in tensile strains [67].

Moreover, the TRIP effect has been utilized in bcc-based HEAs to enhance ductility by introducing a secondary phase. Huang et al. [68] fabricated TiZrHfTax (x = 1, 0.6, 0.5, 0.4) HEAs with varying Ta content to destabilize the bcc phase. A single bcc phase is obtained in the quaternary equiatomic TiZrHfTa HEAs, while more hcp phase is detected as the Ta content decreases, as shown in Figure 1.14. This increase in the hcp phase content significantly improves the ductility of the specimens, with the uniform strain increasing by over 27%. The phase transformation alleviates stress localization at the interface between the bcc and hcp phases, facilitating plastic deformation and preventing early crack formation. The TRIP effect endows HEAs with multiple-stage strain hardening dominated by dislocation slip or martensitic phase transformation, which eventually increases strength and maintains ductility simultaneously. The strengthening effect of two phases can be expressed as, i.e. [12],

$$\Delta\sigma_{pht} = \sigma_{par} \times f_{par} + \sigma_{mar} \times f_{mar} \tag{1.2-2}$$

where σ_{par}, and σ_{mar} are the strengths of the parent and martensitic phases, respectively. f_{par} and f_{mar} are the volume fractions of the parent phase and the martensitic phase, respectively.

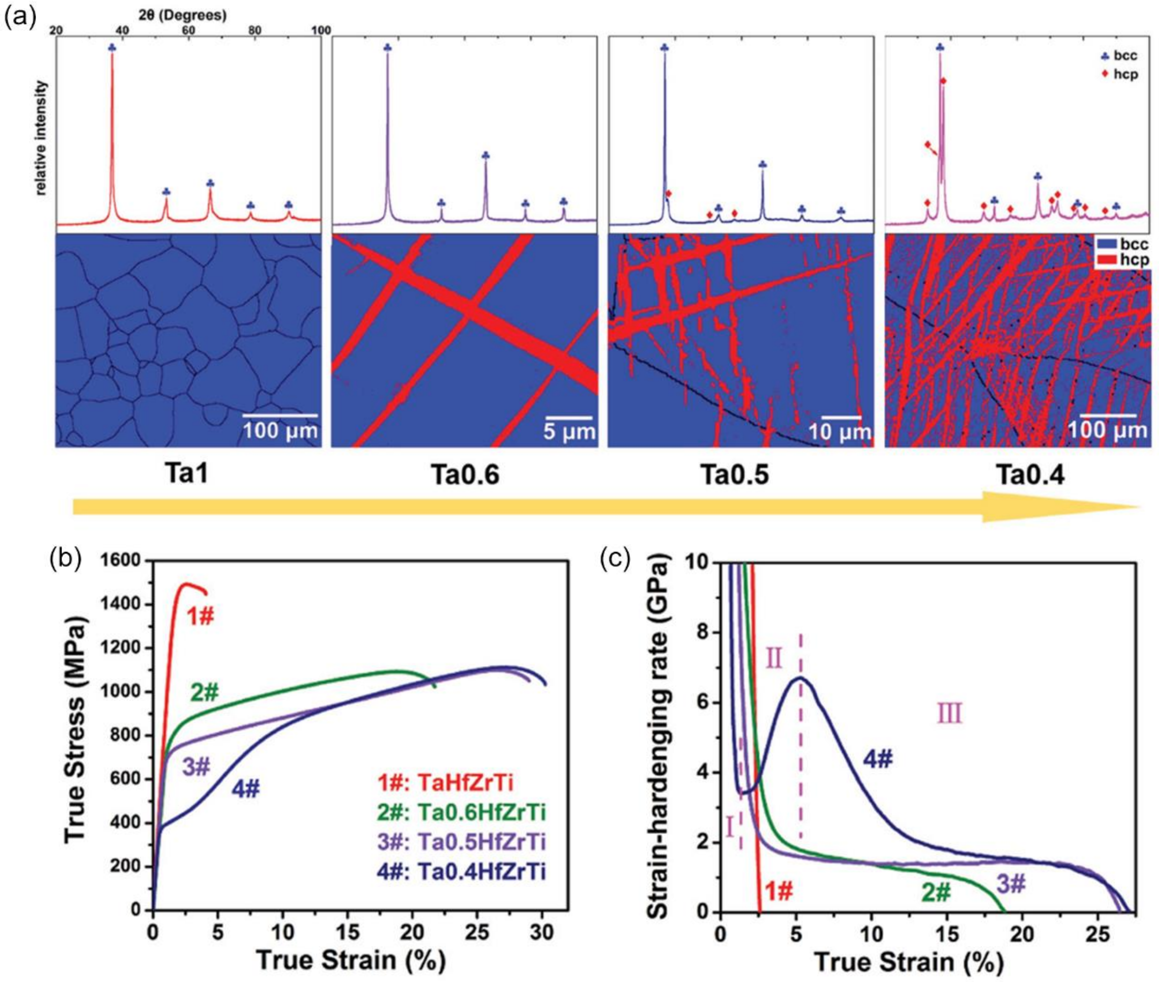

Figure 1.14 (a) Microstructure of TiZrHfTax HEAs with different content of Ta. (b) Representative tensile true stress–strain curves. (c) The corresponding strain-hardening rate curves.

The enhancement of strength and strain hardening by twins has also been reported in various HEA systems, such as the fcc-based CrMnFeCoNi [61] and the AlCoCrFeNi [69] HEA with $L1_2$ and B_2 phases. For example, the research results of tension test of AlCoCrFeNi2.1 HEA revealed that deformation twinning is the primary mechanism dominating the plastic deformation [69]. With the twin-twin deformation mechanism, the alloy can exhibit excellent mechanical properties at high temperatures. Similarly, during the deformation process at low temperatures, the twinning deformation mechanism accompanied by limited prior slip was also activated in FeNiCoCrMn HEAs [70]. Su et al. [65] investigated that twinning in the parent fcc grains made the primary contribution to the improvement in the yield strength of the microstructures created by tempering and annealing in the interstitial TRIP-TWIP Fe49.5Mn30Co10Cr10C0.5 HEAs with the phase transformation from fcc to hcp. In the TRIP-TWIP HEAs with low SFE, which exhibit fcc → hcp martensite phase transformation and deformation twins, the phase boundaries and twin boundaries significantly contribute to the improved yield strength, sometimes even more so than grain refinement [71]. For example, a decrease in grain size leads to a reduction in twin thickness and an increase in twin spacing in $Al_{0.1}$CoCrFeNi HEA, as illustrated in Figure 1.15 [72]. Grain refinement significantly inhibits the twinning activity in this recrystallized HEA, which reduces the development of twinning on strain-hardening ability and tensile ductility.

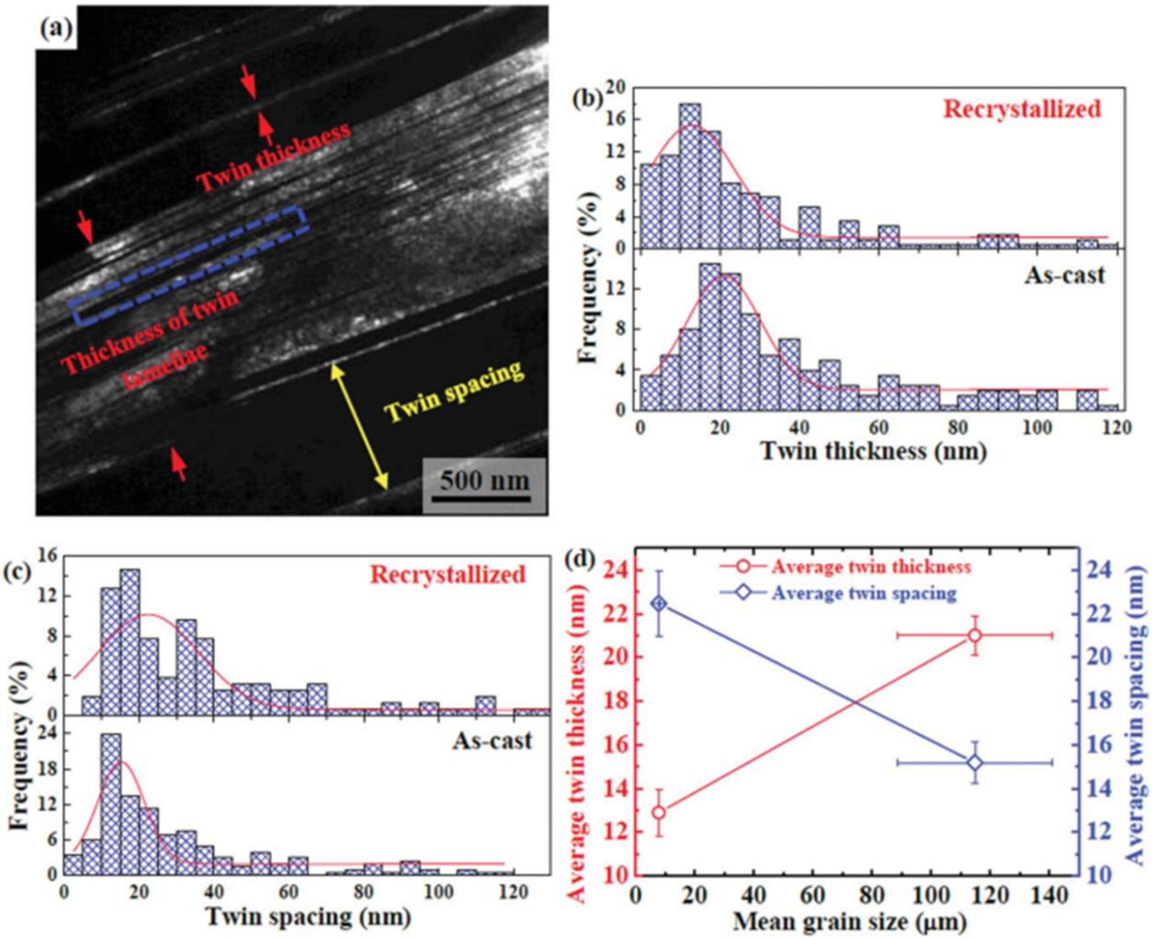

Figure 1.15 (a) Twins in Al0.1CoCrFeNi HEAs; (b) the twin thickness and (c) twin spacing distributions of the as-cast and recrystallized HEAs; (d) the average values of twin thickness and twin spacing versus mean grain size [72].

The strengthening effect of twins can be accomplished via the blockage of twin boundaries to dislocation movement, therefore, the twin spacing plays a vital role in deciding the strengthening effect of twins. Thus, the strengthening effect of twins can be typically characterized by a Hall-Petch-type equation [12, 65, 73], denoted as

$$\Delta\sigma_{tb} = f_t k_{tb} \lambda_t^{-1/2} \qquad (1.2\text{-}3)$$

where k_{tb} is the twin boundary strengthening coefficient, f_t is the volume fraction of the grains with twins and λ_t is the average twin spacing (i.e., the average twin thickness).

Normally, the strengthening mechanism in HEAs is a combination of different ways rather than a simple method as the complicated microstructures and element composition in HEAs, for example, in the Cr26Mn20Fe20Co20Ni14 [74], Fe50Mn30Co10Cr10 [75]and Fe40Mn40Co10Cr10 [76] HEAs. The strengthening mechanisms include phase transformation, deformation twinning and dislocation slipping, which are responsible for the extraordinary ductility and strain hardening capability. Deformation twins offer more obstacles against dislocation motion via cut-free path of dislocation, resulting in increased stress. Meanwhile, the lamellae twin became thinner with the increased density of TBs, which retains the dislocations motion.

1.2.3 Solid Solution Strengthening

HEAs comprise several principal elements, primarily forming a random solid solution. Incorporating solute atoms into the solvent matrix enhances the mechanical properties of HEAs through a mechanism known as solid solution strengthening [77]. This strengthening mechanism arises from interactions between solute atoms and gliding dislocations. Consequently, solid solution strengthening significantly contributes to the high yield strength (YS) observed in some HEAs, with approximately half of the YS attributed to solid solution strengthening and the other half to additional strengthening effects, i.e. grain boundary strengthening [78]. The solid solution strengthening in (CoCrNi)94Al3Ti3, caused by the addition of substitutional Al and Ti solutes, which increased yield strength to ~750 MPa and tensile strength of ~1.3 GPa, while maintaining ~45% ductility, as shown in Figure 1.16(a-c) [79]. High-density stacking faults prevail in the precipitation-hardened alloys, as denoted in Figure 1.16(d-e). Solid solution strengthening in binary or multicomponent alloys resulted from variations in lattice coordinates relative to ideal positions, with lattice distortion induced by different elements considered a fundamental factor in the general formulation of solid solution strengthening for both binary and highly concentrated alloys [80].

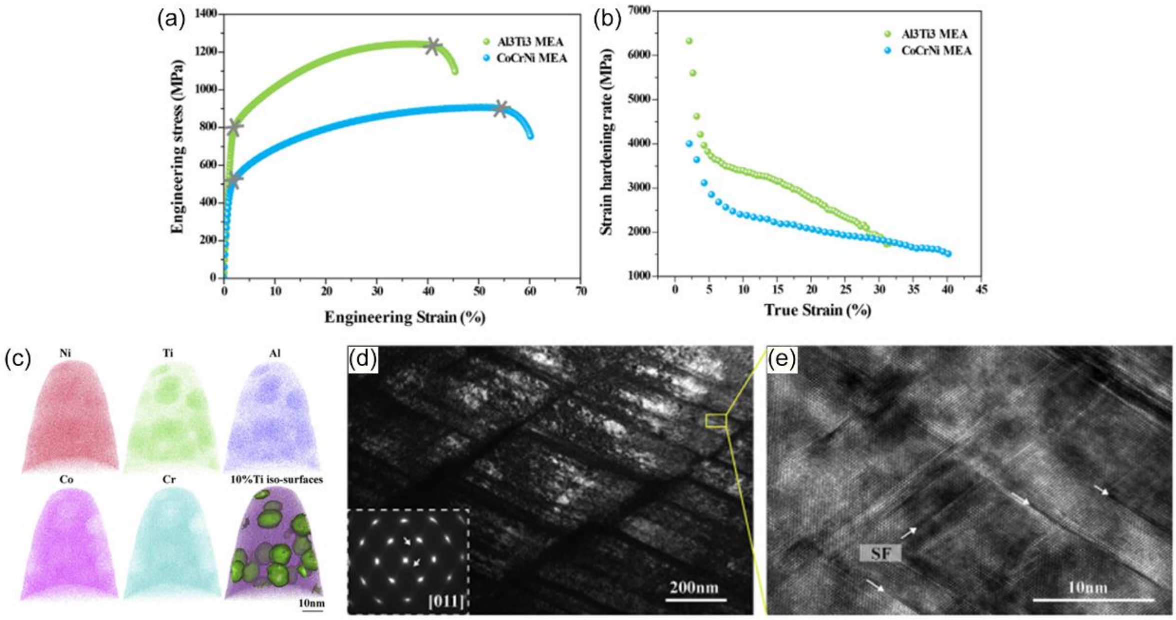

Figure 1.16 (a) Engineering stress-strain curves and (b)the corresponding strain hardening rate of the CoCrNi and (CoCrNi)94Al3Ti3 MEAs. (c) Ni, Ti, Al, Co and Cr atom maps in a typical APT tip of (CoCrNi)94Al3Ti3 MEAs. (d-e) Prevalence of SFs with the solid solution strengthening [79].

Moreover, adding interstitial elements like C, N, O and B is an effective method to trigger solid solution strengthening. For example, Son et al. [81] studied the impact of co-doping interstitials on the mechanical properties of HEAs through doping CoCrFeMnNi HEA with B and N, which significantly increased its yield strength by approximately 95%, while maintaining substantial ductility at around 49.8%. The segregation along GB decreases the phase stability and activate phase transformation, thereby improving the plasticity. Similarly, the interstitial elements (oxygen, carbon, nitrogen) existed in the highly distorted substitutional solid solution matrix in the form of solid solution, rather than forming brittle ceramic phases, which resultes in high YS at 4.2GPa and elongation at 65% in TiNbZr-O-C-N HEA [80], as shown in Figure 1.17(a-d). The pillars with high content of interstitial elements depict a good deformation ability without obvious shear band. Besides, Liu et al. [80] calculated the contribution of these interstitial elements enriched in different regions in Figure 1.17(e-f): O, N, and C solid solution strengthening are 2.2 GPa,0.7 GPa, and 0.3 GPa, respectively. The interstitial strengthening in this RHEA maintains ductility due to the highly distorted substitute solid solution matrix, which incorporates many interstitial elements without forming brittle phases.

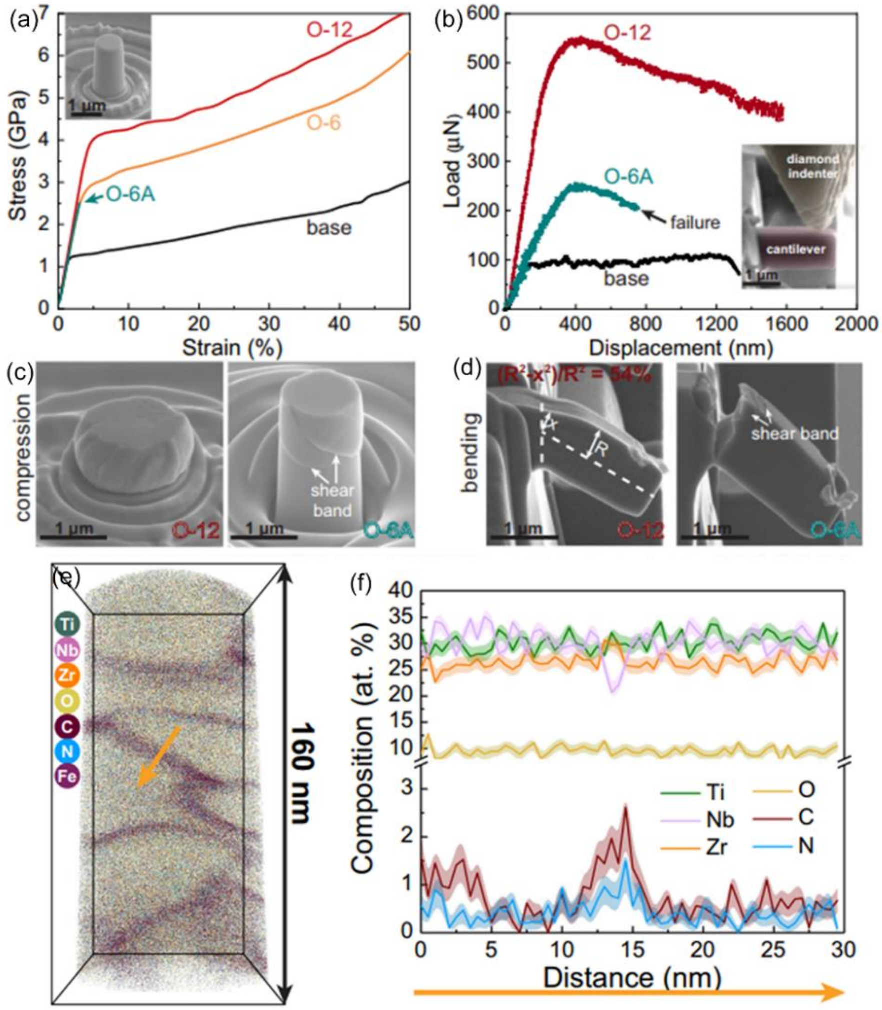

Figure 1.17 Mechanical properties of TiNbZr-O-N-C HEAs with different content of O. (a) Compressive engineering stress-strain curves. (b) Load-displacement curves measured by bending. SEM images of (c) micro-pillar and (d) cantilevers after deformation. (e) 3D reconstruction of a typical APT specimen taken from the deformed material. (f) Compositional profile acquired from APT [80].

1.2.4 Precipitation Strengthening

Precipitation strengthening is widely utilized to enhance the mechanical properties of metallic materials [82]. This technique utilizes the solid solubility of solute atoms at specific treatment temperatures, where the formation of dispersed particles or secondary phases interacts with defects to produce a hardening effect. The function of precipitation strengthening is determined by the capacity to generate a high density of uniformly distributed nanoscale, strong precipitates, either through thermo-mechanical processing or subsequent heat treatment [83]. The development and processing of various HEAs focus on optimizing and maximizing this precipitation process to enhance their mechanical properties.

So far, the formation of advantageous precipitates like $L1_2$ precipitate, B_2 precipitate, σ precipitate, carbide precipitate and so on induced by composition variation contributes to enhancement of strength in HEAs [84, 85]. It is found that Ni, Fe, Cr, Co, and Al are widely applied elements in nanoprecipitate-strengthened HEAs [85]. Yang et al. [86] proposed a method to introduce high-density, ductile multi-component intermetallic compound nanoparticles (MCINPs) into complex alloy systems by uniformly distributing $L1_2$ precipitates within an fcc-based FeCoNi HEA matrix through minor additions of Ti and Al. This MCINP-reinforced alloy demonstrates exceptional mechanical performance, achieving ultra-high strength of up to 1.5 GPa and a significant elongation of up to 50% at room temperature, thereby overcoming the typical trade-off between strength and ductility (Figure 1.18). The controlled nanoscale precipitation and in-situ toughening of MCINPs via manipulation of order-disorder phase transformation and elemental partitioning contribute to the mechanical performance. The coherence of MCINPs with the matrix fosters a unique multi-stage work-hardening behavior, effectively mitigating plastic instability typical in high-strength materials.

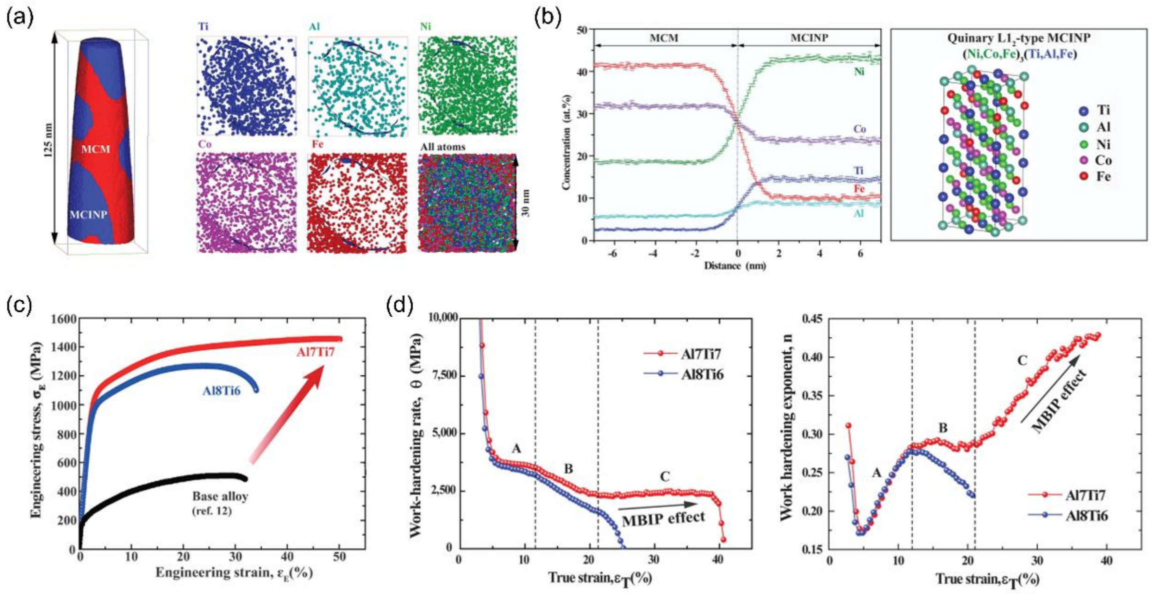

Figure 1.18 (a) The precipitates used in HEAs and (b) the ordering crystallographic structure and site occupancy of the $L1_2$ MCINP by density functional theory (DFT) calculations of the Al7Ti7 alloy. (c) Engineering stress-strain curves. (c) work hardening rate curves of the MCINPS alloys [86].

The precipitates are introduced with the change of element composition; however, the phase stability is changed together. Wang et al. [87] investigated the relationship between heat temperature and phase transition in Al0.5Cr0.9FeNi2.5V0.2 HEAs, and discovered a sequence of phase transition fcc → fcc + $L1_2$ + bcc → fcc + $L1_2$ + bcc + B_2 → fcc + B_2 → fcc when the temperature increased from 200 °C to 1100 °C. The $L1_2$ precipitates are unstable at extremely high temperatures, limiting the application of precipitation strengthening of $L1_2$ below a critical temperature. The size of $L1_2$ increases from 93.7 nm to 780.4 nm from 800 °C to 1000 °C with a corresponding decrease of volume fractions of about 37–17% as the GB stabilization slows the elemental diffusion [88]. Moreover, the introduction of B_2 precipitates in the

Al0.5CoCrFeNi HEA notably enhances its fatigue life with the number of reversals to failure over 10^6 by improving yield strength, work hardening capability, and ductility, which is shown in Figure 1.19 [89]. This enhanced low-cycle fatigue resistance primarily due to the unique properties of the B_2 precipitate phase, which exhibits high elasticity, plastic deformability, and reversible martensitic transformation. When microcracks develop, the high elasticity of B_2 precipitates and ability to undergo reversible martensitic transformation effectively slow down dislocation consumption and suppress cyclic softening, significantly extending the fatigue life.

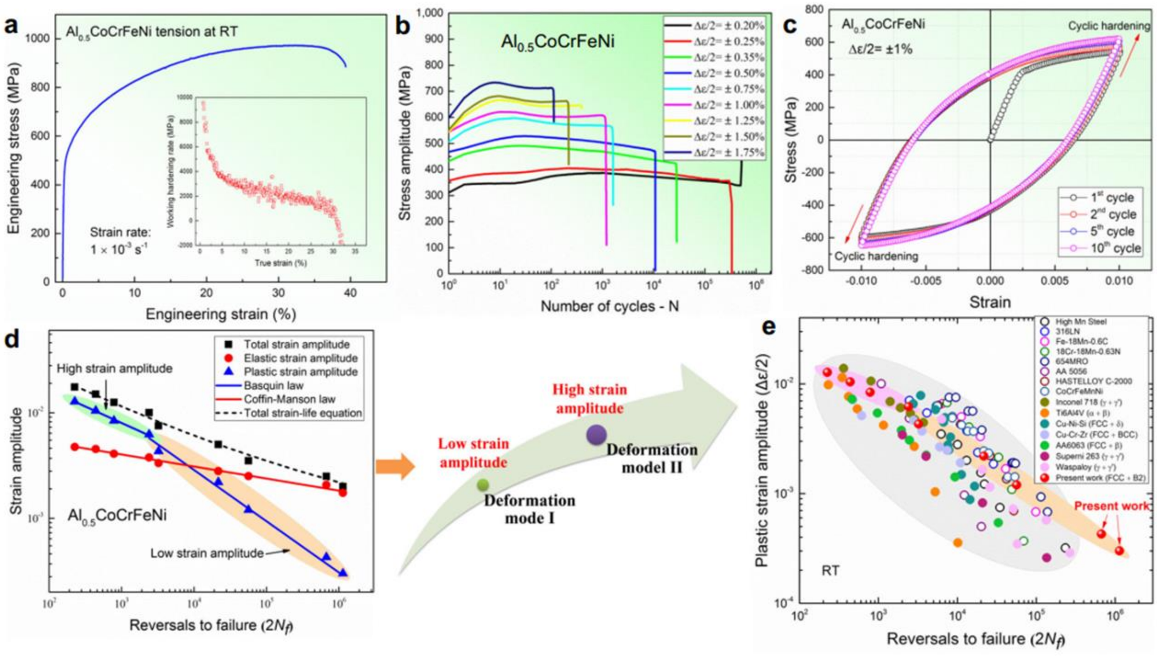

Figure 1.19 Mechanical properties of Al0.5CoCrFeNi HEA. (a) Engineering stress-strain curves. (b) Cyclic stress response curves. (c) Hysteresis loops at selected numbers of cycles fatigued at the strain amplitude of ±1%. (d) Total strain amplitude, elastic-strain amplitude, and plastic strain amplitude versus the number of reversals to failure. (e) The comparison of Coffin–Manson fatigue data for Al0.5CoCrFeNi HEA and other conventional alloys [89].

1.3 Heterogeneous Structure in HEAs

Like traditional alloys, HEAs face the challenge of the strength-ductility trade-off, which is the inherent compromise between strength and ductility observed in materials with homogeneous structures. Several strategies have been developed to optimize the mechanical properties of HEAs through careful tuning of their chemical composition and microstructure. Compared with conventional methods of adjusting chemical composition, manipulating the microstructure offers a promising approach.

1.3.1 Gradient Nanostructure (GNS) in HEAs

To widen the application fields, high strength and excellent ductility are necessary. These mechanical properties are primarily influenced by dislocation movement: restricting dislocation movement increases deformation resistance, while allowing dislocation motions ensures plastic deformation. Therefore, strengthening mechanisms that improve strength often results in reduced ductility. The key to retaining ductility as strength increases is to enhance strain hardening ability, enabling the material to cope with rising flow stress and delay plastic instability [90].

To facilitate strain hardening and strain delocalization within homogeneous nanograins or coarse grains, the GNS designed in the mid-2000s with an internal gradient microstructure from surface to the interior of grain size, phase composition, and twin thickness ranging from nanoscale to microscale has been devised, which can overcome the strength–ductility trade-off of metallic materials [91]. Unlike homogeneous coarse grains or nanograins, GNS materials display heterogeneous deformation mechanisms. The deformation limited in the gradient microstructure endows GNS materials with superior properties, including high strength, strong ductility, fatigue resistance and friction properties [92-94]. This microstructure combines a nanograined layer adhered to a ductile coarse-grained substrate composed of the same material, with a transition layer possessing a graded grain structure positioned between them. As shown in Figure 1.20 [91, 95], compared with the homogeneous, the transition layer features a variation of grain sizes (or grain-boundary density) that exhibits elastic homogeneity but demonstrates a gradient in plastic behavior. This GNS has been applied in some conventional materials like copper [96], steels [97, 98] and magnesium [99]. For example, the GNSed copper with a grain size at about 40 nm in the topmost surface overcame the inverse Hall-Petch effect with the deformation twining and detwinning process during plastic deformation, which exhibits dislocation activities-mediated mechanisms in coarse grains and sub-grains and twinning-mediated mechanisms in ultra-fine grains [96].

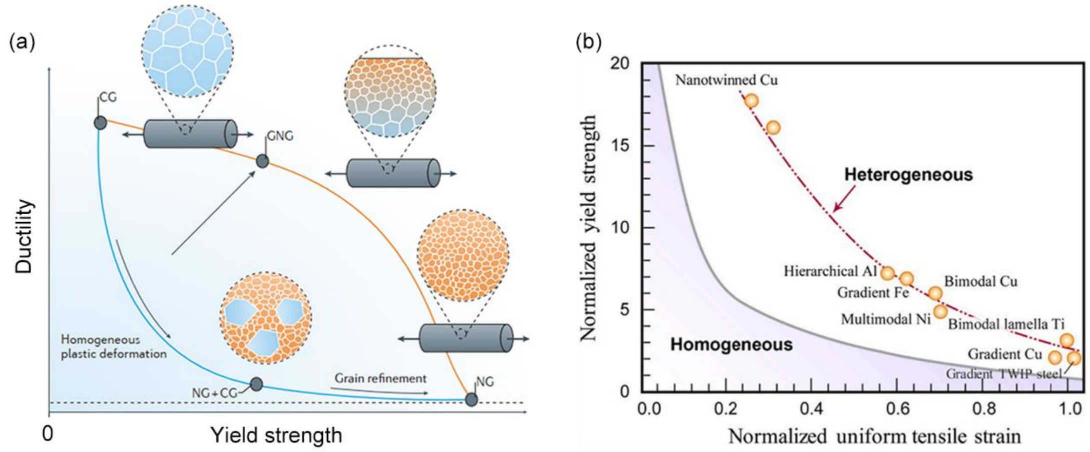

Figure 1.20 (a) Strength–ductility synergy of GNS combining nanograins and coarse grains. (b) Normalized yield strength versus normalized uniform tensile strain of homogeneous and heterogeneous materials [91, 95].

Currently, the GNS has been successfully fabricated in HEAs [100-102], i.e. CrCoNi MEA [103], (Fe40Mn40Co10Cr10)C3.3 [104], CoCrFeNiMo0.15 HEAs [105]. Stress and strain partitioning occurs at the interface between hard domains, comprising ultrafine grains and nanograins, and soft domains, constituted by micron-size grains [106]. This phenomenon leads to significant stress concentration at the contact points within the ultrafine grains during tensile deformation. The elevated stress levels at the borders of the ultrafine grains trigger the emission of partial dislocations, subsequently leading to the formation of deformation twinning or phase transformation. Moreover, the dislocation movement increases progressively with the accumulation of plastic strain, which generates newly formed nanograins and imparts a higher degree of heterogeneity to the overall structure.

For instance, the rotationally accelerated shot peening (RASP) technique was applied in CrCoFeNiMn to fabricate GNS, as shown in Figure 1.21, resulting in an increase in yield strength from 323MPa to 610MPa [107]. The change of average grain size along the depth from surface to interior induces the microhardness decrease away from the surface. Dislocation slip and deformation twinning are the two main deformation mechanisms in this GNSed HEA. The gradient structure is treated like a CG sandwich in the core, and the surface layer with defined grain presented high strength/hardness. However, the core structure remains undeformed, so there is a significant difference between the surface layers and the core, which evades strength-ductility trade-off.

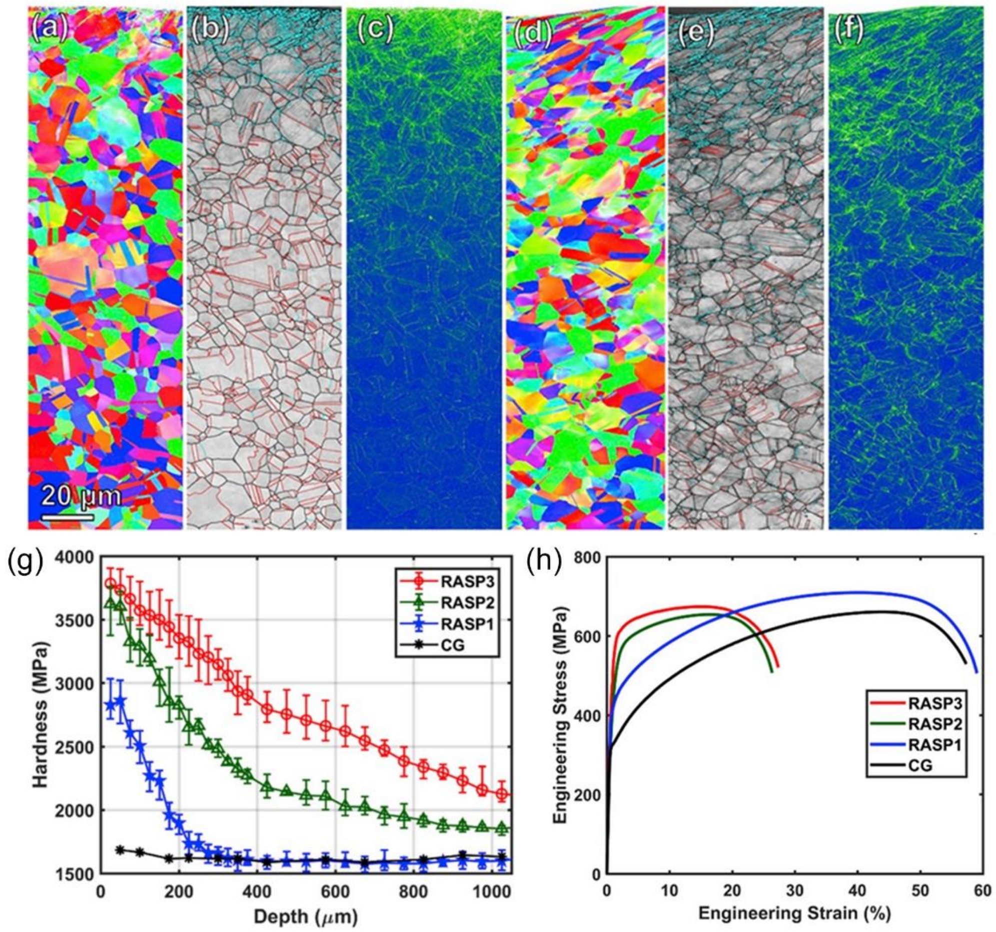

Figure 1.21 Typical microstructure of GNSed CoCrFeNiMn HEA. (a-f) EBSD images of GNS generated by different parameters. (g) Microhardness distribution and (h) Engineering stress-strain curves [107].

Similarly, Wu et. al [108] fabricated heterogeneous structure in Al0.1CoCrFeNi HEAs through cold working and intermediate-temperature-annealing non-recrystallization with subgrain boundaries, numerous dislocations, SFs an annealing twins in Figure 1.22. The variation of density of dislocation inside the partially recrystallized and fully recrystallized grains cause dislocation-density heterogeneity, which enable HEAs to exhibit a high ultimate strength at 928MPa and elongation at 30%.

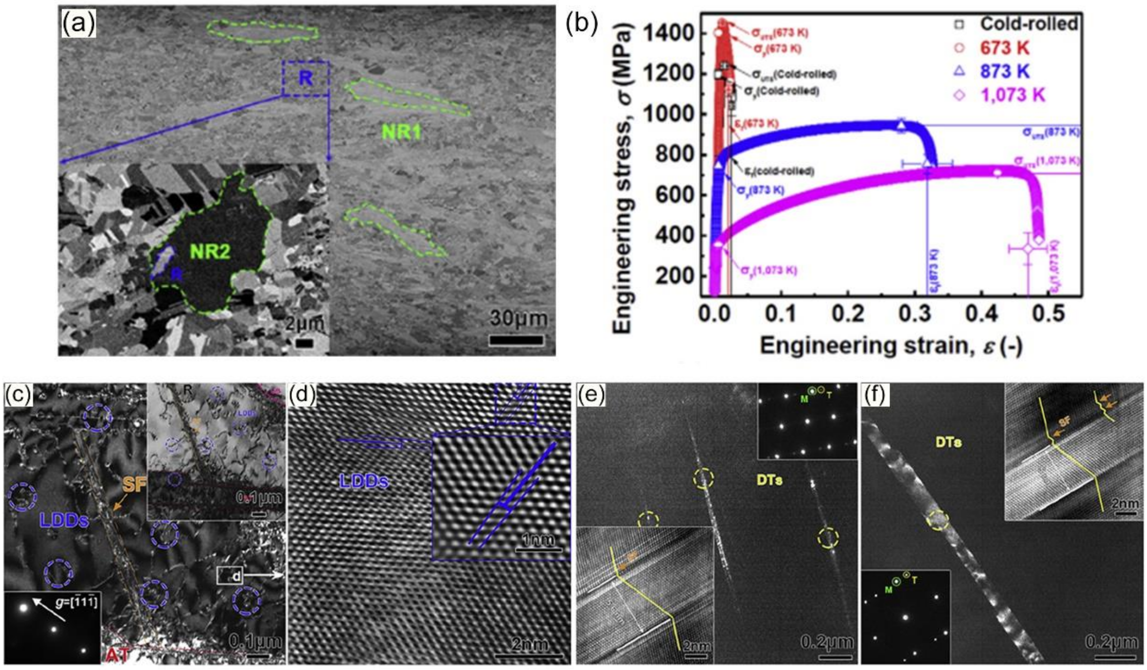

Figure 1.22 (a) Typical heterogeneous microstructure; (b) Engineering stress–strain curves; (c-d) SFs and dislocations along subgrain boundaries. (e-f) Dark field TEM images of deformation twins [108].

Pan et al. [109] introduced a novel gradient nanoscale dislocation cell structure within a stable single-phase Al0.1CoCrFeNi HEA depicted in Figure 1.23, achieving enhanced strength without significant loss of ductility. This gradient structure is formed via cyclic torsion treatment, resulting in a hierarchical dislocation arrangement throughout the specimen. The nanoscale dislocation cell structure contributes to continuous hardening and an unusual work-hardening response by effectively impeding dislocation motion. The deformation mechanism is characterized by the progressive formation of high-density SFs and twins, originating from the abundant low-angle dislocation cells.

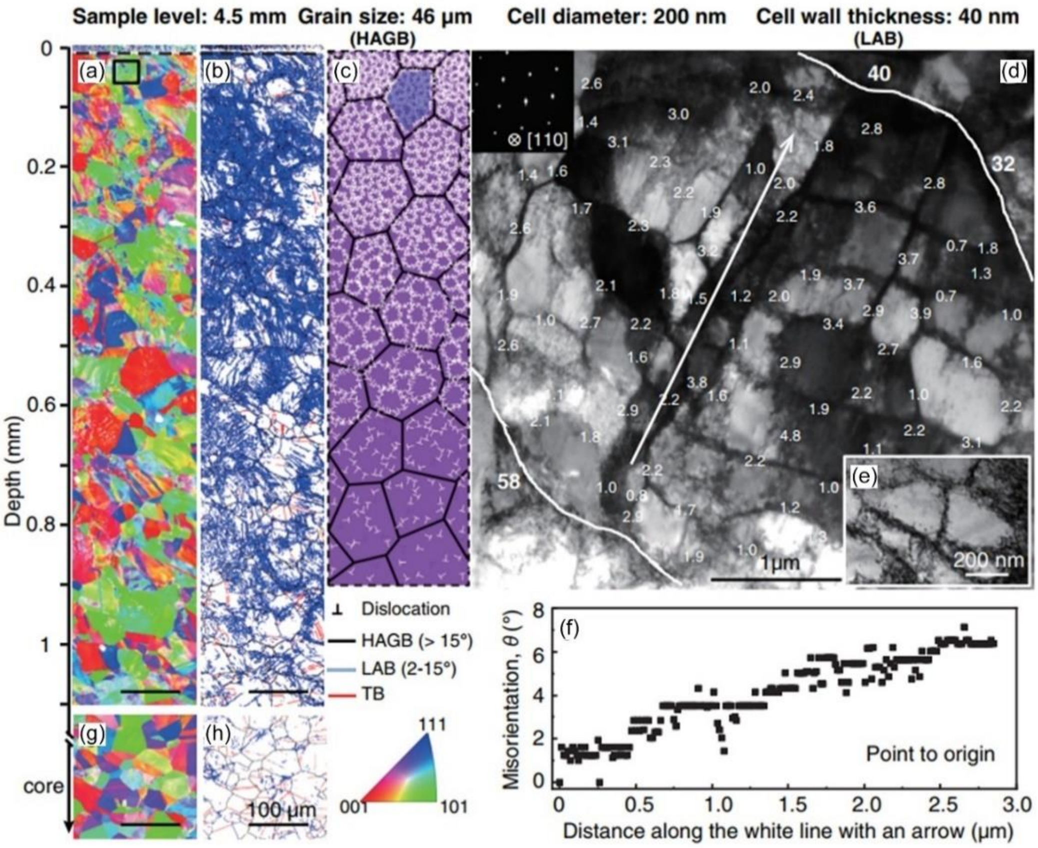

Figure 1.23 Typical gradient dislocation structure in Al0.1CoCrFeNi HEA processed by cyclic torsion processing. EBSD images of (a-b) gradient microstructure and (g-h) core region. (c) Schematic of gradient dislocation structure with a gradient distributed low angle dislocation structure. (d-e) Corresponding TEM image of dislocation structure at the topmost surface. (f) Plots of misorientation-angle variation [109].

1.3.2 Multi-phase Heterogeneous Structure in HEAs

Due to the deformation-induced phase transformation and deformation twins, the HEAs with low SFE exhibit high ductility and high strength. Therefore, they have the potential to be used as base alloys for microstructure modification, wherein precipitation strengthening and heterogeneous grain structures can be added to obtain the ideal combination of ductility and strength. For example, spinodal decomposition structure is a typical dual-phase structure with different composition but the same crystal structure [110]. A popular class of materials developed using the dual-phase concept like dual-phase steels [111] have been developed for automobile applications. The advantage of the martensite-ferrite dual-phase steels is that the volume fraction of the martensite phase can be controlled by adjusting the austenitization temperature in the ferrite–austenite two-phase zone of the phase diagram, which determines the ratio of the austenite to ferrite [112]. Guo et al. [113] outlined phase selection criteria to predict phase composition in HEAs. These criterias include mixing enthalpy, configurational entropy, mismatch entropy, melting point, atomic size mismatch, electronegativity, and valence electron concentration, as illustrated in Figure 1.24.

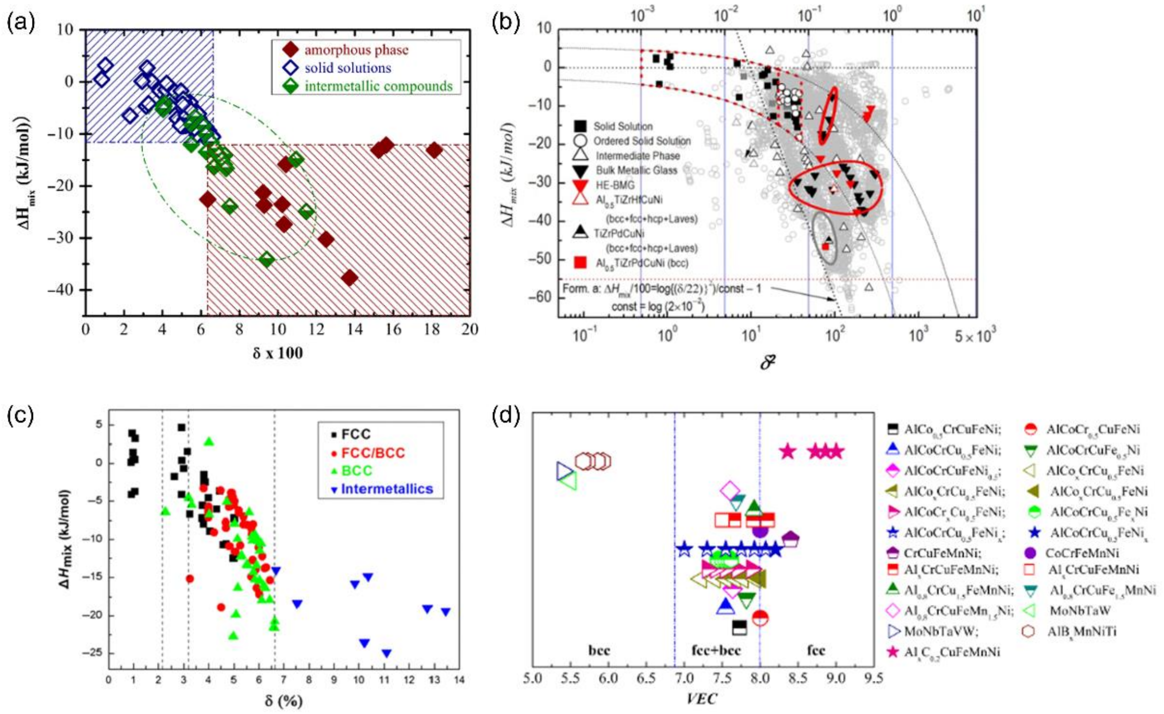

Figure 1. 24 (a) $\triangle H_{mix}$-δ plot (b) $\triangle H_{mix}$-δ^2 plot in HEAs. (c) Dependence of solid solution types on $\triangle H_{mix}$ and δ in HEAs. (d) role of VEC in phase selection between fcc and bcc type

solid solutions in HEAs [113].

Du et al. [114] demonstrated that a dual-phase heterogeneous structure in CrCoNi-based MEA comprising both matrix and precipitates can achieve an ultra-high tensile strength of 2.2 GPa and a uniform elongation of 13% at room temperature. This dual heterogeneous structure featured a matrix with a combination of coarse grains and ultra-fine grains with average grain size at about 1.2 μm, alongside $L1_2$-structured nanoprecipitates of varying sizes from several to hundreds of nanometers are generated by annealing, as shown in Figure 1.25. These $L1_2$ nanoprecipitates, fully coherent with the matrix, minimize elastic misfit strain at the interfaces, reduce stress concentration during deformation, and contribute significantly to enhanced ductility.

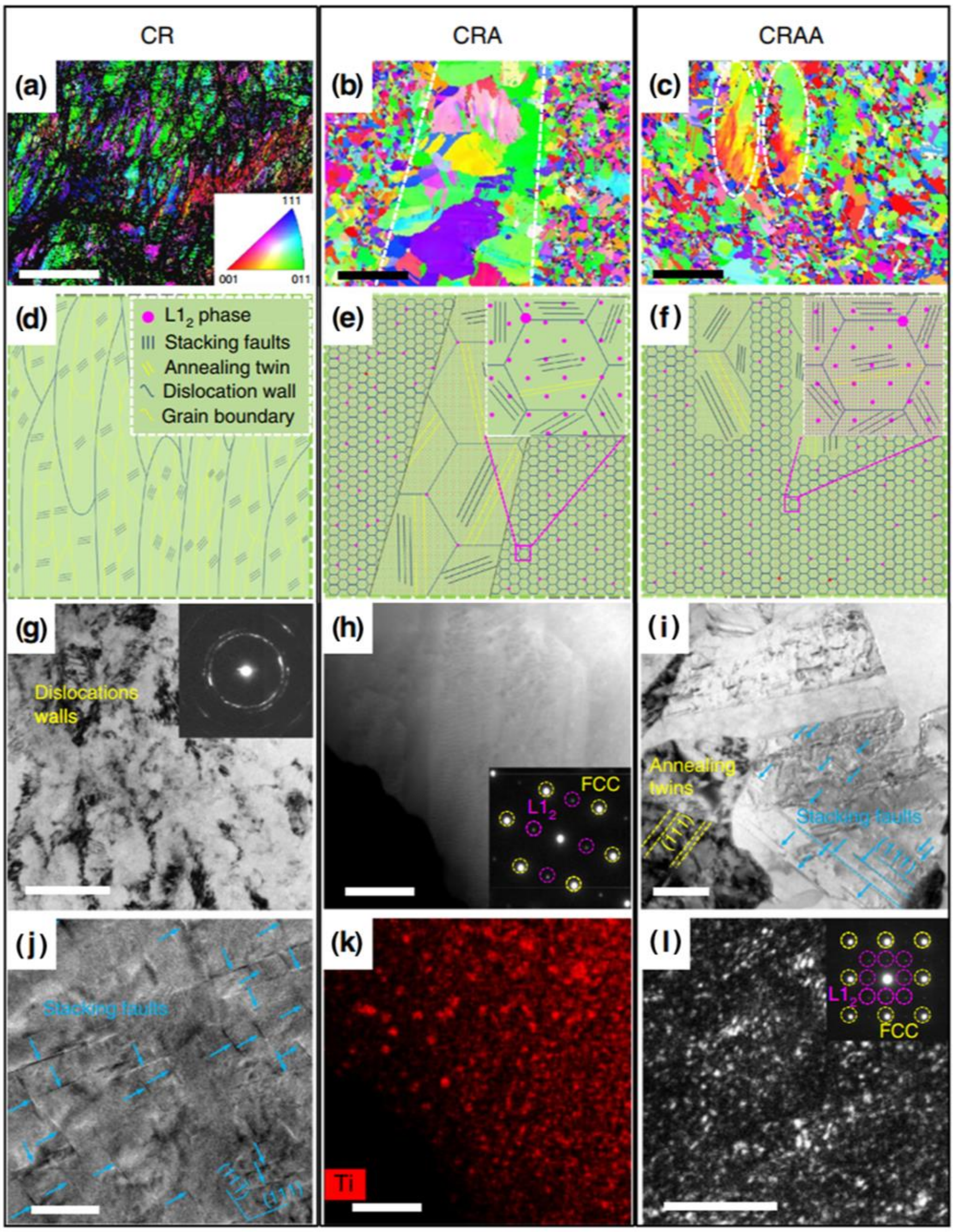

Figure 1.25 The microstructure of dual-phase heterogeneous structure in CrCoNi-based MEA generated by cold-rolling and annealing. (a), (d), (g), (j) for CR (cryo-rolling); (b), (e), (h), (k) for CRA (cryo-rolling followed by a high-temperature annealing); and (c), (f), (i), (l) for CRAA (cryo-rolling followed by high-temperature annealing and a subsequent aging) [114].

Besides, the interaction between local chemical environments and deformation-induced crystal structure changes in Cr20Mn6Fe34Co34Ni6 HEA [57] composed of fcc and hcp phases indicates a link between deformation mechanisms and atomic distribution. In Figure 1.26, as the dual-phase microstructure, more deformation-induced hcp phase is formed along the SFs network boundaries in the fcc phase, which becomes the primary source of strain hardening. This dual-phase structure contributes to forming SFs networks, which drives the phase transformation from fcc to hcp. These networks are formed due to fluctuations in lattice friction, which are inherently associated with concentration waves within the materials.

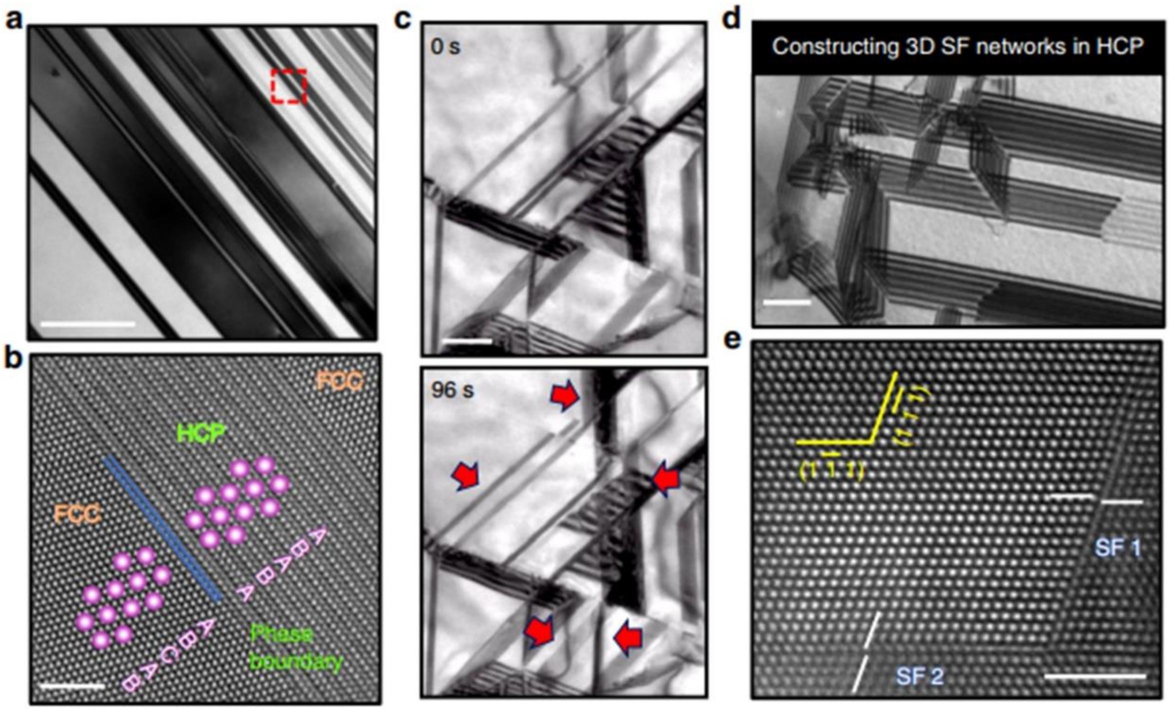

Figure 1.26 (a) TEM image of the dual-phase microstructure in Cr20Mn6Fe34Co34Ni6 HEA. (b) HRTEM image of the interface between fcc and hcp phase. (c-e) are the microstructure of SFs networks and partial dislocations [57].

Except for the above single crystal structured materials, introducing amorphous phase in crystalline materials is also an effective method to modify microstructure and further influence properties. Amorphous metallic alloys are initially regarded as structural materials with high strength [115]. Nevertheless, their widespread applications have been significantly constrained by their inherent limitation of ductility. Meanwhile, nanocrystalline alloys have been extensively studied, but for crystalline alloys with grain sizes smaller than approximately 15 nm, the inverse Hall-Petch effect leads to a softening effect [116]. Therefore, to address the limitations and improve the properties of nanocrystalline and amorphous alloys, one proposed strategy is to combine them, forming amorphous-nanocrystalline metallic materials [117]. On one hand, nanocrystalline-amorphous metallic materials inherit exceptional properties from both their amorphous and nanocrystalline components, including superior magnetic properties, remarkable wear and corrosion resistance, and outstanding hardness and strength [118]. On the other hand, these alloys also demonstrate enhanced thermal stability and ductility, features that are challenging to attain in either amorphous or nanocrystalline alloys [119]. This kind of microstructure can be obtained through the nanocrystallization in metallic glasses and partial amorphization along nanograin boundaries [119], which includes annealing, severe plastic deformation, ball milling, laser, irradiation, and so on (Figure 1.27).

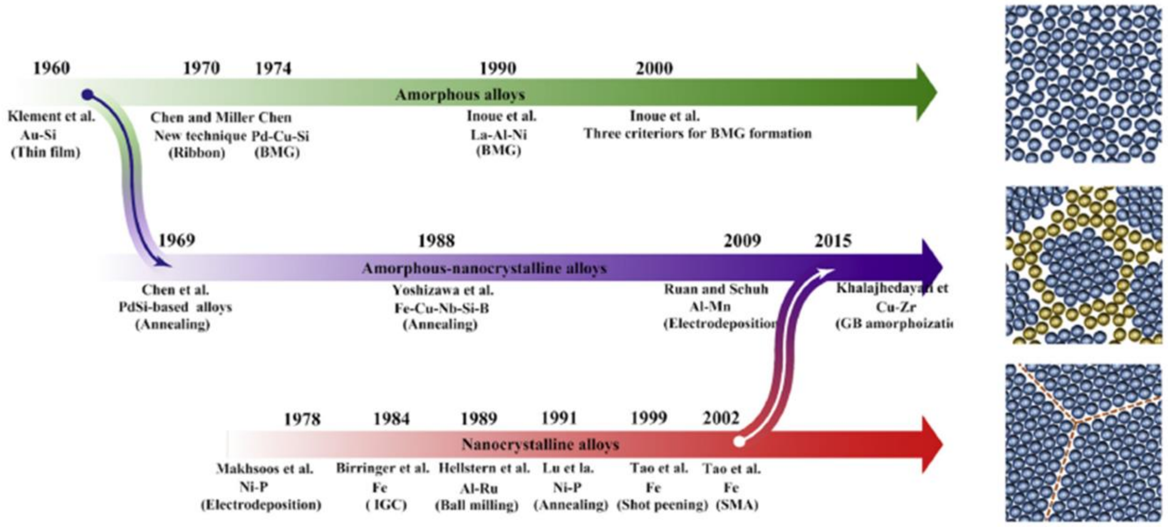

Figure 1.27 Development traces of amorphous alloys, amorphous-nanocrystalline alloys, and nanocrystalline alloys [119].

For example, the rapid solidification process of remelting in the amorphous materials is an effective method of activating partial crystallization and introducing the crystalline phase [119]. The free energy of nonequilibrium solid solution and lattice for crystalline phase is higher than that of the amorphous phase, which could result in the amorphization of the intergranular amorphous layer along GBs [120]. Similarly, some bulk metallic glasses adopt deformation-induced or annealing-induced crystallization to acquire the coexistence of crystalline and amorphous phases [119, 121], like the long-range orders are formed through cold rolling in some amorphous Al-based and Zr-based alloys [122, 123]. This partial crystallization induced by plastic deformation extended solid solubility to soften.

Moreover, amorphous phase can be generated within crystalline HEAs to form crystalline-amorphous nanocomposite through the proper techniques like magnetron sputtering process, laser treatment and so on [124-126]. For example, Wu et al. [127] investigated a Mg-based dual-phase nanostructured material prepared by magnetron sputtering process, which consisted of $MgCu_2$ nanocrystalline cores with a diameter of about 6 nm and a Mg-enriched amorphous shell, forming a "supra-nanometre-sized dual-phase glass-crystal" structure in Figure 1.28(a). This material has a near-ideal strength of 3.3 GPa, attributing to the synergistic strengthening effect of nanocrystals and amorphization, where the amorphous shell hinders dislocation motion and shear band propagation, as shown in Figure 1.28(b-c). Furthermore, this material also exhibited high hardness, low Young's modulus, and size-independent strength characteristics (Figure 1.28(d)).

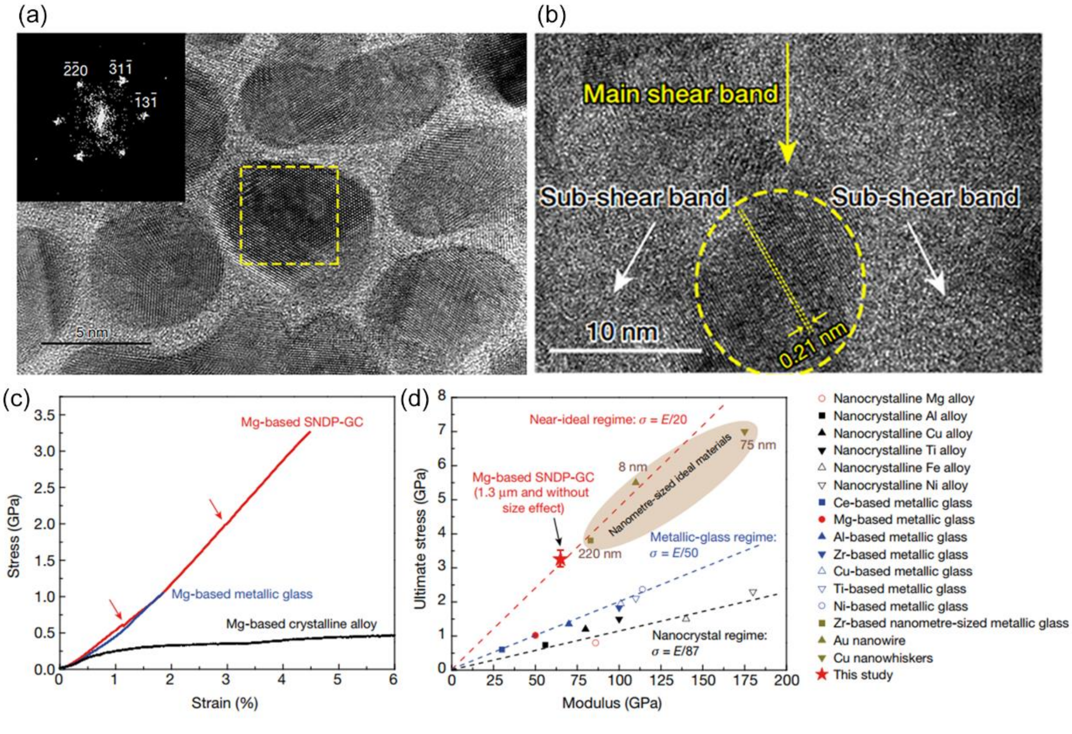

Figure 1.28 (a) Structure of crystalline-amorphous phase dual-phase in magnesium alloys. (b) HRTEM images of arresting the initial shear band generated two sub-shear bands. (c) Engineering stress–strain curves for micropillars in dual-phase magnesium alloys. (d) Curves of Young’s modulus and ultimate stress for compared the dual-phase Mg with other nanocrystalline alloys [127].

Similarly, a crystal-glass HEA nanocomposites was obtained by doping a glass-forming Fe–Si–B system into a crystalline CrCoNi base alloy through magnetron co-sputtering, which allowed the coexistence of a nanocrystalline phase with low SFE and an amorphous phase [128]. The nanocrystalline phase contains high-density nanotwins and SFs, which acts as effective barriers for dislocation motion, as shown in Figure 1.29. The amorphous phase undertakes the main plastic flow during the plastic deformation, absorbing some of the dislocations generated from the grains and migrating towards the grain-amorphous interface. This plastic flow of the amorphous phase helps to suppress the formation of shear bands, improving the uniform plasticity of the material. At the same time, the newly formed grain-amorphous interface also becomes a barrier to dislocation activities, producing a strengthening effect, compensating for the softening caused by the decrease in twin density.

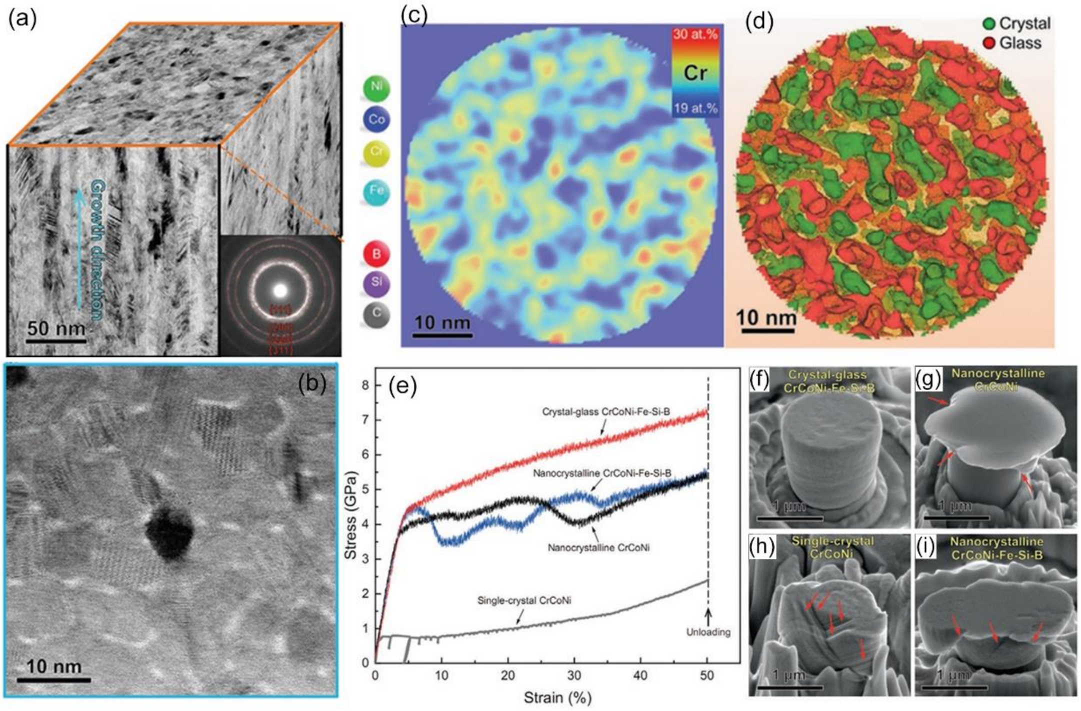

Figure 1.29 (a-b) TEM and HRTEM images of crystal–glass high-entropy nanocomposite. (c-

d) are concentrations of Cr and Fe illustrating crystal and glass. (e) Compressive engineering stress-strain curves. (f-i) SEM images of deformed pillar [128].

Moreover, atomistic models provide crucial insights into the atomic deformation mechanisms involving defect-interface interactions. These models illuminate processes such as GB sliding, GB migration, slip transmission, and dislocation nucleation, which enhances our understanding of the fundamental deformation behaviors in the crystalline-amorphous microstructure. Wang et al. [129] investigated crystal-amorphous nanolayered materials composed of alternating 5-nm-thick Cu layers and 35-nm-thick Cu-Zr glass layers through molecular simulation, which exhibits a high tensile elongation of up to 13.8% and a high flow stress of 1.09 GPa at room temperature. It is found that the nanoscale metallic glass layers can absorb dislocations and achieve a uniform plastic deformation at the crystal-amorphous interface, thereby enhancing the ductility of the entire material. The mechanical performance of this crystal-amorphous composite material surpassed that of single-phase elemental materials, providing a feasible approach to developing new nanomaterials with superior strength and ductility. The dislocation nucleates from the amorphous-crystalline interface (ACI) or GBs, gliding across the nanocrystal layer and being absorbed in the opposite GBs or ACI, as shown in Figure 1.30. The ACIs, compared to the GB or the crystal-crystal interface (CCI), have better slip transfer capability and can eliminate extreme geometric incompatibility. The metallic glass layer serves a dual purpose by acting as a source and sink for dislocations, which mediates inelastic shear and slip transfer, effectively preventing extreme stress concentrations that can otherwise initiate fractures.

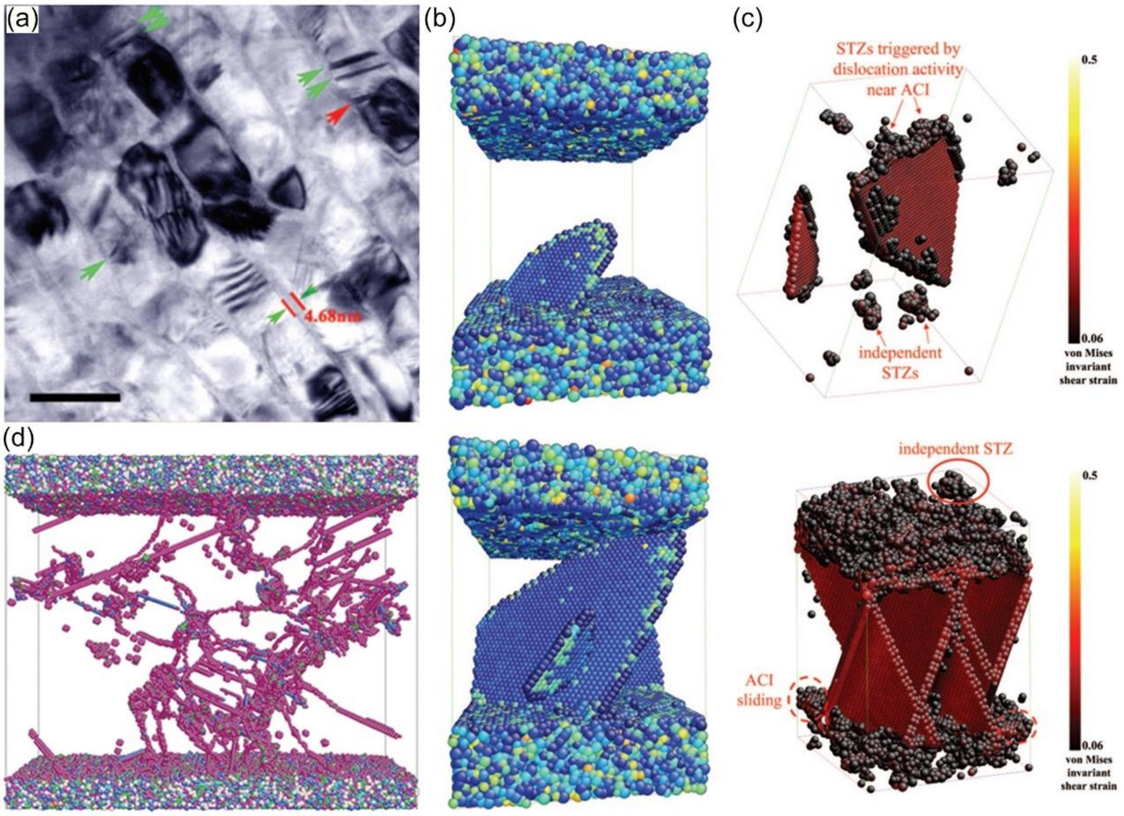

Figure 1.30 (a) HRTEM images of crystalline-amorphous nanolaminates. (b) Dislocation nucleates at ACI. (c) Activation of STZ (shear transformation zone) induced by partial dislocations in the amorphous layer. (d) Incompatibility of dislocations in the amorphous layer [129].

1.4 Processing Methods of Heterogeneous Structure

Currently, several techniques that can be used to generate nanoscale surface layers on CG materials through surface chemical treatment and surface plastic deformation [91]. Surface chemical treatments include surface coating and deposition, and surface plastic deformation involves applying intense strain to the surface layer to refine its microstructure to the nanoscale. These nanoscale surface layers often have a distinct interface with the underlying CG matrix and may differ in composition from the matrix material.

1.4.1 Severe Plastic Deformation

To fabricate GNS surface layer in metallic materials, severe plastic deformation techniques have been developed, including surface mechanical attrition treatment (SMAT) [99], surface mechanical grinding treatment (SMGT) [130], surface mechanical rolling treatment (SMRT) [131], high-energy shot peening (HESP) [132], and ultrasonic surface rolling (USR) [133]. These methods rely on intense localized plastic deformation to refine surface grains into the nanometer regime, while establishing a gradual transition in microstructure from the surface to the bulk, maintaining structural continuity without introducing a distinct interface.

The detailed mechanisms of the above processing methods are shown in Figure 1.31 [99]. The SMAT process introduces plastic deformation by randomly bombarding the surface with high-speed spherical shots, typically several millimeters in diameter, which are accelerated by ultrasonic or mechanical energy. This random multi-directional impact promotes isotropic deformation and high dislocation density, contributing to uniform grain refinement in the top surface layer. In contrast, SMGT involves a controlled grinding action wherein a hemispherical WC/Co tool tip penetrates into a rotating specimen and slides along its axis under lubrication. The contact stress and frictional shear together induce localized plasticity with directional features. SMRT, although similar in tooling, replaces the grinding movement with pure rolling, allowing smoother surface evolution and more uniform stress distribution. These differences influence not only the efficiency of grain refinement but also the morphology of the resulting nanostructure. HESP is a kind of industrial surface treatment method that employs high-pressure or compressed air to propel stainless steel shots onto the material surface, as shown in Fig. 1.31(d), inducing severe plastic deformation and forming a hardened layer. By tuning processing parameters such as peening pressure, injection angle, and spray distance, HESP can further enable surface nanocrystallization. The USR process operates by transmitting ultrasonic vibrations through a rolling tool head, which drives a spherical ball to repeatedly impact the rotating surface of the workpiece at high frequency and under static pressure. This dual action of ultrasonic impact and compressive rolling generates a concentrated stress field beneath the surface, promoting high-density dislocation activity and dynamic recovery.

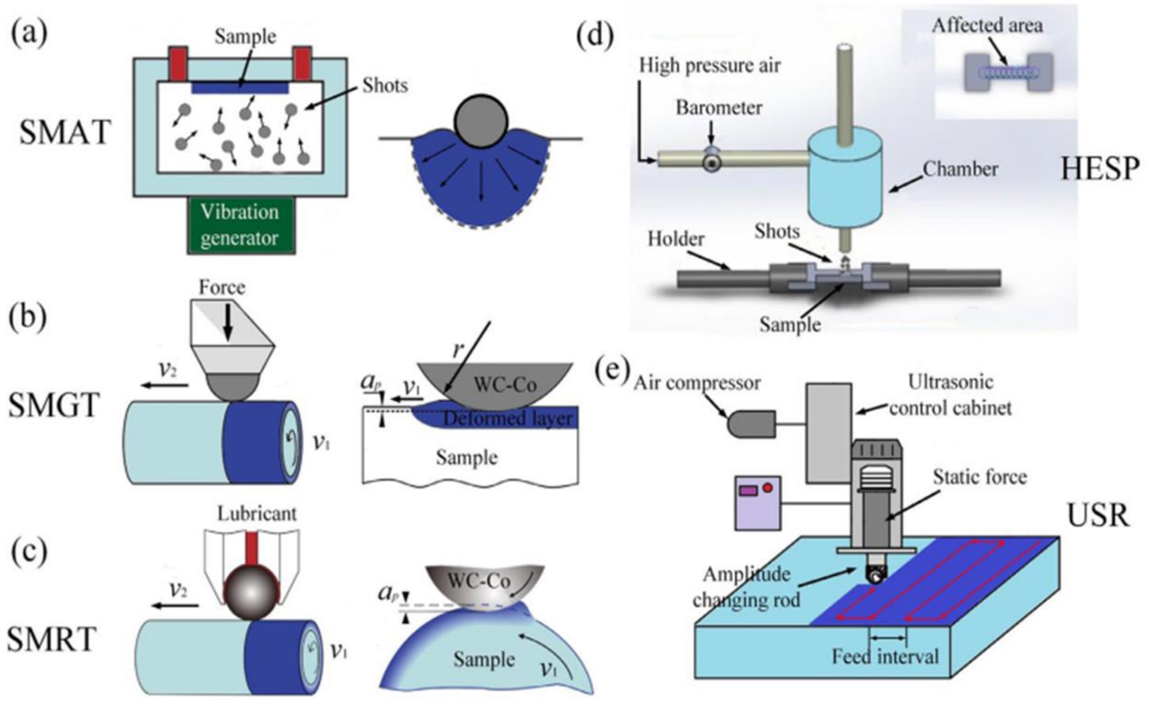

Figure 1.31 Schematic illustrations of (a) SMAT, (b) SMGT, (c) SMRT, (d) HESP and (e) USR techniques [99].

The underlying mechanisms of these fabrication methods involve the generation and accumulation of dislocations during plastic deformation, leading to the formation of dislocation-cell walls with the transformed sub-grains with small misorientation. Then, as the strain accumulates, they gradually transform into GBs with larger misorientations. This process divides the initial coarse grain into multiple fine grains, refining a mean grain size to extremely low (~20 nm) [134]. Specifically, the deformation mechanism driven by phase transformation, SF, deformation twins, and dislocation wall can be activated in the GNS layer for the metallic alloys with low SFE [105, 135]. The resulting grain morphology (e.g., equiaxed or lamellar) depends on the material and strain path and ultimately governs the local properties. The thickness and gradient profile of the GNS layer are primarily determined by the magnitude and distribution of accumulated plastic strain, which are in turn controlled by the process parameters of each technique [136, 137]. These plastic deformation-based methods offer versatile pathways for tailoring surface structure and improving the mechanical performance of metallic alloys.

Except for the specially designed treatment methods designed for the GNS layer, regions close to the contacting surfaces are subjected to large plastic deformation during the sliding wear process of metallic materials. This deformation modifies the microstructure and, thus, the properties of the worn regions, for instance, increasing the hardness through work hardening and grain size reduction [138]. These methods for modifying microstructures are ideal when selecting or designing materials for wear-resistant applications. However, worn surfaces represent non-equilibrium, dissipative systems that exchange energy and matter with their environment. This includes the opposing surfaces, as well as any liquid or solid lubricants present and the gases near the contact area [138]. Addressing these interactions poses ongoing challenges for the wear-induced generation of GNS. Despite these many challenges, an attractive feature of driven materials is their tendency to self-organize in response to external forcing microstructural patterns on a nanometer-length scale. This self-organized ability offers a valuable control parameter in the design of self-adaptive materials. For example, Zhu et al. [139] studied the formation of a gradient microstructure in pure tantalum subjected to a dry sliding wear test at room temperature and 600 °C, as shown in Figure 1.32. They discovered that the compressive stress exerted by the alumina ball induces the formation of gradient microstructure under the wear track. Their results indicate that the friction coefficient and wear were independent of the initial microstructure and hardness, however, the depth of the gradient layer under the wear track depends on the treatment.

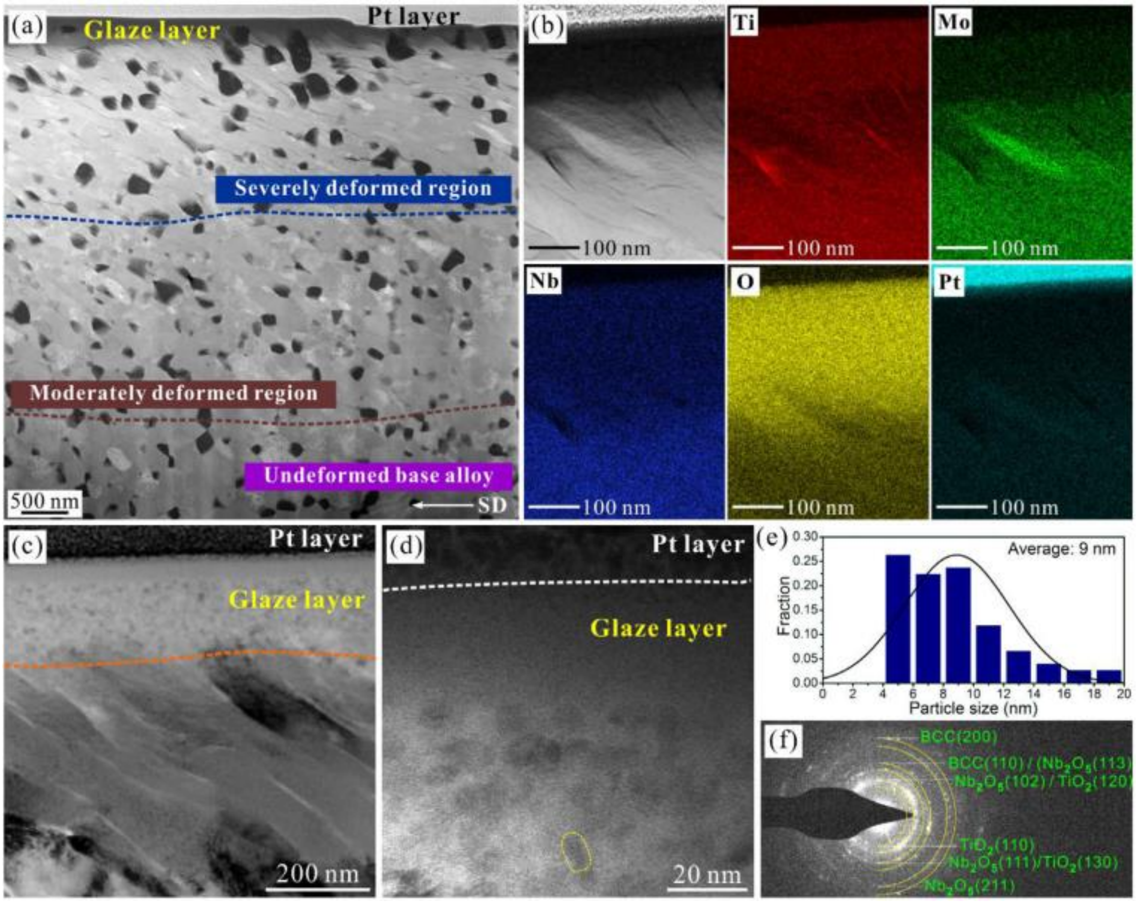

Figure 1.32 (a) Cross-sectional characterization of the TiMoNb alloy after dry sliding. (c-f) bright-field TEM image, HRTEM image, particle size distribution, and SAED pattern of the glaze layer, respectively [139].

In addition, the CoCrFeNi HEA experienced a significant enhancement of friction and wear resistance due to the spontaneous formation of a nanolayered subsurface microstructure during wear [140]. As depicted in Figure 1.33, there are three characteristic layers in the CoCrFeNi HEA. Closest to the surface, an equiaxed nanocrystalline (NC) layer with an average grain size of approximately 41 nm extends to a depth of ~0.8 μm. Beneath this lies a nanolaminated layer, consisting of elongated grains with an average thickness of ~63 nm and a plastically deformed layer marked by high dislocation densities and the presence of nanoscale deformation twins forms with the increase of depth, indicating severe strain accumulation. The formation of this gradient microstructure is attributed to the combined effects of dislocation activity and deformation twinning, both of which are governed by factors such as SFE, initial grain size, and fabrication parameters. The resulting depth-dependent grain refinement, with decreasing structural refinement away from the surface, contributes to a significant reduction in both the coefficient of friction and wear rate, highlighting the critical role of wear-induced nanostructuring in enhancing the tribological performance of HEAs.

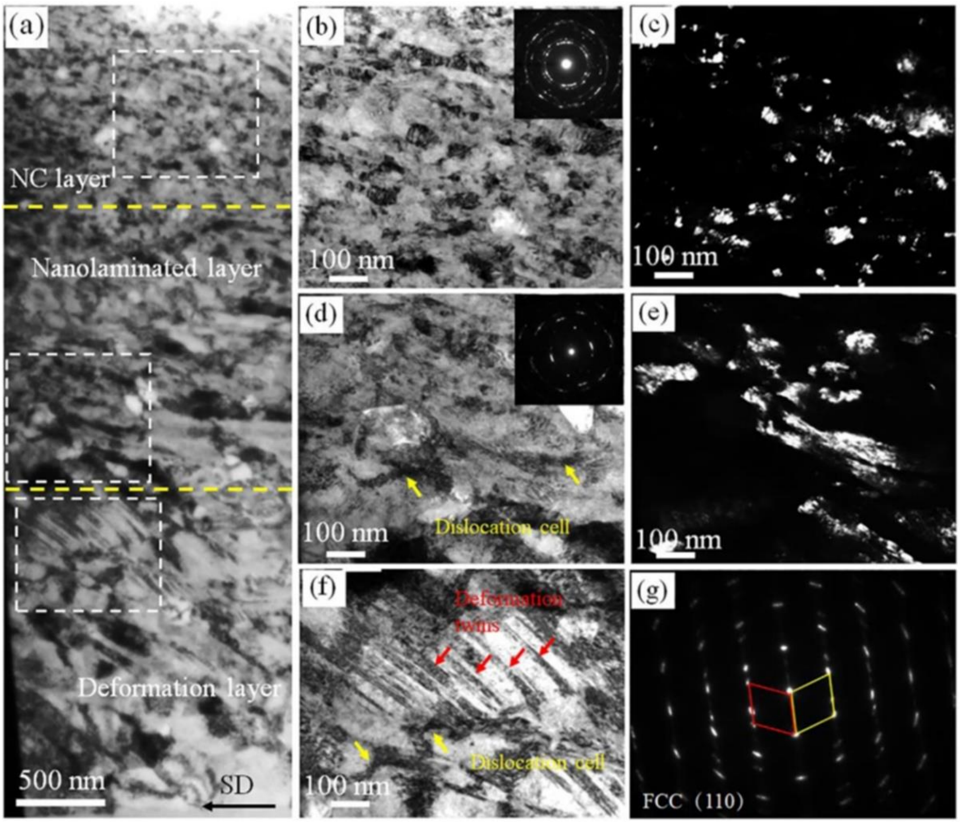

Figure 1.33 Cross-sectional microstructural evolution induced by sliding wear in CoCrFeNi HEA [140].

1.4.2 Ultra-precision Machining

1.4.2.1 Fundamentals of Ultra-precision Machining

With the development of machining precision, ultra-precision machining technologies are used to process materials with a high surface quality and accuracy [141]. Ultra-precision machine technology is suitable for various types of materials including metals such as soft metals and more challenging materials like hardened steel, stainless steel, high-speed steel, and hard alloys [142]. Additionally, it is used for hard-brittle non-metal materials, including semiconductors, ceramics, and glass [142]. Meanwhile, to enhance the properties, surface quality, reliability of products and interchangeability of components in the modern mechanical industries, machining precision is developed [141].

As modern industries and high-tech products demand more remarkable accuracy and surface integrity, research in ultra-precision machining has gained increasing importance. Additionally, this technology significantly impacts other advanced sectors, including nuclear, national defense, and aerospace industries. Current ultra-precision machining technologies include turning, grinding, cutting, polishing, and non-traditional machining [143]. The term "ultra-precision cutting" refers to a cutting technology that fabricates components with low roughness at several nanometers using tools made of tough materials, like diamonds. Based on the fabrication methods, ultra-precise cutting can be divided into precision turning, milling, boring, compound machining, or combining cutting with ultra-sonic vibration [143]. Regarding ultra-precision cutting, single-point diamond turning (SPDT) is the primary technique for achieving nanometer-level surface roughness. In SPDT, a single-crystal diamond is utilized as the cutting tool, characterized by its finely sharpened, small-diameter cutting edge [144]. This method is renowned for producing exceptionally smooth and precise surfaces, making it a cornerstone in high-precision machining applications. The nanoscale cutting edge can produce a smooth surface with minimal surface damage.

To achieve a satisfactory machining result, the optimal circumstances of parameters such as working environment, machine tools, cutting variables, workpiece materials, cutting tools and cutting fluid should be determined appropriately [145]. Although diamond tools, frequently used in the ultra-precision machining, have outstanding properties, there are serious technological limitations for machining carbon-based materials [145]. The working temperature is restricted, and degradation reactions occur with these metals. Therefore, some studies show that turning with the hard cubic boron nitride (CBN) tools has a different cutting mechanism [146]. Furthermore, the cutting edge of CBN tool offers a large negative rake angle to increase the wedge angle and tool strength, which also leads to severe plastic strain in the machined material, as shown in Figure 1.34 [147]. The hardness of CBN-built materials exhibits high hardness at 100GPa, high oxidation temperature at 1294°C and excellent fracture toughness [148]. Particularly, CBN tools allow a commercial and relatively low-cost offer for many technological applications.

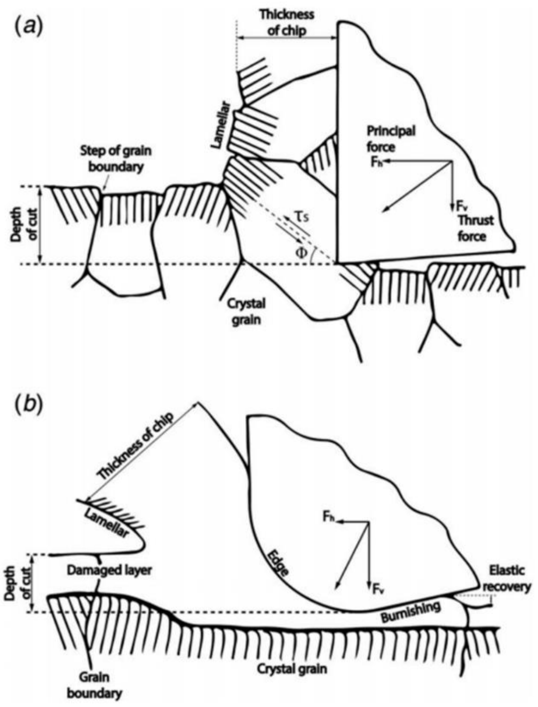

Figure 1.34 Schematic diagram of ultra-precision cutting with different tool edge [147].

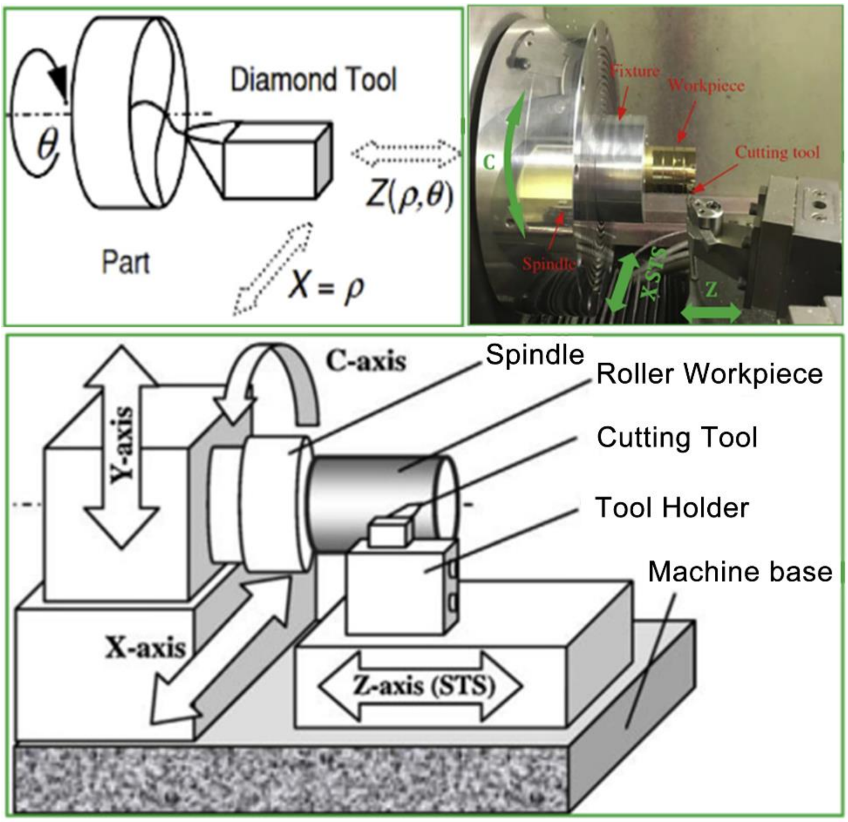

Figure 1.35 Set-up of ultra-precision turning under three axis [149].

Ultra-precision cutting is typically performed using a precision computer numerical control (CNC) lathe. The process begins by securing the workpiece in a vacuum chuck, which is then placed on an air bearing spindle, as illustrated in Figure 1.35 [149]. The cutting tool is mounted opposite the workpiece. To ensure proper lubrication during machining, coolants may be fed through a nozzle. The single-point cubic boron nitride turning (SPCBNT) is employed in copper to fabricate heterogeneous structures, including a sub-layer region of nano-crystalline-nano-twinned and a highly refined nano-twinned nanocrystalline top layer region (grain size around 10 nm), which resulted in the enhancement of mechanical properties, as shown in Figure 1.36 [96]. The accumulated plastic strain on the surface induced grain refinement along the depth direction. Also, a strengthening-soften transition of the deformation mechanism is generated in the affected region. Similarly, the gradient nanotwin structure is also successfully fabricated in CrCoNi MEA through the same SPCBNT method, resulting in the strengthening mechanism having a transition from the parallel grain refinement, twin-twin intersections, and nanograin rotation, and finally to the zero-macrostrain deformation nano-twinning in the refined nanograins [150]. This heterogeneous structure exhibits enhanced yield strength from 450MPa to 1100MPa and well-retained ductility of 27%.

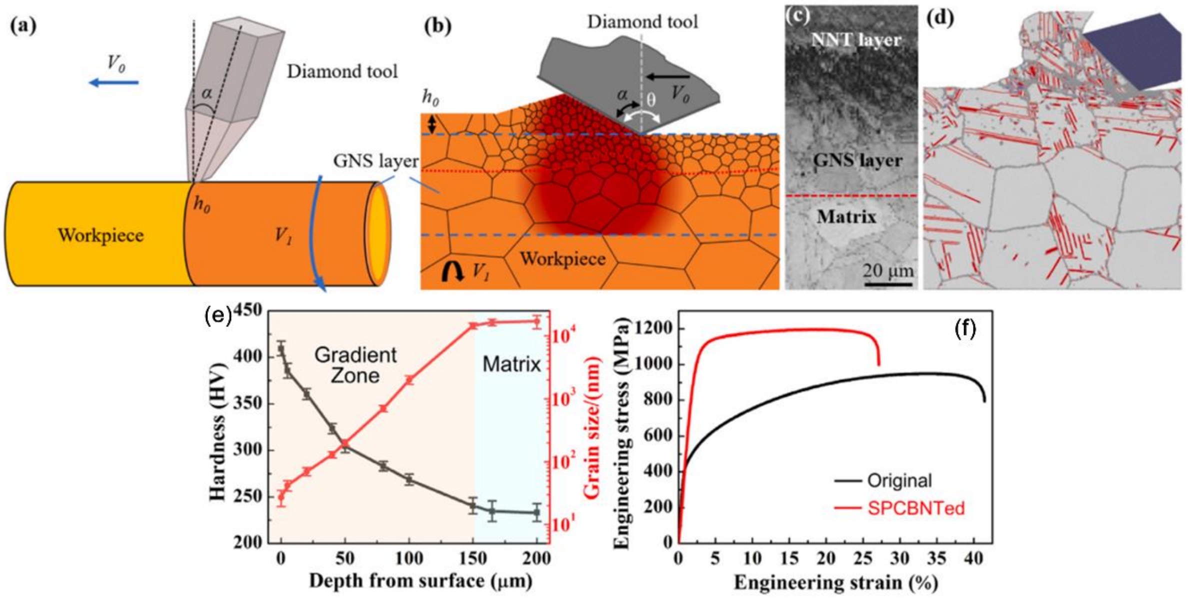

Figure 1.36 (a-b) Schematic diagrams of the SPCBNT process. (c) Cross-sectional OM image showing the heterogeneous structure. (d) MD simulation of SPCBNT process [96]. (e) Hardness and grain size variation at the different depths. (f) Engineering stress-strain curves of the generated heterogeneous structure in CrCoNi MEA [150].

1.4.2.2 Applications of Ultra-precision Machining in Heterogeneous Structure

The term "ultra-precision" addresses the challenges of accomplishing specified goals at technical levels and the specific index of profile accuracy and surface quality. Although surface roughness is already at the sub-nanometer level, in some applications, ultra-precision machining technology presents a problem at the nano level (i.e., machining accuracy is nearing several nanometers). Research on ultraprecision machining has become more pertinent since modern industries and high-tech goods demand more rigorous accuracy and surface integrity, which also widen the application fields [147].

Traditional machining methods for fabricating gradient structures require post procedures, which lead to complex machining procedures and energy waste. Compared with surface mechanical treatment for producing GNS, the more feasible and economic machining procedures like ultra-precision machining technologies are suitable for mass production in HEAs, which is beneficial for expanding application fields like high-tech areas, such as nuclear, national defense, and aerospace [106, 151]. Gradient-structured HEAs generated by ultra-precision machining exhibit excellent wear resistance, which is suitable for coatings with high demand of surface roughness and friction resistance at high and low temperatures, like excellent mechanical properties of AlCoCrFeNi2.1 HEAs from 77 K to 1000 K [152, 153]. For example, the fcc-based gradient HEAs coating shown in Figure 1.37 exhibits superior mechanical properties and wear resistance, making gradient-structured HEAs suitable for abrasive environments [154].

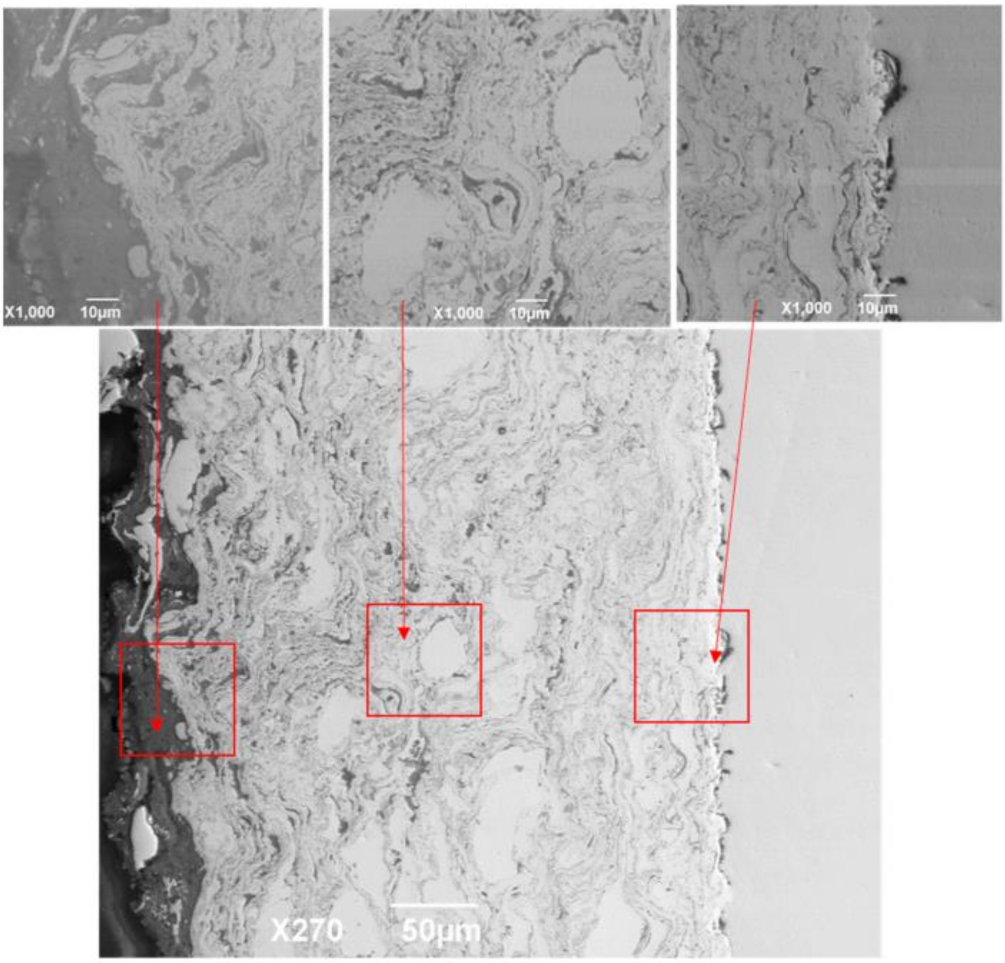

Figure 1.37 SEM image of the cross-section of NiCrAl gradient coating [154].

With their excellent mechanical properties and seawater corrosion resistance, gradient-structured HEAs are ideal for various applications. These include ice-breakers, ship pipelines, motor housings, valves, offshore oil platforms, and acid pump components, offering a superior alternative to copper alloys and stainless steel [91, 155]. They are also suitable for complex structural castings requiring high mechanical performance and corrosion resistance. Furthermore, their exceptional strength and crack propagation resistance make them well-suited for safety-critical, load-bearing structural applications. Thus, materials with smooth surface finishes are also highly appropriate for use in dental and orthopedic implants [93].

Gradient-structured HEAs present fascinating potential as functional materials, especially when produced in large quantities and with high surface quality through ultra-precision machining, as illustrated in Figure 1.38 [149]. The lightweight gradient-structured HEAs can serve as casings for mobile facilities, battery anode materials, and in the transportation sector and some HEAs possess effective dampening characteristics, making them suitable as shock absorbers [95]. Micro-structured functional surfaces, including micro-pyramids, microgrooves, and structured riblet surfaces, enable HEAs to demonstrate unique properties conducive to energy conversion [156]. The ultra-precision-machined HEAs facilitate the creation of these specialized surfaces, making them suitable for applications such as cooling, drag reduction, and self-cleaning [156]. Exploring the use of gradient-structured HEAs across interdisciplinary domains such as tribology, geology, optoelectronics, biomechanics, and nanotechnology holds great promise due to the inherent multifunctionality of these metals and alloys[157].

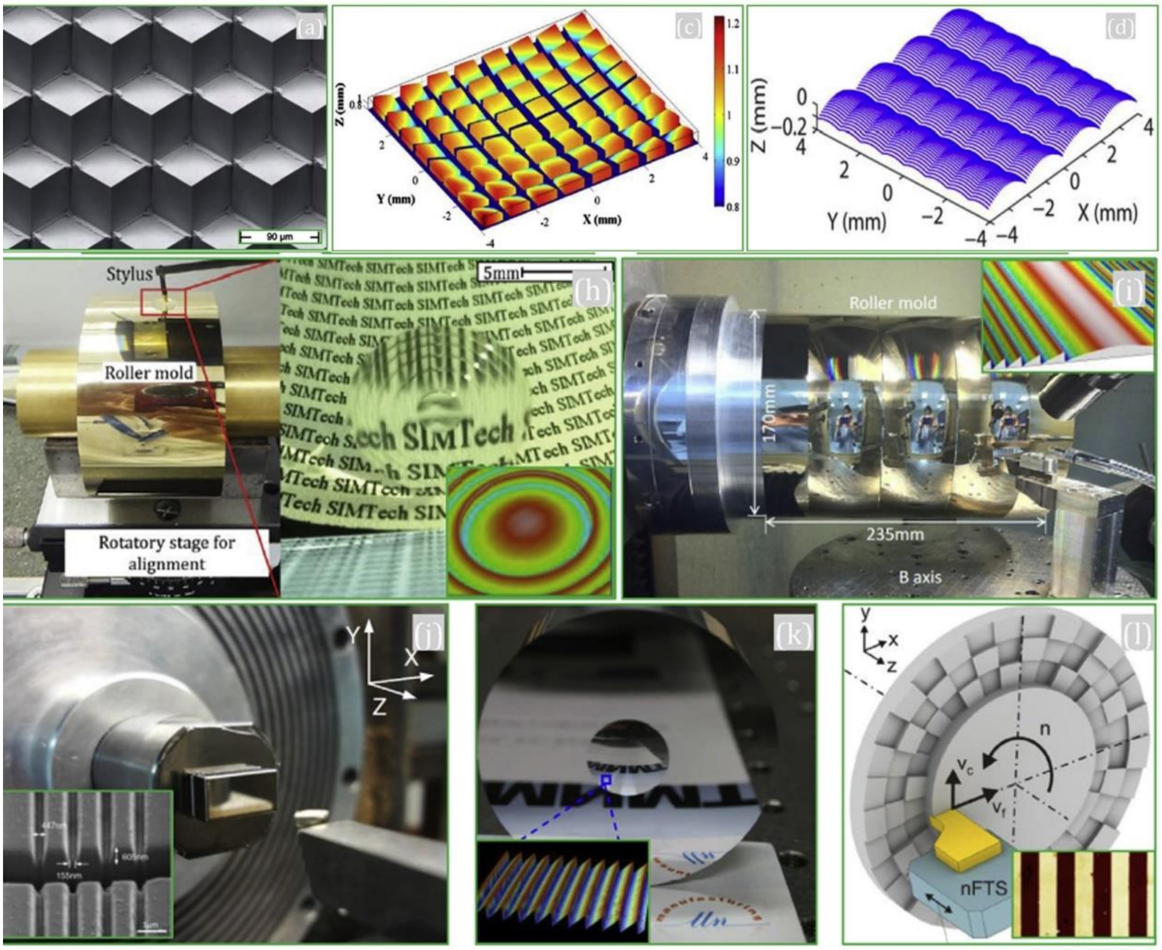

Figure 1.38 Typical micro-structures of ultra-precision machining for optical applications [149].

1.4.3 Laser surface treatment

With high-density energy, precise control, flexibility, and high precision, laser surface treatment has emerged as an advanced technique for fabricating GNSed metallic alloys with varied dimensions and complex shapes, which improves the strength, corrosion resistance, and fatigue resistance of the remelted zone by optimizing the microstructure or precipitation characteristics [98, 158]. This technique encompasses methods such as laser shock peening (LSP), laser surface remelting (LSR), and laser surface quenching (LSQ) [159]. The gradient refinement mechanisms achieved through LSR and LSQ involve the rapid heating and cooling induced by high-power laser beams, with a very high cooling rate at 10^4–10^6 °C/s [98, 160]. The rapid thermal cycles in LSR and LSQ generate ultra-high thermal and residual plastic strains along the specimen depth during solidification and self-quenching. While extreme temperatures promote the nucleation of new phases, the short cooling duration inhibits significant growth of nanosized nuclei, resulting in the formation of GNS that enhance the mechanical properties of HEAs. For example, the microstructure of the prepared CoCrFeMnNi HEAs [161] consists of four distinct sections due to varying heat inputs: a fine-grained region, a transition region, a coarse-grained zone, and a partially recrystallized region, as shown in Figure 1.39. The combination of partially recrystallized regions, noted for their high yield strength, with fully recrystallized regions, which exhibit enhanced strain hardenability and elongation, significantly improved the mechanical performance. This enhancement is primarily driven by additional strengthening from back stress.

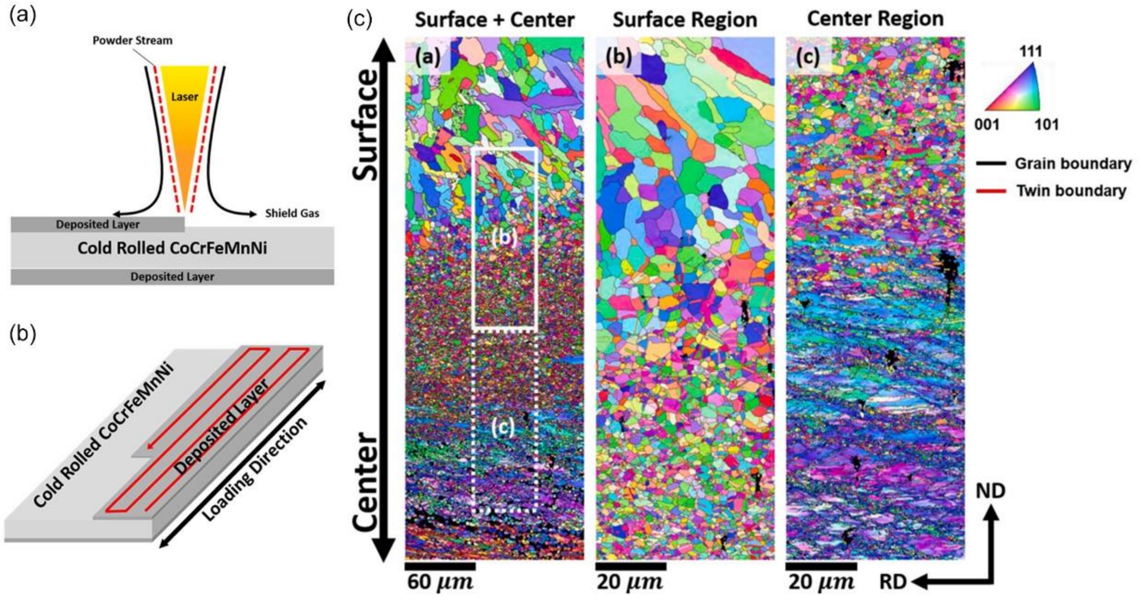

Figure 1.39 (a) Schematic diagram of laser metal deposition and (b) scanning pattern. (c) Cross-

sectional images of-gradient structured CoCrFeMnNi HEA [161].

Lou et al. [162] employed high-energy laser pulses to generate high-pressure shockwaves, which induce ultra-high plastic strain along the depth direction and lead to the formation of gradient nanostructures on the treated surface. Similarly, Fu et al. [163] studied CrFeCoNiMn0.75Cu0.25 HEAs specimen with gradient microstructures fabricated by LSP processing exhibited improved yield strength, attributed to the defects generated by laser impact illustrated in Figure 1.40. As summarized in Figure 1.40(c), the strengthening can contribute from the dense dislocation, refined grains, low angle grain boundaries (LAGB) and nanotwins (NTs). The synergy of dislocation hardening and mechanical twinning significantly enhances the strain-hardening capability of the LSP-treated HEA, resulting in excellent plasticity under tensile loading. During subsequent tensile deformation, the core region of the specimen, unaffected by the LSP treatment, primarily accommodates dislocation activity. In contrast, the top layer affected by the LSP exhibits minimal additional plasticity due to sufficient initial hardening.

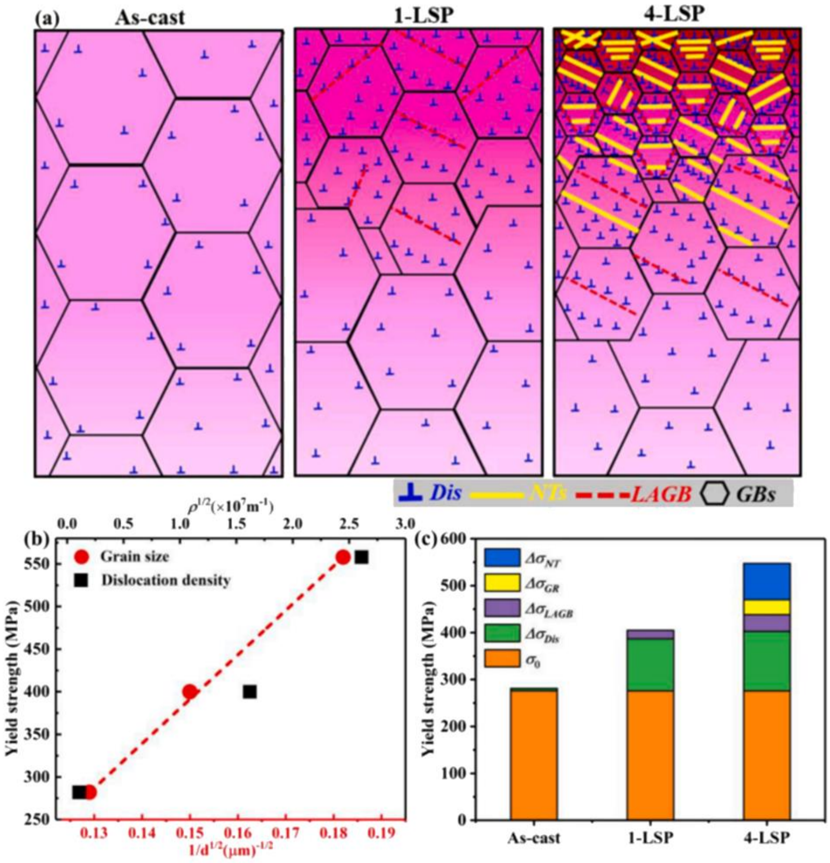

Figure 1.40 (a) The schematic illustrations of the strengthening mechanisms of laser shock peening. (b) Relations between the yield strength with grain size and dislocation density, and (c) contribution of strengthening mechanism of refined-grains, NTs, dislocations and LAGBs into the yield strength of the studied $CrFeCoNiMn_{0.75}Cu_{0.25}$ HEA specimens before and after treatment [163].

1.5 Research gaps

HEAs have garnered significant attention because of their exceptional properties and potential applications across various fields. Furthermore, introducing a heterogeneous structure in HEAs can improve their mechanical properties, such as addressing the balance between strength and ductility, as well as enhancing wear resistance. Therefore, it is crucial to establish a theoretical foundation regarding the microstructure and properties of HEAs with heterogeneous structures to facilitate their potential applications. Current research has demonstrated the feasibility and considerable potential of integrating heterogeneous structures into HEAs. However, there are still several issues that require further investigation.

(1) The development of fabrication methods of heterogeneous structure/GNS in HEAs

The fabrication methods for heterogeneous structure and GNS are currently limited in scientific research, such as through surface mechanical treatment. This limitation makes them unsuitable for industrial applications, particularly in terms of production scale and surface quality. Therefore, it is essential to discuss newly developed machining methods with optimized processing parameters that are suitable for mass production when fabricating heterogeneous structure in HEAs.

i) Traditional machine methods usually fabricate heterogeneous structure accomplished with inferior surfaces. The need for additional procedures to modify machined surfaces complicates the machining process and leads to energy waste. This situation highlights the demand for more efficient and cost-effective fabrication methods, such as ultra-precision machining, which is suitable for mass production with high surface quality. However, current ultra-precision machining techniques only produce limited volume fractions of heterogeneous structured layers that are localized near the surface, resulting in a negligible degree of gradient structure in the depth direction. Consequently, the limited thickness of these layers adversely affects the mechanical properties of the entire processed specimen. Therefore, there is a need for optimized processing methods to reduce the ratio of the thickness of the bulk specimens to that of the hardened heterogeneous structured surface layer.

ii) Laser treatment techniques that use a high-energy laser beam to create a remelting zone are an effective method for controlling the depth of heterogeneous structure. However, excessively high laser power can negatively affect the microstructure, which in turn influences the mechanical properties of the material. Therefore, optimizing the processing parameters is essential for effectively applying laser surface treatment in the fabrication of heterogeneous structure.

(2) The formation mechanism of heterogeneous structure in HEAs

The formation of heterogeneous structure is primarily attributed to gradient plastic deformation from the surface to the matrix. This process is influenced by dislocation slip, deformation twins, and phase transformations, all of which occur at different strains and various strain rates. However, due to a lack of atomic-scale understanding, such as the sites of dislocation initiation, the types of dislocations, and their interaction activities, these actual formation mechanisms are difficult to explore. Therefore, a deeper understanding of heterogeneous structure formation mechanisms at the atomic level is necessary.

(3) The treatment-microstructure-properties correlation during plastic deformation

Most of the studies mentioned above aimed to understand the fundamental mechanisms that affect the mechanical properties of heterogeneous structure in HEAs. However, the behavior of dislocations and their interactions with other defects, such as twins, GBs, and phase transformations during plastic deformation, are intricate. Consequently, it is necessary to conduct quantitative studies on atomic evolution to directly assess the deformation mechanisms in the specific structure.

1.6 Research objectives

This research aims to investigate the underlying formation mechanisms, mechanical properties with the corresponding deformation mechanism of heterogeneous-structured HEAs fabricated using various methods. The specific objectives are as follows:

1. To examine the tribological properties of the bcc-based $TiZrHfTa_{0.5}$ RHEA and to analyze that GNS and phase evolution affect wear performance through exploring the microstructural characteristics and deformation mechanisms after friction.
2. To assess the impact of gradient plastic deformation under ultra-high strain on the microstructural characteristics within the heterogeneous structure, phase composition, and mechanical properties along the gradient direction of the fcc-based $Fe_{45}Mn_{35}Cr_{10}Co_{10}$ HEA with low SFE.
3. To develop a multi-phase heterogeneous nanostructure comprising both crystalline and amorphous phases in the fcc-based $Fe_{45}Mn_{35}Cr_{10}Co_{10}$ HEA processed through laser surface treatment, and to reveal the cooperative co-deformation mechanisms of nanosized amorphous structures and nanograins.

1.7 Organization of the Thesis

The thesis investigates the microstructural evolution and deformation mechanisms of heterogeneous structures in HEAs produced through various surface processing techniques. It specifically examines atomic dislocation movements, phase transformations in GNS, and the corresponding deformation mechanisms in detail. The thesis is organized into five chapters:

Chapter 1: This chapter introduces the research background, motivation, and objectives. It provides a comprehensive literature review focusing on HEAs and heterogeneous structures, covering their microstructure, mechanical properties, strengthening mechanisms, fabrication methods, and the challenges and issues identified in previous studies.

Chapter 2: The methodology chapter outlines the surface treatment techniques used to create heterogeneous structures, as well as the mechanical testing and microstructural characterization methods employed in the research.

Chapter 3: This chapter investigates a repeated sliding wear process on the surface is adopted to generate GNS on a bcc-based dual-phase $TiZrHfTa_{0.5}$ RHEAs experienced pre-plastic deformation and thermal treatment, which accommodates sliding-caused gradient plasticity and contributes to the enhanced wear resistance. It discusses the wear mechanisms, revealing wear-induced microstructural evolution, phase transformation from bcc to hcp through two distinct mechanisms, and the associated deformation mechanisms.

Chapter 4: This chapter investigates the GNS surface layer generated by high-strain rate single point cubic boron nitride turning on a fcc-based dual-phase $Fe_{45}Mn_{35}Cr_{10}Co_{10}$ HEAs with typical phase transition and significantly enhanced strength. The plastic deformation with an ultra-high strain rate triggers a phase transition sequence of fcc → hcp → bcc, examined in detail using High-Resolution Transmission Electron Microscopy (HRTEM). The cooperative action between partial dislocation dipoles and atomic shuffling is crucial for introducing the bcc phase within the nanograins.

Chapter 5: This chapter analyzes a GNS surface layer with a crystalline-amorphous nanostructure in fcc-based $Fe_{45}Mn_{35}Cr_{10}Co_{10}$ HEA generated by laser surface treatment. It discusses the mechanical properties as assessed through nanoindentation and micro-pillar compression tests and the microstructural evolution from the matrix to the surface. Additionally, it highlights dislocation movements, deformation-induced crystallization, grain coalescence and grain coarsening of cooperative deformation mechanisms.

Chapter 6: The final chapter summarizes the overall conclusions of the study and offers suggestions for future research directions.

Chapter 2 Research Methodology

2.1 Specimen preparation

This research focuses on two types of HEAs, including bcc-based $TiZrHfTa_{0.5}$ RHEA and fcc-based $Fe_{45}Mn_{35}Cr_{10}Co_{10}$ HEAs. For the first work, the alloys with nominal compositions of $TiZrHfTa_{0.5}$ RHEA with the lowered Ta content were fabricated by vacuum arc melting using high-purity metals (>99.9 wt.%) in a Ti-gettered high-purity argon atmosphere with a water-cooled copper mold. The specimens were remelted five times and flipped for each melt to produce homogenous components in the alloys. Subsequently, the as-cast specimens were subjected to cold rolling to achieve a 55% reduction in thickness. Different annealing treatments were applied at 200 ºC, 420 ºC and 870 ºC, respectively, for 20 minutes in Ar atmosphere followed by furnace cooling.

For the second and third research investigations, the $Fe_{45}Mn_{35}Cr_{10}Co_{10}$ HEA specimens were produced using vacuum arc-melting. This melting of the constituent elements was maintained under vacuum conditions to ensure a homogenous mixture and to avoid contamination. Following the arc-melting stage, the alloys underwent a hot-rolling process, which involved a thickness reduction of 60% performed at a temperature of 900 °C. After the hot-rolling process, the hot-rolled plates were subjected to an annealing treatment at 900 °C for 1 hour. In addition, Oxygen / Nitrogen / Hydrogen Analyzer (TCH600, LECO) and Carbon/Sulfur Analyzer (CS844, LECO) were used to check the contents of impurity elements

C, N, and O in the specimens, which are as low as 0.0181 wt.%, 0.0026 wt.% and 0.055 wt.%, respectively.

2.2 Surface treatment methods

This research uses two different methods to generate heterogeneous structure in the specimens. For the Single Point Cubic Boron Nitride Turning (SPCBNT) process used in the second research, the plate specimens were mounted on a holder of a Moore Nanotech 450UPL precision machine, as shown in Figure 2.1. The SPCBNT procedure was executed with specific processing parameters to achieve the desired material characteristics in 2-axis Ultra-precision Machine– Nanoform 200. These processing parameters employed for the SPCBNT included a spindle speed of V_1 = 200 rpm, a tool rake angle of α = 20°, a feed rate of V_0 = 1 mm/min, and a cutting depth of 10 μm. This process was repeated for 20 passes to ensure uniform plastic deformation.

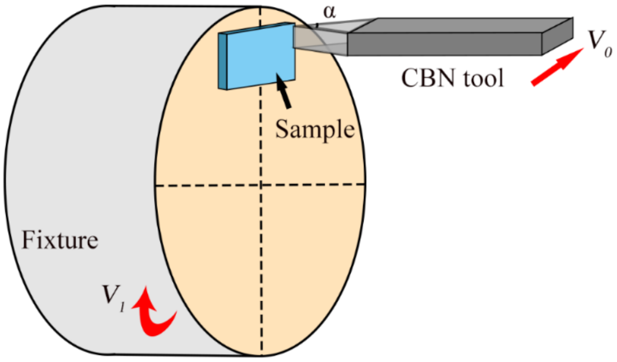

Figure 2.1 Schematic of SPCBNT technique.

The machining method discussed in the third research is laser surface treatment (LST). The plate specimens were polished to complete the LST process with 2kW fiber laser system (MSV-200 W, M-SOLV). As shown in Figure 2.2, the laser beam along a continuous zigzag-path was incident perpendicularly during the LST process onto the surface. To achieve the high cooling rates required for this process, the specimens were placed in a specialized holder designed to enhance thermal dissipation. Liquid nitrogen surrounded the specimens within the holder, creating an extremely cold environment that facilitated rapid cooling immediately after laser exposure. Additionally, Ar gas was injected directly into the specimen surface during the LST process. This injection serves multiple purposes: it provides a controlled atmosphere to prevent oxidation and other surface reactions, and it further enhances the cooling rate by aiding in the efficient removal of heat from the laser-affected zone. Together, these measures ensure that the LST process effectively modified the surface properties of the plate specimens while maintaining the structural integrity.

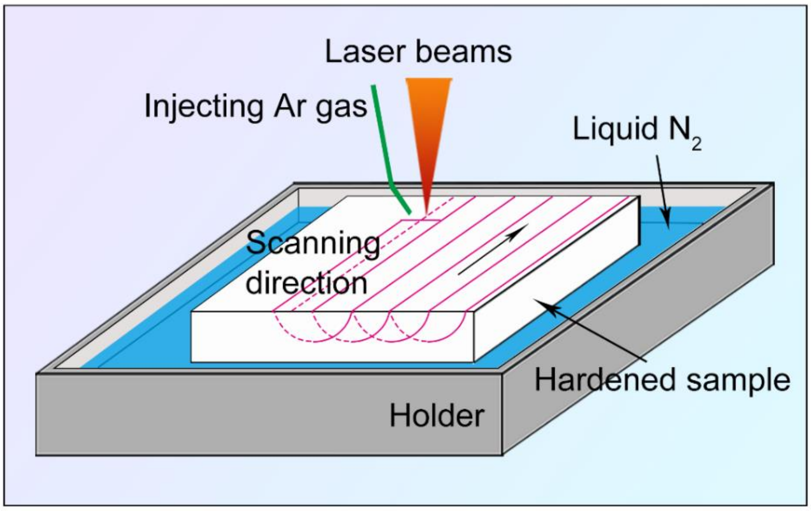

Figure 2.2 Schematic of LST technique.

2.3 Microstructural characterization

The phase constitutions of the specimens were thoroughly examined using X-ray diffraction (XRD) with Cu-Kα radiation. The diffraction measurements were performed within the 2θ range of 20º to 110º, with a scanning rate of 0.02º per minute, ensuring precise phase identification. Simultaneously, GIXRD was used with a small fixed incident angle at 2°, limiting the X-ray penetration depth to identify the phase constitutions for GNS samples at different depths. For each desired analysis depth (e.g., 10 μm, 20 μm, etc.), the surface was carefully ground using fine SiC abrasive papers to remove material down to the target depth. An Optical Microscope (OM, Zeiss) provided initial observations, while Scanning Electron Microscopy (SEM, TESCAN VEGA3) equipped with an Energy Dispersive X-ray Spectrometer (EDS) detector offered detailed compositional analysis. Additionally, Electron Backscatter Diffraction (EBSD, Oxford) equipped in SEM (Helios G4) was utilized for investigating crystallographic features. Transmission Electron Microscopy (TEM, JEOL-2100F operating at 200 kV) and Scanning TEM (STEM) were performed to observe microstructural evolution at higher resolutions. Plan-view specimens at specific depths were prepared by mechanically sanding the specimens to the targeted depth layer, followed by further thinning to a ~20 μm-thick TEM foil from the opposite side. These foils were then glued to a copper ring and thinned further by ion-milling using a Gatan Model 691. Cross-sectional specimens were prepared using a Focused Ion Beam (FIB, Helios 600i) to accurately identify and analyze the microstructural evolution within the gradient nanostructure.

2.4 Mechanical properties tests

The mechanical properties were examined using microhardness, nanohardness, compressive test and wear test. Microhardness tests were performed at room temperature using a Matsuzawa Via-F automatic Vickers hardness tester. These tests applied a load of 1N with a dwell time of 15s. A nanomechanical test instrument (Hysitron TI 900, USA) equipped with a diamond tip featuring a three-sided pyramid shape was utilized for the nanoindentation tests. Each test point was subjected to a force of 10 mN for 2s, with the procedure repeated three times to ensure accuracy. A two-step milling method was used to prepare micro-pillars for compressive testing with a focused ion beam (FIB) system (Helios Nanolab 600i, FEI). The coarse milling was performed with currents ranging from 9.3 to 2.5 nA, followed by fine milling using currents between 10 and 40 pA. The resulting micro-pillars had diameters of approximately 800 nm and aspect ratios ranging from 2 to 3. At least four pillars from each depth were compressed using the nanoindenter (Hysitron TI 900, USA) equipped with a diamond flat-punch tip (10 μm in diameter). These compression tests were conducted in displacement control mode, achieving a ~32% height reduction, with a strain rate of 1×10^{-3} s^{-1}. The reciprocal dry-sliding wear tests (12000 cycles) under loads ranging from 16 N to 64 N at room temperature were then conducted on all specimens by TE99 universal wear machine with 6 mm-diameter Si_3N_4 balls. Throughout the sliding wear test, the coefficients of friction (COF) were recorded constantly. The wear volume and wear rate were determined through the measurement of depth and width of the wear stroke by using the white-light interferometers with a three-dimensional(3D) surface profiler (ZYGO, USA). The wear rate ω was calculated according to Eq. 3.1:

$$\omega = \frac{V_{loss}}{L \times F} \tag{3.1}$$

where V_{loss} is the wear volume loss(mm^3), L is the sliding distance (m) and F is the applied normal load (N).

Chapter 3 Heterogeneous structure on the bcc-based TiZrHfTa$_{0.5}$ RHEA

3.1 Introduction

M/HEAs consisting of three or more equiatomic/near-equiatomic elements have drawn significant attention due to some impressive properties, such as high strength and toughness, as well as relatively good corrosion resistance [2, 109]. However, the strength-ductility tradeoff exists in many HEAs since their plastic characteristics are similar to conventional metals [12]. Strength-ductility dilemma would cause the stain localization (e.g., surface roughening, cracking, and delaminating) during the repeated sliding wear, thus leading to high COFs and wear loss [164]. In contrast to the traditional uniform grain refinement method [90, 165], the strength-ductility synergy has been documented in the dual- or multi-phase metals and M/HEAs [22, 68]. The co-deformation cooperative effects of the newly transited and parent phases with distinct plastic characteristics (i.e., TRIP effect) could significantly enhance the strength/hardness-ductility synergy [64, 166] and the resultant tribological performance [167-169].

The bcc-TiZrHf-based alloys are the most promising RHEAs owing to extraordinary mechanical properties, e.g., ultra-high and-stable strength [29] and elastic modulus [170] at elevated temperatures. The phase transition from bcc to hcp/ fcc structures can be manipulated to further improve the strength-ductility combination for better tribological performance [159, 171]. For example, lowering the content of Ta element in TiZrHfTa-based HEAs can not only destabilize the bcc matrix to construct a dual-phase structure through forming hcp phase but also facilitate the TRIP effect in the following thermomechanical treatments (e.g., cold rolling plus annealing treatment) [68, 159, 171, 172]. Noticeably, annealing temperature after the cold rolling process also plays a critical role in tailoring the microstructures (e.g., recrystallization degree, grain structures, and phase constitutions) [173]. In addition, bcc → hcp phase transition might also be triggered by the gradient plastic strain/strain rate in the worn subsurface during the repeated sliding process, thus possibly forming a self-organized gradient structure toward the lowered steady-state COFs and wear rates [138, 174]. Nonetheless, function, compositional segregation, and atomic mechanisms of bcc → hcp phase transition during the sliding of TiZrHfTa-based HEAs should be in-depth elucidated, especially via atomic-scale characterizations. Atomic-scale observations dissected two kinds of atomic movement mechanisms of the composition-segregated bcc → hcp phase transition that continue accommodating the sliding-caused gradient plastic strain/strain rate in a self-organized worn subsurface to further improve tribological performance.

3.2 Results and discussion

Figure 3.1 and Figure 3.2 summarize the grain structures (backscattered electron microscope (BSE)) images and corresponding EBSD images and phase constitutions (XRD) patterns of the as-cast and cold-rolled plus annealed specimens, respectively. The as-cast specimen with an average grain size of ~ 450 μm has the dual-phase microstructure, as BSE and EBSD images shown in Figure 3.1(a) and XRD pattern shown in Figure 3.2, respectively, in which the volume fraction of small-sized hcp phase uniformly distributed in bcc matrix is estimated as ~ 27% based on the integrated intensities of the reflecting planes [175]. It is noted that annealing temperature apparently affects the grain structures and the fraction of hcp phase in the cold-rolled specimens. Deformed and elongated microstructures are still retained in the 200 ºC- and 420 ºC-annealed specimens (Figure 3.1(b-c). More and more nanostructured hcp phase is found to mainly nucleate from bcc grain boundary with annealing temperature, as the BSE and corresponding EBSD images shown in Figure 3.1(a-d), which might induce a strong intergranular strengthening effect and thus inverse the softening tendency caused by annealing [176, 177]. Finally, a typical homogeneous equiaxed microstructure (an average grain size of ~ 30 μm) with the highest fraction of nanosized hcp phase (i.e. ~ 66%) is obtained in the 870 ºC-annealed specimen (Figure 3.1(d)).

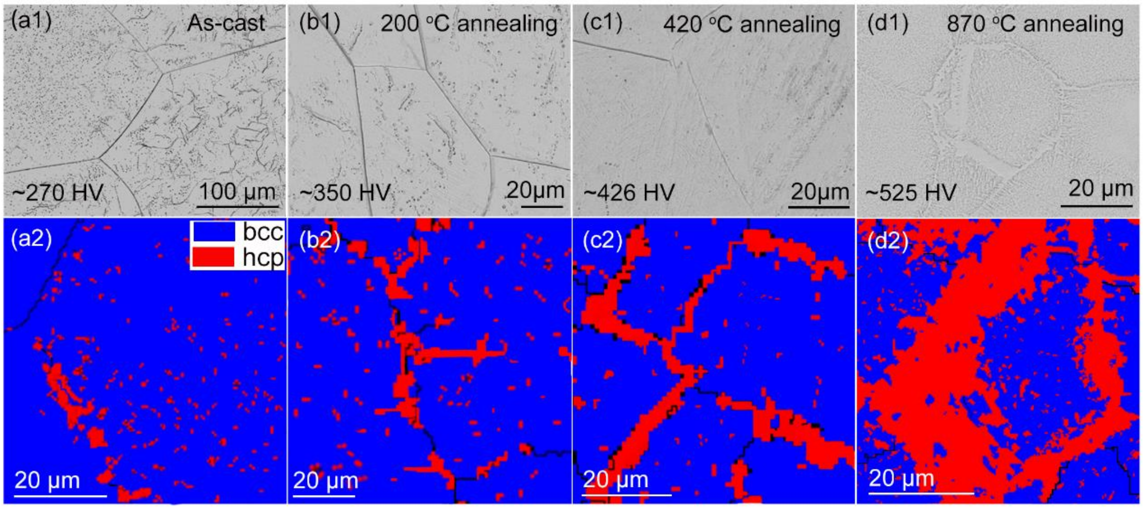

Figure 3.1 BSE and EBSD images of the (a1-a2) as-cast TiZrHfTa$_{0.5}$ RHEA and the cold-rolled plus (b1-b2) 200 °C-, (c1-c2) 420 °C-, and (d1-d2) 870 °C-annealed specimens, respectively.

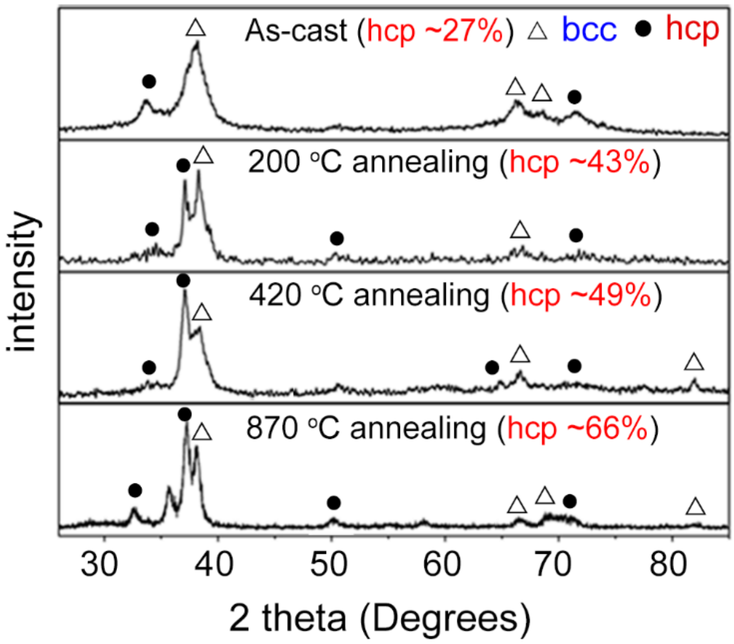

Figure 3.2 XRD patterns of the TiZrHfTa$_{0.5}$ RHEA after cold rolling and annealing at different temperatures.

The TEM images with SAED patterns reveal that the orientation relationships (ORs) between the bcc and hcp phases are the same in both as-cast and cold-rolled plus annealed specimens, i.e. $[1\bar{1}1]$bcc//$[11\bar{2}0]$hcp and $[00\bar{1}]$bcc//$[11\bar{2}0]$hcp directions, as the selected area electron diffraction (SAED) patterns indicated in Figure 3.3. Furthermore, higher-magnification TEM image of 870 ºC-annealed specimens in Figure 3.3(c) shows that the nanosized hcp phase with an average size of ~ 100 nm is TiTa-rich, different from the ZrHf-rich bcc phase, different from the relatively homogeneous elemental distribution in as-cast specimens shown in Figure 3.3(b). Furthermore, owing to its strongest strengthening effect caused by the highest-fraction nanosized hcp phase accumulated at GB, the cold-rolled plus 870 ºC-annealed specimens with complete recrystallization structure exhibits the highest microhardness of ~ 525 HV, obviously harder than the as-cast (~ 270 HV), 200 ºC-annealed (~ 350 HV), and 420 ºC-annealed (~ 426 HV) specimens.

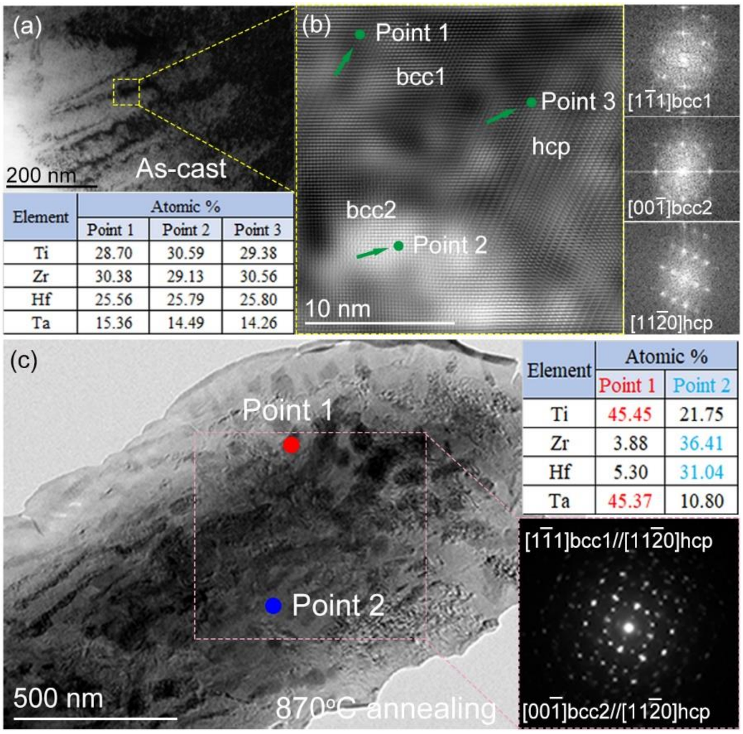

Element	Atomic %		
	Point 1	Point 2	Point 3
Ti	28.70	30.59	29.38
Zr	30.38	29.13	30.56
Hf	25.56	25.79	25.80
Ta	15.36	14.49	14.26

Element	Atomic %	
	Point 1	Point 2
Ti	45.45	21.75
Zr	3.88	36.41
Hf	5.30	31.04
Ta	45.37	10.80

Figure 3.3 (a) TEM images with the (b) corresponding EDS results of as-cast samples,

indicating the elemental composition of different phases. (c) TEM images and EDS results of bcc and hcp phases in 870 °C-annealed specimens.

Figure 3.4(a) and (b) present the steady-state COFs and wear rates for the as-cast and three cold-rolled plus annealed specimens, respectively, under varying loads ranging from 16 N to 64 N. As anticipated, the specimens annealed at 870°C, which have the highest fraction of the hcp phase, demonstrate superior tribological performance, characterized by the lowest COFs (0.12-0.15) and wear rates ((4.08-9.68) $\times 10^{-5}$ $mm^3/N\bullet m$). These values are significantly improved compared to the as-cast specimen, which exhibits COFs between 0.33 and 0.35 and wear rates of (5.34-7.10) $\times 10^{-4}$ $mm^3/N\bullet m$. Similarly, the 200°C-annealed specimens show COFs ranging from 0.26 to 0.34 and wear rates of (1.82-4.32) $\times 10^{-4}$ $mm^3/N\bullet m$, while the 420°C-annealed specimens record COFs between 0.26 and 0.31 and wear rates of (1.34-2.47) $\times 10^{-4}$ $mm^3/N\bullet m$. Moreover, Figure 3.4(c) provides a comprehensive summary of the variation in COFs as a function of hardness for this study and for several referenced HEAs [53, 54, 171, 178-187]. It is widely recognized that soft metals tend to deform too easily under mechanical stress, whereas excessively hardened metals may suffer significant reductions in plasticity. Consequently, reducing COFs through simple hardening processes is not straightforward, as evidenced by the data presented in Figure 3.4(c). Nonetheless, Figure 3.4(c) reveals that the bcc to hcp phase transition in the cold-rolled and annealed $TiZrHfTa_{0.5}$ RHEA fosters a synergistic improvement in hardness and ductility, thereby effectively reducing COFs in conjunction with increased hardness.

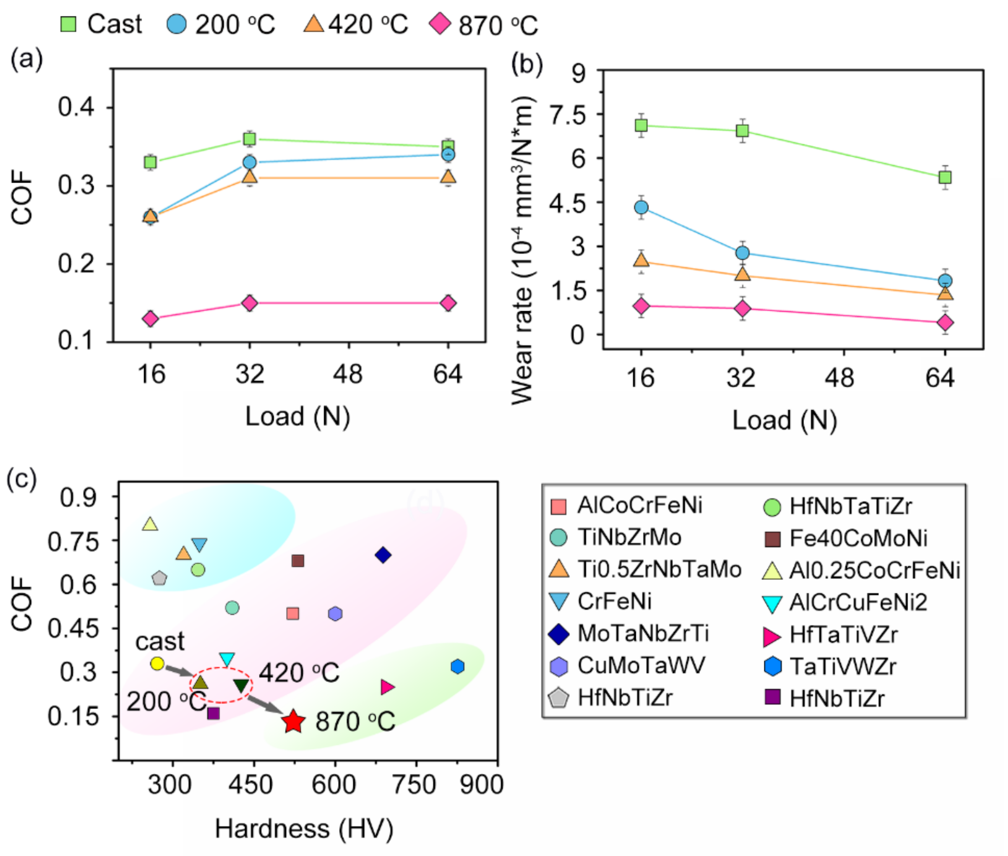

Figure 3.4 (a) Steady-state COFs and (b) wear rates of the as-cast and cold-rolled plus annealed specimens under the loads of 16-64 N. (c) The variation of COFs with the hardness in this work and some referenced HEAs.

Figure 3.5 presents representative SEM images along with associated 3D surface profiles of the worn surface morphologies of four specimens, each subjected to a 12,000-cycle wear test under a load of 16 N. The as-cast specimen, characterized by the largest grain size and the lowest extent of bcc to hcp phase transition, exhibits a significant amount of plate-like debris, wear particles, and peeling parallel to the sliding direction, as depicted in Figure 3.5(a). This results in an average surface roughness of approximately 1.61 μm. Similarly, the cold-rolled and 200°C-annealed specimens, which have undergone incomplete recrystallization and phase transition, also demonstrate poor surface integrity. This is evident from the presence of debris, cracks, and delamination, leading to a high average surface roughness of around 1.38 μm, as shown in Figure 3.5(b). The observed rough surface and numerous defects indicate suboptimal wear resistance in these specimens due to the insufficient phase transformation and microstructural refinement. In contrast, as the annealing temperature increases, particularly at 870°C, there is a marked improvement in the phase transition, which significantly enhances the wear performance of the specimens. Figures 3.5(c) and 3.5(d) illustrate that the specimens annealed at higher temperatures exhibit much smoother worn surfaces with markedly less debris and a considerable reduction in surface roughness. For instance, the 870°C-annealed specimens display an average surface roughness of approximately 0.53 μm. This reduction in surface roughness, coupled with the absence of substantial wear debris and surface damage, implies a significant improvement in wear resistance.

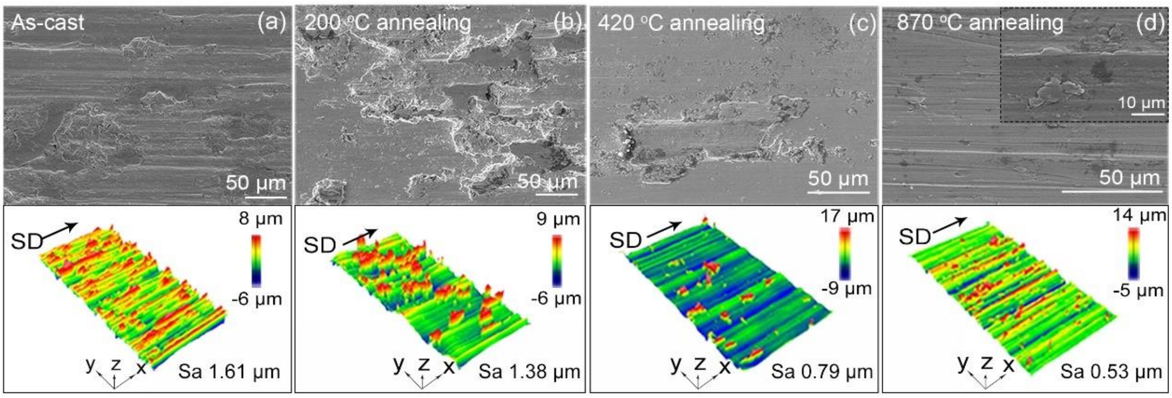

Figure 3.5 SEM images and inserted 3D surface profiles of the 12000-cycled worn surface morphologies of four specimens under a load of 16 N: (a) As-cast, (b) 200 °C-, (c) 420 °C-, and (d) 870 °C-annealed specimens.

The enhanced tribological performance of the higher-temperature annealed specimens can be attributed to the more complete bcc to hcp phase transition, which contributes to the formation of a more stable and homogeneous microstructure. This phase transition results in better mechanical stability and resistance to wear, as the hcp phase provides superior lattice structure stability under load. This is reflected in the lower COFs, wear rates and smooth surface compared to the as-cast and lower-temperature annealed specimens. Figure 3.6(a) provides a cross-sectional SEM image of the specimen annealed at 870°C after enduring 12,000 cycles under a load of 16 N, revealing a crack-free, gradient nanostructured worn subsurface layer approximately 8 μm in thickness. This gradient layer is generated through the plastic deformation occurring during the sliding wear process, which promotes the refinement of grains and the stabilization of the hcp phase in the subsurface region. More detailed structural information is provided in Figure 3.6(b), which presents a cross-sectional TEM image extending from the surface to a depth of around 2 μm. Accompanying this image are SAED patterns taken from three distinct rectangular regions labeled I, II, and III. These patterns elucidate a laminated gradient nanostructured worn subsurface characterized by an increased fraction of the hcp phase, with grain orientations that are nearly parallel to the surface shear sliding direction.

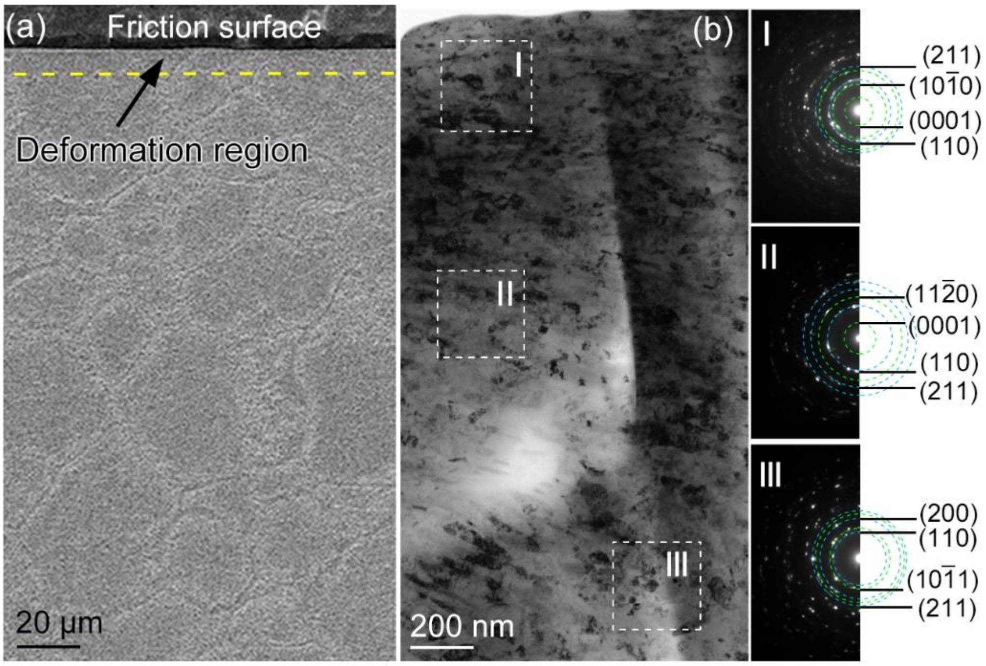

Figure 3.6 Cross-sectional (a) SEM image, (b) TEM image with corresponding SAED patterns taken from I, II, and III regions.

To further investigate the structural changes at varying depths, TEM images are taken at several representative depths, as shown in Figure 3.7(a-d). These images reveal that the average grain size decreases significantly with decreasing distance to the worn surface. For example, at a depth of approximately 3 μm, the average grain size is around 100 nm, whereas in the topmost worn surface region, the average grain size reduces dramatically to about 30 nm. This gradation in grain size is summarized in Figure 3.7(e), which highlights the correlation between grain size and proximity to the worn surface.

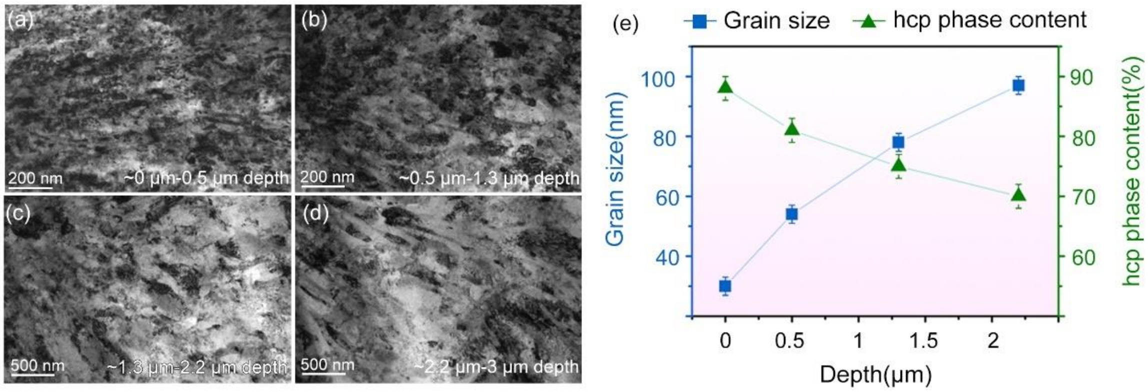

Figure 3.7 (a-d) TEM images at different depths away from surface and the corresponding (e) statistical grain size and hcp phase content.

Figure 3.8(a) and the associated EDS maps illustrate the compositional differences between two distinct phases: a TiTa-rich hcp phase (with lattice parameters *a* = ~ 2.958 Å, *c* = ~ 4.860 Å) in the bright areas, and a ZrHf-rich bcc phase (with a lattice parameter *a* = ~ 3.295 Å) in the dark areas. By analyzing the fraction of the bright area in Figure 3.8(a) along the depth direction, it is observed that the volume fraction of the hcp phase gradually increases from approximately 70% at a depth of around 3 μm to approximately 88% in the surface region, as summarized in Figure 3.7(e). This increase is primarily attributed to the severe plastic deformation experienced during repeated shear sliding. Additionally, a ~10 nm-thick oxide debris layer on the worn surface, rich in O, Ti, and Ta, is identified through HAADF-STEM in Figure 3.8(b). However, this oxide debris is characterized by its discontinuity, random spatial distribution, and extremely limited thickness with several nanometers. Under continuous sliding conditions, such nano-thick oxide particles are prone to displacement or mechanical fragmentation, rendering them largely ineffective in significantly reducing friction or enhancing wear resistance. Similar observations have been reported in prior studies [188, 189], emphasizing that the formation of a mechanically solid tribolayer depends not solely on the presence of oxides, but also critically on their volume fraction, adhesion, and continuity [190]. In contrast, deformation-induced phase transformation and the development of friction-induced gradient nanostructures play a more dominant role in enhancing tribological performance in this work, which will be discussed in the following sections.

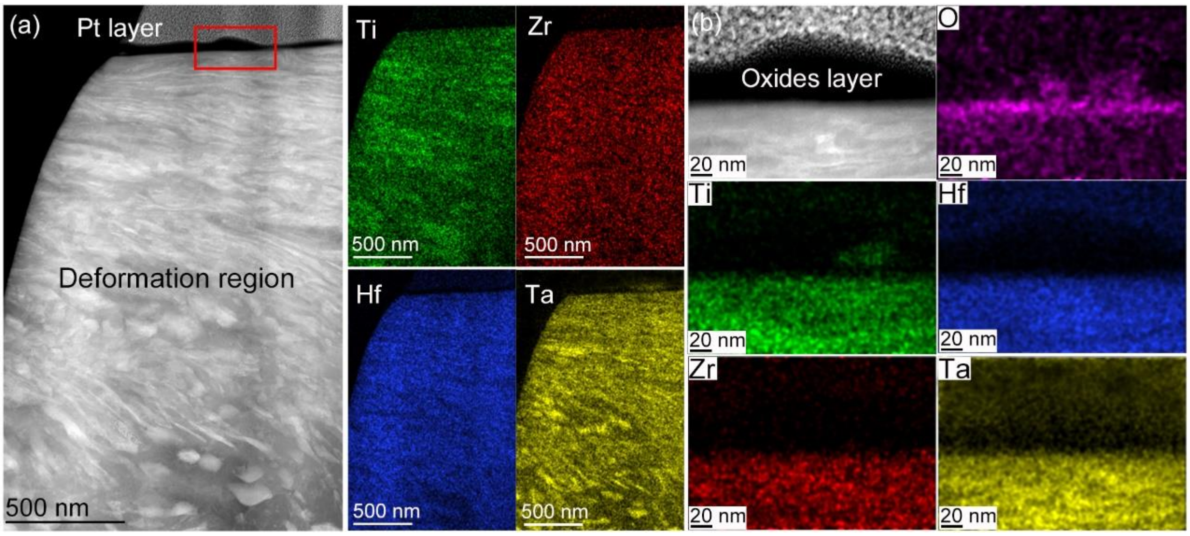

Figure 3.8 Cross-section (a) HAADF-STEM image and corresponding EDS elemental maps of the cold-rolled plus 870°C-annealed specimen after 12000 cycles under a load of 16 N. (b) HAADF-STEM image of the red rectangle in (a) and EDS elemental maps of the oxides layer.

The above findings reveal that the cold-rolled plus 870 °C-annealed TiZrHfTa0.5 RHEA with the highest content of hcp phase possesses the best tribological performance. On one hand, the repeated sliding-caused gradient plasticity can be effectively accommodated via dual-phase structure in the cold-rolled plus 870 ºC-annealed specimens, generating a dual-phase gradient nanostructured worn subsurface [140, 164, 174]. On the other hand, gradient bcc → hcp phase transition is evidenced to further trigger the worn subsurface during such an accommodation process. As a result, the self-organized dual-phase gradient nanostructure with extra activated phase transition continues accommodating the gradient plasticity and suppressing the strain localization toward the further improvement of the wear resistance. Figure 3.9 provides HRTEM and corresponding Fourier-filtered images that confirm the presence of the hcp phase at the atomic level, projected along the $[11\bar{2}0]$hcp direction. Moreover, Figure 3.10(a) presents an HRTEM image and associated SAED patterns of the interfacial regions, demonstrating two distinct orientation relationships (ORs) between bcc and hcp phases, i.e., $[1\bar{1}1]$bcc$_1$//$[11\bar{2}0]$hcp and $[00\bar{1}]$bcc$_2$//$[11\bar{2}0]$hcp, respectively, according to the schematics as summarized in Figure 3.10(b). The atomic arrangements and defects in their interfacial regions should be dissected to uncover the underlying atomic processes accomplishing these two bcc → hcp phase transitions.

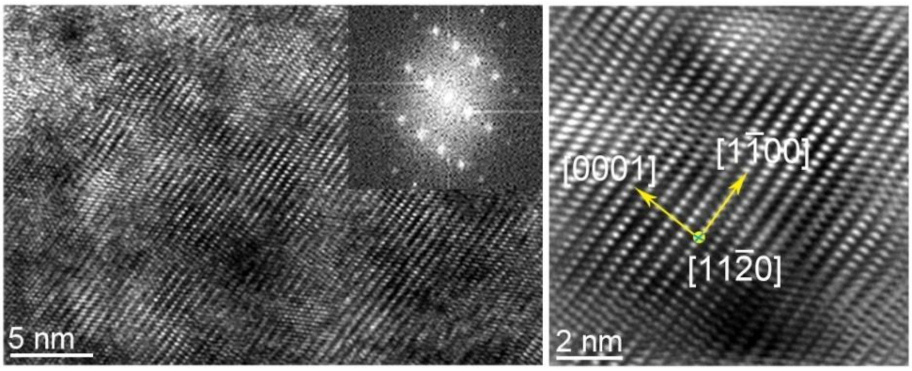

Figure 3.9 HRTEM image with inserted corresponding SAED patterns and corresponding atomic Fourier-filtered image of hcp phase.

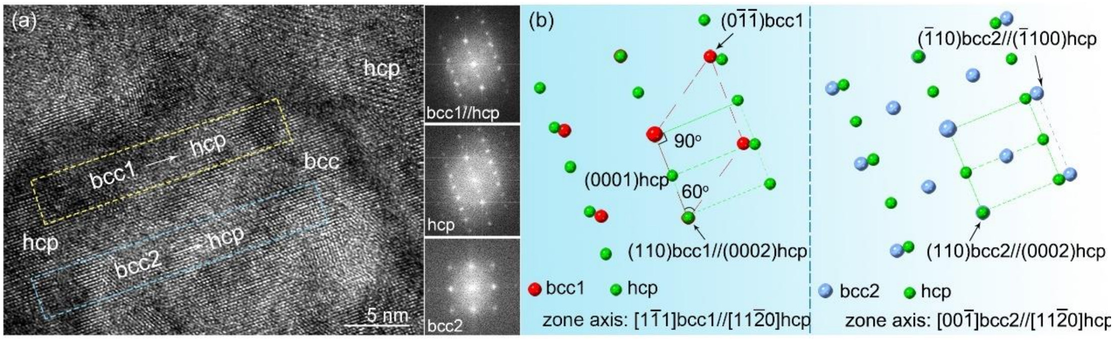

Figure 3.10 (a) HRTEM image and associated SAED patterns of the interfacial regions between bcc and hcp phases. (b) Schematic summarizing the diffraction spots for the ORs between the bcc and hcp phases.

Figure 3.11(a) gives an HRTEM image that captures the interfacial region involved in the first type of bcc → hcp transition, characterized by the OR following $[1\bar{1}1]$bcc$_1$//$[11\bar{2}0]$hcp and (110)bcc$_1$//(0001)hcp. Based on the OR summarized in Figure 3.10(b) and lattice structures in Figure 3.11(a), two noticeable actions can be executed to complete this bcc → hcp transition. The first action is related to the evolution of the inclined angle of (011)bcc plane to $[\bar{1}12]$bcc direction, slightly transiting from the original 60° to ~70.5° of $(3\bar{3}02)$hcp plane (a typical group of planes only follow the stacking order CA, i.e., CA//CA//CA….) to $[1\bar{1}00]$hcp direction. While the second action is to expand the atomic spacing from 2.72 Å along the $[\bar{1}12]$bcc direction to 2.82 Å along the $[1\bar{1}00]$hcp direction. Accordingly, the atomic-level characterization in the interfacial region (i.e., transition zone) illustrates these two actions completed by atom shuffling along the $[\bar{1}12]$bcc direction on (110)bcc plane. On the one hand, the incline angle (011)bcc plane to $[\bar{1}12]$bcc direction gradually increases from 60° to ~64° in the transition zone and eventually reaches ~70.5° in the hcp phase (i.e. $(3\bar{3}02)$hcp plane to

$[1\bar{1}00]$hcp direction), as representative lattice structures marked in Figure 3.11(b). On the other hand, Figure 3.11(c) indicates the gradual expansion of the measured atomic spacing along the $[\bar{1}12]$bcc direction from bcc to hcp phases. The above atom shuffling actions are schematically summarized in Figure 3.11(d), in which an extra compression via atom shuffling along the $[1\bar{1}1]$bcc direction should be executed to achieve the final bcc lattice structure. In this connection, the first bcc → hcp transition obeys the classical Burgers mechanism [191-194]. Specifically, the lattice correspondence between hcp and bcc structures is depicted in Figure 3.11(e-f) to illustrate the atom shuffling actions along the $[\bar{1}12]$bcc (expansion) and $[1\bar{1}1]$bcc directions (compression), respectively, on (110)bcc planes.

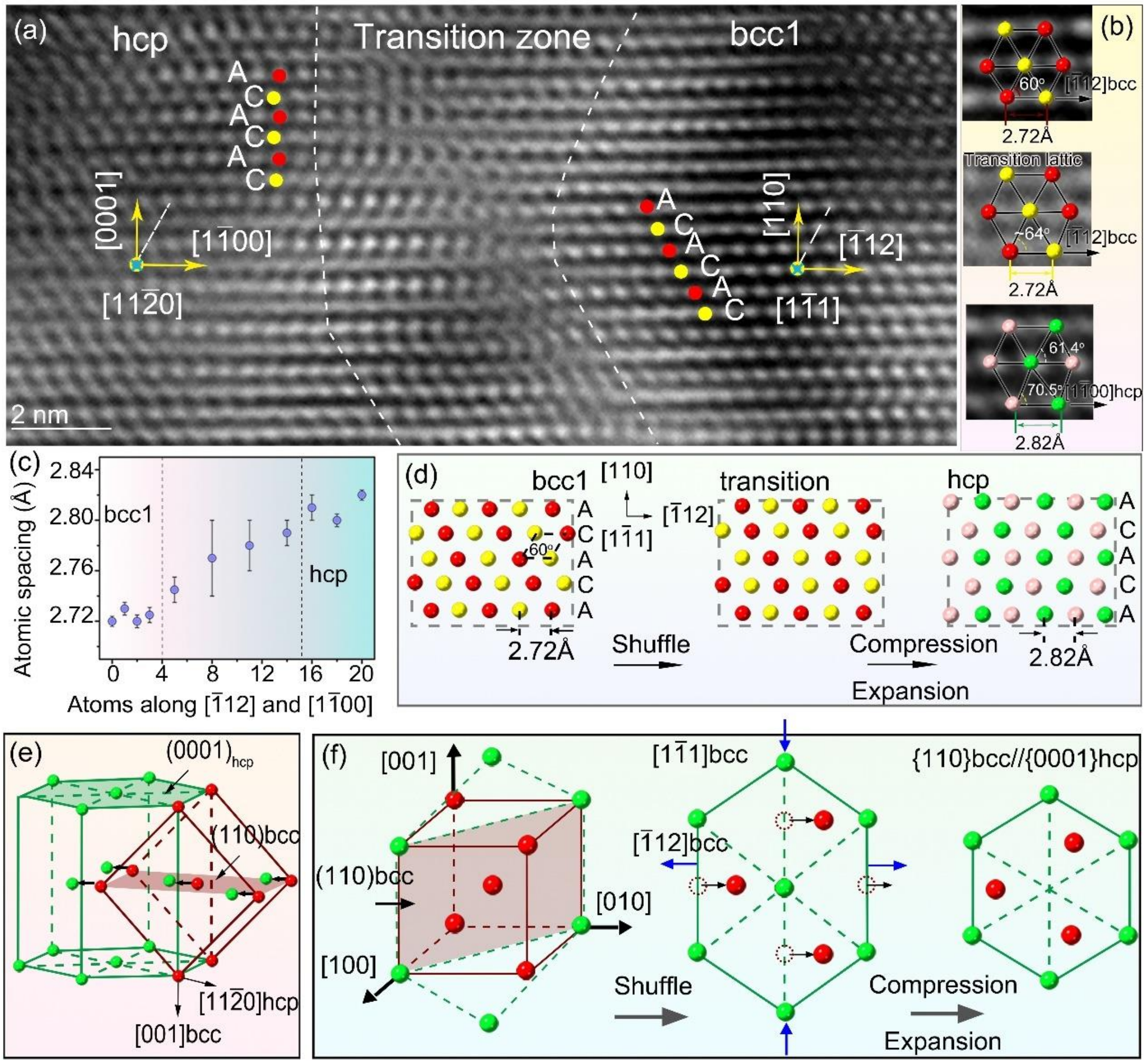

Figure 3.11 (a) An HRTEM image capturing the interfacial region of the first bcc → hcp transition following [1$\bar{1}$1]bcc1//[11$\bar{2}$0]hcp. (b) The evolution of the representative lattices and (c) atomic spacing versus the atomic distance along the [$\bar{1}$12]bcc direction in the transition zone. (d) Schematics illustrating the atom shuffling along [$\bar{1}$12]bcc and [1$\bar{1}$1]bcc directions for completing bcc → hcp transition. (e-f) Schematic diagrams of the Burgers mechanism of bcc → hcp transition describing the atom shuffling including the expansion and compression on (110)bcc plane.

In addition, HRTEM image in the interfacial region of another type of bcc → hcp transition following OR of $[00\bar{1}]$bcc$_2$//$[11\bar{2}0]$hcp and (110)bcc$_2$//$[1\bar{1}00]$hcp is provided in Figure 3.12(a). Different from the first transition case, the incline angle of $(\bar{1}10)$bcc plane to $[\bar{1}10]$bcc should be largely decreased from 90° to 61.4° in hcp phase, which is proposed to be completed by partial dislocation dipoles as in our previous work [195, 196]. The indexed Burgers circuit in Figure 3.12(a) shows that one positive partial glide on one side of (110) plane while the negative partner glides on the other side of the same plane. The dislocation reaction in bcc structure could occur as $\frac{a}{2}[\bar{1}11] \rightarrow \frac{a}{8}[\bar{1}10] + \frac{a}{4}[\bar{1}12] + \frac{a}{8}[\bar{1}10]$, where $\boldsymbol{b}_{p1} = \boldsymbol{b}_{p3} = \frac{a}{8}[\bar{1}10]$ and $\boldsymbol{b}_{p2} = \frac{a}{4}[\bar{1}12]$, respectively, are all activated on close-packed (110)bcc plane [197]. Accordingly, the partial dislocation dipoles, i.e., $8/3\boldsymbol{b}_{p1}$: $-8/3\boldsymbol{b}_{p1}$, on every second (110)bcc planes are proposed to accomplish the decrease of the inclined angle. On the other side, the atom shuffling is also found to gradually increase the atomic spacing from the original value of 2.41 Å along the $[\bar{1}10]$bcc direction to 2.82 Å along the $[1\bar{1}00]$hcp direction in the hcp phase, as evidenced in Figure 3.12(b), generating a macro shear strain of ~ 17% along the $[\bar{1}10]$bcc direction. Partial dislocation dipoles gliding and atom shuffling on (110)bcc planes cooperatively accomplish the second bcc → hcp transition, as the lattice correspondence schematically summarized in Figure 3.12(c).

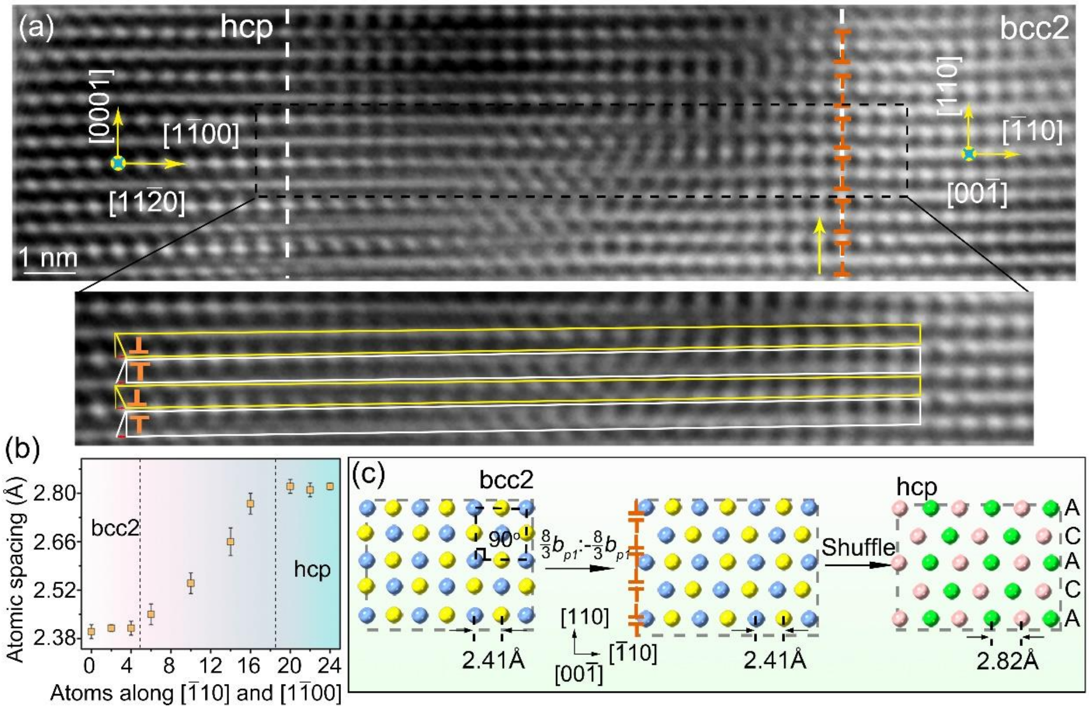

Figure 3.12 (a) An HRTEM image capturing the interfacial region of the second bcc → hcp transition following $[00\bar{1}]$bcc//$[11\bar{2}0]$hcp directions. (b) Atomic spacing versus the atomic distance along the along $[\bar{1}10]$bcc direction in the interfacial region from bcc to hcp. (c) Schematic diagrams for the cooperative of partial dislocation dipoles and atom shuffling in the lattice evolutions from bcc to hcp.

It is important to note that the bcc to hcp phase transition, facilitated by the cooperation of atomic shuffling and/or the gliding of partial dislocation dipoles, plays a significant role in relieving and accommodating the stress and strain fields induced by sliding in the worn subsurface. This transition mechanism effectively mitigates the mechanical stress experienced during wear. Furthermore, in addition to the initial bcc to hcp transition that follows the classical Burgers mechanism, the phenomenological theory of martensitic transformation, such as the W-L-R method [198, 199], provides a valuable framework for future investigations into the second type of bcc to hcp transition. Given that the atomic movements involved in this transition have been meticulously dissected in the current study, the W-L-R method could offer deeper insights into the underlying processes. The insights gained from this study illuminate the atomic mechanisms of phase transformation in RHEAs, which are instrumental in enhancing wear resistance. By thoroughly understanding these transitions and the conditions under which they occur, researchers can develop more effective strategies for improving the durability and performance of RHEAs. The findings highlight the critical role of phase transformations, not only in stress accommodation but also in contributing to the overall mechanical stability of the material. This comprehensive understanding underscores the potential for optimizing RHEAs for various demanding applications where wear resistance is dominant.

3.3 Conclusions

This section used the repeated sliding process to generate a heterogeneous structure on the $TiZrHfTa_{0.5}$ RHEA, which accommodates sliding-caused gradient plasticity and contributes to the enhanced wear resistance. The resulting gradient structure, characterized by variations in grain size and hcp phase content, exhibits an exceptionally low coefficient of friction (0.12–0.15) and a wear rate of $4.08–9.68 \times 10^{-5}$ $mm^3/N\cdot m$, marking a substantial improvement in tribological performance. Atomic-scale analysis reveals that a composition-segregated bcc → hcp phase transition occurs in the self-organized gradient subsurface, enabling the dual-phase structure with increased hcp phase content to effectively accommodate sliding-induced plasticity. Two distinct atomic mechanisms were identified for the bcc → hcp phase transition. The first mechanism follows the classical Burgers model, involving atom shuffling along the $[\bar{1}12]$bcc (expansion) and $[1\bar{1}1]$bcc (compression) directions on (110)bcc planes. The second mechanism combines partial dislocation dipole gliding and cooperative atom shuffling on (110)bcc planes. This research highlights the potential of wear-induced surface engineering as a powerful tool to enhance the tribological properties of advanced materials.

Chapter 4 Heterogeneous structure on fcc-based $Fe_{45}Mn_{35}Cr_{10}Co_{10}$ HEA

4.1 Introduction

Solid-to-solid martensitic phase transition, involving collective atomic displacements smaller than the nearest interatomic spacing, plays a crucial role in the mechanical behaviours of materials [200]. When coupled with plasticity, it is referred to as plastic deformation-induced martensitic transformation (PDIMT) [201]. PDIMT, in conjunction with the transformation-induced plasticity (TRIP) effect, significantly contributes to the overall plasticity and work-hardening capabilities of materials [64, 166]. The characteristics of PDIMTs, including their types, pathways, and underlying atomic movement mechanisms, are highly sensitive to factors such as composition, microstructure, and process conditions [202]. Various hard-sphere shear models based on Bain correspondence have been proposed to describe the atomic movement mechanisms in metals [203, 204]. Our previous studies on gradient nanostructured (GNS) steels have captured atomic-scale evidence of transition features, including lattice rotation, transition lattices, dislocation dipoles, and atom shuffling [195, 196, 205]. These results elucidated the atomic mechanisms of polymorphic PDIMTs, such as fcc → hcp → bcc [71], fcc → hcp → bct [196, 206], and fcc → hcp → bct → bcc [197, 207], for the first time validating the 60-year-old Bogers-Burgers-Olson-Cohen (BBOC) model [208] and further developing novel models incorporating partial dislocation dipoles and atom shuffling [209].

HEAs represent a new class of advanced structural metals with superior mechanical properties [2, 12, 13]. Like the traditional alloys, PDIMTs have been realized to create dual- or multi-phase hetero-structured HEAs, enabling a desirable strength-ductility combination [22, 68, 108]. For instance, various PDIMTs, such as fcc → hcp in FeMnCrCoNi [22, 61], bcc → hcp in TiZrHfTaNb [68, 205], fcc → bcc in CoNiFeAlCu and FeMnCrCoNi [210, 211], hcp → bcc following BBOC model in $Fe_{38.5}Mn_{20}Cr_{15}Co_{20}Si_5Cu_{1.5}$ HEAs [212-216], have been documented to enhance the strength-ductility combination. Notably, the distinct characteristics of HEAs (e.g. compositions) may exert a more complex influence on phase transition characteristics, such as the phase stability and boundaries, transition conditions, pathways and kinetics. Consequently, it can lead to the manifestation of diverse underlying atomic movement mechanisms governing their PDIMTs. As a result, detailed atomic-scale observations are imperative to capture PDIMTs in HEAs and reveal the associated mechanisms.

The present work unveils a notable fcc → hcp → bcc PDIMT within a GNS surface layer on a $Fe_{45}Mn_{35}Cr_{10}Co_{10}$ HEA processed by a severe plastic deformation technique, i.e. single point cubic boron nitride turning (SPCBNT) [106]. The ultra-precision SPCBNT process enables an ultrahigh strain rate (even reaching up to ~ 10^5-10^6 s^{-1}), thus creating high stress and strain fields that refine and strengthen the specimen surface [96] [141]. Notably, the fcc → hcp → bcc PDIMT is discerned mainly through high-resolution transmission electron microscope (HRTEM), exhibiting a distinctive Nishiyama-Wassermann (N-W) orientation relationship (OR) [196], different from conventional observations in metals like steels [195]. Consequently, a novel atomic movement mechanism crucial for accomplishing the fcc → hcp → bcc PDIMT is unveiled in this work, involving the cooperation of two sets of Shockley partial dislocation dipoles and associated atomic shuffling along two directions.

4.2 Results and discussion

The cross-sectional OM image and EBSD images presented in Figure 4.1 illustrate the microstructures of the $Fe_{45}Mn_{35}Cr_{10}Co_{10}$ HEA following the SPCBNT process. These images reveal the presence of a coarse-grained structure with an average grain size of approximately 30 μm in the matrix region, alongside a gradient refined surface layer that extends to a thickness of about 60 μm. XRD patterns in Figure 4.2(a) show a progression in the number and intensity of hcp phase peaks from the matrix to the surface of the SPCBNTed HEA, indicating the occurrence of the fcc → hcp phase transition during the gradient refinement process and the resultant increase in hcp phase content. The volume fraction of hcp phase gradually increases to ~ 29%, calculated based on integrated intensities of the reflecting planes [175, 217, 218]. The SPCBNTed surface keeps a high quality with a low surface roughness (Sa) at 10 nm, as shown in Figure 4.2(b).

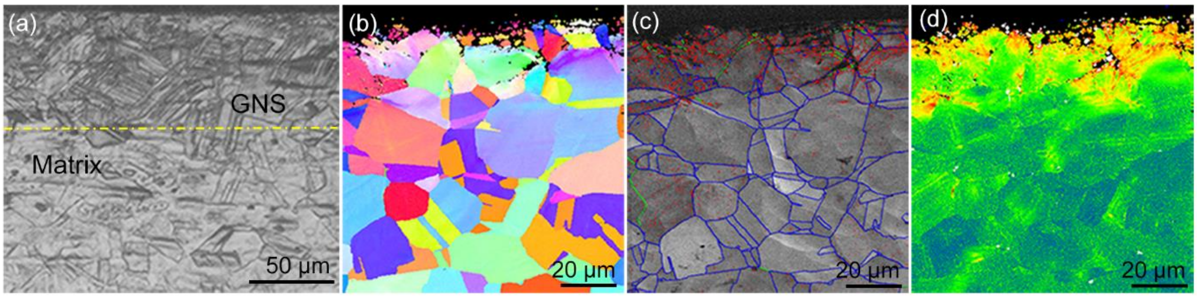

Figure 4.1 Typical cross-sectional microstructures of GNS surface layer on $Fe_{45}Mn_{35}Cr_{10}Co_{10}$ HEA after the SPCBNT process. (a) OM image, (b) IPF map, (c) grain boundary and phase

boundary map, and (d) Kernel average misorientation (KAM) map of the SPCBNTed HEA. The phase boundaries, high-angle grain boundaries (HAGBs) and low-angle grain boundaries (LAGBs) are represented by green, blue and red lines, respectively.

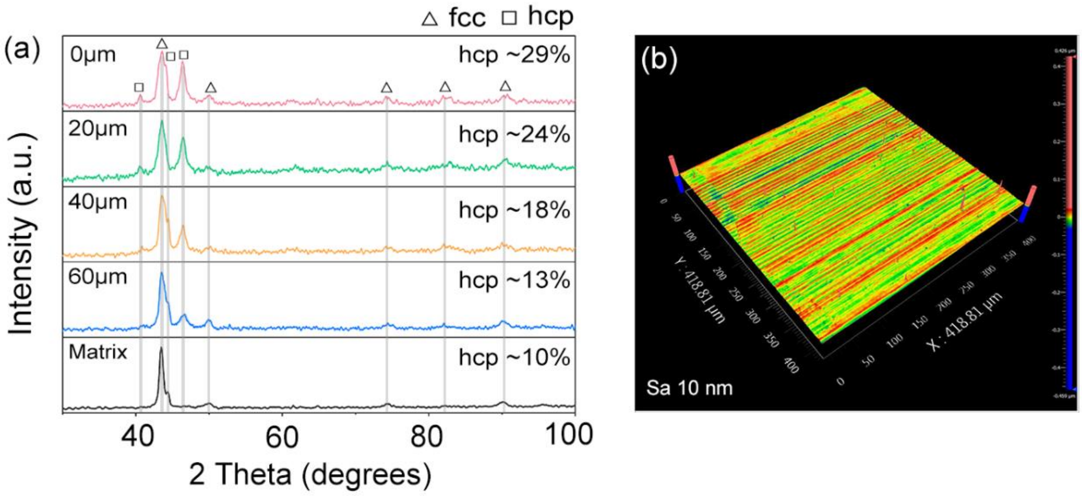

Figure 4. 2 (a) XRD patterns of matrix and top surface. (b) Surface roughness of treated Fe$_{45}$Mn$_{35}$Cr$_{10}$Co$_{10}$ HEA.

The nanohardness and compressive stress-strain curves at different depths are shown in Figure 4.2, demonstrating an increase in nanohardness from ~ 4.3 GPa in the matrix core to ~ 6.7 GPa at the surface (Figure 4.3 (a)). The stress-strain curves reveal an enhanced yield strength as the depth approaches the surface, with the yield strength at the surface being ~ 2.4 times higher than that in the matrix region, as shown in Figure 4.3(b). Additionally, the observed reduction in average grain size from ~ 30 μm in the matrix core to ~ 13 nm at the surface, based on TEM observations. The gradual enhancement of hardness and compressive strength should be attributed to the combination of grain refinement/boundary strengthening and TRIP effects along the depth direction. Several obvious load drops exhibit in some micro-pillar compressive stress-strain curves, especially at matrix region and topmost surface layer.

The load drops in micro-pillar compressive stress-strain curves might be related to the activities of shear bands, dislocation, and phase transition, influenced by some factors such as grain orientation, and ratio between diameter of pillars and grain size [219-221]. When the grain size significantly exceeds the pillar diameter, as in the matrix region, load drops may be easily triggered in the stress-strain curves due to the transient activation of dislocation slip systems. In contrast, the severely refined nanograins (such as ~ 50 μm and ~ 30 μm depth layers) with random orientation would lead to uniform distributions of stress and deformation, potentially alleviating or eliminating the occurrence of load drops. While the recurrence of the slight load drops at the topmost surface with the smallest grain size might be correlated to the relatively large uneven stress distribution through further fcc → hcp → bcc phase transition activated within some certain fcc-dominated nanograins, which will be observed by HRTEM in the next section. This uneven stress distribution may induce temporary material softening, contributing to the manifestation of load drops. Additionally, SEM images in Figure 4.3(b) reveal the slip bands in the deformed pillars, indicating the retention of good plasticity in the GNS surface layer.

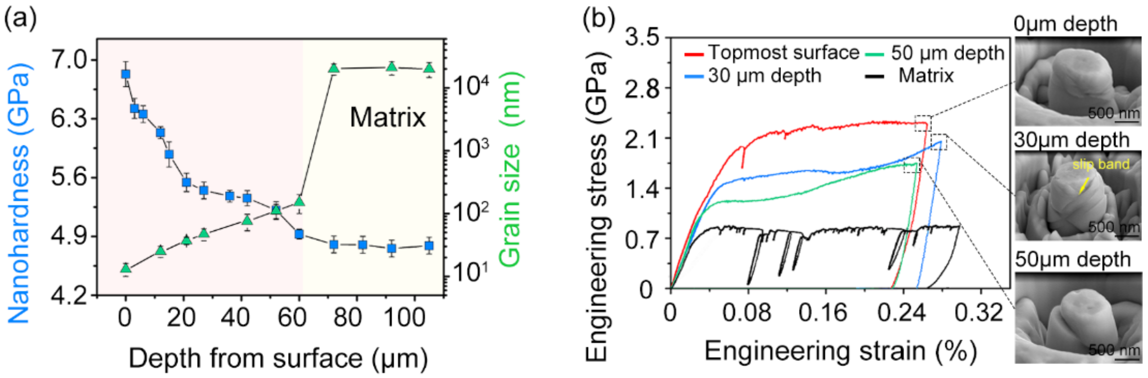

Figure 4.3 Mechanical property of the gradient nanograined surface layer in $Fe_{45}Mn_{35}Cr_{10}Co_{10}$ HEA after the SPCBNT process. (a) The plot showing the variations in grain size and nanohardness with depths. (b) Micro-pillar compressive engineering stress-strain curves and SEM images of the deformed pillars at several representative depth layers.

Representative plane-view TEM images and the associated diffraction patterns at various depths along the gradient direction are provided in Figure 4.4 to elucidate the phase evolution pathway. Figure 4.4(a) shows that only the fcc phase is detected in the core matrix region. In contrast, at depths of approximately 40 μm and 20 μm, plate-shaped hcp phases become apparent, as illustrated in Figure 4.4(b-c) and Figure 4.4(d), respectively. Moreover, bright-field and dark-field TEM images, along with SAED patterns in Figure 4.5(a-c), reveal the formation of nanoscale hcp laths within the further refined fcc nanograins at the topmost surface layer. The atomic Fourier-filtered and HRTEM images in Figure 4.5(c-d) are magnified views from regions marked by yellow circles in the dark-field TEM images in Figure 4.5(b). Figure 4.5(c) reveals dense stacking faults within these nanoscale hcp laths. Interestingly, Figure 4.5(d) provides compelling evidence that the nanoscale hcp laths can act as intermediate phases, serving as nucleation sites for the subsequent formation of the bcc phase within the nanograins. Furthermore, the enlarged HRTEM images of the phase interfaces in Figure 4.5(e-f), along with the corresponding FFT diffraction patterns in Figure 4.5(g-i), confirm the presence of the transformed phases. These observations support the existence of a polymorphic fcc → hcp → bcc transformation pathway during the grain refinement process. The detailed atomic-scale characterizations elucidate how the sequential phase transformations contribute to the microstructural evolution and the enhancement of mechanical properties in the GNS surface layer, thereby highlighting the effectiveness of the severe plastic deformation technique applied in this study.

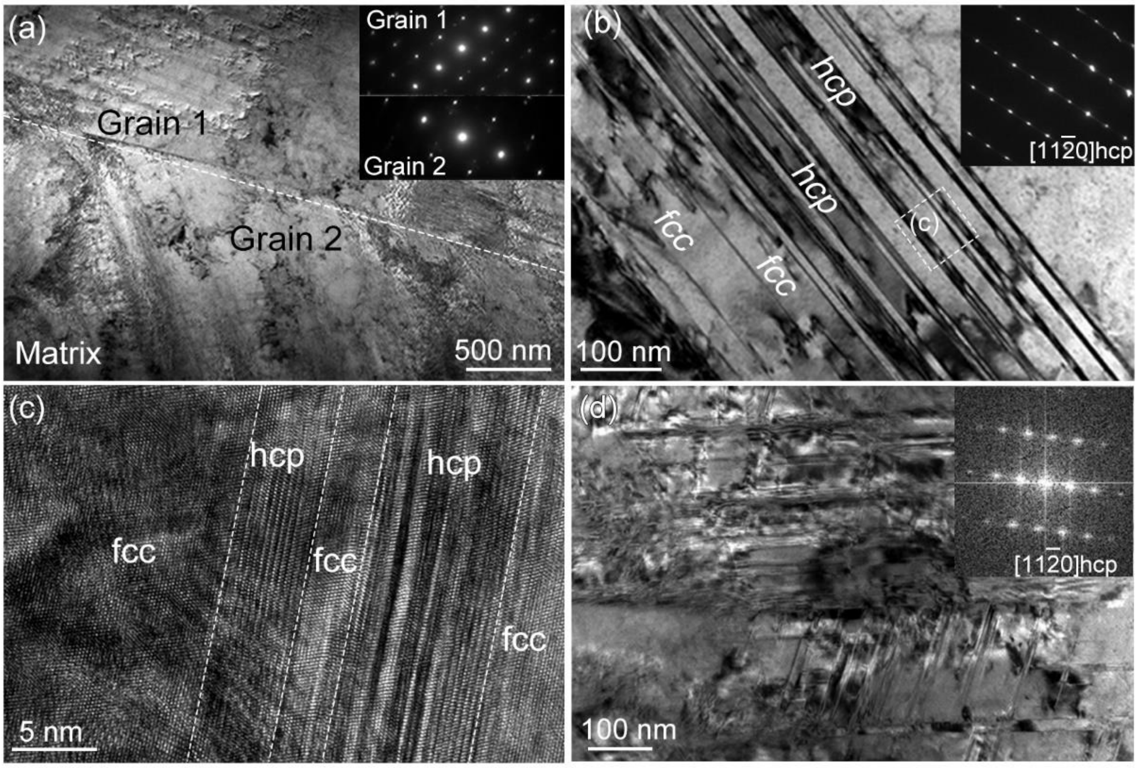

Figure 4.4 Microstructures of fcc, hcp and bcc phases in GNS surface layer on $Fe_{45}Mn_{35}Cr_{10}Co_{10}$ HEA after the SPCBNT process. (a-d) A series of plane-view TEM images with corresponding SAED patterns taken at different depth layers showing (a) fcc phase in the un-SPCBNTed matrix and hcp laths formed at (b-c) ~40 µm and (d) ~20 µm depth, respectively.

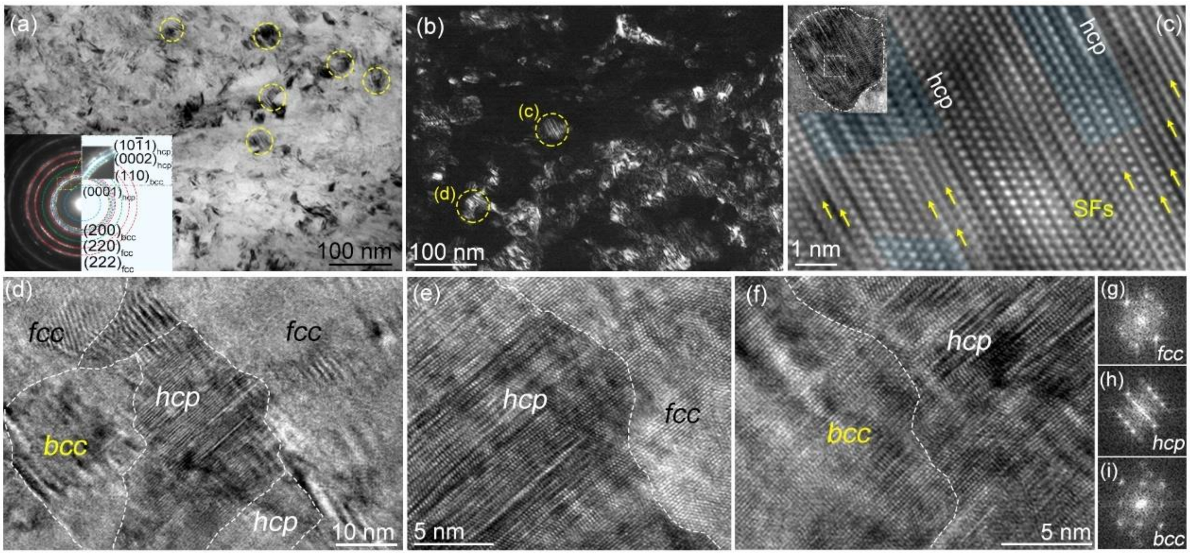

Figure 4.5 (a) bright-field and (b) dark-field TEM images at the topmost surface layer showing the formation of nanoscale hcp phase observed with the refined fcc nanograins. (c) An atomic Fourier-filtered image showing the nanoscale hcp laths with dense stacking faults. (d) A typical HRTEM image showing that nanoscale hcp lath is partially transformed to bcc phase. (e-f) Interfaces between fcc phase, nanoscale hcp lath, and bcc phase and (g-i) corresponding FFT diffraction patterns of fcc, hcp and bcc phases.

Figure 4.6(a-b) illustrates another typical case of polymorphic fcc → hcp → bcc phase transition within a nanograined fcc matrix phase. Similar to the observations in Figure 4.5 (d), a smaller nanosized hcp lath is formed at the grain boundary of the nanograined fcc matrix phase, and subsequently, a bcc phase nucleates from this hcp lath, as indicated by the dashed lines in Figure 4.6(a). Based on the FFT diffraction patterns in Figure 4.6(b-c), the orientation relationship (OR) between the three phases can be summarized schematically in Figure 4.6(d). The OR follows $(111)\mathrm{fcc}$ // $(0002)\mathrm{hcp}$ // $(110)\mathrm{bcc}$ viewed along $[\bar{1}10]\mathrm{fcc}//[11\bar{2}0]\mathrm{hcp}//[00\bar{1}]\mathrm{bcc}$ directions, corresponding to the Nishiyama-Wassermann (N-

W) OR [196]. Note that the OR of the fcc → hcp → bcc transition in the current SPCBNTed HEA differs from our previous work on stainless steel, which followed the Pistch OR with $(00\bar{2})$fcc // $(\bar{1}01)$bcc and K-S OR with (111)fcc // (0002)hcp // (110)bcc under the $[\bar{1}10]$fcc//$[11\bar{2}0]$hcp//$[1\bar{1}1]$bcc directions [195].

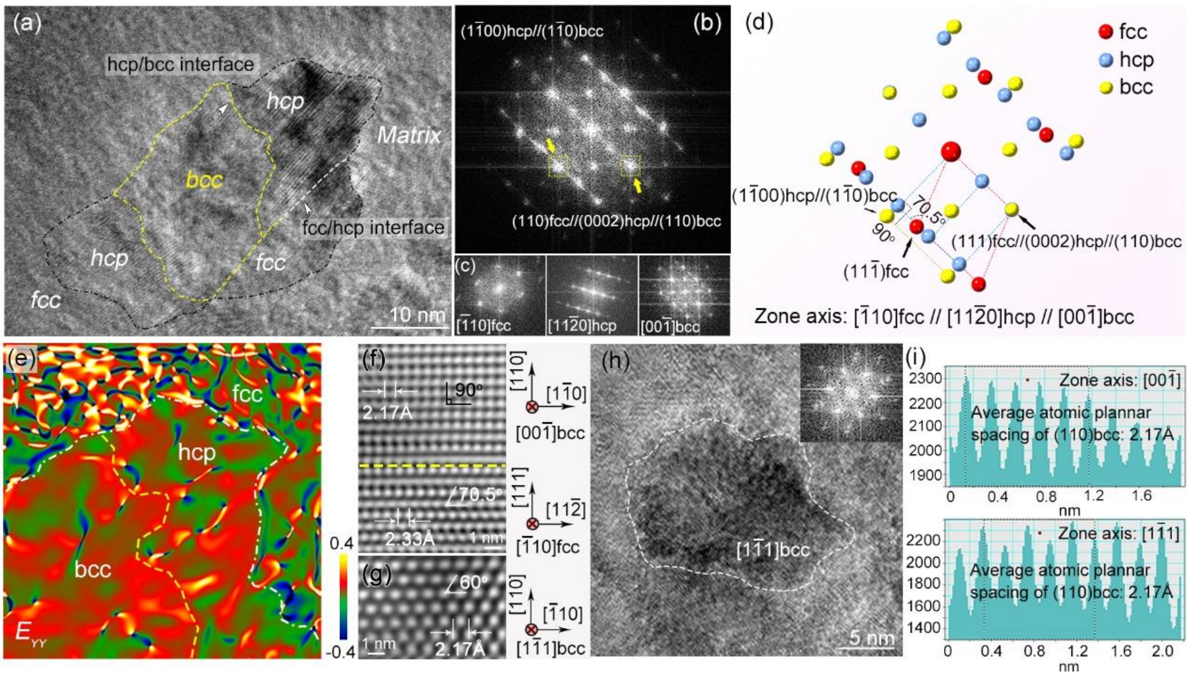

Figure 4.6 Microstructural characteristics of fcc → hcp → bcc transition. (a) A typical HRTEM image and (b) corresponding FFT diffraction spot showing the fcc → hcp → bcc PDIMT. (c) FFT diffraction spots for fcc, hcp, and bcc phases along $[\bar{1}10]$fcc, $[11\bar{2}0]$hcp, and $[00\bar{1}]$bcc directions, respectively. (d) Schematic summarizing the ORs between fcc, hcp, and bcc phases viewed along $[\bar{1}10]$fcc//$[11\bar{2}0]$hcp//$[00\bar{1}]$bcc directions. (e) E_{yy} GPA map analysis of the interfacial region taken from (a). (f) An atomic Fourier-filtered image taken from (a) showing the interface between fcc and bcc phases with the N-W OR. (g-h) an atomic Fourier-filtered image, TEM image and its corresponding FFT pattern of bcc phase projected along $[1\bar{1}1]$bcc direction. (i) Atomic planar spacing intensity profiles of bcc phase projected along $[00\bar{1}]$bcc and $[1\bar{1}1]$bcc directions, respectively.

The strain distributions within the interfacial regions among the three phases are depicted using a geometric phase analysis (GPA) map in Figure 4.6(e). This map illustrates an increased out-of-plane strain (E_{yy}) and significant strain localization within these interfacial regions. Such strain localization is indicative of the complex interactions and mechanical responses at the boundaries between different phases. In addition, Figure 4.6(f) presents an atomic Fourier-filtered image that directly shows the atomic structure at the fcc/bcc interfacial region, adhering to the N-W OR. Notably, the inclined angle of the $(1\bar{1}0)$bcc plane to $[1\bar{1}0]$bcc direction is 90º, which contrasts with the 60° inclined angle of the (110)bcc plane to $[\bar{1}12]$bcc direction following the K-S OR as reported in our previous study [195]. This discrepancy highlights the variability in atomic arrangements and the complexity of phase transitions in these materials.

To determine the bcc lattice constant, an atomic Fourier-filtered image, a TEM image, and its corresponding FFT pattern of the bcc phase projected along the to $[1\bar{1}1]$bcc direction is provided in Figures 4.6(g-h). These images offer a clear and detailed view of the atomic structure, facilitating precise measurement of the lattice constants. Consequently, Figure 4.6(i) presents the atomic planar spacing intensity profiles viewed along the $[00\bar{1}]$bcc and $[1\bar{1}1]$bcc directions, respectively. The lattice constants of the three phases are determined to be as follows: for the fcc phase, $a = b = c =$ ~ 3.81 Å; for the hcp phase, $a =$ ~ 2.69 Å, $c =$ ~ 4.35 Å; and for the bcc phase, $a = b = c =$ ~3.07 Å. These values are consistent with those reported in the literature [222]. The phase transition characteristics described above suggest an unconventional atomic motion mechanism during the second-step hcp → bcc transition. This transition involves complex atomic movements and reconfigurations that deviate from traditional models. Understanding these unique mechanisms requires detailed atomic-level observations and analyses, which can provide insights into the fundamental processes governing phase transformations in HEAs.

To the best of our knowledge, there are no referenced experiment results reporting the fcc → hcp →bcc PDIMT in HEAs, particularly with a new OR differing from the previously reported cases, such as in steels [195]. Therefore, it is crucial to uncover the underlying atomic movement mechanisms by dissecting the atomic arrangements and defects present in the interfacial regions. Firstly, Figure 4.7(a-c) present an HRTEM image and associate FFT patterns, which are enlarged and extracted from Figure 4.6(a), showing the interface between fcc and hcp phases viewed along the $[\bar{1}10]\mathrm{fcc}//[11\bar{2}0]\mathrm{hcp}$ directions. In Figure 4.7(e), an even further enlarged atomic Fourier-filtered image, extracted from Figure 4.7(a), reveals that the formation of hcp phase can be completed by the gliding of Shockley partial dislocations on every second (111)fcc planes from the grain boundary of the nanograined fcc matrix phase, as mentioned in Figure 4.5(a). These partial dislocations have three Burges vectors (i.e. $\boldsymbol{b_{p1}} = \frac{a}{6}[2\bar{1}\bar{1}]$, $\boldsymbol{b_{p2}} = \frac{a}{6}[\bar{1}2\bar{1}]$ and $\boldsymbol{b_{p3}} = \frac{a}{6}[\bar{1}\bar{1}2]$) on (111)fcc planes, as indexed in Figure 4.7(e). They cause different shear components along the $[\bar{1}10]\mathrm{fcc}$ direction but contribute to the same actions to form the hcp lath [208], as schematically shown in Figure 4.7(d). Secondly, Figure 4.8(a) and Figure 4.8(b-c) respectively provide an enlarged HRTEM image and associated FFT spots taken from Figure 4.6(a) for the hcp →bcc transition.

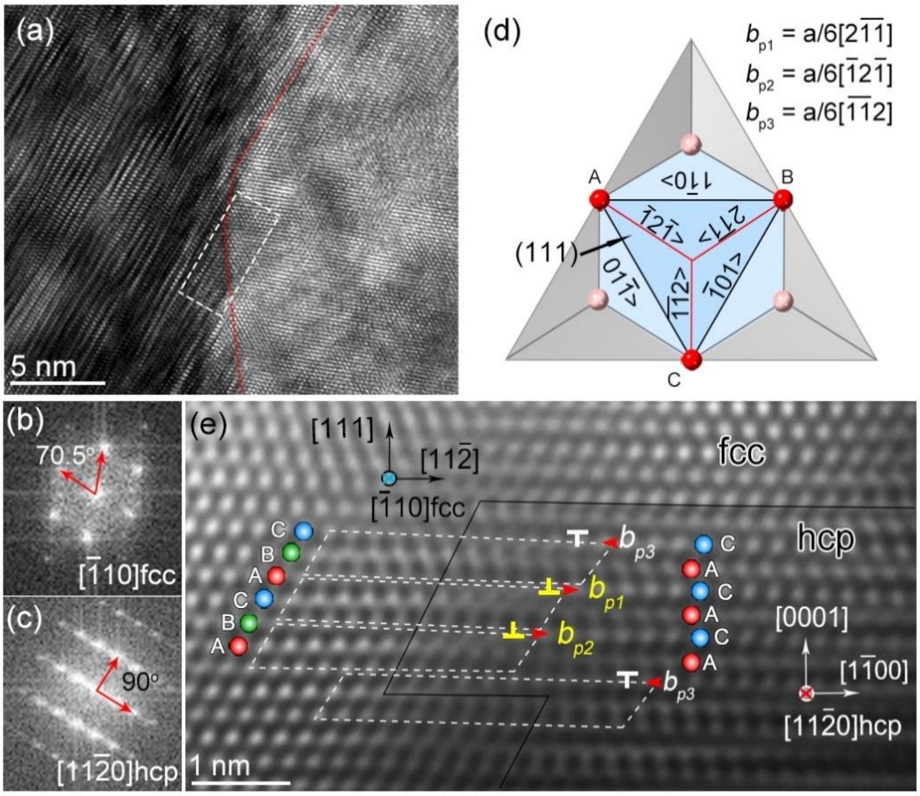

Figure 4.7 Atomic movement mechanism of fcc → hcp → bcc transition. (a) An HRTEM image and (b-c) corresponding FFT diffraction spots showing fcc → hcp transition. (d) An atomic Fourier-filtered image of the interfacial region between fcc and hcp phases showing the gliding of Shockley partial dislocations on every second (111)fcc planes. (e) Schematics showing three types of Shockley partial dislocations on (111)fcc plane.

Furthermore, an enlarged atomic Fourier-filtered image taken from Figure 4.8(a) is provided in Figure 4.8(d) to analyze detailed atomic arrangements and crystalline defects in the diffuse interface region between hcp and bcc phases. On one hand, the original inclined angle of $(3\bar{3}02)$hcp plane to $[1\bar{1}00]$hcp direction (a typical group planes following the stacking order of CA//CA//CA…) is ~70.5°, which eventually changes to 90° for $(1\bar{1}0)$bcc plane to $[1\bar{1}0]$bcc direction, as indicated in Figure 4.8(e), following the N-W OR. On the other hand, the atomic spacing along $[11\bar{2}]$fcc and $[1\bar{1}00]$hcp is equivalent (2.33 Å), which changes to 2.17 Å along $[1\bar{1}0]$bcc direction, facilitating the inclined angle change in the fcc → hcp → bcc transition. Figure 4.8(f) plots the measured evolution of atomic spacing along the $[1\bar{1}00]$hcp direction in the hcp/bcc interfacial region, suggesting that gradual decrease in atomic spacing is completed by the atomic shuffling with localized motions along the $[1\bar{1}00]$hcp direction.

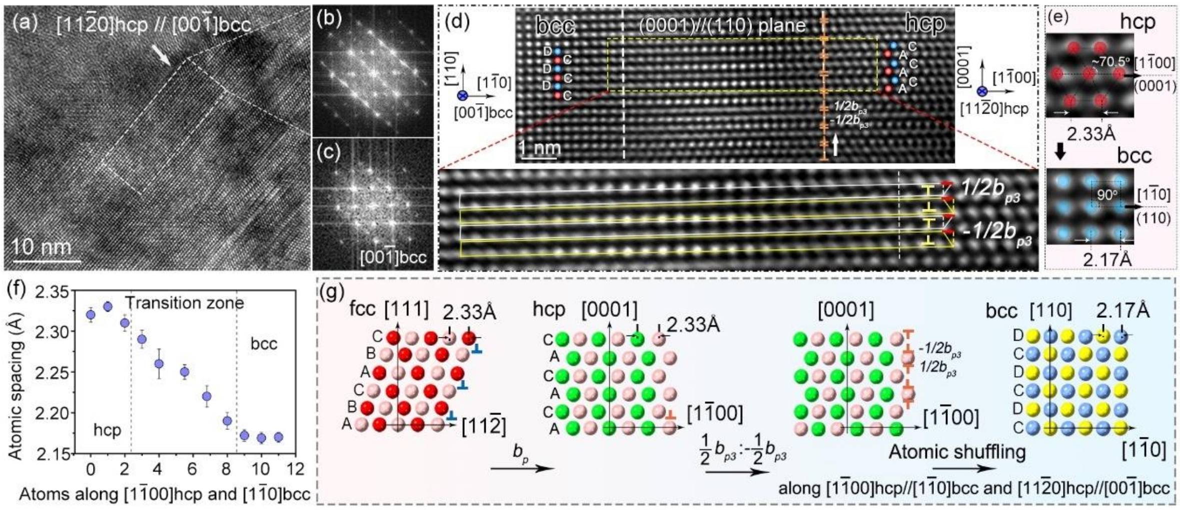

Figure 4.8 (a) An HRTEM image and (b-c) corresponding FFT spots showing hcp → bcc transition. (d-e) Atomic Fourier-filtered images and (f) measured atomic spacing along the $[1\bar{1}00]$hcp direction in the diffuse interfacial region between hcp and bcc phases showing the partial dislocations dipoles and atom shuffling. (g) Schematic illustrating the lattice evolution from fcc to intermediate hcp and finally the bcc phases viewed along $[\bar{1}10]$fcc//$[11\bar{2}0]$hcp//$[00\bar{1}]$bcc directions.

Note that gliding any Shockley partial dislocation $\boldsymbol{b_p}$ ($\boldsymbol{b_{p1}}$, $\boldsymbol{b_{p2}}$ or $\boldsymbol{b_{p3}}$) in the fcc phase can convert the stacking sequence as follows: A → B, B → C, C → A, which completes the fcc → hcp transition with…ACACAC… by gliding $\boldsymbol{b_p}$ on every second (111)fcc planes. However, gliding $\boldsymbol{b_{p1}}$ and $\boldsymbol{b_{p2}}$, unlike $\boldsymbol{b_{p3}}$, induce shear components along the $[\bar{1}10]$fcc direction, causing a witch in the arrangement of "in" and "out" atoms on $(\bar{1}10)$fcc planes. Consequently, only one type of partial dislocation dipoles, namely $-\frac{1}{2}\boldsymbol{b_{p3}}$:$\frac{1}{2}\boldsymbol{b_{p3}}$, can be indexed through the Burgers circuits in Figure 4.8(d). With $\frac{1}{2}\boldsymbol{b_{p3}}$ and $-\frac{1}{2}\boldsymbol{b_{p3}}$ gliding along the two sides of every (0001)hcp planes in a "sandwich" manner, it can eliminate this switch "in" and "out" status and thus generate the …CDCDCD… stacking order in the bcc phase. Figure 4.8(g) provides a schematic of the lattice evolution from fcc to intermediate hcp and finally the bcc phases viewed along $[\bar{1}10]$fcc//$[11\bar{2}0]$hcp//$[00\bar{1}]$bcc directions. During this process, the inclined angle changes from the original 70.5° for $(11\bar{1})$fcc plane to $[11\bar{2}]$fcc and eventually reaches 90° for $(1\bar{1}0)$bcc plane to $[1\bar{1}0]$bcc direction. Through atomic shuffling, the atomic spacing along $[1\bar{1}00]$hcp // $[1\bar{1}0]$bcc directions is gradually reduced from 2.33 Å to 2.17 Å. Additionally, atomic spacing expansion along the $[11\bar{2}0]$hcp // $[00\bar{1}]$bcc directions is necessary to form the final bcc phase. This atomic movement action will be further illustrated in the following Figure 4.9 by analyzing the lattice correspondences.

The fcc → hcp → bcc transition in steels is illustrated by the lattice correspondence depicted in Figure 4.9(a), which adheres to the Pistch OR [195] and is executed according to the BBOC model. This model incorporates two shear components: T/3 = $\frac{a}{18}[\bar{1}2\bar{1}]$on every

$(11\bar{1})$ fcc plane and 3T/8 = $\frac{a}{16}[\bar{1}2\bar{1}]$ on every (111)fcc plane, respectively. These shear components are accommodated by two intermediate hcp phases, which involve the slipping of dislocations of T/2 on each {111}γ plane. The transition from fcc to bcc through the hcp intermediate phase is facilitated by these specific shear and dislocation mechanisms, ensuring a smooth transformation of the lattice structure. Furthermore, the lattice correspondence following the N-W OR [196] for the fcc → hcp → bct transition is illustrated in Figure 4.9(b). This transition involves one set of partial dislocation dipoles, $-\frac{1}{2}\boldsymbol{b}_{\boldsymbol{p3}}$:$\frac{1}{2}\boldsymbol{b}_{\boldsymbol{p3}}$, on the (111)fcc plane. These dislocation dipoles alter the inclined angle of the plane, and atomic shuffling progressively narrows the atomic spacing along the $[1\bar{1}00]$hcp//$[11\bar{2}]$fcc directions by 5.88%. Eventually, the lattice constants reach $a_{bct} = b_{bct} = \sqrt{2}a_{fcc}/\sqrt{3}$, while the c_{bct} parameter remains unchanged at $c_{bct} = a_{fcc}/\sqrt{2}$ throughout the transition process. This is due to the absence of shear and shuffling actions along the $[\bar{1}10]$fcc//$[11\bar{2}0]$hcp//$[00\bar{1}]$bct directions, ensuring that the transformation from fcc to bct maintains a consistent lattice parameter along this axis.

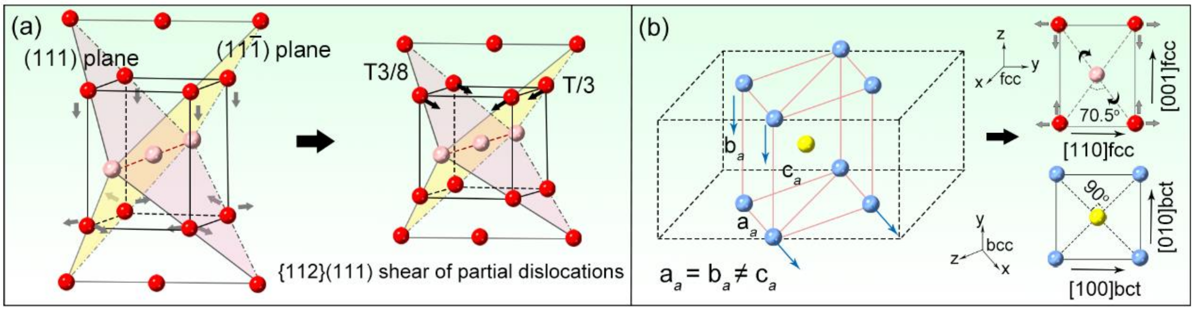

Figure 4.9 Atomic movement mechanisms schematically illustrated by lattice correspondences. (a) Lattice correspondence for the fcc → hcp→ bcc transition completed by the BBOC model [195]. (b) Lattice correspondence for the fcc → hcp→ bct transition completed by one set of

partial dislocation dipoles and associated atomic shuffling [196]

The lattice correspondence for the fcc → hcp→ bcc transition in the current HEA is analyzed in Figure 4.10(a). The bcc lattice constants are initially $a_{bcc} = c_{bcc} = a_{fcc}/\sqrt{2} = 2.69$ Å and $b_{bcc} = a_{fcc} = 3.81$ Å, and then transits to $a_{bcc} = b_{bcc} = c_{bcc} = 3.07$ Å, following N-W OR as indicated in Figure 4.6. Obviously, the atomic movement mechanism for the current transition differs from the cases illustrated in Figure 4.9 (a) and (b) which have either different transition types or different ORs. As observed in Figure 4.7 and Figure 4.8 schematically depicted in Figure 4.10(a), gliding of dislocations is accomplished on two planes: (111)fcc//(0001)hcp and $(1\bar{1}1)$ fcc// $(30\bar{3}2)$ hcp planes. Firstly, the concurrent gliding of dislocation dipoles $-\frac{1}{2}\boldsymbol{b}_{\boldsymbol{p3}}$:$\frac{1}{2}\boldsymbol{b}_{\boldsymbol{p3}}$ on every second (0001)hcp planes and atom shuffling of 6.86% along the $[1\bar{1}00]$hcp//$[11\bar{2}]$fcc directions lead to the following change: an increase in the inclined angle of $(11\bar{1})$fcc plane to $[11\bar{2}]$fcc direction, a compression along $[00\bar{1}]$fcc//$[0\bar{1}0]$bcc directions, and an expansion along [110]fcc//[100]bcc directions. The stacking order and atomic spacing along the $[\bar{1}10]$fcc // $[11\bar{2}0]$hcp // $[00\bar{1}]$bcc directions stay unchanged as these activities exclude shear and shuffling along those directions. However, it is noted that the atomic spacing along $[11\bar{2}]$fcc//$[1\bar{1}00]$hcp//$[1\bar{1}0]$bcc directions should gradually decrease from 2.33 Å to 2.17 Å in Figure 4.8(g). Similarly, we propose that concurrent gliding of a second set of partial dislocation dipoles $-\frac{1}{2}\boldsymbol{b}'_{\boldsymbol{p3}}$:$\frac{1}{2}\boldsymbol{b}'_{\boldsymbol{p3}}$ (i.e. $\boldsymbol{b}'_{\boldsymbol{p3}} = \frac{a}{6}[\bar{1}12](1\bar{1}1)$) on $(1\bar{1}1)$fcc planes along with atomic shuffling of 6.86% along $[\bar{1}12]$ fcc// $[01\bar{1}]$ bcc directions. The first set of partial dislocation dipoles and related atomic shuffling are perpendicular to these actions. Subsequently, the second set of partial dislocation dipoles and associated atomic shuffling also induce the change of angle in different planes: an increase in the inclined angle of $(1\bar{1}1)$fcc plane to $[\bar{1}12]$fcc direction, a compression along $[00\bar{1}]$fcc//$[0\bar{1}0]$bcc directions, and an expansion along $[\bar{1}10]$fcc//$[00\bar{1}]$bcc directions, respectively. Consequently, fcc → hcp→ bcc transition in the current HEA is cooperatively completed by two sets of partial dislocation dipoles ($-\frac{1}{2}\boldsymbol{b_{p3}}$:$\frac{1}{2}\boldsymbol{b_{p3}}$ on (111)fcc and $-\frac{1}{2}\boldsymbol{b'_{p3}}$:$\frac{1}{2}\boldsymbol{b'_{p3}}$ and $(1\bar{1}1)$fcc planes) and associated atom shuffling of 6.86% (along $[11\bar{2}]$fcc and $[\bar{1}12]$fcc directions), as schematically shown in Figure 4.10(c). However, due to the specific transition morphology and perpendicular relation between the two transition actions, it is challenging to observe the second set of dislocation dipoles and associated atomic shuffling using HRTEM, except through atomic movement schematics and simulations [196, 223].

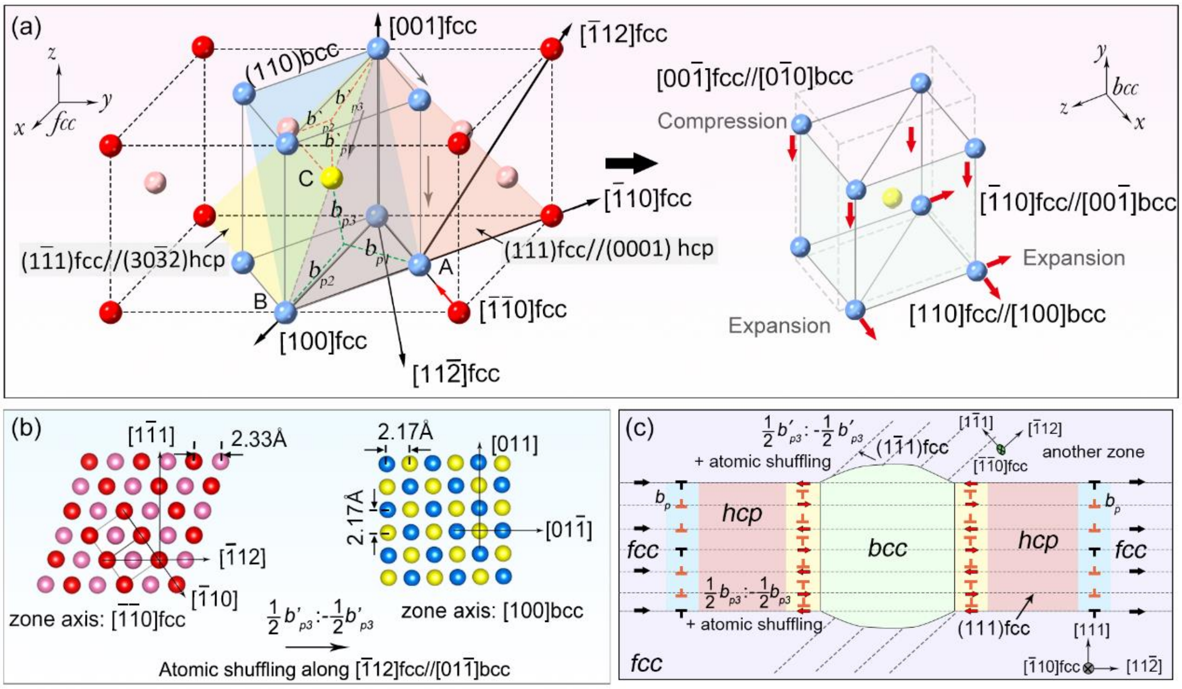

Figure 4.10 (a) Lattice correspondence for the fcc → hcp→ bcc transition in the current HEA and (b) lattice evolution projected along $[\bar{1}10]$fcc//$[\bar{1}100]$hcp//$[100]$bcc directions (rotated 90º from the HRTEM view), schematically illustrating the concurrent gliding of the second set of partial dislocation diploes and associated shuffling to change the length of the c_{bcc}. (c) Schematic diagram of two sets of partial dislocation dipoles associated with atomic shuffling along two vertical directions to form the bcc phase.

To recapitulate, our atomic-scale observations provide profound insights into the transition mechanism of the fcc → hcp → bcc PIDMT occurring in an ultra-strong GNS surface layer on $Fe_{45}Mn_{35}Cr_{10}Co_{10}$ HEA processed by SPCBNT. Unlike the previously validated BBOC model in steels [224], the transition mechanism in this HEA involves the cooperative action of two sets of Shockley partial dislocation dipoles and associated atomic shuffling along perpendicular directions. The presence and movement of partial dislocation dipoles and atomic shuffling are believed to play a crucial role in altering the stacking orders within low-energy or mobile boundaries, particularly in low-SFE metals [196, 205]. These mechanisms may also have the capability to locally customize atomic spacings [205, 225]. Such transition activities are likely triggered in HEAs, which possess unique and complex characteristics due to their specific compositions, especially under extremely high-loading conditions accompanied by ultra-high strain rates [61, 226-228]. Based on the Johnson-Cook model [229]: $\sigma = (A + B\varepsilon^{n})(1 + Cln(\frac{\dot{\varepsilon}}{\dot{\varepsilon_0}})$, the strain ε and strain rate $\dot{\varepsilon}$ generated by the machining process are expressed as: $\varepsilon = \frac{\sqrt{3}}{3}\left(\frac{\lambda}{cos\alpha} + \frac{cos\alpha}{\lambda} - 2 \cdot tan\alpha\right)$ and $\dot{\varepsilon} = \frac{d\varepsilon}{dt} = \frac{\varepsilon V}{\Delta}$, respectively [230, 231]. In this work, the tool rake angle α is 20°, V is the cutting speed (1570 mm/s), Δ is the deformation zone (60 μm) and $\lambda = \frac{t_c}{t_d}$ (t_c is chip thickness at 8 μm and t_d is cutting depth at 10 μm). The yield strength (*A*), hardening modulus (*B*), strain rate sensitivity (*C*) and hardening coefficient (*n*) are determined from the dataset as 350MPa, 1344MPa, 0.013 and 0.312, respectively. The $\dot{\varepsilon_0}$ is the reference strain rate of 1 s^{-1}. Accordingly, the strain rate and equivalent stress of SPCBNT in this work are estimated to be ~4.4×10^{4} s^{-1} and ~2.28 GPa, respectively, which also equivalent to the micro-pillar compressive strength at the top surface (~2.1 GPa) for the activation of the fcc → hcp→ bcc phase transition. The strain fields induced by high strain rate during machining process could be relieved and accommodated by the fcc → hcp → bcc PIDMT through the cooperation of dual-directional dislocation dipoles and associated atomic shuffling. At high strain rates, the generation and movement of partial dislocations are intensified, facilitating atomic rearrangement into the hcp structure. In contrast, perfect dislocations mainly contribute to bulk plastic deformation and can inhibit hcp formation if overly active, as they do not produce the stacking faults necessary for phase transformation. Therefore, under high strain rates, the combination of increased partial dislocation activity, high internal stresses, and shear localization collectively promotes bcc to hcp transformation.

4.3 Conclusions

This part demonstrates the fabrication of a heterogeneous nanostructure on $Fe_{45}Mn_{35}Cr_{10}Co_{10}$ HEA using single-point cubic boron nitride turning (SPCBNT), a cost-effective ultra-precision machining technology that applies a high strain rate (~10^4 s^{-1}) to the surface layer. This method achieves nanometre-level surface roughness while reducing the average grain size from ~30 µm in the matrix core to ~13 nm at the surface. The machining process activates a deformation-induced phase transition sequence of fcc → hcp → bcc, with the fcc → hcp transition occurring throughout the gradient nanostructured surface (GNS) and the complete fcc → hcp → bcc sequence limited to the topmost surface layer due to the gradient distribution of plastic strain and strain rate. The nanohardness of the top surface reaches ~6.7 GPa, significantly exceeding the matrix nanohardness of ~4.3 GPa. The fcc → hcp transition is driven by the movement of Shockley partial dislocations on alternate (111)fcc planes, while the subsequent hcp → bcc transition is enabled by the interaction of two sets of Shockley partial dislocation dipoles on (0001)hcp planes and atomic shuffling along perpendicular directions. This cooperative mechanism highlights the intricate interplay between dislocation dynamics and atomic rearrangements in driving phase transitions within nanograins, offering valuable insights into plastic deformation-induced phase transformations and their potential applications in designing advanced structural materials.

Chapter 5 Crystalline-amorphous heterogeneous structure on the fcc-based $Fe_{45}Mn_{35}Cr_{10}Co_{10}$ HEA

5.1 Introduction

Achieving ultrahigh strength with good ductility is the most crucial for the metallic structural components to resist their mechanical failures [2, 35]. Metallic materials could be either periodic atomic ordered crystalline or amorphous structures without any long-range atomic order [12, 232]. Generally, dislocation activities-dominated plastic deformation makes crystalline metals relatively soft but ductile, different from the ultra-strong but brittle amorphous counterparts without lattice dislocation slips [90, 233]. Noticeably, nanosized effects on mechanical properties of crystalline and amorphous metals are quite different [234]. In conventional nanocrystalline metals, multiplication and motion of dislocations are severely impeded by the significantly reduced grain size and increased density of GBs, obviously strengthening metals (Hall-Petch effect [235, 236]) but largely scarifying ductility. Moreover, GB-mediated plasticity would predominate once the grain size below a certain critical value, causing a strengthening-softening transition (Hall-Petch breakdown [237, 238]).

In contrast, the nanosized amorphous metals exhibits increased ductility due to the suppression of localized shear bands [239]. Therefore, a novel approach has been proposed to construct crystalline-amorphous nanocomposites with special structural heterogeneity, where nanograins are encapsulated by nanosized thick amorphous phases that replace the conventional GBs [240, 241]. It can integrate the structural advantages of crystalline and amorphous phases to achieve a synergistic enhancement of mechanical properties [128, 242, 243]. On one side, the dislocation nucleation and motion located at thick amorphous GBs would be exterminated to keep the strengthening effect via dislocation slips inside nanograins, maintaining the Hall-Petch strengthening effect even at extremely refined grain size [127]. On the other side, nanograins not only could facilitate impeding the propagation of localized shear bands but also hardening and resisting the softening effect of the localized shear band because of the division and rotation of the embedded nanograins [244, 245]. As a result, the co-deformation and interaction between nanograined and amorphous phases causes a more homogenous distribution of plastic deformation for strain hardening.

A large number of experimental methods, such as nanocrystallization in amorphous matrix alloys [123], amorphization in nanostructured alloys [125], and physical vapor deposition or magnetron sputtering [126, 246], etc., have been reported to fabricate various nanostructured crystalline-amorphous alloys. Multi-principal HEAs with single solid-solution or multi-phase structures have drawn great attention due to their exceptional properties [89, 247]. Nanostructured crystalline-amorphous HEAs, especially for those with similar compositions to some typical amorphous metals, have also been fabricated by some techniques, such as magnetron sputtering [124], severe plastic deformation [248], and rapid cooling methods [249], showing the remarkably improved mechanical properties. Particularly, laser processing-related techniques (e.g. selective laser melting (SLM) [250] and laser surface remelting (LSR) [251, 252]) can provide exceptional high cooling rates and thus limited crystallization duration during the subsequent solidification process, resulting in the possible incomplete/partial crystallization for formation of nanostructured crystalline-amorphous alloys [159, 253]. For example, laser processing-based techniques have been successfully used to fabricate crystalline-amorphous HEAs [254], e.g. an LSR-fabricated ZrHf-rich reinforcement amorphous phase in the TiZrHfTaNb HEA matrix enhances strength due to its distinct nanostructure that modifies the mechanical response [252].

The unique cooperative deformation behavior of crystalline-amorphous nanostructures, characterized by the strengthening effect of amorphous GBs and dislocation activities within nanograins, has been well established as a key factor in enhancing mechanical performance [252]. Nevertheless, as deformation progresses, amorphous GBs cannot consistently provide strengthening effects, such as blocking dislocations. Instead, their interaction with dislocations introduces additional pathways for deformation mechanism transitions in the crystalline-amorphous nanostructure like the amorphization [125, 255] and the crystallization of amorphous GBs [120]. Notably, these complex interactions emphasize the significance of co-deformation, rather than the independent contributions of the crystalline and amorphous phases [120]. Consequently, the changes of microstructure and the associated evolution of deformation mechanisms have a direct impact on mechanical properties [118, 239], as reported in some traditional materials [256]. For instance, in Al-based alloys subjected to severe plastic deformation, partial crystallization leads to nanograin formation within amorphous regions, inducing a softening effect that offsets ductility [257]. However, the accomplishment of deformation-induced crystallization is highly dependent on elemental composition and pre-deformation microstructure generated by different fabrication techniques [119, 246, 258, 259]. While some studies have demonstrated the accommodation of dislocations from amorphous phases in crystalline-amorphous nanostructures [260], the atomic-scale interactions between dislocations and amorphous phases, particularly regarding crystallization, remain insufficiently explored. This lack of understanding limits our ability to fully elucidate the cooperative co-deformation mechanisms and optimize the mechanical properties in the nanostructured crystalline-amorphous materials. Therefore, it is necessary to uncover the atomic-scale dynamic process of microstructural characteristics with deformation, such as the possible deformation-induced crystallization in amorphous phase and consequent microstructural evolution e.g. grain coalescence [261] and grain coarsening [262], in nanostructured crystalline-amorphous metals.

In this study, we explore the cooperative deformation mechanisms of a nanostructured crystalline-amorphous layer on $Fe_{45}Mn_{35}Cr_{10}Co_{10}$ HEA fabricated using laser surface treatment (LST). The HRTEM observations reveal the well-preserved dislocation activities in nanograins, deformation-induced crystallization of amorphous GBs activated by pile-up dislocation, and subsequent grain coarsening of nanograins with low-angle misorientations with the deformation progressed. Moreover, MD simulations unveil the dynamic process of interactions between dislocations and amorphous GBs and grain coalescence with the evolution of misorientation. Comprehensive observations clarify cooperative co-deformation mechanisms in crystalline-amorphous nanostructures, evidencing how the amorphous phase inhibits dislocation movement while allowing some dislocation activities to persist during crystallization. This work provides new insights into the interplay between dislocations and amorphous phases, advancing our understanding of the deformation mechanisms in crystalline-amorphous nanostructured materials.

5.2 Results

5.2.1 Microstructural evolution after the laser treatment

Figure 5.1(a) illustrates the cross-sectional microstructure and corresponding microhardness profiles along the depth from the surface. The data reveals that increasing laser power from 70 W to 150 W significantly enhances the affected depth and surface microhardness. However, excessive deformation power, such as at 180 W, induces defects like cracks, reducing microhardness as shown in Figure 5.2. Compression tests conducted with laser powers of 130 W and 150 W indicate a notable improvement in strength, as seen in Figure 5.1(b). Among them, the 130 W condition was chosen for further investigation of the microstructural evolution due to its balance between strength improvement and defect suppression. Typical cross-sectional SEM and EBSD images in Figure 5.3(a-c) show refined grains with random crystallographic orientations in a molten pool and coarse grains with an average grain size of about 30 μm in the matrix. Specifically, the cell grains with an average grain size of ~2 μm are embedded within each individual large grain in Figure 5.3(a-c). Although the differences among cell grains cannot be detected as their similar orientation, massive LAGBs with misorientation <15° are introduced in the molten pool, indicating the existence of cell grain close to the treated surface in Figure 5.3(c).

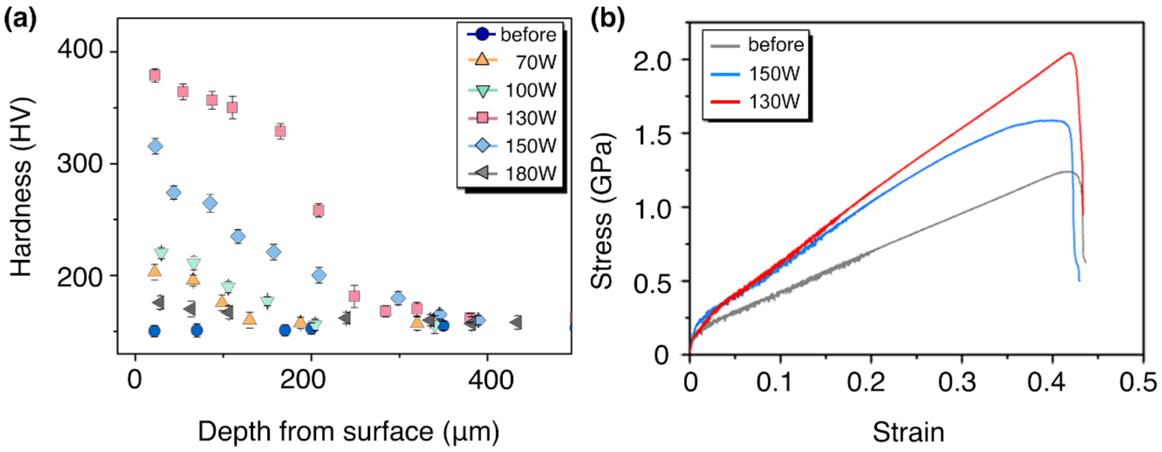

Figure 5.1 (a) hardness and (b) strain-stress curves of $Fe_{45}Mn_{35}Cr_{10}Cr_{10}$ HEAs after laser surface treatment with different power.

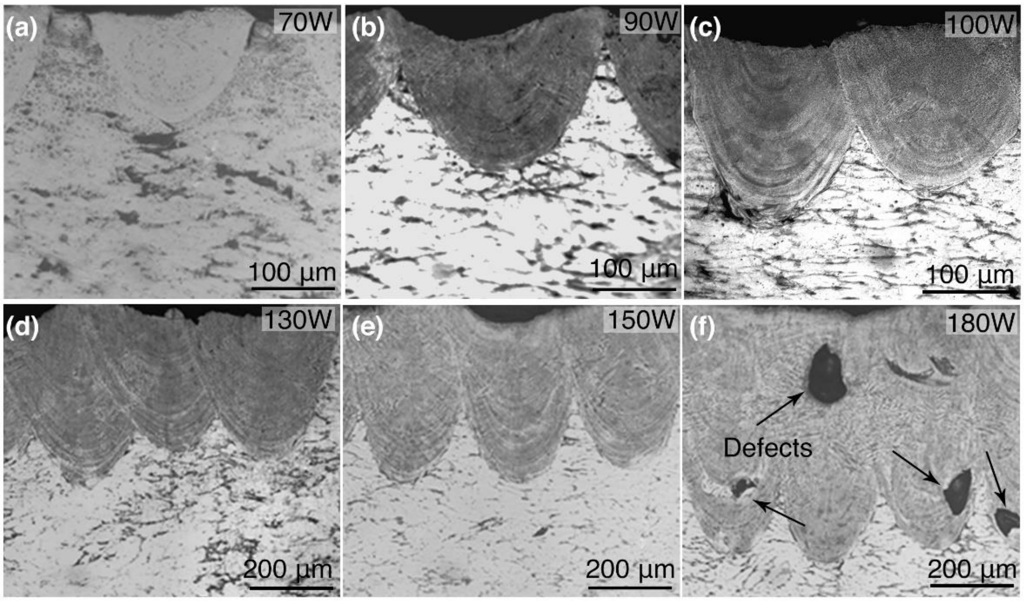

Figure 5.2 Cross-sectional OM image of laser-treated $Fe_{45}Mn_{35}Cr_{10}Cr_{10}$ HEAs at different

powers. (a) 70 W, (b) 90 W, (c) 100 W, (d) 130 W, (e) 150 W, (f) 180 W.

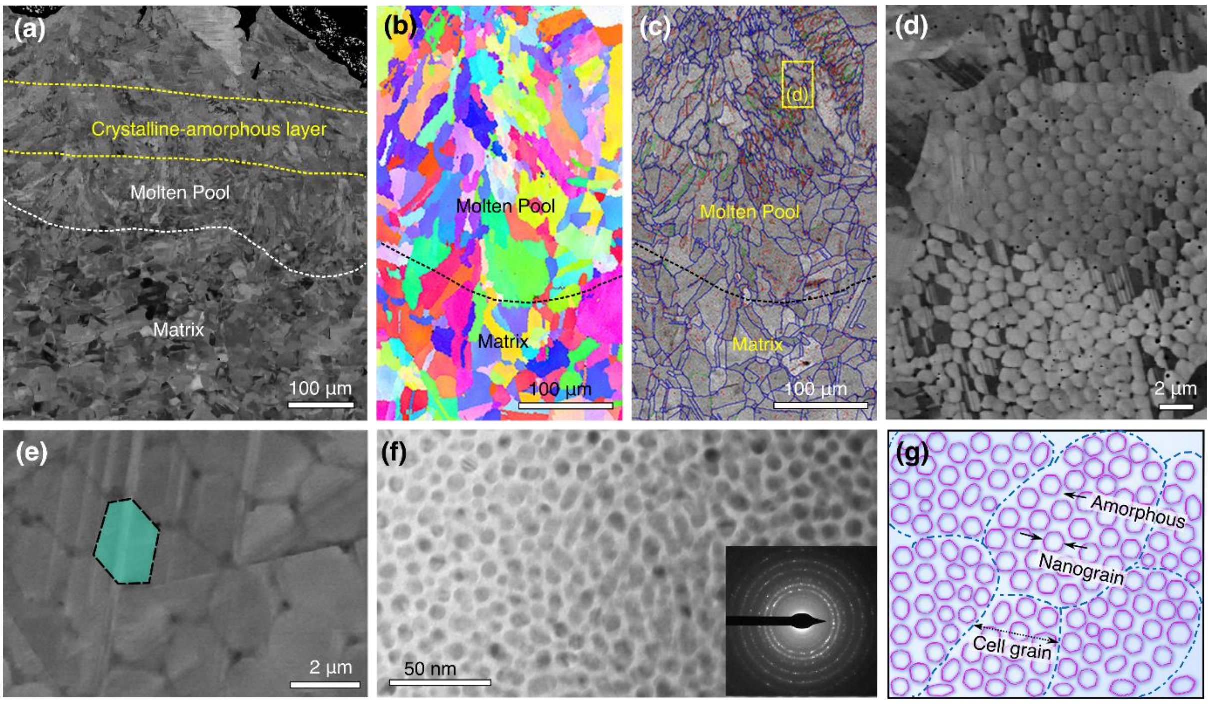

Figure 5.3 Typical microstructure of molten pool after LST. (a) Cross-sectional SEM image, (b) IPF map and (c) GB and phase boundary map show the morphology along the depth direction of the laser-treated sample. (d-e) Cell grain in the refined grains of molten pool. (f) Bright-field TEM image and the associated selected area electron diffraction (SAED) pattern of the crystalline-amorphous nanostructure at the depth of 100 μm away from surface of the treated samples. (g) Schematic of crystalline-amorphous nanostructure distributed within cell grains.

To further explore the microstructure evolution within the molten pool, we randomly selected a cell grain approximately 100 μm beneath the treated surface for detailed transmission electron microscopy (TEM) analysis, as schematically illustrated in Figure 5.3(e) and (g). TEM observations, exemplified in Figure 5.3(f), reveal a distinct crystalline-amorphous structure comprising randomly distributed nanograins surrounded by amorphous GBs. The selected area electron diffraction (SAED) pattern confirms the coexistence of both crystalline and amorphous phases, indicating the heterogeneous distribution of nanograins and amorphous areas induced by high cooling rate of laser treatment [263]. We exam the microstructure through a series of TEM observations along the depth direction depicted in Figure 5.4 to support the microstructural evolution of this crystalline-amorphous nanostructure in the molten pool. The nanograins gradually recrystallize from topmost surface to the depth of ~140 μm and the corresponding grain size at different depths is shown in Figure 5.5. Such change is also confirmed by the SAED patterns that more diffraction spots are situated around the discontinued rings with the increase of depth away from the surface. Compared with the microstructure at the matrix (~200 μm depth), there are no obvious nanograins and only diffraction spots are found. The difference in microstructure between the molten pool and the matrix is also reflected in the phase composition along the depth direction, as presented in Figure 5.6. All depths exhibit an fcc-hcp dual-phase structure, but an increased number of hcp phase peaks are observed closer to the topmost surface. This gradient phase composition suggests that the LST process induces significant phase transformation and grain refinement near the surface.

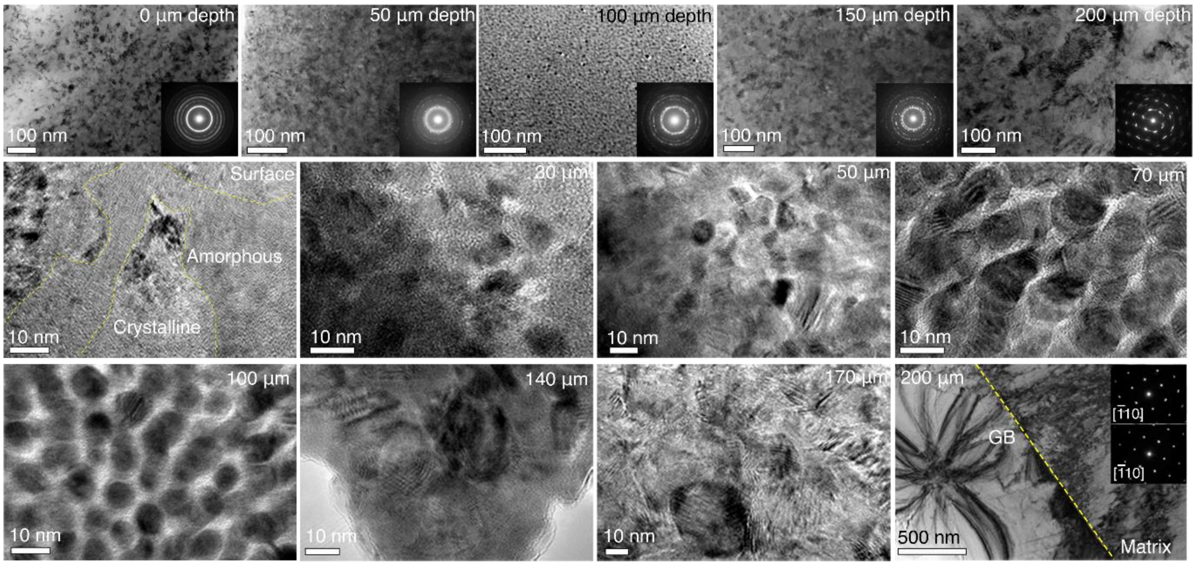

Figure 5.4 Microstructure of nanograins and amorphous GBs at different depths in the $Fe_{45}Mn_{35}Cr_{10}Co_{10}$ HEA after laser surface treatment.

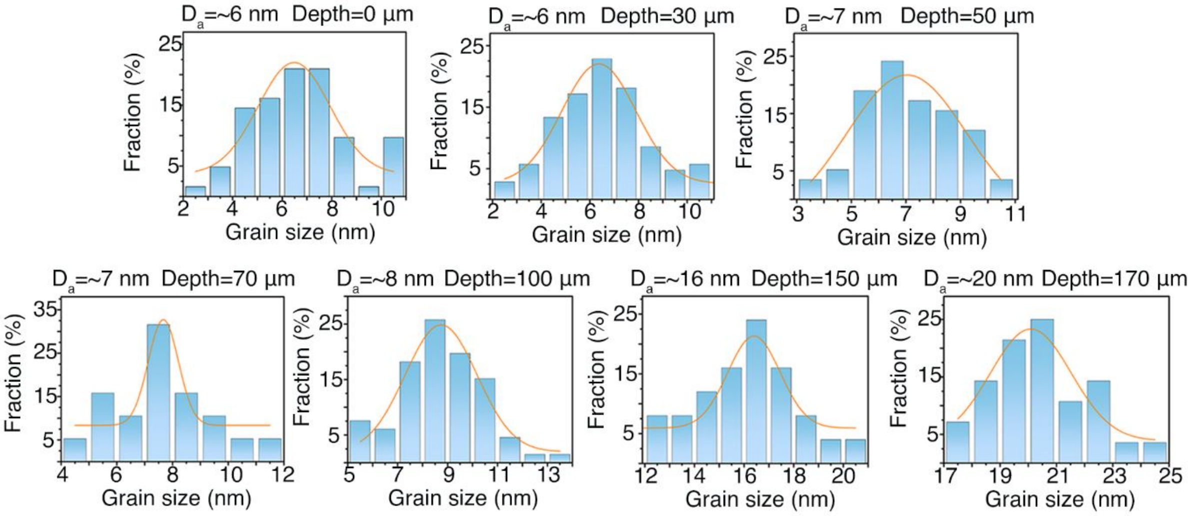

Figure 5.5 The statistical distributions for grain size at different depths on laser-treated $Fe_{45}Mn_{35}Cr_{10}Co_{10}$ HEA.

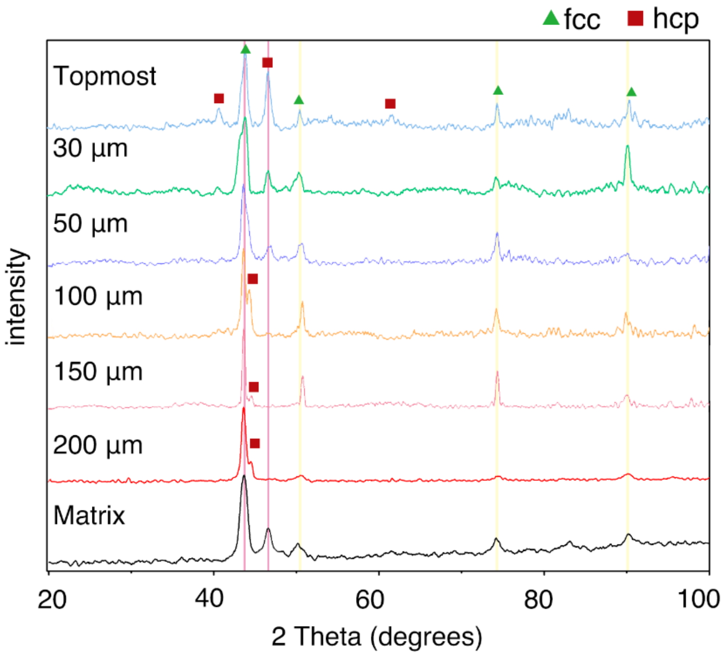

Figure 5.6 GIXRD patterns of laser-treated specimens at different depths

Notably, an ideal crystalline-amorphous region is identified in Figure 5.3, where crystalline and amorphous phases are uniformly distributed within cell grain. In detail, the Fast Fourier transformation (FFT) patterns of two selected areas of Area I and Area II acquired from Figure 5.7 (a) and (b) show crystalline phase viewed along the $[\bar{1}10]$ direction in Figure 5.7 (c) and an amorphous ring in Figure 5.7 (d), respectively. The nanograins with an average grain size of ~8 nm encapsulated by amorphous GBs with a thickness of ~2 nm is statistically summarized in Figure 5.7 (j). By calculating from the HAADF-STEM image in Figure 5.7 (e), the volume of crystalline and amorphous phases is about 60% and 40%, respectively. Elemental composition analysis in Figure 5.7 (f-i) and (k) highlight the compositional segregation between the two phases, with the Co and Cr partition strongly to nanograin and amorphous GB respectively. This Cr segregation is consistent with previous studies [128], which have reported Cr enrichment at amorphous GBs in a CrCoNi-based alloys driven by the Gibbs adsorption isotherm and enhanced glass forming ability according to Fe–Cr, Co–Cr, and Ni–Cr phase diagrams[264, 265].

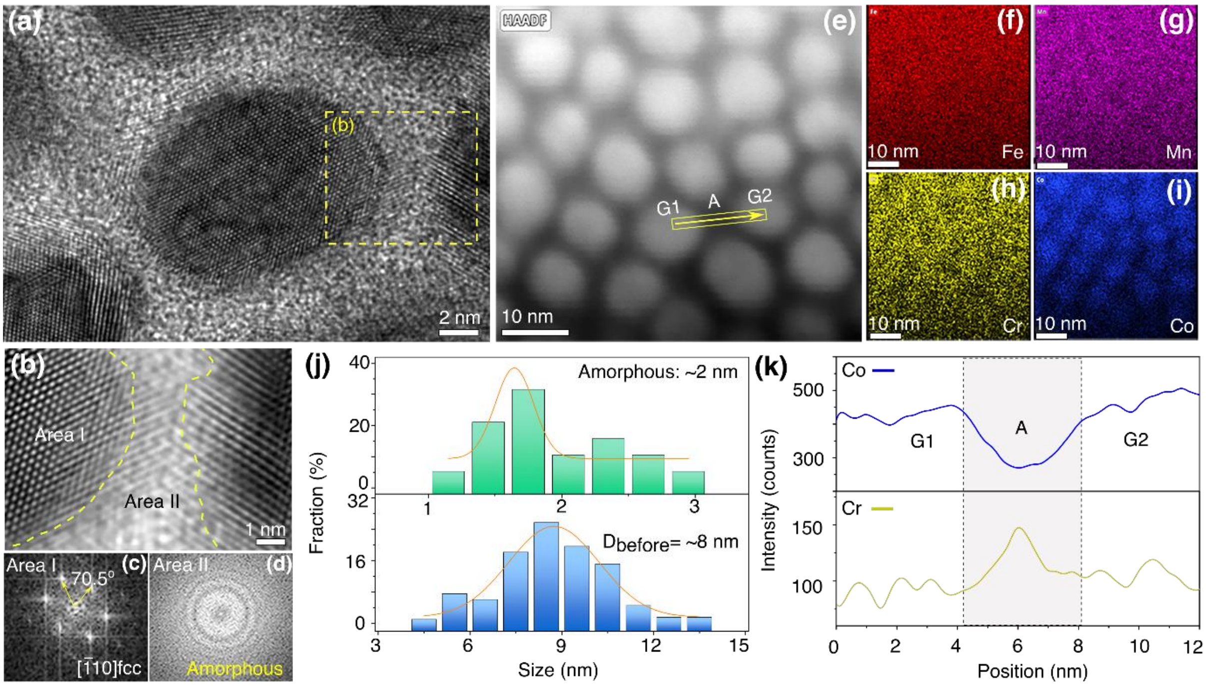

Figure 5.7 Crystalline-amorphous nanostructure. (a) High-resolution TEM (HRTEM) images of nanograins with amorphous GBs in the laser-treated $Fe_{45}Mn_{35}Cr_{10}Co_{10}$ HEA at the depth of ~100 μm. (b) Magnified HRTEM image from (a) and Fast Fourier transformation (FFT) patterns of (c) Area I and (d) Area II selected from (b), exhibiting the coexistence of crystalline and amorphous phases. (e) High-angle annular dark-field scanning transmission electron microscopy (HAADF-STEM) image and (f-i) corresponding electron dispersive spectrometry (EDS) map about the distribution of Fe, Mn, Cr, Co. (j) Statistical gain size and amorphous thickness of the crystalline-amorphous nanostructure at the depth of ~100 μm. (k) EDS -line profiles of crystalline and amorphous phases selected from (e). The EDS map and line profiles show the crystalline and amorphous phases are enriched in Co and Cr, respectively.

5.2.2 Thermal profile of LST process

The formation of a typical molten pool shown in Figure 5.3 (a) results from the rapid remelting and subsequent solidification during laser treatment, where temperature distribution and cooling rates play a critical role in shaping the microstructure. To assess these thermal profiles, we use FEA method to simulate the LST process under conditions identical to experiments and analyze the formation of amorphous phase within the molten pool. The simulation results of thermal gradient along the depth direction in Figure 5.8 (a) indicate the distribution of heat flux. Specifically, as shown in Figure 5.8 (b), the temperature increases from 1734 K (the melting point of $Fe_{45}Mn_{35}Cr_{10}Co_{10}$ HEA [8, 266]) at the edge of the molten pool to 3220 K at the topmost surface, aligning well with the experimentally observed molten pool in Figure 5.3 (a). This wide temperature gradient, combined with the rapid movement of the laser beam and the cooling effect of liquid nitrogen, induces varying cooling rates, leading to formation of new phase beyond the prediction of the equilibrium phase diagram [267] and heterogeneity in the molten pool [268, 269]. In addition, rapid cooling has been recognized as a potential strategy for amorphous phase formation in crystalline materials through suppressing long-range atomic diffusion and preventing full crystallization when the cooling rate attains $10^5 \sim 10^6$ K/s [267, 270-272]. As depicted in Figure 5.8 (c), the calculated cooling rate can reach the critical value of ~ 10^5 K/s at depth of ~ 170 μm away from topmost surface, indicating the theoretical potential for amorphous phase formation in LSTed $Fe_{45}Mn_{35}Cr_{10}Co_{10}$ HEA, which is consistent with the experimentally observed crystalline-amorphous layer shown in Figure 5.3. During solidification, the high cooling rate restricts crystal nucleation and inhibits grain growth [249], thereby stabilizing the amorphous phase and facilitating the development of the crystalline-amorphous nanostructure in studied $Fe_{45}Mn_{35}Cr_{10}Co_{10}$ HEA.

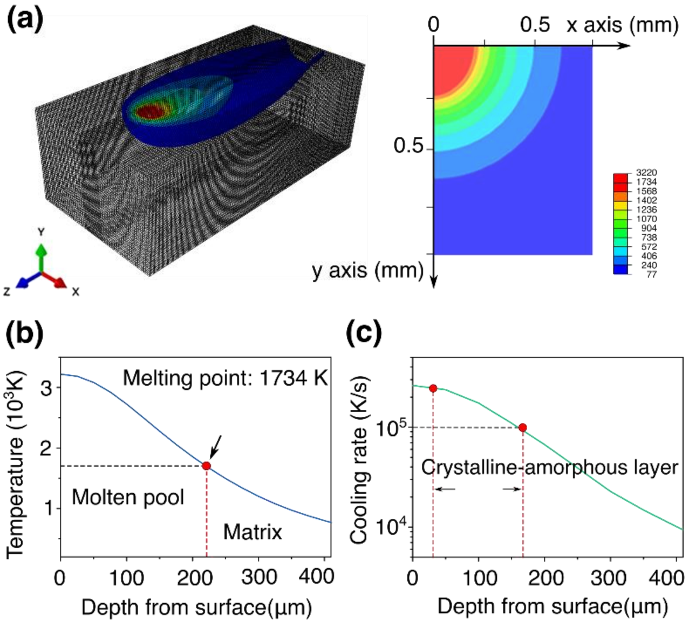

Figure 5.8 FEA results of thermal profile of the molten pool generated by LST. (a) Temperature distribution during the treatment process. Laser beam scanning direction is along the positive z-axis. Variation of (b) temperature and (c) cooling rate acquired from (a) along the y-axis from the top towards the bottom of the molten pool.

5.3.1 Localized mechanical properties

Figure 5.9 presents the results of nanoindentation and localized micro-pillar compression tests for crystalline-amorphous layer. As shown in Figure 5.9 (a), the crystalline-amorphous layer (30-140 μm) can exhibit a nanohardness of ~12 GPa, more than twice the hardness of the matrix (~5 GPa). Similarly, the localized micro-pillar compression tests in Figure 5.9 (b) also reveal a significant hardening effect in the crystalline-amorphous layer compared to the CG matrix. The Hall-Petch plot in Figure 5.9 (c) further illustrates the influence of the amorphous phase on yield strength, which increases from ~2.9 GPa at a depth of 150 μm to ~3.8 GPa at ~100 μm and ultimately attains ~5.7 GPa in the topmost surface compared to ~1 GPa at the matrix. These findings highlight the impact of LST-induced microstructural evolution on mechanical properties, indicating a potential for property optimization by incorporating amorphous phases and tailoring the grain size. Compared to established nanocrystalline and nanocrystalline-amorphous alloys in the literature [126-128, 242, 243, 273-279], our designed alloys show even improved hardening when the grain size is dramatically reduced below ~8 nm, presenting promising in overcoming the strengthening-softening transition and maintaining the Hall-Petch strengthening [238]. As shown in Figure 5.9 (d), the pillar with uniform crystalline-amorphous nanostructure and a grain size of 8 nm at a depth of ~100 um deforms in a manner of shear banding, suggesting homogeneous plastic flow accomplished by distinctive cooperative co-deformation of crystalline-amorphous nanostructure.

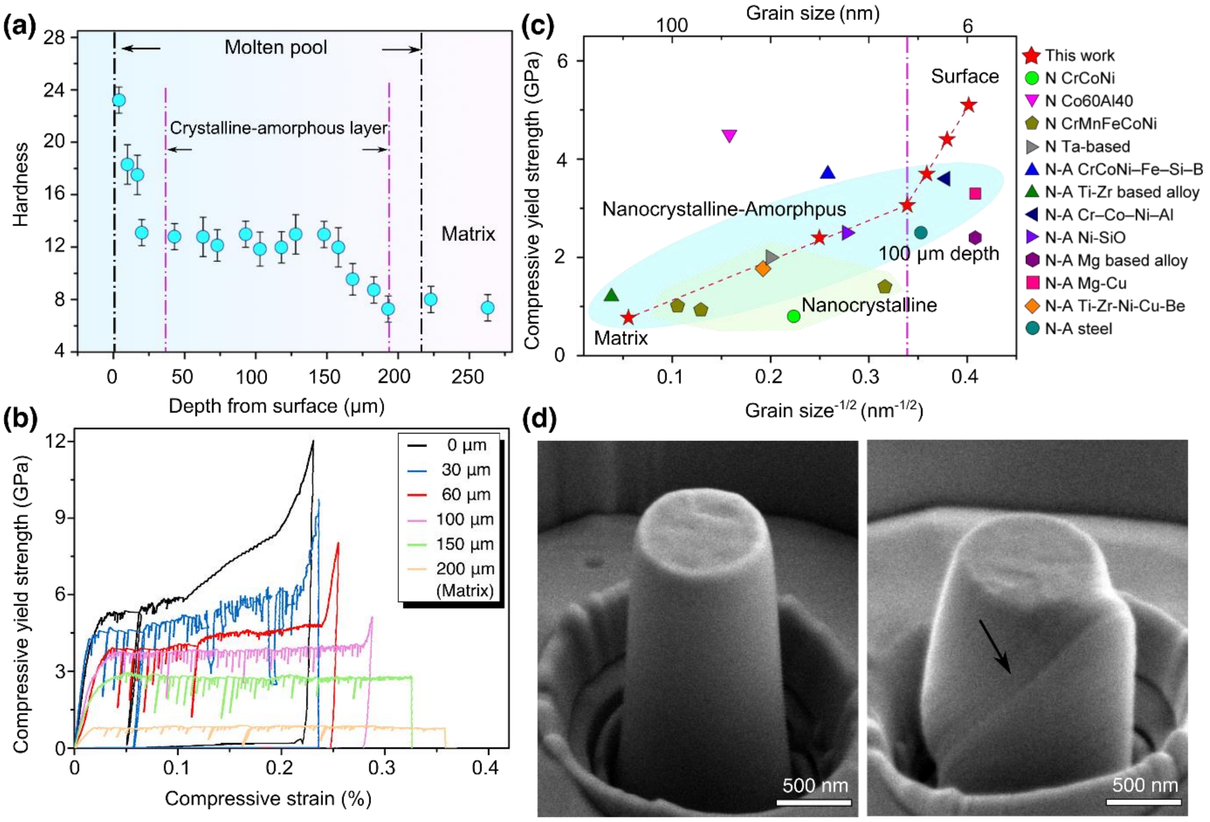

Figure 5.9 Localized mechanical properties of the crystalline–amorphous layer in molten pool. (a) Nanohardness varying along the depth away from the treated surface. (b) Compressive engineering stress–strain curves of pillar samples with the same diameter. (c) Hall-Petch plot of the yield strength for LSTed samples in this work compared with other nanocrystalline and nanocrystalline-amorphous HEAs. N represents nanocrystalline and N-A represents nanocrystalline-amorphous. (d) SEM images of the same samples before and after compression, revealing the shear bands denoted by the black arrow.

5.3 Discussion

The co-deformation behavior of crystalline-amorphous nanostructures observed in this study represents a complex mechanism governed by multiple interrelated processes at the nanoscale.

To elucidate this dynamic phenomenon, several representative regions were analyzed to illustrate the cooperative deformation mechanisms. Initially, dislocation motion is largely confined within nanograins, however, as deformation progresses, dislocations accumulate at the interfaces between amorphous GBs and nanograins due to the barrier effect of the amorphous phase, ultimately activating deformation-induced crystallization to sustain dislocation activity. This process gradually refines the amorphous GBs and results in formation of nanograin boundary due to the reduction of amorphous phase and promotes the final coarsening of nanograins with low-angle misorientations. The continuous evolution of amorphous GBs and their dynamic interactions with dislocations govern the co-deformation process and the resulting structural transitions, ultimately shaping the overall co-deformation behavior.

5.3.1 Cooperative co-deformation behavior of crystalline-amorphous nanostructure

The amorphous phase inevitably contributes to deformation behaviors, cooperating with nanograins to determine the mechanical properties and underlying deformation mechanisms of nanostructured crystalline-amorphous HEA. To explore the interactions between nanograins and amorphous GBs, we investigate the microstructural characteristics of representative crystalline-amorphous nanostructure at the depth of ~100 μm after compression. A comparison of the pre-deformed microstructure (Figure 5.3 (f)) with the post-deformation microstructure (Figure 5.10 (a)) reveals significant grain growth, with average grain size increasing from ~8 nm to ~16 nm (Figure 5.10 (b)). Simultaneously, the initially well-defined amorphous GBs become thinner (average thickness at ~1.2 nm), resulting in formation of nanograin-nanograin boundaries (N-N GBs) in Figure 5.10 (c). Notably, we observe high-density dislocation-induced faulted bands, including stacking faults (SFs), deformation twins, and hexagonal close packed (hcp) laths denoted by the blue arrows in Figure 5.10 (d) both within nanograins and in some specific regions of newly formed N-N GBs. These faulted bands emerge at amorphous GBs and extend into the grain interiors as linear features driven by internal dislocation activity [280], which induces the couple interaction between nanograin and amorphous phases. Under this situation, the presence of dislocation-induced faulted bands facilitates the disappearance of amorphous GBs, resulting in grain coalescence and contributing to grain coarsening, which is highlighted in the magnified TEM observations in Figure 5.10 (e).

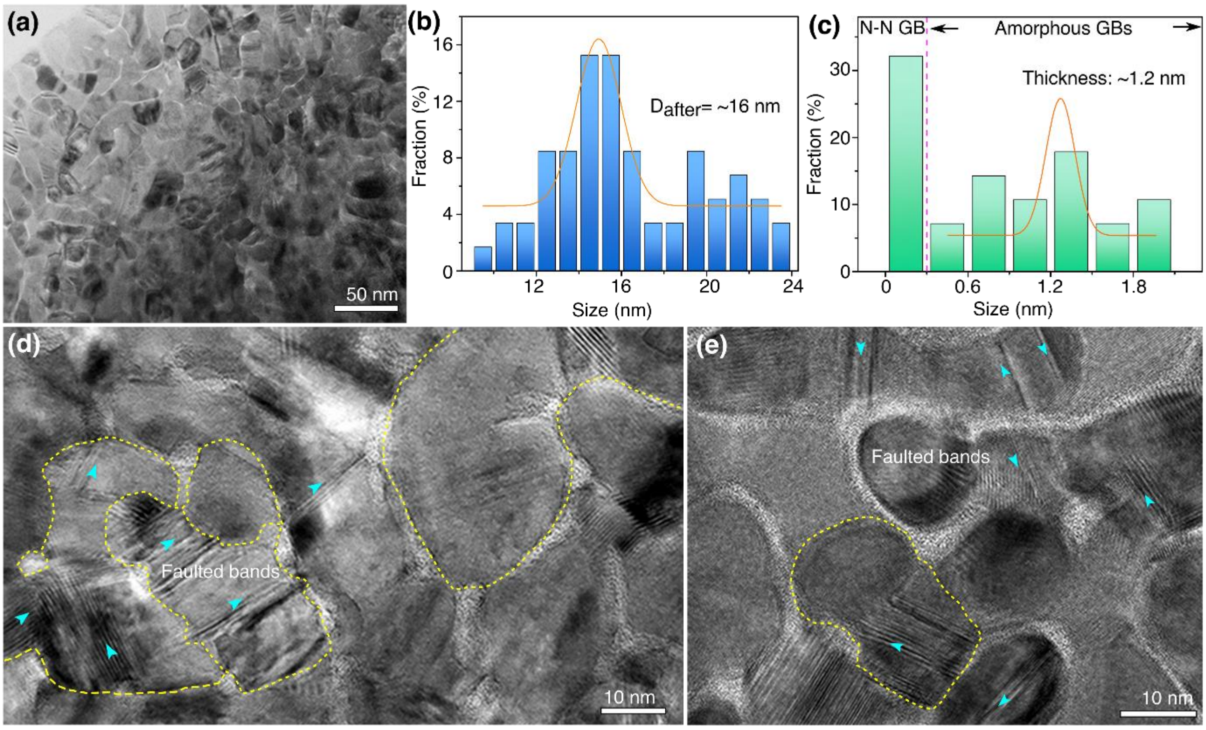

Figure 5.10 Crystalline-amorphous nanostructure after plastic deformation. (a) Bright-field

TEM image after compression. (b) Statistical grain size distribution after deformation. (c) Two types of GBs are formed after plastic deformation: the amorphous GBs with an average thickness at ~1.2 nm and newly formed nanograin-nanograin boundary (N-N GB). (d) and (e) are magnified TEM images from (a) exhibit the dislocation-induced faulted bands including SFs, deformation twins and hcp laths within nanograins, representative grain coalescence and grain coarsening.

Figure 5.11 presents a representative nanograin with interior confined dislocation-induced faulted bands. The observed formation of SFs and deformation twins is similar to the formation process in nanocrystalline materials, which involves successive emission of partial dislocations and dislocation slip [281]. For this crystalline-amorphous nanostructure under plastic deformation, dislocations nucleate at the interface between crystalline and amorphous phases, then propagate across the nanograin, followed by the formation of faulted bands but restricted within the grain, as shown in Figure 5.11 (a) and (b). Specifically, two types of Shockley partial dislocations nucleated from amorphous GB are marked in Figure 5.11 (c), which have representatively Burgers vectors of $b_{p1} = \frac{a}{6}[2\overline{11}]$ and $b_{p3} = \frac{a}{6}[\overline{11}2]$ on (111) plane. In addition, the dislocation activities like the hcp laths, the $(111)[11\overline{2}]$ type coherent twin planes are also activated with the increased strain within nanograins in Figure 5.11 (d) and (e) from the magnified image. Shockley partial dislocations move along twinning planes and contribute to the growth of the deformation twins within the nanograins [282]. The high density of dislocation-induced faulted bands confined within nanograins highlights the role of amorphous GBs as strong barriers that effectively hinder dislocation slips. This impedes softening effect in extremely refined nanograins and enhances mechanical strength, counteracting the inverse Hall-Petch effect [238]. Additionally, the interaction between these dislocation-induced faulted bands and the amorphous phase could provide new opportunities for cooperative co-deformation mechanisms, such as the deformation-induced crystallization of amorphous GBs, which maintain the dislocation movement in these specific regions, as shown in Figure 5.12.

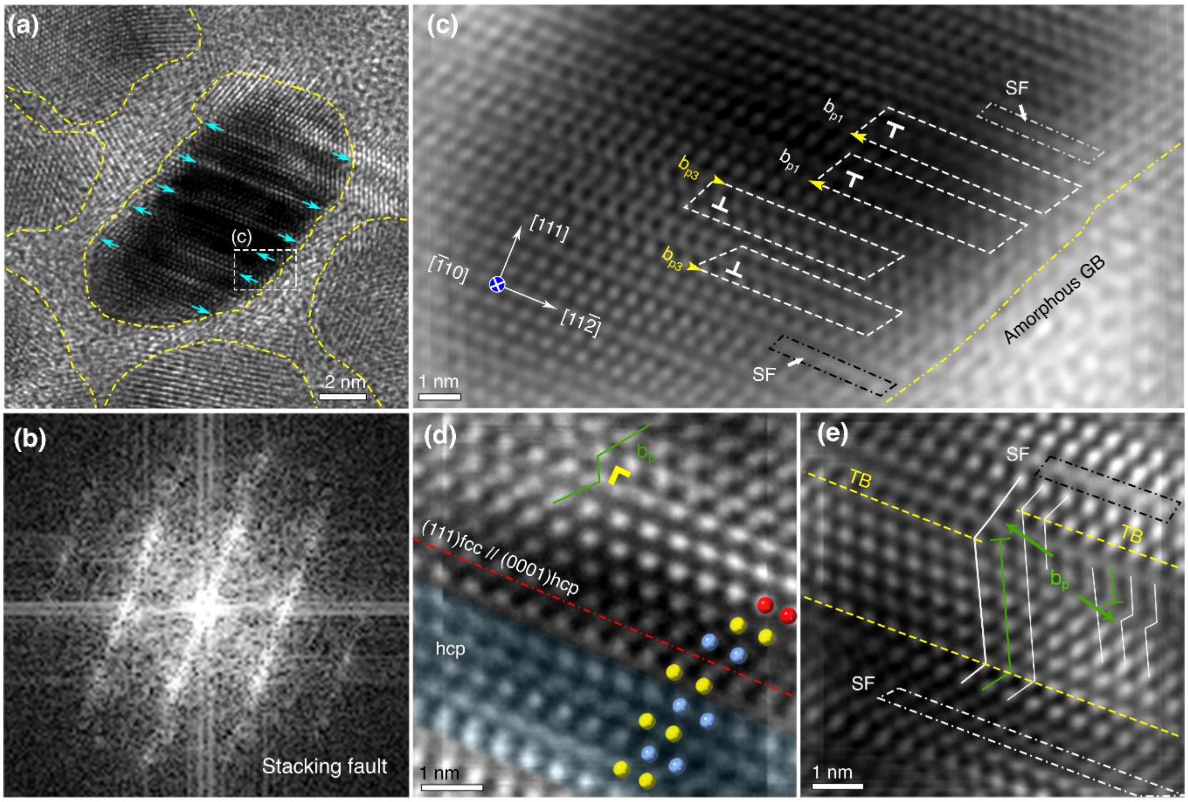

Figure 5.11 The dislocation-induced faulted bands maintained within nanograins in crystalline-amorphous nanostructure. (a) A typical HRTEM image of a representative nanograin containing high-density dislocation-induced faulted bands including SFs, hcp laths and deformation twins. (b) The corresponding FFT pattern of SF acquired from (a). (c) Atomic Fourier-filtered image of the selected region in (a) indicates the two types of Shockley partial dislocations ($b_{p1} = \frac{a}{6}[2\overline{1}\overline{1}]$ and $b_{p3} = \frac{a}{6}[\overline{1}\overline{1}2]$) on (111) plane nucleated from amorphous GB. Atomic Fourier-filtered images acquired from (a) to indicate (d) hcp laths, (e) SFs and

twin boundaries formed by Shockley partial dislocations within the nanograin.

5.3.2 Crystallization of amorphous boundaries

With plastic deformation progressing, the limited space within extremely refined nanograins restrict dislocation movement, leading to dislocation accumulation at crystalline-amorphous interface, which promotes amorphous crystallization as dislocations are absorbed and further facilitates cooperative co-deformation in crystalline-amorphous nanostructured layer. Theoretically, plastic deformation has been applied to activate crystallization in various materials from the view of crystallization kinetics [122, 283]. The relationship between energy barrier of deformation-induced crystallization and the applied stress is expressed as: $\frac{\partial(\Delta G)}{\partial P} = -\frac{64\pi\gamma^3}{3}(\frac{\Delta V_m}{\Delta G_m+E+P\Delta V_m})$ [120, 123]. The ΔG is the Gibbs free energy for the crystal formation, P is the hydrostatic pressure, γ is the interfacial energy between crystalline and amorphous phase, ΔG_m is the driving force for the transformation from amorphous to crystalline phase, E is the elastic energy induced by the volume change during the phase transformation, ΔV_m^c is the molar volume of crystalline phase and ΔV_m^a is the molar volume of amorphous phase (ΔV_m= ΔV_m^c - ΔV_m^a). With increasing hydrostatic pressure during plastic deformation, the free energy required for crystallization decreases, which offers the possibility of deformation-induced amorphous crystallization to induce progressive thinning of amorphous phase and final grain coarsening. This process is experimentally evident on Figure 5.12, where dislocation-induced faulted bands are halted at amorphous GBs, leading to partial disappearance of the amorphous phase and the formation of circular remnants (Figure 5.12 (a)). A closer examination of the amorphous GB in colored TEM image from Figure 5.12 (b) reveals that faulted bands extend across the nanograins along the direction of the white arrows, with the disordered region partially rearranging into an ordered structure, confirming deformation-induced crystallization at the interface. This kind of interaction between dislocations and the amorphous phase drives the crystallization of amorphous GBs, leading to their thinning, as shown in Figure 5.12 (c). The localized transformation not only refines the interface but also sustains dislocation activity, thereby contributing to continued plastic deformation.

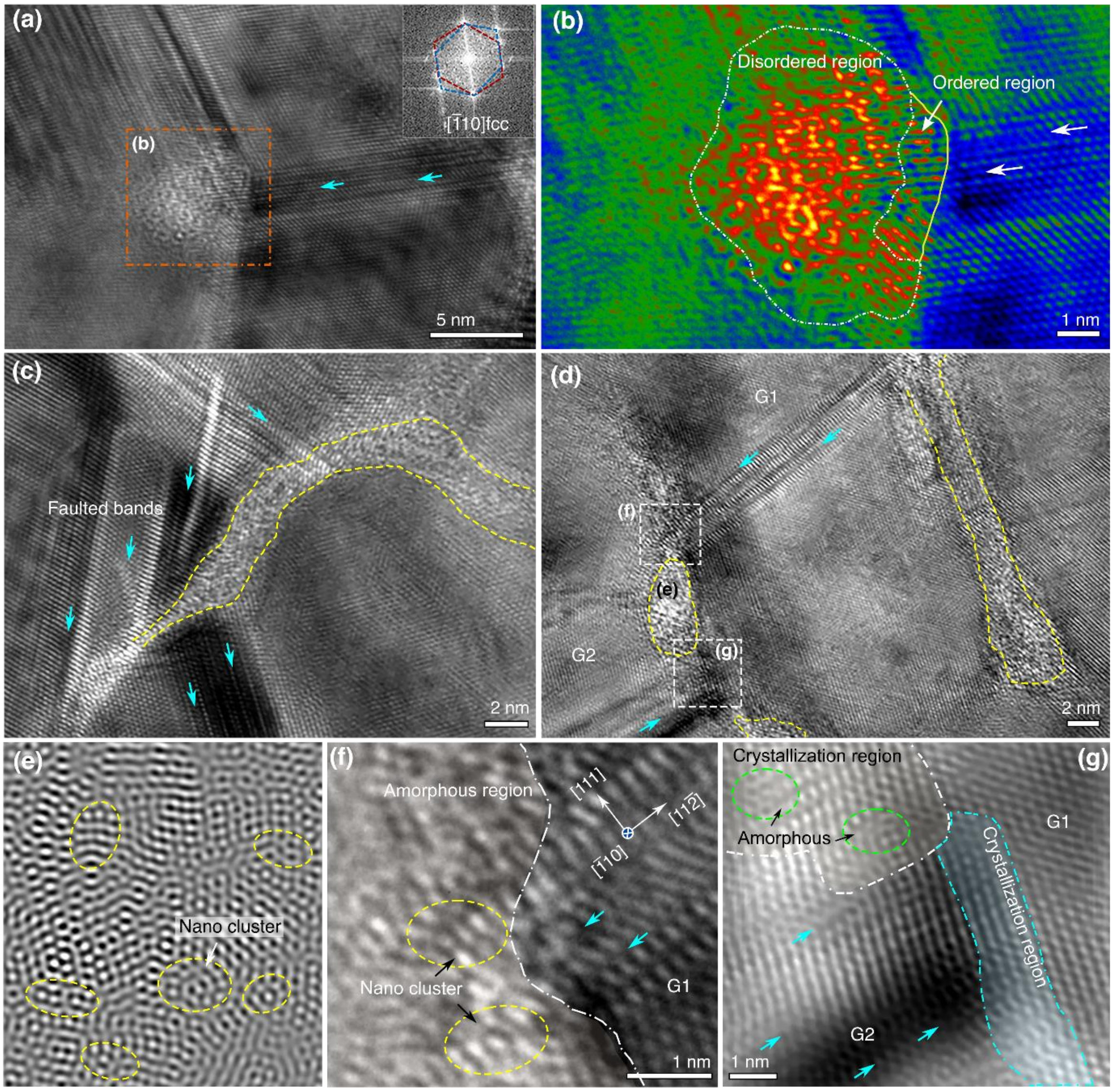

Figure 5.12 Deformation-induced crystallization of amorphous GBs. (a) HRTEM image with the corresponding FFT showing dislocations impeded by amorphous GBs. The magnified, colored HRTEM image in (b) highlights the rearrangement of atoms within the amorphous GB, forming an ordered region associated with faulted bands. (c) HRTEM image of a thinned amorphous GB with confined SFs inside nanograins. (d) HRTEM image showing crystallization at the connection point between nanograins G1 and G2. (e) Atomic Fourier-filtered image of nano clusters with ordered structures embedded in the amorphous GBs, serving as nucleation sites for crystallization. (f) HRTEM image of dislocations generated from G1 propagate along SFs and are obstructed by the amorphous phase, resulting in dislocation pile-up. (g) Atomic Fourier-filtered image indicates that crystallization at the interface connects G1 and G2 through dislocation activities.

Herein, the deformation-induced amorphous crystallization is suggested to be completed by the rearrangement of nano cluster and disordered atoms in the amorphous region when interacting with dislocations [257, 259]. During the LST process, partial recrystallization and rapid cooling preserve some nano clusters as ordered structures within the amorphous GB in Figure 5.12 (e) which give priority to the formation of long-order range and ultimately facilitate crystallization during plastic deformation. The amorphous regions in the two sides of G1 are thinned due to the traversed SFs and the clear connection points between G1 and G2 in Figure 5.12 (d) highlight clear crystallization sites in Figure 5.12 (f) and (g). In Figure 5.12 (f), dislocations move along the (111) planes to trigger the transformation of the amorphous phase into a crystalline structure, particularly at the crystalline-amorphous interface. As dislocation-induced faulted bands propagate and are trapped in the amorphous phase, dislocations accumulate at the interface, causing the amorphous regions to split into smaller segments which serve as new nucleation sites for further dislocation activities [284]. Meanwhile, the pre-existing nano clusters accelerate nearby atoms move and dislocations motion. Under this situation, the atoms in the disordered state jump to the crystal front to contact the nano cluster to accomplish crystallization [120]. Similarly, Figure 5.12 (g) shows a fully crystallized region, where the rearranged amorphous phase aligns with G1 along the $[\bar{1}10]$fcc direction, while some residual regions within the crystallized area retain a disordered state, as indicated by green circles. This cooperative deformation mechanism, where the amorphous phase initially blocks and absorbs dislocations, facilitates sustained dislocation activities through deformation-induced crystallization, ultimately improving both strength and plasticity in crystalline-amorphous nanostructures.

5.3.2 Boundary crystallization-assisted grain coalescence

Due to deformation-induced crystallization along amorphous GBs, the volume fraction of homogeneous nanograins is reduced, while the proportion of larger, coarsened nanograins significantly increases (as shown in Figure 5.10 (a)). Figure 5.13 demonstrates that, after the thinning amorphous GBs, N-N interfaces are formed, which creates the opportunity for neighboring grains to coalesce, resulting in the formation of nanograins with increased grain size. Notably, this process facilitates dislocation movement, which helps delay fracture initiation during plastic deformation. The G3 and G4 are an example that they are partially coalesced into the same orientation with isolated amorphous region in Figure 5.13 (a). In the FFT patterns in Figure 5.13 (b-c), both G3 and G4 are projected along $[\bar{1}10]$fcc direction. The dislocations-induced faulted bands follow the direction denoted by the blue arrows in Figure 5.13 (d) reorientates the amorphous GB to the G3/G4 with clear rearranged region. Meanwhile, the newly formed crystallization region accompanied with abundant dislocations accumulation affords more strain [124]. Taking the crystalline viewed along the $[\bar{1}10]$fcc direction as the reference lattice, the distributions of in-plane strain (E_{xx}) in the interface regions between SFs/crystalline and amorphous/crystalline are shown in Figure 5.14 (a-b). The clear higher E_{xx} fluctuates in SFs/crystalline and amorphous/crystalline interfaces, which is caused by the accumulation of dislocations (Figure 5.14 (c)). As a result, dislocations blocked at the nanograin-amorphous GB interfaces facilitate the rearrangement of the disordered atoms of amorphous phase, effectively prevent shear strain localization [274, 285].

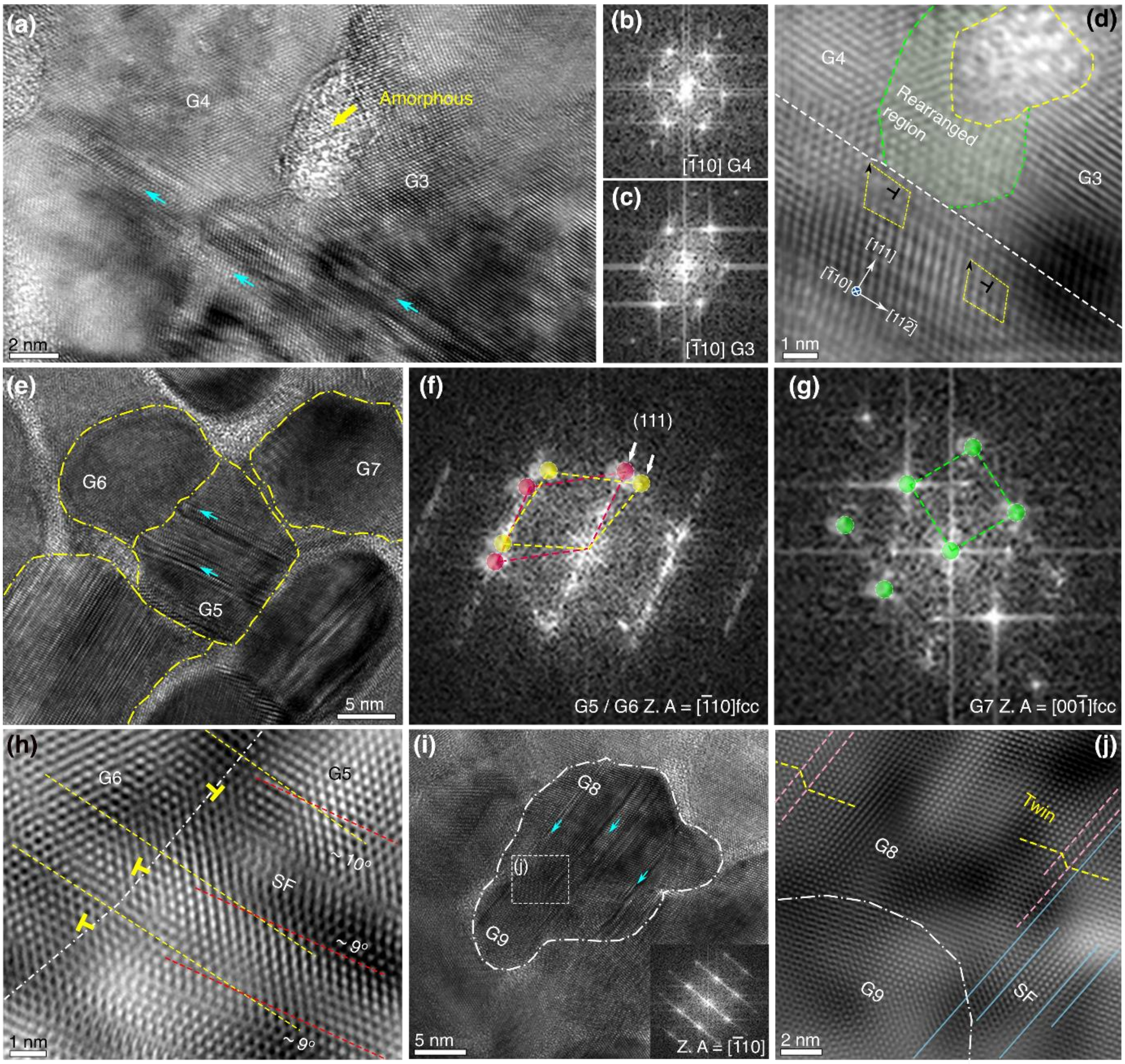

Figure 5.13 Microstructure of crystallization-assisted grain coalescence. (a) Crystallization of amorphous GBs and partly grain coalescence of G3 and G4. (b-c) FFT diffraction patterns of G3 and G4 along $[\bar{1}10]$fcc direction. (d) Atomic Fourier-filtered image of the crystallization area for G3 and G4. (e) A typical HRTEM image shows that two nearby nanograins have small misorientation angles when they begin to coalesce through dislocation-induced faulted bands. (f-g) The corresponding FFT images of G5, G6 and G7, respectively, evidencing that G5 and G6 have the same orientation as $[\bar{1}10]$ direction, while G7 is viewed along $[00\bar{1}]$ direction. (h) Atomic Fourier-filtered image indicates the low misorientation angle at ~10° between G5 and G6. (i) The accomplishment of coalescence for G8 and G9 with the same orientation of

$[\bar{1}10]$ is identified in HRTEM. (j) Corresponding atomic Fourier-filtered image of the selected region from (i), implying the parallel (111) plans in the two different nanograins.

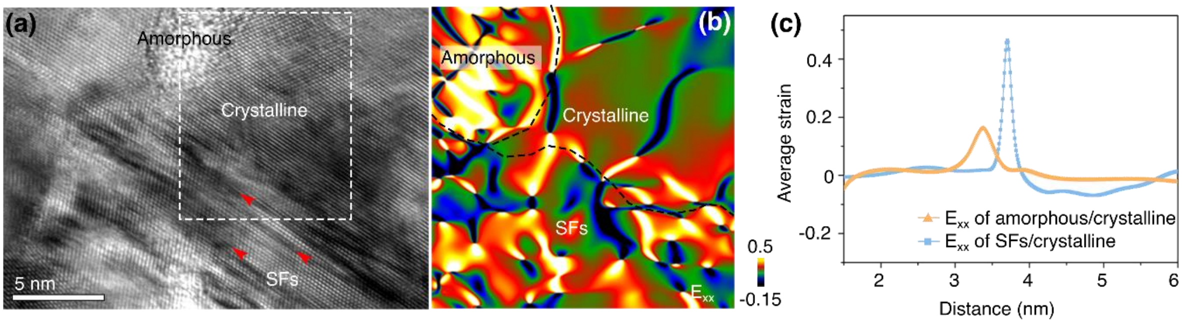

Figure 5.14 (a) HRTEM image of interfacial structures between two adjacent grains crossed by SFs. (b) Exx map of amorphous/crystalline grains/SFs taken from the white dash square region in (a). (c) Average strains in amorphous/crystalline grains/SFs interfaces.

Grain coalescence facilitated by the crystallization of amorphous GBs is another key co-deformation mechanism in our work. The continued dislocation-induced faulted bands in the form of SFs or hcp laths offer the driving force to grain coalescence for specific neighboring nanograins with similar orientations [286, 287] contact and form LAGBs when amorphous GBs thinning through crystallization. In Figure 5.13 (e-h), G5 and G6, projected along the $[\bar{1}10]$ direction with a low misorientation angle of approximately 10°, demonstrate the onset of grain coalescence after the formation of N-N GBs through crystallized GBs. In contrast, G7, oriented along $[00\bar{1}]$ direction, forms a HAGB with G5, preventing coalescence despite the thinning of the amorphous GBs. The newly formed N-N GB between G5 and G6 serves as a preferential dislocation nucleation site, lowering the activation energy barrier for grain growth and grain coalescence [261]. Crystallized GB segments between coalescing grains are fragmented by dislocation-induced faulted bands, creating highly mobile nanometer-sized regions [287]. These dislocations, approaching from opposite sides of the grains, further drive the coalescence process by facilitating GB motion [288]. Figure 5.13 (i) illustrates an accomplishment state of grain coalescence where G9 is fully entrapped by G8. The (111) planes of the G8 and G9 are totally parallel without misorientation angle, as shown in the atomic Fourier-filtered image of Figure 5.13 (j). Accordingly, the dislocation-mediated GB movement mechanism is responsible for the grain coalescence and grain coarsening during the plastic deformation process in our work. This process aligns well with the deformed microstructural features in Figure 5.10 (d-e), where coalesced grains and thinning amorphous GBs indicate significant structural evolution.

Ultimately, we summarize the underlying cooperative co-deformation mechanisms for crystalline-amorphous nanostructure in LSTed $Fe_{45}Mn_{35}Cr_{10}Co_{10}$ HEA, including the deformation-induced crystallization and crystallization-assisted grain coalescence, as schematically illustrated in Figure 15. Rapid cooling during LST shapes unique nanostructures, which comprise extremely refined nanograins surrounded by nanometer-sized amorphous GBs having embedded nano clusters. As shown in Figure 5.15 (a), interactions between crystalline and amorphous phases play a crucial role in determining the mode of cooperative co-deformation, wherein nucleation-propagation-absorption of dislocation-induced faulted bands promote the activation of both crystallization and grain coalescence. Firstly, dislocations emitted from amorphous GBs are confined within the nanograins, while the amorphous phase acts as a barrier, absorbing and/or blocking dislocations (Figure 5.15 (b)). This cooperative deformation mode, driven by the interaction between dislocations and the amorphous phase, governs the early stages of plastic deformation. Furthermore, with continued deformation, dislocation accumulation at amorphous GBs drives atomic rearrangement, assisted by nano clusters, leading to crystallization (Figure 5.15 (c)). As crystallization progresses, thinning of amorphous GBs and increased grain size lead to the formation of N-N GBs, yielding enhanced capacity to sustain extra dislocation activities (Figure 5.15 (d)). With intensified dislocation activities, the deformation-induced crystallization of amorphous GBs facilitates the grain coalescence with close orientations and contributes to potential grain coarsening (Figure 5.15 (e)). As expected, the intricate interplay between nanograins and amorphous GBs provides an alternative to foster homogeneous and compatible deformation behavior, breaking the limitations of solely nanostructuring crystalline or amorphous phases on mechanical properties. By leveraging this cooperative co-deformation, crystalline-amorphous nanostructured materials achieve both enhanced strength and ductility, offering a promising strategy for optimizing mechanical performance in complex alloys.

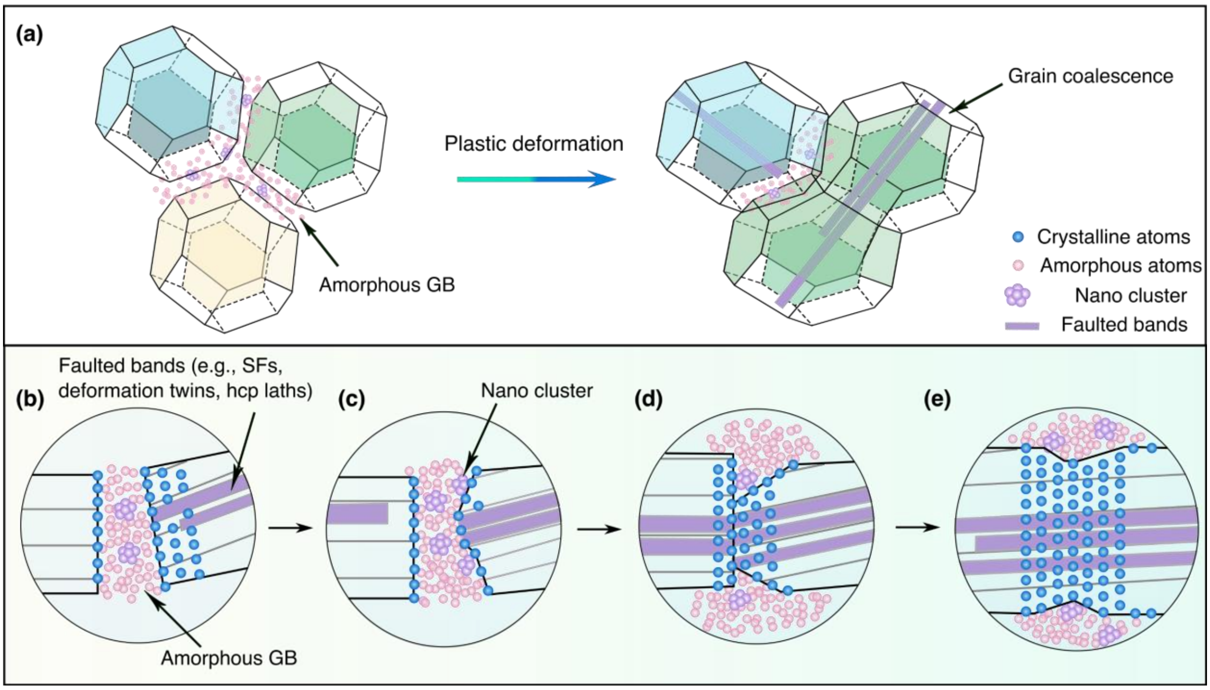

Figure 5.15 The schematic diagram of grain growth mechanism through dislocation movement.

5.4 Conclusions

This work systematically investigates the cooperative co-deformation mechanisms in a crystalline-amorphous nanostructured layer formed in $Fe_{45}Mn_{35}Cr_{10}Co_{10}$ HEA through laser surface treatment. The exceptionally high cooling rates ($>10^5$ K/s) achieved during processing form unique nanostructures with nanograins encapsulated by nanosized amorphous phase along GBs. Under compressive deformation, high-density faulted bands such as stacking faults, hcp laths, and deformation twins are confined within nanograins. Amorphous GBs act as strong barriers that hinder dislocation motion and provide significant strengthening, counteracting the softening effect of extremely refined nanograins. The interactions between dislocations and amorphous GBs reveal two key mechanisms of cooperative co-deformation, which are deformation-induced crystallization and crystallization-assisted grain coalescence. Dislocation accumulation at nanograin-amorphous interfaces triggers a disorder-to-order transition facilitated by nanoclusters that promote crystallization and grain growth. As amorphous GBs diminish, this interaction further enables grain coalescence by forming nanograin-nanograin boundaries between adjacent grains, ultimately leading to grain coarsening. Detailed microstructural observations highlight the dual role of the amorphous phase in obstructing dislocation motion while preserving dislocation activity through deformation-induced crystallization. These findings provide insight into the intricate interplay between dislocation dynamics, amorphous boundary evolution, and crystallization, offering a deeper understanding of how these factors contribute to the improved mechanical performance of crystalline-amorphous nanostructured materials.

Chapter 6 Conclusions and Suggestions for Future Research

6.1 Overall Conclusions

In summary, different techniques have been employed to generate heterogeneous structure in bcc-based and fcc-based HEAs. The underlying microstructural evolution and mechanical properties are comprehensively analyzed in these HEAs with distinguished heterogeneous structure. Meanwhile, the corresponding deformation mechanisms are discussed through atomic-scale observations. The main conclusions can be briefly summarized as follows:

Firstly, a heterogeneous structure is generated on a bcc-based $TiZrHfTa_{0.5}$ RHEA by repeated sliding process on the surface. The average grain size decreases significantly as the distance to the worn surface decreases; from ~100 nm at a depth of about 3 μm to ~30 nm in the top-worn surface region. Additionally, an increased amount of hcp phase forms due to the deformation-induced transition from bcc to hcp, which is activated within the self-organized gradient of the worn subsurface. This heterogeneous structure exhibits an exceptionally low coefficient of friction at 0.12-0.15 and wear rate at $4.08\text{-}9.68\times10^{-5}$ $mm^3/N\cdot m$, demonstrating the potential of wear-induced surface treatments to enhance tribological properties. The structure, characterized by gradients in grain size and hcp phase content, redistributes strain, suppresses localization and accommodates sliding-caused gradient plasticity, significantly improving wear resistance. Atomic-scale observations reveal that two types of phase transformation from bcc to hcp are activated beneath the worn surface, which adapts to the repeated sliding deformation, through atom shuffling or/and partial dislocation dipoles gliding, thereby further improving the wear resistance.

Secondly, a heterogeneous structure is generated by ultra-precision machining with ultra-high strain rate on the surface in $Fe_{45}Mn_{35}Cr_{10}Co_{10}$ HEA, which enhances the nanohardness from 4.3 GPa to about 6.7 GPa and activates the phase transformation fcc → hcp → bcc. This phase transformation sequence accommodates plastic deformation on the surface, which contributes to the formation of heterogeneous structure. The fcc firstly transits to the intermediate hcp occur via the movement of Shockley partial dislocations on every second (111)fcc plane. Then, the final transition step to bcc involves the interaction of two sets of Shockley partial dislocation dipoles on either side of the (0001)hcp planes, coupled with atomic shuffling along perpendicular directions. This coordinated activity of dislocation dipoles and atomic shuffling is critical for the formation of the bcc phase within the nanograins.

Thirdly, a heterogeneous structure with crystalline-amorphous nanostructure, namely, the refined grain with an average grain size at about 8 nm and amorphous along GBs, in the molten pool is created in $Fe_{45}Mn_{35}Cr_{10}Co_{10}$ HEA using laser surface treatment with rapid cooling. This crystalline-amorphous nanostructured layer exhibits high strength, approximately 3.8 GPa, and a compression strain of around 28% during localized micro-pillar compression testing. The underlying cooperative deformation mechanism is elucidated, which includes the movement of dislocations inside the nanograins and along amorphous GBs. Furthermore, the accumulation of dislocations at amorphous GBs enhances the rearrangement of disordered atoms, leading to deformation-induced crystallization that facilitates the coalescence of grains through a GB-mediated mechanism, ultimately resulting in grain coarsening.

6.2 Suggestions for Future Research

The current work successfully fabricated three types of heterogeneous structure of grain size and phase composition in two types of HEAs. Meanwhile, the microstructural evolution and mechanical properties are explained. However, there is still some work that should be done in the future:

1. In-situ TEM observation of the grain coarsening induced by plastic deformation and thermal treatment of crystalline-amorphous nanostructure in laser-treated $Fe_{45}Mn_{35}Cr_{10}Co_{10}$ HEA

For receiving the direct evidence of crystallization of amorphous along GBs and the final grain coarsening, in-situ TEM examination is more convincing for an in-depth understanding of the plastic deformation mechanism. Also, the in-situ TEM of thermal treatment observation of crystalline-amorphous nanostructure about microstructural evolution offers the design pathway to increase thermal stability in HEAs with amorphous GBs.

2. Fabrication of crystalline-amorphous nanostructure with controllable and homogeneous thickness of amorphous GB through laser-based treatment

Although laser surface treatment generates the surface layer with crystalline-amorphous nanostructure as a heterogeneous structure, to widen the application field of this kind of fabrication methods about crystalline-amorphous nanostructure in bulk materials, treating methods like repeated melting or melting direction and subsequent possessing way is significant. In addition, adding more elements with high glass-forming ability to enhance the thickness of amorphous regions.

3. Exploring the tribological performance at an elevated temperature and corresponding deformation mechanism

   The mechanical properties, including nanohardness and micro-pillar compression, were carefully examined in heterogeneous structured $Fe_{45}Mn_{35}Cr_{10}Co_{10}$ HEA. However, it is meaningful to study tribological performance at an elevated temperature and to clarify the microstructural evolution of a heterogeneous structure with gradient grain size and phase composition during repeated plastic deformation to reveal the underlying phase transformation and deformation mechanism.

References

[1] D.B. Miracle, O.N. Senkov, A critical review of high entropy alloys and related concepts, Acta Mater. 122 (2017) 448-511.

[2] E.P. George, D. Raabe, R.O. Ritchie, High-entropy alloys, Nat. Rev. Mater. 4(8) (2019) 515-534.

[3] F.D.C. Garcia Filho, R.O. Ritchie, M.A. Meyers, S.N. Monteiro, Cantor-derived medium-entropy alloys: bridging the gap between traditional metallic and high-entropy alloys, J. Mater. Res. Technol. 17 (2022) 1868-1895.

[4] J. Li, Y. Huang, X. Meng, Y. Xie, A Review on High Entropy Alloys Coatings: Fabrication Processes and Property Assessment, Adv. Eng. Mater. 21(8) (2019).

[5] S. Chen, Y. Tong, P. Liaw, Additive Manufacturing of High-Entropy Alloys: A Review, Entropy 20(12) (2018) 937.

[6] S.A. Krishna, N. Noble, N. Radhika, B. Saleh, A comprehensive review on advances in high entropy alloys: Fabrication and surface modification methods, properties, applications, and future prospects, J. Manuf. Process 109 (2024) 583-606.

[7] S. Salifu, P.A. Olubambi, Effects of fabrication techniques on the mechanical properties of high entropy alloys: A review, Int. J. Lightweight Mater. Manuf. 7(1) (2024) 97-121.

[8] Z. Yong, High entropy materials, Rijeka: IntechOpen2023.

[9] Y.F. Ye, Q. Wang, J. Lu, C.T. Liu, Y. Yang, High-entropy alloy: challenges and prospects, Mater. Today 19(6) (2016) 349-362.

[10] Y. Zhang, T.T. Zuo, Z. Tang, M.C. Gao, K.A. Dahmen, P.K. Liaw, Z.P. Lu, Microstructures and properties of high-entropy alloys, Prog. Mater. Sci. 61 (2014) 1-93.

[11] O.N. Senkov, D.B. Miracle, K.J. Chaput, J.-P. Couzinie, Development and exploration of refractory high entropy alloys—A review, J. Mater. Res. 33(19) (2018) 3092-3128.

[12] W.D. Li, D. Xie, D.Y. Li, Y. Zhang, Y.F. Gao, P.K. Liaw, Mechanical behavior of high-entropy alloys, Prog. Mater. Sci. 118 (2021) 100777.

[13] B. Cantor, I.T.H. Chang, P. Knight, A.J.B. Vincent, Microstructural development in equiatomic multicomponent alloys, Mater. Sci. Eng. A 375 (2004) 213-218.

[14] Z. Li, S. Zhao, R.O. Ritchie, M.A. Meyers, Mechanical properties of high-entropy alloys with emphasis on face-centered cubic alloys, Prog. Mater. Sci. 102 (2019) 296-345.

[15] A. Gali, E.P. George, Tensile properties of high- and medium-entropy alloys, Intermetallics 39 (2013) 74-78.

[16] F. Otto, A. Dlouhý, C. Somsen, H. Bei, G. Eggeler, E.P. George, **The influences of temperature and microstructure on the tensile properties of a CoCrFeMnNi high-entropy alloy**, Acta Mater. 61(15) (2013) 5743-5755.

[17] S.H. Joo, H. Kato, M.J. Jang, J. Moon, C.W. Tsai, J.W. Yeh, H.S. Kim, Tensile deformation behavior and deformation twinning of an equimolar CoCrFeMnNi high-entropy alloy, Mater. Sc. Eng. A 689 (2017) 122-133.

[18] H. Shahmir, M.S. Mehranpour, S.A. Arsalan Shams, T.G. Langdon, Twenty years of the CoCrFeNiMn high-entropy alloy: achieving exceptional mechanical properties through

microstructure engineering, J. Mater. Res. Technol. 23 (2023) 3362-3423.

[19] M. Tian, C. Wu, Y. Liu, H. Peng, J. Wang, X. Su, Phase stability and microhardness of CoCrFeMnxNi2-x high entropy alloys, J. Alloys Compd. 811 (2019).

[20] J. Moon, O. Bouaziz, H.S. Kim, Y. Estrin, Twinning Engineering of a CoCrFeMnNi High-Entropy Alloy, Scr. Mater. 197 (2021).

[21] G. Laplanche, A. Kostka, C. Reinhart, J. Hunfeld, G. Eggeler, E.P. George, Reasons for the superior mechanical properties of medium-entropy CrCoNi compared to high-entropy CrMnFeCoNi, Acta Mater. 128 (2017) 292-303.

[22] Z.M. Li, K.G. Pradeep, Y. Deng, D. Raabe, C.C. Tasan, Metastable high-entropy dual-phase alloys overcome the strength-ductility trade-off, Nature 534(7606) (2016) 227-30.

[23] S. Zhu, D. Yan, K. Gan, W. Lu, Z. Li, Awakening the metastability of an interstitial high entropy alloy via severe deformation, Scr. Mater. 191 (2021) 96-100.

[24] J.-K. Kim, J.H. Kim, H. Park, J.-S. Kim, G. Yang, R. Kim, T. Song, D.-W. Suh, J. Kim, Temperature-dependent universal dislocation structures and transition of plasticity enhancing mechanisms of the Fe40Mn40Co10Cr10 high entropy alloy, Int. J Plasticity 148 (2022).

[25] O.N. Senkov, J.M. Scott, S.V. Senkova, D.B. Miracle, C.F. Woodward, Microstructure and room temperature properties of a high-entropy TaNbHfZrTi alloy, J. Alloys Compd. 509(20) (2011) 6043-6048.

[26] M.E. Torki, A.A. Benzerga, J.B. Leblond, On Void Coalescence Under Combined Tension and Shear, J. Appl. Mech. 82(7) (2015) 071005.

[27] V. Tvergaard, Material Failure by Void Growth to Coalescence, Adv. Appl. Mech.1989, pp. 83-151.

[28] O.N. Senkov, G.B. Wilks, J.M. Scott, D.B. Miracle, Mechanical properties of Nb25Mo25Ta25W25 and V20Nb20Mo20Ta20W20 refractory high entropy alloys, Intermetallics 19(5) (2011) 698-706.

[29] O.N. Senkov, S.L. Semiatin, Microstructure and properties of a refractory high-entropy alloy after cold working, J. Alloys Compd. 649 (2015) 1110-1123.

[30] R. Feng, B. Feng, M.C. Gao, C. Zhang, J.C. Neuefeind, J.D. Poplawsky, Y. Ren, K. An, M. Widom, P.K. Liaw, Superior High-Temperature Strength in a Supersaturated Refractory High-Entropy Alloy, Adv. Mater. 33(48) (2021) e2102401.

[31] U.S. Anamu, O.O. Ayodele, E. Olorundaisi, B.J. Babalola, P.I. Odetola, A. Ogunmefun, K. Ukoba, T.C. Jen, P.A. Olubambi, Fundamental design strategies for advancing the development of high entropy alloys for thermo-mechanical application: A critical review, J. Mater. Res. Technol. 27 (2023) 4833-4860.

[32] Q.J. Li, H. Sheng, E. Ma, Strengthening in multi-principal element alloys with local-chemical-order roughened dislocation pathways, Nat. Commun. 10(1) (2019) 3563.

[33] R.R. Chen, G. Qin, H.T. Zheng, L. Wang, Y.Q. Su, Y.L. Chiu, H.S. Ding, J.J. Guo, H.Z. Fu, Composition design of high entropy alloys using the valence electron concentration to balance strength and ductility, Acta Mater. 144 (2018) 129-137.

[34] M. Ghanbariha, M. Farvizi, T. Ebadzadeh, A.A. Samiyan, H.S. Kim, AlCoCrFeNi-NiTi

high entropy alloy composites: Microstructure and wear performance, Mater. Today Commun. 32 (2022).

[35] E.P. George, W.A. Curtin, C.C. Tasan, High entropy alloys: A focused review of mechanical properties and deformation mechanisms, Acta Mater. 188 (2020) 435-474.

[36] M. Vaidya, G.M. Muralikrishna, B.S. Murty, High-entropy alloys by mechanical alloying: A review, J. Mater. Res. 34(5) (2019) 664-686.

[37] M.Y. He, Y.F. Shen, N. Jia, P.K. Liaw, C and N doping in high-entropy alloys: A pathway to achieve desired strength-ductility synergy, Appl. Mater. Today 25 (2021).

[38] B.A. Memon, H. Yao, A fracture-resistant high-entropy alloy for cryogenic application, Entropy 21(3) (2019).

[39] B. Gorr, S. Schellert, F. Müller, H.-J. Christ, A. Kauffmann, M. Heilmaier, Current Status of Research on the Oxidation Behavior of Refractory High Entropy Alloys, Adv. Eng. Mater. 23(5) (2021).

[40] M. Yang, X.J. Liu, H.H. Ruan, Y. Wu, H. Wang, Z.P. Lu, High thermal stability and sluggish crystallization kinetics of high-entropy bulk metallic glasses, J. Appl. Phys. 119(24) (2016).

[41] J.H. Zhao, X.L. Ji, Y.P. Shan, Y. Fu, Z. Yao, On the microstructure and erosion–corrosion resistance of AlCrFeCoNiCu high-entropy alloy via annealing treatment, Mater. Sci. Technol. 32(12) (2016) 1271-1275.

[42] G. Qin, R. Chen, H. Zheng, H. Fang, L. Wang, Y. Su, J. Guo, H. Fu, Strengthening FCC-CoCrFeMnNi high entropy alloys by Mo addition, Journal of Materials Science & Technology 35(4) (2019) 578-583.

[43] L. Rogal, U.D. Wdowik, M. Szczerba, N. Yurchenko, T. Czeppe, P. Bobrowski, Deformation induced twinning in hcp/bcc Al10Hf25Nb5Sc10Ti25Zr25 high entropy alloy – microstructure and mechanical properties, Mater. Sci. Eng. A 802 (2021).

[44] B. Gludovatz, E.P. George, R.O. Ritchie, Processing, Microstructure and Mechanical Properties of the CrMnFeCoNi High-Entropy Alloy, JOM 67(10) (2015) 2262-2270.

[45] O.N. Senkov, J.M. Scott, S.V. Senkova, F. Meisenkothen, D.B. Miracle, C.F. Woodward, Microstructure and elevated temperature properties of a refractory TaNbHfZrTi alloy, J. Mater. Sci. 47(9) (2012) 4062-4074.

[46] Y. Lu, X. Gao, L. Jiang, Z. Chen, T. Wang, J. Jie, H. Kang, Y. Zhang, S. Guo, H. Ruan, Y. Zhao, Z. Cao, T. Li, Directly cast bulk eutectic and near-eutectic high entropy alloys with balanced strength and ductility in a wide temperature range, Acta Mater. 124 (2017) 143-150.

[47] Y.B. Kang, S.H. Shim, K.H. Lee, S.I. Hong, Dislocation creep behavior of CoCrFeMnNi high entropy alloy at intermediate temperatures, Materials Research Letters 6(12) (2018) 689-695.

[48] D.-H. Lee, M.-Y. Seok, Y. Zhao, I.-C. Choi, J. He, Z. Lu, J.-Y. Suh, U. Ramamurty, M. Kawasaki, T.G. Langdon, J.-i. Jang, Spherical nanoindentation creep behavior of nanocrystalline and coarse-grained CoCrFeMnNi high-entropy alloys, Acta Mater. 109 (2016) 314-322.

[49] P. Kral, W. Blum, J. Dvorak, N. Yurchenko, N. Stepanov, S. Zherebtsov, L. Kuncicka, M. Kvapilova, V. Sklenicka, Creep behavior of an AlTiVNbZr0.25 high entropy alloy at 1073 K, Materials Science and Engineering: A 783 (2020).

[50] W. Li, S. Chen, P.K. Liaw, Discovery and design of fatigue-resistant high-entropy alloys, Scr. Mater. 187 (2020) 68-75.

[51] Z. Tang, T. Yuan, C.-W. Tsai, J.-W. Yeh, C.D. Lundin, P.K. Liaw, Fatigue behavior of a wrought Al0.5CoCrCuFeNi two-phase high-entropy alloy, Acta Mater. 99 (2015) 247-258.

[52] K.V.S. Thurston, B. Gludovatz, A. Hohenwarter, G. Laplanche, E.P. George, R.O. Ritchie, Effect of temperature on the fatigue-crack growth behavior of the high-entropy alloy CrMnFeCoNi, Intermetallics 88 (2017) 65-72.

[53] J. Joseph, N. Haghdadi, K. Shamlaye, P. Hodgson, M. Barnett, D. Fabijanic, The sliding wear behaviour of CoCrFeMnNi and AlxCoCrFeNi high entropy alloys at elevated temperatures, Wear 428-429 (2019) 32-44.

[54] N. Hua, W. Wang, Q. Wang, Y. Ye, S. Lin, L. Zhang, Q. Guo, J. Brechtl, P.K. Liaw, Mechanical, corrosion, and wear properties of biomedical Ti–Zr–Nb–Ta–Mo high entropy alloys, J. Alloys Compd. 861 (2021).

[55] Y. Lu, Y. Dong, H. Jiang, Z. Wang, Z. Cao, S. Guo, T. Wang, T. Li, P.K. Liaw, Promising properties and future trend of eutectic high entropy alloys, Scr. Mater. 187 (2020) 202-209.

[56] D. Kumar, Recent advances in tribology of high entropy alloys: A critical review, Prog. Mater. Sci. 136 (2023).

[57] Q.Q. Ding, X.Q. Fu, D.K. Chen, H.B. Bei, B. Gludovatz, J.X. Li, Z. Zhang, E.P. George, Q. Yu, T. Zhu, R.O. Ritchie, Real-time nanoscale observation of deformation mechanisms in CrCoNi-based medium- to high-entropy alloys at cryogenic temperatures, Mater. Today 25 (2019) 21-27.

[58] N. Ali, L.Q. Zhang, D.M. Liu, H.W. Zhou, K. Sanaullah, C.J. Zhang, J.H. Chu, Y. Nian, J.J. Cheng, Strengthening mechanisms in high entropy alloys: A review, Mater. Today Commun. 33 (2022).

[59] S.J. Sun, Y.Z. Tian, H.R. Lin, H.J. Yang, X.G. Dong, Y.H. Wang, Z.F. Zhang, Transition of twinning behavior in CoCrFeMnNi high entropy alloy with grain refinement, Mater. Sci. Eng. A 712 (2018) 603-607.

[60] C.-C. Juan, M.-H. Tsai, C.-W. Tsai, W.-L. Hsu, C.-M. Lin, S.-K. Chen, S.-J. Lin, J.-W. Yeh, Simultaneously increasing the strength and ductility of a refractory high-entropy alloy via grain refining, Mater. Lett. 184 (2016) 200-203.

[61] X.X. Wu, D. Mayweg, D. Ponge, Z.M. Li, Microstructure and deformation behavior of two TWIP/TRIP high entropy alloys upon grain refinement, Mater. Sci. Eng. A 802 (2021) 140661.

[62] G. Qin, W. Xue, R. Chen, H. Zheng, L. Wang, Y. Su, H. Ding, J. Guo, H. Fu, Grain refinement and FCC phase formation in AlCoCrFeNi high entropy alloys by the addition of carbon, Materialia 6 (2019).

[63] T. Yang, Y.L. Zhao, W.P. Li, C.Y. Yu, J.H. Luan, D.Y. Lin, L. Fan, Z.B. Jiao, W.H. Liu, X.J. Liu, J.J. Kai, J.C. Huang, C.T. Liu, Ultrahigh-strength and ductile superlattice alloys

with nanoscale disordered interfaces, Science 369(6502) (2020) 427-432.

[64] Z.M. Yang, D.S. Yan, W.J. Lu, Z.M. Li, A TWIP-TRIP quinary high-entropy alloy: Tuning phase stability and microstructure for enhanced mechanical properties, Mater. Sci. Eng. A 801 (2021) 140441.

[65] J. Su, D. Raabe, Z. Li, Hierarchical microstructure design to tune the mechanical behavior of an interstitial TRIP-TWIP high-entropy alloy, Acta Mater. 163 (2019) 40-54.

[66] S.S. Nene, M. Frank, K. Liu, R.S. Mishra, B.A. McWilliams, K.C. Cho, Extremely high strength and work hardening ability in a metastable high entropy alloy, Scientific Reports 8(1) (2018).

[67] J.W. Bae, J.B. Seol, J. Moon, S.S. Sohn, M.J. Jang, H.Y. Um, B.-J. Lee, H.S. Kim, Exceptional phase-transformation strengthening of ferrous medium-entropy alloys at cryogenic temperatures, Acta Mater. 161 (2018) 388-399.

[68] H.L. Huang, Y. Wu, J.Y. He, H. Wang, X.J. Liu, K. An, W. Wu, Z.P. Lu, Phase-Transformation Ductilization of Brittle High-Entropy Alloys via Metastability Engineering, Adv. Mater. 29(30) (2017).

[69] Y.L. Zhang, J.G. Li, X.G. Wang, Y.P. Lu, Y.Z. Zhou, X.F. Sun, The interaction and migration of deformation twin in an eutectic high-entropy alloy AlCoCrFeNi2.1, J. Mater. Sci. Technol. 35(5) (2019) 902-906.

[70] W. Abuzaid, H. Sehitoglu, Critical resolved shear stress for slip and twin nucleation in single crystalline FeNiCoCrMn high entropy alloy, Mater. Charact. 129 (2017) 288-299.

[71] H. Shahmir, P. Asghari-Rad, M.S. Mehranpour, F. Forghani, H.S. Kim, M. Nili-Ahmadabadi, Evidence of FCC to HCP and BCC-martensitic transformations in a CoCrFeNiMn high-entropy alloy by severe plastic deformation, Mater. Sci. Eng. A 807 (2021) 140875.

[72] S.W. Wu, G. Wang, J. Yi, Y.D. Jia, I. Hussain, Q.J. Zhai, P.K. Liaw, Strong grain-size effect on deformation twinning of an Al0.1CoCrFeNi high-entropy alloy, Mater. Res. Lett. 5(4) (2016) 276-283.

[73] X.H. Chen, L. Lu, K. Lu, Grain size dependence of tensile properties in ultrafine-grained Cu with nanoscale twins, Scripta Mater. 64(4) (2011) 311-314.

[74] X. Gao, Y. Lu, J. Liu, J. Wang, T. Wang, Y. Zhao, Extraordinary ductility and strain hardening of Cr26Mn20Fe20Co20Ni14 TWIP high-entropy alloy by cooperative planar slipping and twinning, Materialia 8 (2019).

[75] W. Lu, C.H. Liebscher, G. Dehm, D. Raabe, Z. Li, Bidirectional Transformation Enables Hierarchical Nanolaminate Dual-Phase High-Entropy Alloys, Adv. Mater. 30(44) (2018).

[76] Z.F. He, N. Jia, D. Ma, H.L. Yan, Z.M. Li, D. Raabe, Joint contribution of transformation and twinning to the high strength-ductility combination of a FeMnCoCr high entropy alloy at cryogenic temperatures, Materials Science and Engineering: A 759 (2019) 437-447.

[77] C.R. LaRosa, M. Shih, C. Varvenne, M. Ghazisaeidi, Solid solution strengthening theories of high-entropy alloys, Mater. Character. 151 (2019) 310-317.

[78] I. Basu, J.T.M. De Hosson, Strengthening mechanisms in high entropy alloys: Fundamental issues, Scr. Mater. 187 (2020) 148-156.

[79] Y.L. Zhao, T. Yang, Y. Tong, J. Wang, J.H. Luan, Z.B. Jiao, D. Chen, Y. Yang, A. Hu, C.T. Liu, J.J. Kai, Heterogeneous precipitation behavior and stacking-fault-mediated deformation in a CoCrNi-based medium-entropy alloy, Acta Mater. 138 (2017) 72-82.

[80] C. Liu, W. Lu, W. Xia, C. Du, Z. Rao, J.P. Best, S. Brinckmann, J. Lu, B. Gault, G. Dehm, G. Wu, Z. Li, D. Raabe, Massive interstitial solid solution alloys achieve near-theoretical strength, Nat. Commun. 13(1) (2022) 1102.

[81] S.J. Son, J.W. Lee, P. Asghari-Rad, G.H. Gu, F. Haftlang, H.S. Kim, A facile strengthening method by co-doping boron and nitrogen in CoCrFeMnNi high-entropy alloy, Mater. Sci. Eng. A 846 (2022).

[82] J. Chen, X. Zhou, W. Wang, B. Liu, Y. Lv, W. Yang, D. Xu, Y. Liu, A review on fundamental of high entropy alloys with promising high–temperature properties, J. Alloys Compd. 760 (2018) 15-30.

[83] Z.P. Xiong, I. Timokhina, E. Pereloma, Clustering, nano-scale precipitation and strengthening of steels, Prog. Mater. Sci. 118 (2021).

[84] L. Liu, Y. Zhang, J. Han, X. Wang, W. Jiang, C.T. Liu, Z. Zhang, P.K. Liaw, Nanoprecipitate-Strengthened High-Entropy Alloys, Adv. Sci. 8(23) (2021) e2100870.

[85] J.Y. He, H. Wang, H.L. Huang, X.D. Xu, M.W. Chen, Y. Wu, X.J. Liu, T.G. Nieh, K. An, Z.P. Lu, A precipitation-hardened high-entropy alloy with outstanding tensile properties, Acta Mater. 102 (2016) 187-196.

[86] T. Yang, Y.L. Zhao, Y. Tong, Z.B. Jiao, J. Wei, J.X. Cai, X.D. Han, D. Chen, A. Hu, J.J. Kai, K. Lu, Y. Liu, C.T. Liu, Multicomponent intermetallic nanoparticles and superb mechanical behaviors of complex alloys, Science 362(6417) (2018) 933-937.

[87] L.J. Wang, L. Wang, S.C. Zhou, Q. Xiao, Y. Xiao, X.T. Wang, T.Q. Cao, Y. Ren, Y.J. Liang, L. Wang, Y.F. Xue, Precipitation and micromechanical behavior of the coherent ordered nanoprecipitation strengthened Al-Cr-Fe-Ni-V high entropy alloy, Acta Mater. 216 (2021).

[88] T. Yang, Y.L. Zhao, L. Fan, J. Wei, J.H. Luan, W.H. Liu, C. Wang, Z.B. Jiao, J.J. Kai, C.T. Liu, Control of nanoscale precipitation and elimination of intermediate-temperature embrittlement in multicomponent high-entropy alloys, Acta Mater. 189 (2020) 47-59.

[89] R. Feng, Y. Rao, C. Liu, X. Xie, D. Yu, Y. Chen, M. Ghazisaeidi, T. Ungar, H. Wang, K. An, P.K. Liaw, Enhancing fatigue life by ductile-transformable multicomponent B2 precipitates in a high-entropy alloy, Nat. Commun. 12(1) (2021) 3588.

[90] X. Li, L. Lu, J. Li, X. Zhang, H. Gao, Mechanical properties and deformation mechanisms of gradient nanostructured metals and alloys, Nat. Rev. Mater. 5(9) (2020) 706-723.

[91] K. Lu, Stabilizing nanostructures in metals using grain and twin boundary architectures, Nat. Rev. Mater. 1(5) (2016).

[92] Z. Zeng, X. Li, D. Xu, L. Lu, H. Gao, T. Zhu, Gradient plasticity in gradient nano-grained metals, Extreme Mech. Lett. 8 (2016) 213-219.

[93] Z. Cheng, H. Zhou, Q. Lu, H. Gao, L. Lu, Extra strengthening and work hardening in gradient nanotwinned metals, Science 362(6414) (2018).

[94] J. Ding, Q. Li, J. Li, S. Xue, Z. Fan, H. Wang, X. Zhang, Mechanical behavior of structurally gradient nickel alloy, Acta Mater. 149 (2018) 57-67.

[95] Y. Ma, M. Yang, F. Yuan, X. Wu, A Review on Heterogeneous Nanostructures: A Strategy for Superior Mechanical Properties in Metals, Metals 9(5) (2019).

[96] B. Wu, H. Fu, X.Y. Zhou, L. Qian, J.S. Luo, J.M. Zhu, W.B. Lee, X.S. Yang, Severe plastic deformation-produced gradient nanostructured copper with a strengthening-softening transition, Mater. Sci. Eng. A 819 (2021) 141495.

[97] Y. Sun, Z. Hou, Z. Yao, Y. Hu, Gradient structure and mechanical behavior induced by multiple laser peening in 304 austenitic stainless steel, Int. J. Adv. Manuf. Tech. 120(5-6) (2022) 3383-3392.

[98] Y. Liu, J.P. Sun, Y.T. Fu, B.Q. Xu, B.J. Li, S.S. Xu, P.L. Huang, J.N. Cheng, Y. Han, J. Han, G.S. Wu, Tuning strength-ductility combination on selective laser melted 316L stainless steel through gradient heterogeneous structure, Addit. Manuf. 48 (2021).

[99] X. Chen, J.L. Zhang, M. Wang, W.Z. Wang, D. Zhao, H.M. Huang, Q. Zhao, X.F. Xu, H.X. Zhang, G.S. Huang, Research progress of heterogeneous structure magnesium alloys: A review, J. Magnes. Alloy. 12(6) (2024) 2147-2181.

[100] Z. An, S. Mao, Y. Liu, H. Zhou, Y. Zhai, Z. Tian, C. Liu, Z. Zhang, X. Han, Hierarchical grain size and nanotwin gradient microstructure for improved mechanical properties of a non-equiatomic CoCrFeMnNi high-entropy alloy, J. Mater. Sci. Technol. 92 (2021) 195-207.

[101] J.L. Dai, H.Y. Song, M.R. An, J.Y. Wang, Q. Deng, Y.L. Li, Atomic simulation of interaction mechanism between dislocation and amorphous phase in dual-phase crystalline/amorphous Mg/MgAl alloys, J. Appl. Phys. 127(13) (2020).

[102] Z.H. Han, S. Liang, J. Yang, R. Wei, C.J. Zhang, A superior combination of strength-ductility in CoCrFeNiMn high-entropy alloy induced by asymmetric rolling and subsequent annealing treatment, Mater. Charact. 145 (2018) 619-626.

[103] R. Wen, C. You, L. Zeng, H. Wang, X. Zhang, Achieving a unique combination of strength and ductility in CrCoNi medium-entropy alloy via heterogeneous gradient structure, J. Mater. Sci. 55(26) (2020) 12544-12553.

[104] L. Chen, T. Cao, R. Wei, K. Tang, C. Xin, F. Jiang, J. Sun, Gradient structure design to strengthen carbon interstitial Fe40Mn40Co10Cr10 high entropy alloys, Mater. Sci. Eng. A 772 (2020).

[105] L. Guo, W. Wu, S. Ni, Z. Yuan, Y. Cao, Z. Wang, M. Song, Strengthening the FeCoCrNiMo0.15 high entropy alloy by a gradient structure, J. Alloys Compd. 841 (2020).

[106] P. Sathiyamoorthi, H.S. Kim, High-entropy alloys with heterogeneous microstructure: Processing and mechanical properties, Prog. Mater. Sci. (2020) 100709.

[107] M.N. Hasan, Y.F. Liu, X.H. An, J. Gu, M. Song, Y. Cao, Y.S. Li, Y.T. Zhu, X.Z. Liao, Simultaneously enhancing strength and ductility of a high-entropy alloy via gradient hierarchical microstructures, Int. J. Plast. 123 (2019) 178-195.

[108] S.W. Wu, G. Wang, Q. Wang, Y.D. Jia, J. Yi, Q.J. Zhai, J.B. Liu, B.A. Sun, H.J. Chu, J. Shen, P.K. Liaw, C.T. Liu, T.Y. Zhang, Enhancement of strength-ductility trade-off in a high-entropy alloy through a heterogeneous structure, Acta Mater. 165 (2019) 444-458.

[109] Q. Pan, Zhang Liangxue, Feng Rui, Lu Qiuhong, An Ke , Chuang Andrew Chihpin , Poplawsky Jonathan D. , Liaw Peter K. , L. Lei., Gradient cell–structured high-entropy alloy

with exceptional strength and ductility, Science 374(6570) (2021) 984-989.

[110] H.W. Luan, L.F. Huang, J.Y. Kang, B.S. Luo, X.L. Yang, J.F. Li, Z.D. Han, J.J. Si, Y. Shao, J. Lu, K.F. Yao, Spinodal decomposition and the pseudo-binary decomposition in high-entropy alloys, Acta Mater. 248 (2023).

[111] Y. Yuan, W. Ma, Q.Q. Jin, Y.B. Ke, Y.S. Xie, Z.H. Bei, H.Y. Yu, P. Hedström, D.B. Sun, X. Xu, On the divergent effects of stress on the self-organizing nanostructure due to spinodal decomposition in duplex stainless steel, Mater. Sci. Eng. A 898 (2024).

[112] Y. Zhu, X. Wu, Heterostructured materials, Prog. Mater. Sci. 131 (2023) 101019.

[113] S. Guo, Phase selection rules for cast high entropy alloys: An overview, Mater. Sci. Technol. 31(10) (2015) 1223-1230.

[114] X.H. Du, W.P. Li, H.T. Chang, T. Yang, G.S. Duan, B.L. Wu, J.C. Huang, F.R. Chen, C.T. Liu, W.S. Chuang, Y. Lu, M.L. Sui, E.W. Huang, Dual heterogeneous structures lead to ultrahigh strength and uniform ductility in a Co-Cr-Ni medium-entropy alloy, Nat. Commun. 11(1) (2020) 2390.

[115] C. Schuh, T. Hufnagel, U. Ramamurty, Mechanical behavior of amorphous alloys, Acta Mater. 55(12) (2007) 4067-4109.

[116] Y. Ito, K. Edalati, Z. Horita, High-pressure torsion of aluminum with ultrahigh purity (99.9999%) and occurrence of inverse Hall-Petch relationship, Mater. Sci. Eng. A 679 (2017) 428-434.

[117] C. Brandl, T.C. Germann, A. Misra, Structure and shear deformation of metallic crystalline–amorphous interfaces, Acta Mater. 61(10) (2013) 3600-3611.

[118] H. Kou, J. Lu, Y. Li, High-strength and high-ductility nanostructured and amorphous metallic materials, Adv. Mater. 26(31) (2014) 5518-24.

[119] F.C. Li, T. Liu, J.Y. Zhang, S. Shuang, Q. Wang, A.D. Wang, J.G. Wang, Y. Yang, Amorphous–nanocrystalline alloys: fabrication, properties, and applications, Mater. Today Adv. 4 (2019) 100027.

[120] K. Lu, Nanocrystalline metals crystallized from amorphous solids: nanocrystallization, structure, and properties, Mater. Sci. Eng. R 16(4) (1996) 161-221.

[121] Á. Révész, Z. Kovács, Severe Plastic Deformation of Amorphous Alloys, Mater. Trans. 60(7) (2019) 1283-1293.

[122] H.W. Bi, A. Inoue, F.F. Han, Y. Han, F.L. Kong, S.L. Zhu, E. Shalaan, F. Al-Marzouki, A.L. Greer, Novel deformation-induced polymorphic crystallization and softening of Al-based amorphous alloys, Acta Mater. 147 (2018) 90-99.

[123] S.-W. Lee, M.-Y. Huh, E. Fleury, J.-C. Lee, Crystallization-induced plasticity of Cu–Zr containing bulk amorphous alloys, Acta Mater. 54(2) (2006) 349-355.

[124] L.L. Xiao, Z.Q. Zheng, S.W. Guo, P. Huang, F. Wang, Ultra-strong nanostructured CrMnFeCoNi high entropy alloys, Mater. Design 194 (2020) 108895.

[125] P. Hua, B. Wang, C. Yu, Y. Han, Q. Sun, Shear-induced amorphization in nanocrystalline NiTi micropillars under large plastic deformation, Acta Mater. 241 (2022).

[126] L. Wang, H. Wang, X. Zhou, H. Fu, J.U. Surjadi, S. Qu, X. Song, R. Fan, Y. Lu, Hierarchical crystalline–amorphous nanocomposites with high strength and large

deformability enabled by elemental diffusion, J. Mater. Sci. Technol. 171 (2024) 150-161.

[127] G. Wu, K.C. Chan, L. Zhu, L. Sun, J. Lu, Dual-phase nanostructuring as a route to high-strength magnesium alloys, Nature 545(7652) (2017) 80-83.

[128] G. Wu, S. Balachandran, B. Gault, W. Xia, C. Liu, Z. Rao, Y. Wei, S. Liu, J. Lu, M. Herbig, W. Lu, G. Dehm, Z. Li, D. Raabe, Crystal-Glass High-Entropy Nanocomposites with Near Theoretical Compressive Strength and Large Deformability, Adv. Mater. 32(34) (2020) 2002619.

[129] Y. Wang, Ju Li, A.V. Hamza, J. Troy W. Barbee, Ductile crystalline–amorphous nanolaminates, Proc. Nat. Acad. Sci. 104(27) (2007) 11155-11160.

[130] W.L. Li, N.R. Tao, K. Lu, Fabrication of a gradient nano-micro-structured surface layer on bulk copper by means of a surface mechanical grinding treatment, Scr. Mater. 59(5) (2008) 546-549.

[131] H.W. Huang, Z.B. Wang, J. Lu, K. Lu, Fatigue behaviors of AISI 316L stainless steel with a gradient nanostructured surface layer, Acta Mater. 87 (2015) 150-160.

[132] M. Jamalian, D.P. Field, Effects of shot peening parameters on gradient microstructure and mechanical properties of TRC AZ31, Mater. Character. 148 (2019) 9-16.

[133] M.H. Zhou, Y.H. Xu, Y. Liu, M. Duan, Z.Y. Xia, L.S. Huang, R.Z. Zhu, H. Ye, L.M. Peng, Y.J. Wu, Y. Liu, Microstructures and mechanical properties of Mg-15Gd-1Zn-0.4Zr alloys treated by ultrasonic surface rolling process, Mater. Sci. Eng. A 828 (2021).

[134] Y. Lin, J. Pan, H.F. Zhou, H.J. Gao, Y. Li, Mechanical properties and optimal grain size distribution profile of gradient grained nickel, Acta Mater. 153 (2018) 279-289.

[135] Z. Wang, L. Guo, W. Xia, Z. Yuan, Y. Cao, S. Ni, M. Song, An SEM-based approach to characterize the microstructural evolution in a gradient CoCrFeNiMo0.15 high-entropy alloy, Mater. Charact. 161 (2020).

[136] X. Wu, P. Jiang, L. Chen, F. Yuan, Y.T. Zhu, Extraordinary strain hardening by gradient structure, Proc. Nat. Acad. Sci. 111(20) (2014) 7197-201.

[137] R. Shi, H. Fu, K. Chen, W. Sun, Z. Wang, L. Qiao, X.-S. Yang, X. Pang, Combining synergetic effects of gradient nanotwins and nanoprecipitates in heterogeneous bronze alloy, Acta Mater. 229 (2022).

[138] F. Ren, P. Bellon, R.S. Averback, Nanoscale self-organization reaction in Cu–Ag alloys subjected to dry sliding and its impact on wear resistance, Tribol. Int. 100 (2016) 420-429.

[139] W. Zhu, C. Zhao, Y. Zhang, C.T. Kwok, J. Luan, Z. Jiao, F. Ren, Achieving exceptional wear resistance in a compositionally complex alloy via tuning the interfacial structure and chemistry, Acta Mater. 188 (2020) 697-710.

[140] L. Yang, Z. Cheng, W. Zhu, C. Zhao, F. Ren, Significant reduction in friction and wear of a high-entropy alloy via the formation of self-organized nanolayered structure, J. Mater. Sci. Technol. 73 (2021) 1-8.

[141] S.S. To, Hao Wang, W.B. Lee, Materials characterisation and mechanism of cutting in ultra-precision diamond turning, Springer, Berlin, 2018.

[142] X. Sun, P. Yao, S. Qu, S. Yu, X. Zhang, W. Wang, C. Huang, D. Chu, Material properties and machining characteristics under high strain rate in ultra-precision and ultra-high-speed

machining process: a review, Int. J. Adv. Manuf. Tech. 120(11-12) (2022) 7011-7042.

[143] J. Yuan, B. Lyu, W. Hang, Q. Deng, Review on the progress of ultra-precision machining technologies, Front. Mech. Eng. 12(2) (2017) 158-180.

[144] J. Zhang, J. Wang, G. Zhang, Z. Huo, Z. Huang, L. Wu, A review of diamond synthesis, modification technology, and cutting tool application in ultra-precision machining, Mater. Design 237 (2024).

[145] S.N. Monteiro, A.L.D. Skury, M.G. de Azevedo, G.S. Bobrovnitchii, Cubic boron nitride competing with diamond as a superhard engineering material – an overview, J. Mater. Res. Technol. 2(1) (2013) 68-74.

[146] K. Bouacha, M.A. Yallese, S. Khamel, S. Belhadi, Analysis and optimization of hard turning operation using cubic boron nitride tool, Int. J. Refract. Met. Hard Mater. 45 (2014) 160-178.

[147] D.A. Lucca, M.J. Klopfstein, O. Riemer, Ultra-Precision Machining: Cutting With Diamond Tools, J. Manuf. Sci. Eng. 142(11) (2020).

[148] G. Poulachon, A. Albert, M. Schluraff, I.S. Jawahir, An experimental investigation of work material microstructure effects on white layer formation in PCBN hard turning, Int. J. Mach. Tool. Manu. 45(2) (2005) 211-218.

[149] S. Zhang, Y. Zhou, H. Zhang, Z. Xiong, S. To, Advances in ultra-precision machining of micro-structured functional surfaces and their typical applications, Int. J. Mach. Tool. Manu. 142 (2019) 16-41.

[150] S. Yuan, B. Gan, L. Qian, B. Wu, H. Fu, H.-H. Wu, C.F. Cheung, X.-S. Yang, Gradient nanotwinned CrCoNi medium-entropy alloy with strength-ductility synergy, Scripta Mater. 203 (2021).

[151] F. Schneider, J. Das, B. Kirsch, B. Linke, J.C. Aurich, Sustainability in Ultra Precision and Micro Machining: A Review, Int. J.Pr. Eng. Man-GT 6(3) (2019) 601-610.

[152] L. Tian, M. Fu, W. Xiong, Microstructural Evolution of AlCoCrFeNiSi High-Entropy Alloy Powder during Mechanical Alloying and Its Coating Performance, Materials 11(2) (2018).

[153] J. Li, Q. Zhang, R. Huang, X. Li, H. Gao, Towards understanding the structure–property relationships of heterogeneous-structured materials, Scr. Mater. 186 (2020) 304-311.

[154] B. Rakhadilov, M. Maulet, M. Abilev, Z. Sagdoldina, R. Kozhanova, Structure and Tribological Properties of Ni–Cr–Al-Based Gradient Coating Prepared by Detonation Spraying, Coatings 11(2) (2021).

[155] L. Zhu, C. Wen, C. Gao, X. Guo, Z. Chen, J. Lu, Static and dynamic mechanical behaviors of gradient-nanotwinned stainless steel with a composite structure: Experiments and modeling, Int. J. Plast. 114 (2019) 272-288.

[156] D. Li, B. Wang, Z. Tong, L. Blunt, X. Jiang, On-machine surface measurement and applications for ultra-precision machining: a state-of-the-art review, Int. J. Adv. Manuf. Tech. 104(1-4) (2019) 831-847.

[157] E. Ma, T. Zhu, Towards strength–ductility synergy through the design of heterogeneous nanostructures in metals, Mater. Today 20(6) (2017) 323-331.

[158] D. Tang, J. Li, L. Wang, Z. Wang, C. Kong, H. Yu, Fabrication of gradient-structure CuNiBe alloy bars by laser remelting and water-cooling, Mater. Manuf. Processes 35(3) (2020) 337-345.

[159] J. Luo, W. Sun, R. Duan, W. Yang, K.C. Chan, F. Ren, X.-S. Yang, Laser surface treatment-introduced gradient nanostructured TiZrHfTaNb refractory high-entropy alloy with significantly enhanced wear resistance, J. Mater. Sci. Technol. 110 (2022) 43-56.

[160] A. Sharma, Sanjeev Kumar, e. Zoia Duriagina, Engineering Steels and High Entropy-Alloys, BoD–Books on Demand2020.

[161] G.H. Gu, E.S. Kim, H. Kwon, S. Son, R.E. Kim, T.G. Oh, H.S. Kim, Fabrication of multi-gradient heterostructured CoCrFeMnNi high-entropy alloy using laser metal deposition, Materials Science and Engineering: A 836 (2022).

[162] S. Lou, Y. Li, L. Zhou, X. Nie, G. He, Y. Li, W. He, Surface nanocrystallization of metallic alloys with different stacking fault energy induced by laser shock processing, Mater. Design 104 (2016) 320-326.

[163] W. Fu, Y. Huang, J. Sun, A.H.W. Ngan, Strengthening CrFeCoNiMn0.75Cu0.25 high entropy alloy via laser shock peening, Int. J. Plast. 154 (2022).

[164] X. Chen, Z. Han, K. Lu, Friction and Wear Reduction in Copper with a Gradient Nano-grained Surface Layer, ACS Appl. Mater. Inter. 10(16) (2018) 13829-13838.

[165] J.X. Hou, M. Zhang, S.G. Ma, P.K. Liaw, Y. Zhang, J.W. Qiao, Strengthening in Al0.25CoCrFeNi high-entropy alloys by cold rolling, Mater. Sc. Eng. A 707 (2017) 593-601.

[166] Z.M. Li, C.C. Tasan, K.G. Pradeep, D. Raabe, A TRIP-assisted dual-phase high-entropy alloy: Grain size and phase fraction effects on deformation behavior, Acta Mater. 131 (2017) 323-335.

[167] M. Chen, L. Lan, X. Shi, H. Yang, M. Zhang, J. Qiao, The tribological properties of Al0.6CoCrFeNi high-entropy alloy with the σ phase precipitation at elevated temperature, J. Alloys Compd. 777 (2019) 180-189.

[168] D. Kong, J. Guo, R. Liu, X. Zhang, Y. Song, Z. Li, F. Guo, X. Xing, Y. Xu, W. Wang, Effect of remelting and annealing on the wear resistance of AlCoCrFeNiTi0.5 high entropy alloys, Intermetallics 114 (2019).

[169] Z. Cheng, S. Wang, G. Wu, J. Gao, X. Yang, H. Wu, Tribological properties of high-entropy alloys: A review, Int. J. Miner. Metall. Mater. 29(3) (2022) 389.

[170] Q.F. He, J.G. Wang, H.A. Chen, Z.Y. Ding, Z.Q. Zhou, L.H. Xiong, J.H. Luan, J.M. Pelletier, J.C. Qiao, Q. Wang, L.L. Fan, Y. Ren, Q.S. Zeng, C.T. Liu, C.W. Pao, D.J. Srolovitz, Y. Yang, A highly distorted ultraelastic chemically complex Elinvar alloy, Nature 602(7896) (2022) 251-257.

[171] M. Sadeghilaridjani, M. Pole, S. Jha, S. Muskeri, N. Ghodki, S. Mukherjee, Deformation and tribological behavior of ductile refractory high-entropy alloys, Wear 478-479 (2021).

[172] P. Wang, Y. Bu, J. Liu, Q. Li, H. Wang, W. Yang, Atomic deformation mechanism and interface toughening in metastable high entropy alloy, Materials Today 37 (2020) 64-73.

[173] N. Peranio, Y.J. Li, F. Roters, D. Raabe, Microstructure and texture evolution in dual-phase steels: Competition between recovery, recrystallization, and phase transformation,

Materials Science and Engineering: A 527(16-17) (2010) 4161-4168.

[174] L. Kommel, P. Põdra, V. Mikli, B. Omranpour, Gradient microstructure in tantalum formed under the wear track during dry sliding friction, Wear 466-467 (2021).

[175] B.N. Mordyuk, G.I. Prokopenko, M.A. Vasylyev, M.O. Iefimov, Effect of structure evolution induced by ultrasonic peening on the corrosion behavior of AISI-321 stainless steel, Materials Science and Engineering: A 458(1-2) (2007) 253-261.

[176] C.-H. Tu, Y.-C. Lai, S.-K. Wu, Y.-H. Lin, The effects of annealing on severely cold-rolled equiatomic HfNbTiZr high entropy alloy, Mater. Lett. 303 (2021).

[177] B.B. Straumal, A.A. Mazilkin, B. Baretzky, Grain boundary complexions and pseudopartial wetting, Curr. Opin. Solid St. M. 20(5) (2016) 247-256.

[178] Z. Cheng, L. Yang, Z. Huang, T. Wan, M. Zhu, F. Ren, Achieving low wear in a μ-phase reinforced high-entropy alloy and associated subsurface microstructure evolution, Wear 474-475 (2021).

[179] D. Liang, C. Zhao, W. Zhu, P. Wei, F. Jiang, F. Ren, Significantly Enhanced Wear Resistance of an Ultrafine-Grained CrFeNi Medium-Entropy Alloy at Elevated Temperatures, Metall. Mater. Trans. 51(6) (2020) 2834-2850.

[180] C. Mathiou, A. Poulia, E. Georgatis, A.E. Karantzalis, Microstructural features and dry - Sliding wear response of MoTaNbZrTi high entropy alloy, Mater. Chem. Phys. 210 (2018) 126-135.

[181] Y. Wang, Y. Yang, H. Yang, M. Zhang, S. Ma, J. Qiao, Microstructure and wear properties of nitrided AlCoCrFeNi high-entropy alloy, Mater. Chem. Phys. 210 (2018) 233-239.

[182] Y. Liu, S. Ma, M.C. Gao, C. Zhang, T. Zhang, H. Yang, Z. Wang, J. Qiao, Tribological Properties of AlCrCuFeNi2 High-Entropy Alloy in Different Conditions, Metall. Mater. Trans. A 47(7) (2016) 3312-3321.

[183] L.M. Du, L.W. Lan, S. Zhu, H.J. Yang, X.H. Shi, P.K. Liaw, J.W. Qiao, Effects of temperature on the tribological behavior of Al0.25CoCrFeNi high-entropy alloy, J. Mater. Sci. Technol. 35(5) (2019) 917-925.

[184] Y. Huang, Z. Wang, Z. Xu, X. Zang, X. Chen, Microstructure and properties of TiNbZrMo high entropy alloy coating, Mater. Lett. 285 (2021).

[185] S. Alvi, F. Akhtar, High temperature tribology of CuMoTaWV high entropy alloy, Wear 426-427 (2019) 412-419.

[186] M. Pole, M. Sadeghilaridjani, J. Shittu, A. Ayyagari, S. Mukherjee, High temperature wear behavior of refractory high entropy alloys based on 4-5-6 elemental palette, J. Alloys Compd. 843 (2020).

[187] Y.X. Ye, C.Z. Liu, H. Wang, T.G. Nieh, Friction and wear behavior of a single-phase equiatomic TiZrHfNb high-entropy alloy studied using a nanoscratch technique, Acta Mater. 147 (2018) 78-89.

[188] Q.T.F. J., Review of oxidational wear: Part I: The origins of oxidational wear, Tribo. Int. 16(5) (1983) 257-271.

[189] R. Aghababaei, D.H. Warner, J.F. Molinari, Critical length scale controls adhesive wear mechanisms, Nat. Commun. 7 (2016) 11816.

[190] M. J., A discussion of oxidation, oxide thickness and oxide transfer in wear, Wear 40(3) (1976) 277-291.

[191] W.G. Burgers, On the process of transition of the cubic-body-centered modification into the hexagonal-close-packed modification of zirconium, Physica 1(7-12) (1934) 561-586.

[192] V. Riffet, B. Amadon, N. Bruzy, C. Denoual, Role of dislocations in the bcc-hcp transition under high pressure: A first-principles approach in beryllium, Phys. Rev. Mater. 4(6) (2020).

[193] A. Ojha, H. Sehitoglu, Critical stress for the bcc–hcp martensite nucleation in Ti–6.25at.%Ta and Ti–6.25at.%Nb alloys, Comp. Mater. Sci. 111 (2016) 157-162.

[194] P. Chen, F. Wang, B. Li, Transitory phase transformations during {101¯2} twinning in titanium, Acta Mater. 171 (2019) 65-78.

[195] X.S. Yang, S. Sun, T.Y. Zhang, The mechanism of bcc α′ nucleation in single hcp ε laths in the fcc γ → hcp ε → bcc α′ martensitic phase transformation, Acta Mater. 95 (2015) 264-273.

[196] X.S. Yang, S. Sun, H.H. Ruan, S.Q. Shi, T.Y. Zhang, Shear and shuffling accomplishing polymorphic fcc γ → hcp ε → bct α martensitic phase transformation, Acta Mater. 136 (2017) 347-354.

[197] H. Fu, S.Q. Yuan, W.T. Sun, J.Q. Wan, K.C. Chan, J.M. Zhu, X.S. Yang, A novel atomic movement mechanism of intersection-induced bct-α → bcc-α′ martensitic phase transformation, Scr. Mater. 204 (2021) 114153.

[198] H.K.D.H. Bhadeshia, Geometry of crystals, polycrystals, and phase transformations CRC press2017.

[199] M.S. Wechsler, On the theory of martensitic transformations. The generalized lattice invariant shear and the degeneracy of solutions for the cubic to tetragonal transformation, Acta Metall. 7 (1959) 793-802.

[200] T. Zhang, R.D. Zhao, F.F. Wu, S.B. Lin, S.S. Jiang, Y.J. Huang, S.H. Chen, J. Eckert, Transformation-enhanced strength and ductility in a FeCoCrNiMn dual phase high-entropy alloy, Mater. Sci. Eng. A 780 (2020) 139182.

[201] M. Smaga, F. Walther, D. Eifler, Deformation-induced martensitic transformation in metastable austenitic steels, Mater. Sci. Eng. A 483-484 (2008) 394-397.

[202] C. Luo, H. Yuan, Measurement and modeling of deformation-induced martensitic transformation in a metastable austenitic stainless steel under cyclic loadings, Acta Mater. 238 (2022) 118202.

[203] D. Fukui, N. Nakada, S. Onaka, Internal residual stress originated from Bain strain and its effect on hardness in Fe–Ni martensite, Acta Mater. 196 (2020) 660-668.

[204] J.S. Bowles, C.M. Wayman, The bain strain, lattice correspondences, and deformations related to martensitic transformations, Metall. Trans. (1972) 1113-1121.

[205] W.Q. Yang, J.S. Luo, H. Fu, C.F. Cheung, H.H. Ruan, X.S. Yang, bcc → hcp phase transition significantly enhancing the wear resistance of metastable refractory high-entropy alloy, Scr. Mater. 221 (2022) 114966.

[206] Y.S. He, J.B. Gao, Y.Z. He, K. Shin, The mechanisms of γ (fcc) → ε (hcp) → α′ (bcc) and direct γ (fcc) → α′ (bcc) martensitic transformation in a gradient austenitic stainless steel, J.

Mater. Sci. 57(8) (2022) 5230-5240.

[207] M. Durandurdu, Fcc-to-bct phase transformation of aluminum under triaxial stresses: an ab initio constant pressure study, Eur. Phys. J B 72(2) (2009) 241-245.

[208] G.B. Olson, M. Cohen., A general mechanism of martensitic nucleation: Part II. FCC→ BCC and other martensitic transformations, Metall. Trans. A 7 (1976) 1905-1914.

[209] A. Ishii, J. Li, S. Ogata, Shuffling-controlled versus strain-controlled deformation twinning: The case for HCP Mg twin nucleation, Int. J. Plast. 82 (2016) 32-43.

[210] J. Li, Q. Fang, B. Liu, Y. Liu, Transformation induced softening and plasticity in high entropy alloys, Acta Mater. 147 (2018) 35-41.

[211] Y. Zhang, N. Zhang, Y. Tang, Y. Cai, L. Lu, S. Luo, Multiple phase transitions in shock compressed high-entropy alloy Cr9Mn9Fe64Co9Ni9: Experiments and molecular dynamics simulations, Appl. Phys. Lett. 124(10) (2024).

[212] P. Agrawal, S. Shukla, S. Gupta, P. Agrawal, R.S. Mishra, Friction stir gradient alloying: A high-throughput method to explore the influence of V in enabling HCP to BCC transformation in a γ-FCC dominated high entropy alloy, Appl. Mater. Today 21 (2020).

[213] S.Y. Chen, Y. Tong, K.K. Tseng, J.W. Yeh, J.D. Poplawsky, J.G. Wen, M.C. Gao, G. Kim, W. Chen, Y. Ren, R. Feng, W.D. Li, P.K. Liaw, Phase transformations of HfNbTaTiZr high-entropy alloy at intermediate temperatures, Scr. Mater. 158 (2019) 50-56.

[214] J.M. Chen, X.S. Jiang, H.L. Sun, Z.Y. Shao, Y.J. Fang, R. Shu, Phase transformation and strengthening mechanisms of nanostructured high-entropy alloys, Nanotechnol. Rev. 10(1) (2021) 1116-1139.

[215] Q.H. Fang, Y. Chen, J. Li, C. Jiang, B. Liu, Y. Liu, P.K. Liaw, Probing the phase transformation and dislocation evolution in dual-phase high-entropy alloys, Int J Plasticity 114 (2019) 161-173.

[216] Y.F. Zhao, X.B. Feng, J.Y. Zhang, Y. Lu, S.H. Wu, Y.Q. Wang, K. Wu, G. Liu, J. Sun, Tailoring phase transformation strengthening and plasticity of nanostructured high entropy alloys, Nanoscale 12(26) (2020) 14135-14149.

[217] M. Kahle, M. Kleber, R. Jahn, Review of XRD-based quantitative analyses of clay minerals in soils: the suitability of mineral intensity factors, Geoderma 109(3) (2002) 191-205.

[218] L. Lu, V. Sahajwalla, C. Kong, D. Harris, Quantitative X-ray diffraction analysis and its application to various coals, Carbon 39(12) (2001) 1821-1833.

[219] J.T. Pürstl, H.O. Jones, T.E.J. Edwards, R.P. Thompson, F. Di Gioacchino, N.G. Jones, W.J. Clegg, On the extraction of yield stresses from micro-compression experiments, Mater. Sci. Eng. A 800 (2021).

[220] J. Pfetzing-Micklich, R. Ghisleni, T. Simon, C. Somsen, J. Michler, G. Eggeler, Orientation dependence of stress-induced phase transformation and dislocation plasticity in NiTi shape memory alloys on the micro scale, Mater. Sci. Eng. A 538 (2012) 265-271.

[221] Y.F. Zhang, Q. Li, M. Gong, S. Xue, J. Ding, J. Li, J. Cho, T. Niu, R. Su, N.A. Richter, H. Wang, J. Wang, X. Zhang, Deformation behavior and phase transformation of nanotwinned Al/Ti multilayers, Appl. Surf. Sci. 527 (2020).

[222] T. Omori, K. Ando, I. Ohnuma, R. Kainuma, K. Ishida, BCC-HCP-FCC Multiple Transformations and ε Loop in the Fe-Cr-Co-Mn System, J. Phase Equilib. Diff. 42(5) (2021) 735-747.

[223] B. Wang, H.M. Urbassek, Phase transitions in an Fe system containing a bcc/fcc phase boundary: An atomistic study, Phys. Rev. B 87(10) (2013) 104108.

[224] N. Şarlı, Y. Dağdemir, B. Saatçi, Small Thermal Magnetization Loop Revealed by Bain Strain, J. Supercond. Novel Magn. 32(12) (2019) 3933-3938.

[225] H. Wu, G. Fan, An overview of tailoring strain delocalization for strength-ductility synergy, Prog. Mater. Sci. 113 (2020) 100675.

[226] L.J. Zhang, P.F. Yu, J.T. Fan, Y.C. Li, Y.P. Gao, G. Li, High pressure induced the polymorphism phase transition in the Fe40Mn40Co10Cr10 multi-principal element alloy, Intermetallics 136 (2021).

[227] L. Kaushik, M.S. Kim, J. Singh, J.H. Kang, Y.U. Heo, J.Y. Suh, S.H. Choi, Deformation mechanisms and texture evolution in high entropy alloy during cold rolling, Int. J. Plast. 141 (2021) 102989.

[228] A.K. Chandan, S. Tripathy, B. Sen, M. Ghosh, S. Ghosh Chowdhury, Temperature dependent deformation behavior and stacking fault energy of Fe40Mn40Co10Cr10 alloy, Scr. Mater. 199 (2021) 113891.

[229] To S S, Wang H, L.W. B., Materials characterisation and mechanism of micro-cutting in ultra-precision diamond turning, Berlin: Springer2018.

[230] M. Efe, W. Moscoso, K.P. Trumble, W. Dale Compton, S. Chandrasekar, Mechanics of large strain extrusion machining and application to deformation processing of magnesium alloys, Acta Mater. 60(5) (2012) 2031-2042.

[231] Y. Guo, C. Saldana, W. Dale Compton, S. Chandrasekar, Controlling deformation and microstructure on machined surfaces, Acta Mater. 59(11) (2011) 4538-4547.

[232] H. Luan, X. Zhang, H. Ding, F. Zhang, J.H. Luan, Z.B. Jiao, Y.C. Yang, H. Bu, R. Wang, J. Gu, C. Shao, Q. Yu, Y. Shao, Q. Zeng, N. Chen, C.T. Liu, K.F. Yao, High-entropy induced a glass-to-glass transition in a metallic glass, Nat. Commun. 13(1) (2022) 2183.

[233] Y.W. Qi, Z.P. Luo, B. Zhang, X.Y. Li, Plastic deformation induced strong and stable nanograined face-centered cubic Co, Acta Mater. 286 (2025) 120691.

[234] Y. Jiang, X. Zhou, X.Y. Li, K. Lu, Stabilizing nanograined austenitic stainless steel with grain boundary relaxation, Acta Mater. 256 (2023) 119134.

[235] X. Zhang, H. Wang, R.O. Scattergood, J. Narayan, C.C. Koch, A.V. Sergueeva, A.K. Mukherjee, Studies of deformation mechanisms in ultra-fine-grained and nanostructured Zn, Acta Mater. 50(19) (2002) 4823-4830.

[236] T.H. Fang, N.R. Tao, Martensitic transformation dominated tensile plastic deformation of nanograins in a gradient nanostructured 316L stainless steel, Acta Mater. 248 (2023) 118780.

[237] L. Qian, W. Yang, J. Luo, Y. Wang, K.C. Chan, X.S. Yang, Amorphous Thickness-Dependent Strengthening-Softening Transition in Crystalline-Amorphous Nanocomposites, Nano Lett. 23(23) (2023) 11288-11296.

[238] S.N. Naik, S.M. Walley, The Hall–Petch and inverse Hall–Petch relations and the hardness of nanocrystalline metals, J. Mater. Sci. 55(7) (2019) 2661-2681.

[239] L.G. Sun, G. Wu, Q. Wang, J. Lu, Nanostructural metallic materials: Structures and mechanical properties, Mater. Today 38 (2020) 114-135.

[240] H.Y. Song, J.Y. Wang, M.R. An, M.X. Xiao, Y.L. Li, Effect of stacking fault and amorphous boundary on plastic deformation mechanism of dual-phase nanostructure Mg alloys, Comp. Mater. Sci. 162 (2019) 199-205.

[241] M.A. Meyers, A. Mishra, D.J. Benson, Mechanical properties of nanocrystalline materials, Prog. Mater. Sci. 51(4) (2006) 427-556.

[242] G. Wu, J. Zhang, C. Liu, Q. Wang, J. Lu, Ductility of an ultrastrong glass-crystal nano-dual-phase alloy in sub-micron, Scr. Mater. 183 (2020) 17-21.

[243] B. Wei, W. Wu, D. Xie, M. Nastasi, J. Wang, Strength, plasticity, thermal stability and strain rate sensitivity of nanograined nickel with amorphous ceramic grain boundaries, Acta Mater. 212 (2021) 116918.

[244] G. Wu, C. Liu, L. Sun, Q. Wang, B. Sun, B. Han, J.J. Kai, J. Luan, C.T. Liu, K. Cao, Y. Lu, L. Cheng, J. Lu, Hierarchical nanostructured aluminum alloy with ultrahigh strength and large plasticity, Nat. Commun. 10(1) (2019) 5099.

[245] X.-S. Yang, S. Yuan, H. Fu, Y.-J. Wang, Grain boundary-mediated plasticity accommodating the cracking process in nanograined gold: In situ observations and simulations, Scr. Mater. 194 (2021).

[246] G. Wu, C. Liu, Y.Q. Yan, S. Liu, X. Ma, S. Yue, Z.W. Shan, Elemental partitioning-mediated crystalline-to-amorphous phase transformation under quasi-static deformation, Nat. Commun. 15(1) (2024) 1223.

[247] Y. Zou, H. Ma, R. Spolenak, Ultrastrong ductile and stable high-entropy alloys at small scales, Nat. Commun. 6 (2015) 7748.

[248] S.A. V, S. C, V.R. Z, M.A. K, Structure and properties of amorphous and nanocrystalline NiTi prepared by severe plastic deformation and annealing, Mater. Sci. Eng. A 339(1-2) (2003) 159-165.

[249] C.M. Grigorian, T.J. Rupert, Critical cooling rates for amorphous-to-ordered complexion transitions in Cu-rich nanocrystalline alloys, Acta Mater. 206 (2021).

[250] Q. Jiang, H. Liu, J. Li, D. Yang, Y. Zhang, W. Yang, Atomic-level understanding of crystallization in the selective laser melting of Fe50Ni50 amorphous alloy, Addit. Manuf. 34 (2020) 101369.

[251] W. Sun, J. Luo, Y.Y. Chan, J.H. Luan, X.-S. Yang, An extraordinary-performance gradient nanostructured Hadfield manganese steel containing multi-phase nanocrystalline-amorphous core-shell surface layer by laser surface processing, J. Mater. Sci. Technol. 134 (2023) 209-222.

[252] J. Luo, W. Sun, D. Liang, W. Yang, K.C. Chan, F. Ren, X.-S. Yang, An ultra-strong and ductile crystalline-amorphous nanostructured surface layer on TiZrHfTaNb0.2 high-entropy alloy by laser surface processing, Mater. Design 227 (2023) 111710.

[253] T. Han, Y. Liu, M. Liao, D. Yang, N. Qu, Z. Lai, J. Zhu, Refined microstructure and

enhanced mechanical properties of AlCrFe2Ni2 medium entropy alloy produced via laser remelting, J. Mater. Sci. Technol. 99 (2022) 18-27.

[254] F.Y. Shu, S. Liu, H.Y. Zhao, W.X. He, S.H. Sui, J. Zhang, P. He, B.S. Xu, Structure and high-temperature property of amorphous composite coating synthesized by laser cladding FeCrCoNiSiB high-entropy alloy powder, J. Alloys Compd. 731 (2018) 662-666.

[255] S. Zhao, B. Kad, C.E. Wehrenberg, B.A. Remington, E.N. Hahn, K.L. More, M.A. Meyers, Generating gradient germanium nanostructures by shock-induced amorphization and crystallization, P Natl. Acad. Sci. USA 114(37) (2017) 9791-9796.

[256] B.-J. Lee, C.S. Lee, J.C. Lee, Stress induced crystallization of amorphous materials and mechanical properties of nanocrystalline materials: a molecular dynamics simulation study, Acta Mater. 51(20) (2003) 6233-6240.

[257] Z. Kovács, P. Henits, A.P. Zhilyaev, Á. Révész, Deformation induced primary crystallization in a thermally non-primary crystallizing amorphous Al85Ce8Ni5Co2 alloy, Scr. Mater. 54(10) (2006) 1733-1737.

[258] B. Yao, S.E. Liu, L. Liu, L. Si, W.H. Su, Y. Li, Mechanism of mechanical crystallization of amorphous Fe–Mo–Si–B alloy, J. Appl. Phys. 90(3) (2001) 1650-1654.

[259] Y. Zhao, X. Wei, Y. Zhang, J. Wang, D. Huo, Crystallization of amorphous materials and deformation mechanism of nanocrystalline materials under cutting loads: A molecular dynamics simulation approach, J. Non Cryst. Solids 439 (2016) 21-29.

[260] X. Wang, Y. Fu, Y. Wu, J. Wang, J. Fan, F. Zhang, H. Ruan, Y. Wu, Crystalline-amorphous-crystalline two-step phase transformation and the resulting supra-nano structure in a metastable iron-based alloy, Acta Mater. 266 (2024) 119690.

[261] K. Choi, J.W. Choi, D.Y. Kim, N.M. Hwang, Effect of coalescence on the grain coarsening during liquid-phase sintering of TaC–TiC–Ni cermets, Acta Mater. 48(12) (2000) 3125-3129.

[262] M. Jin, A.M. Minor, E.A. Stach, J.W. Morris, Direct observation of deformation-induced grain growth during the nanoindentation of ultrafine-grained Al at room temperature, Acta Mater. 52(18) (2004) 5381-5387.

[263] J.J. De Yoreo, In-situ liquid phase TEM observations of nucleation and growth processes, Prog. Cryst. Growth Charact. Mater. 62(2) (2016) 69-88.

[264] L. Li, Z. Li, A. Kwiatkowski da Silva, Z. Peng, H. Zhao, B. Gault, D. Raabe, Segregation-driven grain boundary spinodal decomposition as a pathway for phase nucleation in a high-entropy alloy, Acta Mater. 178 (2019) 1-9.

[265] Z.P. Lu, H. , S.C.N. Tan, Y. Li., The correlation between reduced glass transition temperature and glass forming ability of bulk metallic glasses, Scr. Mater. 42(7) (2000) 667-673.

[266] M. Laurent-Brocq, A. Akhatova, L. Perrière, S. Chebini, X. Sauvage, E. Leroy, Y. Champion, Insights into the phase diagram of the CrMnFeCoNi high entropy alloy, Acta Mater. 88 (2015) 355-365.

[267] J. Yang, J. Lian, Q. Dong, Z. Guo, Nano-structured films formed on the AISI 329 stainless steel by Nd-YAG pulsed laser irradiation, Appl. Surf. Sci. 229(1-4) (2004) 2-8.

[268] K. Saeidi, X. Gao, Y. Zhong, Z.J. Shen, Hardened austenite steel with columnar sub-grain structure formed by laser melting, Mater. Sci. Eng. A 625 (2015) 221-229.

[269] Elmer J W, Allen S M, E.T. W., Microstructural development during solidification of stainless steel alloys, Metall. Mater. Trans. A 20(10) (1989) 2117-2131.

[270] C. Cui, J. Hu, Y. Liu, K. Gao, Z. Guo, Formation of nano-crystalline and amorphous phases on the surface of stainless steel by Nd:YAG pulsed laser irradiation, Appl. Surf. Sci. 254(21) (2008) 6779-6782.

[271] R.L. Snezhnoi, A.A. Zhukov, A.N. Kokora, Formation of amorphous phase in cast iron, Met. Sci. Heat Treat. 22(12) (1980) 900-901.

[272] S. Guo, Y. Liu, Estimation of critical cooling rates for formation of amorphous alloys from critical sizes, J. Non Cryst. Solids 358(20) (2012) 2753-2758.

[273] R. Su, D. Neffati, J. Cho, Z. Shang, Y. Zhang, J. Ding, Q. Li, S. Xue, H. Wang, Y. Kulkarni, X. Zhang, High-strength nanocrystalline intermetallics with room temperature deformability enabled by nanometer thick grain boundaries Sci. Adv. 7(27) (2021) 8288.

[274] Ming K, Zhu Z, Zhu W, Fang B, Wei B, Liaw PK, Wei X, Wang J, Z. S., Enhancing strength and ductility via crystalline-amorphous nanoarchitectures in TiZr-based alloys, Sci. Adv. 8(10) (2022) 2884.

[275] J.T. Fan, A.Y. Chen, M.W. Fu, J. Lu, A novel structural gradient metallic glass composite with enhanced mechanical properties, Scr. Mater. 61(6) (2009) 608-611.

[276] H. Shahmir, M. Nili-Ahmadabadi, A. Shafiee, M. Andrzejczuk, M. Lewandowska, T.G. Langdon, Effect of Ti on phase stability and strengthening mechanisms of a nanocrystalline CoCrFeMnNi high-entropy alloy, Mater. Sci. Eng. A 725 (2018) 196-206.

[277] H. Shahmir, J. He, Z. Lu, M. Kawasaki, T.G. Langdon, Effect of annealing on mechanical properties of a nanocrystalline CoCrFeNiMn high-entropy alloy processed by high-pressure torsion, Mater. Sci. Eng. A 676 (2016) 294-303.

[278] F. Yin, G.J. Cheng, R. Xu, K. Zhao, Q. Li, J. Jian, S. Hu, S. Sun, L. An, Q. Han, Ultrastrong nanocrystalline stainless steel and its Hall-Petch relationship in the nanoscale, Scripta Mater. 155 (2018) 26-31.

[279] H.S. Chou, X.H. Du, C.J. Lee, J.C. Huang, Enhanced mechanical properties of multilayered micropillars of amorphous ZrCuTi and nanocrystalline Ta layers, Intermetallics 19(7) (2011) 1047-1051.

[280] X. Xi, G. Dong, L. Wang, J. Hu, C. Shen, J. Wang, W. Xu, Formation mechanism of faulted bands and its effect on α′-martensitic transformation, Mater. Design 224 (2022) 111321.

[281] J.-K. Kim, M.-H. Kwon, B.C. De Cooman, On the deformation twinning mechanisms in twinning-induced plasticity steel, Acta Mater. 141 (2017) 444-455.

[282] H. Idrissi, K. Renard, L. Ryelandt, D. Schryvers, P.J. Jacques, On the mechanism of twin formation in Fe–Mn–C TWIP steels, Acta Mater. 58(7) (2010) 2464-2476.

[283] J. Vierke, G. Schumacher, V.P. Pilyugin, I.A. Denks, I. Zizak, C. Wolf, N. Wanderka, M. Wollgarten, J. Banhart, Deformation-induced crystallization in amorphous Al85Ni10La5 alloy, J. Alloys Compd. 493(1-2) (2010) 683-691.

[284] R. Su, D. Neffati, Y. Zhang, J. Cho, J. Li, H. Wang, Y. Kulkarni, X. Zhang, The influence of stacking faults on mechanical behavior of advanced materials, Mater. Sci. Eng. A 803 (2021) 140696.

[285] K. Ming, W. Lu, Z. Li, X. Bi, J. Wang, Amorphous bands induced by low temperature tension in a non-equiatomic CrMnFeCoNi alloy, Acta Mater. 188 (2020) 354-365.

[286] S. Cheng, Y. Zhao, Y. Guo, Y. Li, Q. Wei, X.L. Wang, Y. Ren, P.K. Liaw, H. Choo, E.J. Lavernia, High Plasticity and Substantial Deformation in Nanocrystalline NiFe Alloys Under Dynamic Loading, Adv. Mater. 21(48) (2009) 5001-5004.

[287] X.M. Luo, X.F. Zhu, G.P. Zhang, Nanotwin-assisted grain growth in nanocrystalline gold films under cyclic loading, Nat. Commun. 5 (2014) 3021.

[288] Z. Shan, E. A. Stach, J. M. K. Wiezorek, J. A. Knapp, D. M. Follstaedt, S.X. Mao., Grain boundary-mediated plasticity in nanocrystalline nickel, Science 305(5684) (2004) 654-657.